UNIVERSITÄT BERN

Graduate School for Cellular and Biomedical Sciences

University of Bern

# Characterizing $Na_v1.5$ expression, organization, and electrical behavior in cardiomyocyte domains

PhD Thesis submitted by

**Sarah Helena Vermij**

from **the Netherlands**

for the degree of

PhD in Biomedical Sciences

Supervisor

Prof. Dr. Hugues Abriel

Institute of Biochemistry and Molecular Medicine

Faculty of Medicine of the University of Bern

Co-advisor

Prof. Dr. Stephan Rohr

Department of Physiology

Faculty of Medicine of the University of Bern

Accepted by the Faculty of Medicine, the Faculty of Science and the Vetsuisse Faculty of the University of Bern at the request of the Graduate School for Cellular and Biomedical Sciences

Bern, Dean of the Faculty of Medicine

Bern, Dean of the Faculty of Science

Bern, Dean of the Vetsuisse Faculty Bern

# ABSTRACT

Proper function of the heart depends on the function of voltage-gated ion channels. These channels open and close in a tightly regulated way. The resulting ion currents change the membrane potential and shape the action potential, which initiates cardiac muscle contraction. The sodium channel $Na_v1.5$ is especially important as it generates the initial upstroke of the action potential. In cardiomyocytes, it is expressed in different membrane domains, including the intercalated disc, where two cardiomyocytes are mechanically and electrically coupled; the lateral membrane; and possibly at the T-tubules, which are invaginations of the lateral membrane. Many different proteins and molecules bind $Na_v1.5$, together forming a macromolecular complex, and modulate $Na_v1.5$ expression and/or function. Mutations in the $Na_v1.5$-encoding gene *SCN5A* can confer a loss or gain of channel function, and are associated with several heart rhythm disorders, including Brugada syndrome, long-QT syndrome type 3 (LQTS3), and sick-sinus syndrome. The mechanisms that lead to this phenotypic variability remain unknown. Since $Na_v1.5$ occurs at different cardiomyocyte membrane domains and several interacting proteins are specific to a domain, we hypothesize that the effects of a mutation depend on the subcellular location of $Na_v1.5$ and the composition of the macromolecular complex.

This thesis aims to (1) determine $Na_v1.5$ cluster organization in cardiomyocyte membrane domains from mice with different genetic backgrounds using single-molecule localization techniques; (2) contribute to the fundamental understanding of cardiomyocyte excitability by assessing voltage-gated ion channel expression with next-generation RNA sequencing; and (3) assess passive electrical properties of T-tubules and the effects of a large T-tubular sodium current with an *in silico* model. In addition, this thesis contains two thorough literature reviews on the cardiac intercalated disc and T-tubules.

Firstly, we show that $Na_v1.5$ is expressed in T-tubules of wild-type cells using single-molecule localization microscopy and computational modeling techniques. We observed that $Na_v1.5$ cluster organization and density partly depend on the presence of the large scaffolding protein dystrophin and on the three C-terminal amino acids of $Na_v1.5$, Ser-Ile-Val. Cardiomyocytes expressing C-terminally truncated $Na_v1.5$ (ΔSIV) display a loss of $Na_v1.5$ expression at the lateral membrane and particularly at the lateral membrane groove compared to wild-type cells. Dystrophin-deficient cardiomyocytes also display a reduction of $Na_v1.5$ expression at the lateral membrane, but no groove-specific reduction, and most notably an increase of T-tubular $Na_v1.5$ expression. $Na_v1.5$ cluster shapes are less complex in dystrophin-deficient cells at the lateral membrane and inside the cell compared to wild type. ΔSIV cells show this effect only inside the cells, not at the lateral membrane.

Secondly, we show in murine cardiomyocytes of Black/6J mice that of the voltage-gated sodium channels, mRNAs are expressed encoding mainly $Na_v1.5$ and $Na_v1.4$, and a small amount of $Na_v2.1$-

encoding mRNA. No other isoforms were detected. Of the β-subunits, only $\beta_1$- and $\beta_4$-encoding mRNA are found.

Thirdly, we assessed electrical properties of T-tubules. We compared the depolarization delay of a deep T-tubular segment to the mouth of a T-tubule upon a large depolarizing voltage step reminiscent of the upstroke of the cardiac action potential. We chose to compare the time to reach the activation threshold of voltage-gated calcium channels as these channels are highly expressed in T-tubules and crucial for initiating cardiomyocyte contraction. Deep inside the T-tubule, the activation threshold of voltage-gated calcium channels was reached only 10 microseconds later than at the mouth of the T-tubule. This delay increased 10-20 times when we introduced constrictions. Then, we introduced a large sodium current to the model. We show that the sodium current is smaller deep inside the T-tubule than at the mouth due to the positive extracellular potential, which decreases the driving force of the channels. In the constricted tubules, we observed a stronger sodium current self-attenuation, but an increase of peak sodium current in the first constriction due to an increase in open probability and driving force.

In conclusion, these studies contribute to the fundamental understanding of voltage-gated sodium channel composition, organization, and function in cardiomyocytes, with a focus on $Na_v1.5$. Exciting subjects of further study include the functional implications of the changes in $Na_v1.5$ cluster organization in ΔSIV and dystrophin-deficient mice, the functional contributions of $Na_v1.4$, and $\beta_1$- and $\beta_4$-subunits to murine cardiomyocyte function, and the composition of voltage-gated ion channels in human cardiomyocytes.

# TABLE OF CONTENTS

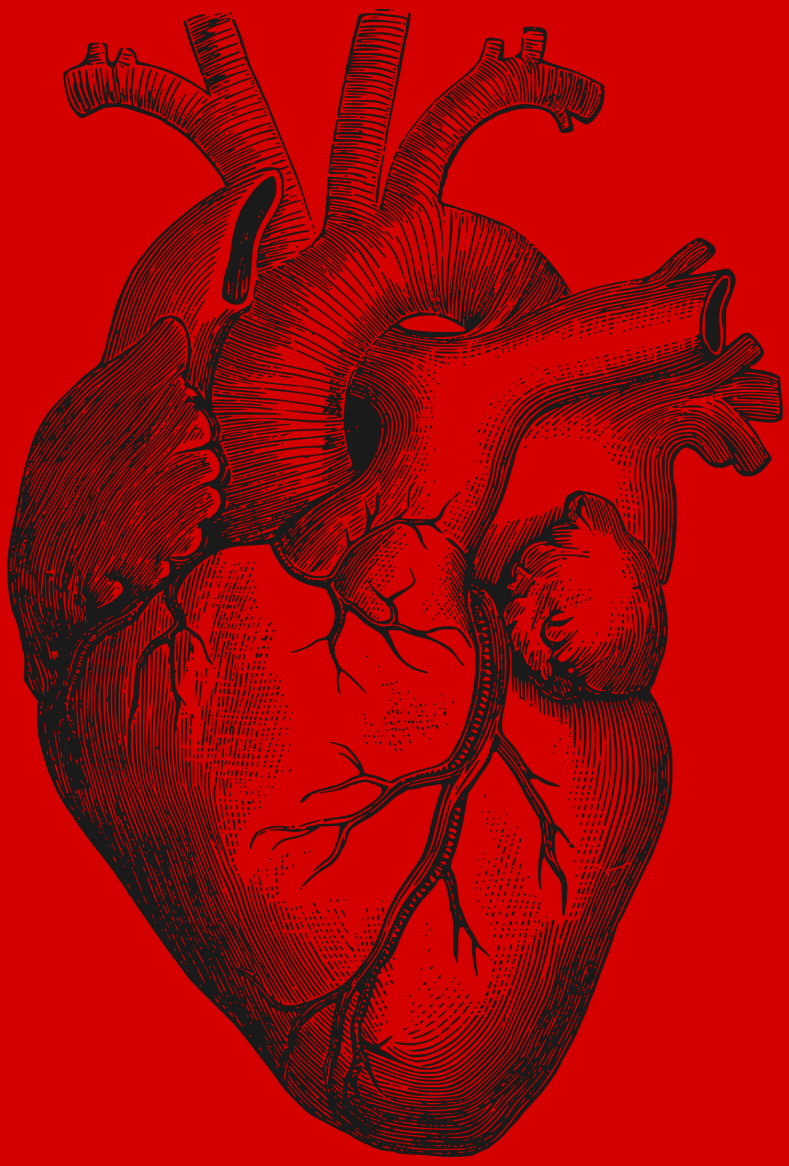

# INTRODUCTION

# 1. INTRODUCTION

This chapter provides a broad introduction to the cardiac field. After discussing the basic anatomy and function of the heart, I will describe the history of our understanding of the heart from the ancient Egyptians to the beginning of the twentieth century. Then, current understanding of cardiac function will be discussed concisely with a special focus on the cardiac sodium channel $Na_v1.5$. Lastly, three domains of the cardiomyocyte will be discussed in detail: the lateral membrane, the intercalated disc, and the T-tubules. Two already published review articles make up the chapters on the intercalated disc and the T-tubules.

## 1.1 Basic anatomy and function of the heart

The heart is a muscular organ that pumps blood to the lungs and the rest of the body to supply organs with oxygen and remove metabolites. Deoxygenated blood enters the right atrium via the venae cavae and flows into the right ventricle, which pumps the blood into the truncus pulmonalis towards the lungs. Oxygenated blood in turn enters the left atrium via the pulmonary veins, and flows into the left ventricle, which pumps the blood into the aorta. Valves prevent the backflow of blood from the ventricle into the atria and from the main arteries into the ventricles. The cardiac muscle itself draws oxygen and nutrients from coronary arteries, the main coronary arteries sprouting from the aorta (**Figure 1**).[4,22]

This thesis aims to contribute to the understanding of the etiology and pathophysiology of cardiac arrhythmias. Arrhythmias are defined as improper beating of the heart, whether irregular, too fast, or too slow, and can arise when the electrical processes in cardiomyocytes are disturbed. To contribute to the fundamental understanding of the mechanisms leading to cardiac arrhythmias, this thesis focuses on the passive electrical behavior of cardiomyocytes, their ion channels, and especially the voltage-gated sodium channel $Na_v1.5$. Before introducing these concepts, however, this introduction first lays out the historical context of the cardiac field.

## 1.2 From poetry to science: A short history of the heart

The history of cardiac physiology and anatomy as it told by science history books and articles is a story about men with – from our modern Western perspective – creative or downright silly ideas of cardiac anatomy and function, which developed into the concepts we are familiar with today in all but a straight line. It is worthwhile to be aware of this history, because science as we know it today is a "man-made construct that answers to certain needs, ideals, and goals"[23]. Our paradigms, epistemological or otherwise, are therefore neither absolute nor timeless.

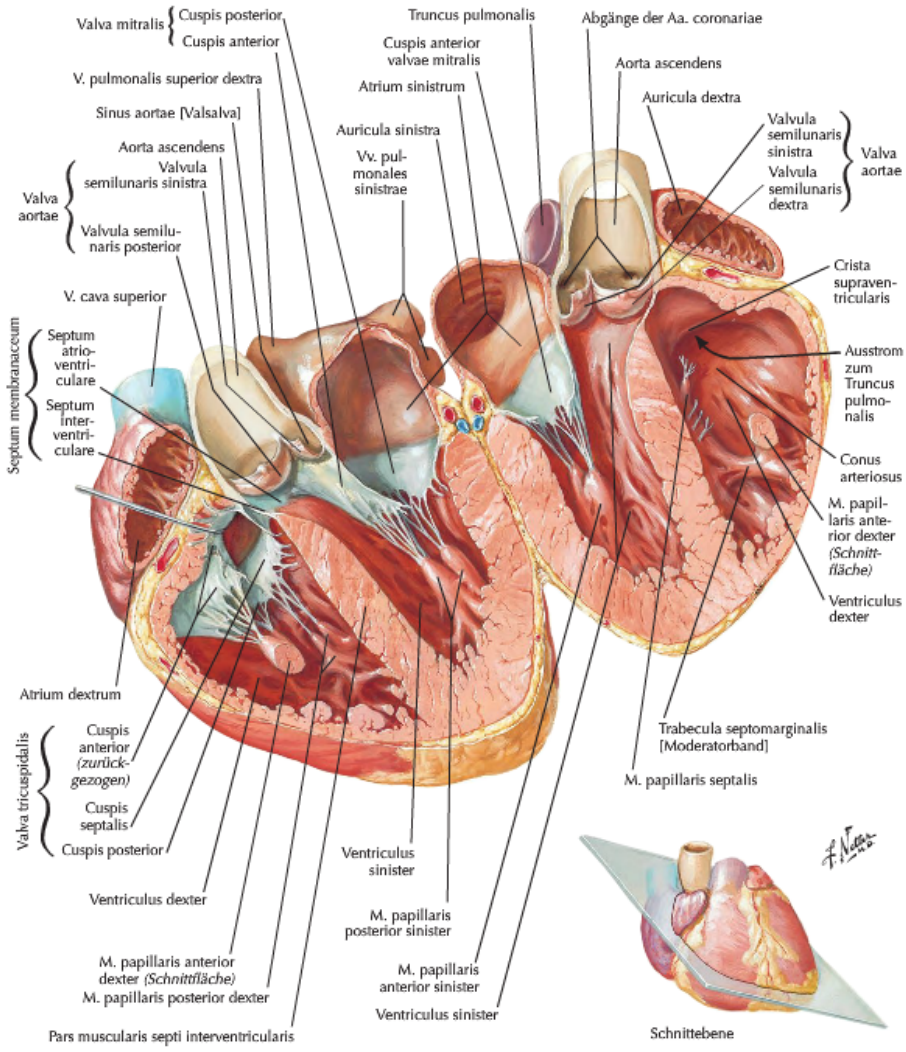


**Figure 1. Structure of the human heart.** Left and right atria and ventricles, veins and arteries, and valves are clearly indicated. Note the papillary muscles attached to the atrioventricular valves, the origin of the coronary arteries in the aorta ascendens, the epicardial adipose tissue, and the differences in wall thickness between right and left ventricles. Reprinted from Netter 2014[4,5].

Important to note is that we cannot speak of "science" or "scientists" before the 17th century. During the 16th and 17th century, some very influential thinkers – Copernicus, Descartes, Galilei, Newton – published their seminal works that would vastly change the general philosophical presumptions about nature and how nature functioned, a process named the Scientific Revolution[23]. Before that, the men I cite in this overview may be called philosophers, natural historians (historia: the study of nature), and before the first philosopher Pythagoras saw the light of day, those who wrote or transmitted anything in ancient Greece and Egypt might be rightfully called poets. To all of them, religion played a large role.

Only since the Scientific Revolution, the theories put forward are recognizable to us, whereas before that time the questions we ask now did not even exist. Since then, more and more conditions for science to thrive have been met: measuring techniques, money, scientific journals and societies[23].

The following chapters give an overview of cardiac anatomy, physiology, and arrhythmias from the first written sources from the Near East and Europe until the start of the twentieth century, with special attention to the historical context where relevant. For the sake of brevity, history of the heart in other parts of the world is not included.

### 1.2.1 Ancient Egypt up to the Renaissance

This history starts with the ancient Egyptian Ebers papyrus, the oldest known anatomical manuscript from 3500 BC. It describes the human heart as the center of the vascular system and the origin of all body channels transporting blood, urine, air, and feces[1]. Although cardiac anatomical structures are not described, the pulse was related to the contractility of the heart, and the heart was thought to house human intelligence[1]. The Egyptian Books of the Dead state that the heart recorded the good and the bad actions of a human's life. The god Anubis would weigh the heart of the deceased against the feather of truth on the scale of Ma'at. If the heart was lighter than the feather, the deceased could continue her journey towards immortality, but if not, the goddess Ammit, a lion-hippopotamus-crocodile tribrid, would eat it, and the soul of the deceased would become restless forever.[24,25]

About 800 BC, Homer was the first ancient Greek to mention the role of the heart in his epic poems *Iliad* and *Odyssey*. He attributed the source of human courage and bravery to the heart[1], and showed that the battlefield was a source of anatomical knowledge. In *Iliad*: "The spear was fixed in his heart, which had not yet stopped beating and shook it to the very butt till at last the god of battle stilled it with his heavy hand."[26] Moreover, he might have published the first case report of pericarditis as he wrote "the hairy hearts of hoary heroes". If this sentence is to be taken literal, it may relate to the "hairy" appearance of a heart due to pericarditis, a common complication of tuberculosis, which was prevalent in those days. Greek soldiers may have observed this as they were accustomed to opening the chest of their slain enemies with an axe[26].

The Greeks believed that nature did not depend on the wishes of the gods, or in other words, that it could be understood. They defined nature as the forces that shape reality[23]. In the fifth century BC, during the pre-Hippocratic area, two theories about the heart coexisted. Firstly, Alcmaeon might have been one of the first to perform a detailed anatomical study (on animals), and vaguely distinguished arteries from veins. He attributed the center of the being, soul, mind, and consciousness to the brain. Secondly, Empedocles accorded with the Egyptians as he stated that the heart was the origin of soul and mind, pumping air through the body[1,23]. Diogenes, in turn, mentioned that air and blood coexisted, and again denied the heart the position as the center of the vascular system[1].

Around 460 BC, the Hippocratic era commenced. *On the heart* (Περί Καρδίης) is one of the Hippocratic writings – but it's impossible to tell whether Hippocrates wrote it himself[1,23]. The writings stated that diseases were not only caused by gods or sorcery but could also have natural causes[23].

Using scientific-like evidence from animal dissections and analytical thinking, they described the heart as a strong muscle surrounded by the lungs. Hippocrates described two ventricles connected by openings through the septum. Following their theoretical preconceptions – the idea that the four humors blood, phlegm, black bile, and yellow bile had to be balanced – the heart was thought to contain only bile and not blood. The left ventricular wall was found thicker than the right, which was explained by the notion that heat and pneuma originated here[1]. Pneuma was a godly airy substance which was "invented" by the Stoa, who proposed that the world was steeped in it. It would remain a central term in medicine for centuries[23,27]. The pericardium was described as a fluid-filled membrane sustaining the heat of the heart and the heartbeat. The atria were thought to capture air, which would be transmitted by the vessels currently known as the pulmonary vein and artery, while the latter also transmitted blood to the lungs. Even cardiac valves were identified[1,28].

Aristotle, who lived in the fourth century BC, would become the most important philosopher for the history of science[23]. Up until the 18th century, his philosophies – although adapted – would be taught at European universities, including his geocentrical model of the universe based on Ptolemy. Central to his philosophies was teleology: all things want to unfold their inner possibilities[23]. Considering the heart, he agreed that the pneuma was contained there, and believed the heart was the origin of sensations, emotions, nerves, veins, and arteries, also identifying the aorta and the "great vein", a combination of the pulmonary artery and venae cavae. However, he thought the heart had only three cavities[1], possibly because he attributed the right atrium to the great vein. He also proposed that the heart was the source of heat, and the surrounding organs existed to cool the heart. In chick embryos he discovered that the heart was the first organ to be formed[29].

In the Alexandrian era (around 300 BC), Alexandria became the center of "scientific" advancement. The Museion functioned as an academy where Greek texts were collected, studied, and taught[23]. Even human dissection was allowed for a while. Here, Herophilus found that the nervous system did not originate in the heart, and was the first to identify four heart chambers. He also studied the pulse (sphygmology), and was said to use a water clock to measure high pulses of feverish patients[14]. Erasistratus was the first to anatomically distinguish between veins and arteries, he precisely described the valves, and coined the concept of the heart as a double pump – although he still stated that the right side of the heart pumped pneuma. He even proposed that arteries and veins would terminate in small vessels and join in "synastomoses", a concept analogous to capillaries[1].

In the Roman era (around 130 AD), Galen wrote his manuscripts that would dominate medicine and the cardiac field for centuries. His teachings would largely replace Aristotle's in the field of medicine. He was greatly influenced by the Greeks, and thus was convinced of the four humors theory[23], that the thick-walled left chamber contained air and pneuma, and that the thin-walled right chamber contained blood. He believed that man has a tripartite soul: the rational soul resided in the brain, the

spiritual soul in the heart, and the appetitive soul in the liver. He also stuck with the notion that the intraventricular septum contained openings. He disagreed with Aristotle as he wrote that nerves did not originate in the heart, and contradicted Erasistratus stating that veins originated in the liver, but agreed with him on the valves. He even noticed that the cardiac inlet valves closed when the outlet valves opened, and vice versa. He stated that all muscle movements are voluntary; therefore the heart cannot be a muscle. He did however recognize that the fibers in the cardiac wall had different orientations and were crucial for the heart's continuous movement[1,23]. He also had a complicated theory to explain pulses: different organs and diseases all have their own pulse, but he did not prescribe to count the pulses within a certain time interval[14].

From the fifth century, the Greek scriptures almost got lost in the times of the European mass migrations. Philosophers' schools were closed, and the Museion attracted less and less people who could read ancient Greek. Much knowledge got lost, but rich Muslims searched for the ancient texts again, and tried to translate them to Arabic. Europeans on the other hand were steeped in Roman Catholicism and did not care for philosophy and mathematics as much[14].

In the eleventh century, the Muslim medical school started to advance. Ibn Sina (also known as Avicenna), Haly Abbas, and Ibn al-Nafis were the most notable figures of the cardiac field. Ibn Sina was the first to describe that the pulse comprises two movements and two pauses. Haly Abbas described cardiac anatomy based on Greek texts, and identified two vessels that most probably correspond to the coronary arteries branching from the aorta. Ibn al-Nafis rejected Galen's notion of interventricular pores and Aristotle's three-chamber model, and is most famous for his description of pulmonary circulation: the right side of the heart pumped blood to the lungs, the left side to the body[1].

In medieval Europe, the first universities were founded in the 11$^{th}$ century and educated lawyers, philosophers and, later, physicians. Understanding ancient Greek texts was central – that is, Latin translations of the Arabic translations[23]. Aristotle came back in fashion and would dominate European thought until the 17$^{th}$-18$^{th}$ centuries, partly because his teachings aligned so well with Christian teachings, if interpreted freely. Whenever ancient texts would conflict, differences were smoothed out to fit into one big system and with the Christian worldview. For physicians, Galen's texts dominated. Medical treatments were based on the humor theory of Galen and on astrology, which was a free interpretation of Aristotle's ideas[23]. Despite the strictly theoretical nature of university education, physicians were confronted with the reality of their patients. Contrary to philosophers and lawyers, they had to resort to the direct study of nature – mainly of stars for astrological purposes, and of plants as sources of medicine. The nature of the disease itself was not investigated[23].

### 1.2.2 Renaissance, Scientific Revolution and beyond

As the Renaissance came about, the human body was not anymore considered a pool of sin or too holy to be investigated, but a source of beauty[30]. Consequently, dissection of executed criminals was

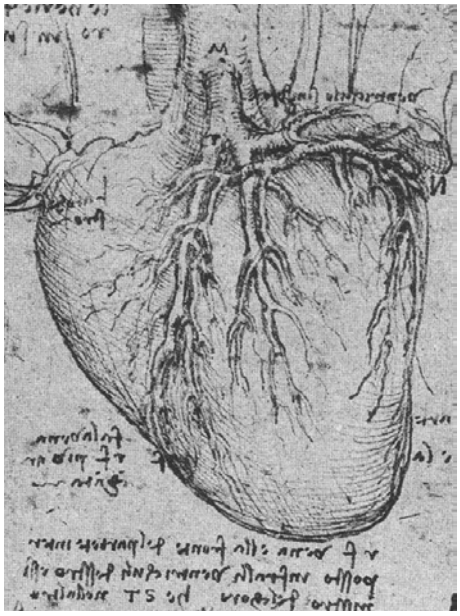

**Figure 2. Drawing of the heart with coronary vessels by Leonardo da Vinci**. Reprinted from Loukas *et al.* 1996[1].

allowed, but mainly to demonstrate already known principles to students[23]. For the cardiac field, this meant some improvements in anatomical knowledge. Leonardo da Vinci around 1400 AD described the four chambers of the heart accurately, with muscular walls supplied by arteries and veins, although he believed Galen's account of cardiac function, and assumed pores existed in the septum. He understood that atria contracted when ventricles relaxed and vice versa – but thought blood was pushed from the ventricles into the atria[1] (**Figure 2**).

#### 1.2.2.1 Sixteenth century

The sixteenth century was an interesting time for science. Unsatisfied by medieval knowledge, new questions were asked, but no alternative for the Aristotelian framework existed yet[1]. Firstly, the humanists – who, contrary to medieval scholars, could read Greek – discovered that Aristotle's teachings had been deformed during the Middle Ages. Some ancient Greek philosophers even contradicted Aristotle, which conflicted with the humanist notion that Greek philosophers represented one "pure" science, so the Aristotelian worldview started to crack. Moreover, the newly developed art of book printing allowed ideas to spread fast. As a result, physicians started to read Galen and Aristotle more closely and critically than before[1]. Another important factor was the discovery of the New World. Europeans were very curious how that looked like, but without any ancient texts to turn to, they had to investigate it themselves. This mindset came in handy in their own old world, too – although texts from these times still inseparably mix new "facts" with old stories[1]. These processes all occurred outside universities, where Aristotle continued to be taught as it was considered solid basic knowledge[1].

1543 was a crucial year. Firstly, the Polish lawyer and physician Nicolaus Copernicus presented his heliocentric theory in *De revolutionibus orbium coelestium,* challenging the Ptolemaic geocentric system that had been widely accepted for more than a millennium[1]. Secondly, Andreas Vesalius published *De humani corporis fabrica*, in which he carefully described anatomical structures exactly how he observed them, not how traditional doctrine said they should look[30,31]. This book revolutionized anatomy and meant a huge reputation loss for classical medicine[23] – although the text had a greater impact than the complicated images, which the contemporary physicians found difficult to interpret[31]. In the early stages of his career, Vesalius would steal bodies from graveyards and gallow fields, keep them in his bedroom for a couple of weeks if he had to, and perform dissections on them[30]. Once he had established a good name, judges would appoint him bodies of criminals with a death sentence. Vesalius described cardiac valves in great detail, and named the left atrioventricular valve the mitralis after the bishop's miter, which also has two "valves"[1]. He confidently broke with Galen's ideas of interventricular pores[1] (**Figure 3**). Vesalius's student Matteo Realdo Colombo in turn was the first in 1561 to show that the pulmonary artery transports blood to the lungs where it is mixed with air before it flows back to the left ventricle through the pulmonary vein[1].

The advances in anatomy led to the question what the functions of these structures were. William Harvey published his seminal book *De motu cordis et sanguinis* (1628), in which he states that the heart pumps blood around the body – not back and forth as the Aristotelian-Galenic tradition had dictated[23]. He also wrote that characteristics of blood in the veins and atria are basically the same, and that the right ventricle did not just provide nourishment to the lungs[1]. He also reversed the common belief that the heart was at work in diastole when it was big and relaxed in systole, when it was small[32]. Like Vesalius, he rejected Galen's notion of pores in the septum. While research slowly became more quantitative, Harvey used the pulse as a natural measure, an idea that had surfaced in the 16$^{th}$ century[14]. Interestingly, in light of the humanists' idea that a perfect science had existed in the past, the findings of Copernicus and Harvey were framed as a rediscovery of ancient truths[23].

#### 1.2.2.2 Seventeenth century

In the seventeenth century, the Aristotelian framework was finally replaced with a new one. René Descartes proposed his mechanical philosophy in his *Principia philosophiae* of 1644, which prescribed the use of ratio, common sense, and experience instead of ancient texts[23]. Teleology was replaced by causality, and by the idea that life as well as the earth, moon, and planets followed the same "laws of nature" – a term coined by Descartes. This meant that the Aristotelian question *why* blood circulates, as Harvey had proposed, did not need an answer[23]. Rather, the human body is a machine that just needs to be understood. Thanks to mechanic philosophy, researchers realized that they were deciphering the secrets of nature together. As a result, the British Royal Society was founded in 1660, followed by the French Académie Royale des Sciences in 1666[23].

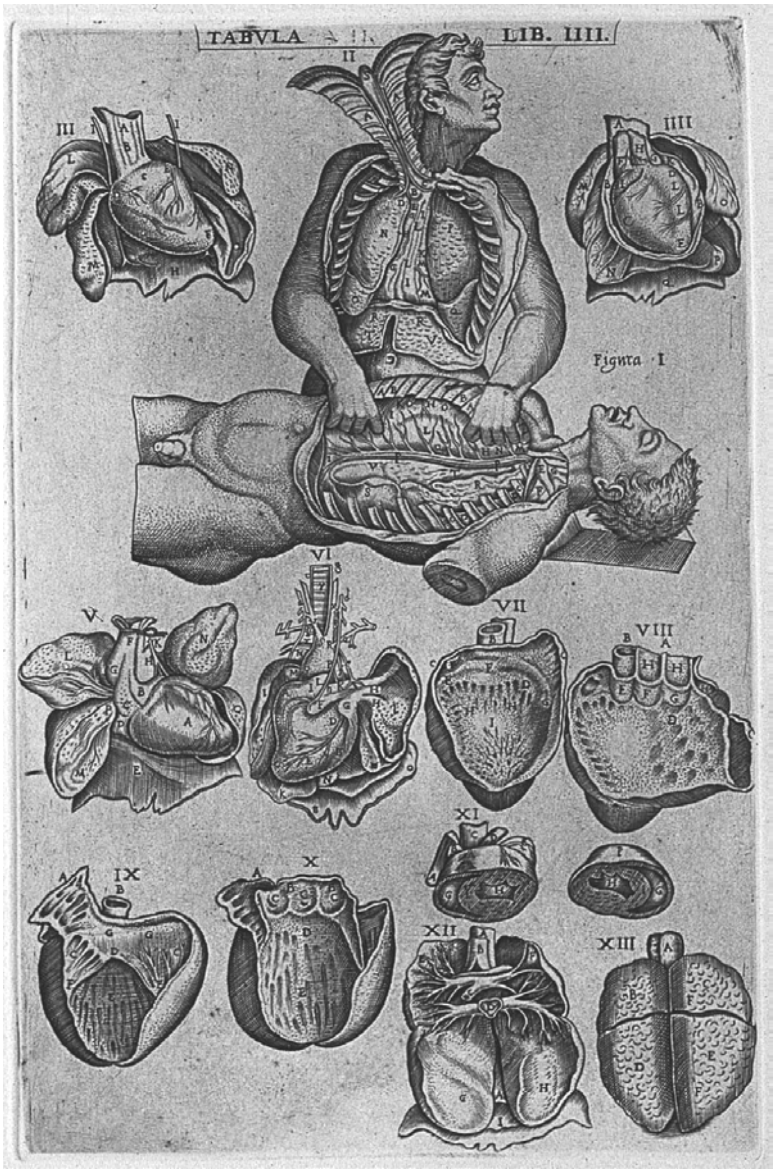


**Figure 3. Two figures with exposed thoracic cavities and illustrations of heart and lungs.** Engraving from 1568 from Vesalius's *De humani corporis fabrica*. Reprinted from Loukas *et al.* 2016[1].

Although Descartes' philosophy was solid, some of his scientific theories were not, with insecurities and debates as a result. The Scientific Revolution is therefore only considered complete with Newton's publication of *Philosophiae naturalis principia mathematica* in 1687, in which he formulated three very sustainable theories, laws even, that definitely established the basis for the natural sciences[23].

Seeing nature in a mechanistic way opened the door for the experimental tradition, as the Aristotelian tradition had prescribed that nature would behave unnaturally in an experiment. The invention of lenses moreover propelled astronomy (telescopes) and physiology (microscopes) forward: Marcello Malpighi identified capillaries in frog lungs in 1661, just as Harvey had predicted[23].

Physicians in the meantime, who used to refer to old texts as the basis for their expertise, now turned to science[23]. Richard Lower for instance published *Tractatus de corde* in 1669, in which he described

the heart as a muscular organ, while contraction of the muscle fibers results in blood flow through the body[1]. He assumed some principles of our modern basic cardiac anatomy – blood flows from the two atria to the two ventricles, and then into the aorta and pulmonary artery – yet he did not recognize pulmonary circulation and he believed blood passed from the right to the left ventricle before distribution to the body. He became the first physician to perform a blood transfusion[1].

Considering cardiac arrhythmias, the pulse slowly became subject of research to understand physiology. Recordings of deviant pulse rates in literature from that time were however measured over half an hour or an hour[14], which did not contribute much to the understanding or identification of cardiac arrhythmias.

Niels Stensen then confirmed the pump function of the heart 1663 – pumping only blood, not heat –, and rejected the belief that the heart is the origin of blood[33]. Lastly, Olaus Rudbeck described cardiac lymphatics in 1653[34].

#### 1.2.2.3 Eighteenth century

During the eighteenth century, the scientific effort became increasingly specialized, professional, and organized[23,35,36]. In the cardiac field, major anatomical structures and pathways were discovered[1], and the invention of reliable clocks that indicated seconds allowed researchers to quantify pulses more precisely[23].

Raymond Vieussens aimed to relate anatomy to function. In his book *Traité nouveau de la structure et des causes du mouvement naturel du cœur* (1715), he described coronary vessels in great detail, including an atrial ring that secured collateral blood flow to the left side of the heart when the left anterior descending artery would become occluded. This structure is now known as the Vieussens arterial ring. He also described the ducti carnosi, connecting the ventricles to the coronary arteries, in 1706[1].

Thanks to the clock and the dawn of the experimental tradition, clinical symptoms and cardiac arrhythmias started to be associated[23]. Arrhythmias were even recorded in musical notation (**Figure 4**). Joannis Maria Lancisi published *De subitaneis mortibu*, on sudden death, in 1707, and associated sudden death with vegetations on the heart valves, cardiac dilatation and hypertrophy[37]. Marcus Gerbezius described complete atrioventricular block in 1717, and although already in 1580 Geronimo Mercuriale had associated a weak pulse with syncope, Giovanni Battista Morgagni described circulatory syncope in greater detail in his classic 1761 work *De sedibus et causis morborum per anatomen indagates*[14]. He also described bradycardia, vasomotoric reactions, and changes in facial color that occur during syncope.

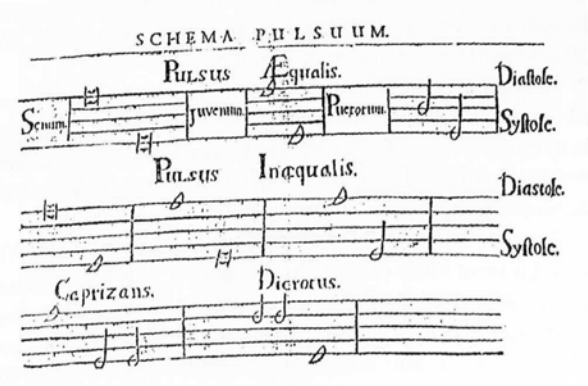


**Figure 4. Musical notation of pulse and cardiac arrhythmias.** Translations: Overview of pulses. Even pulses: old men, adults, boys. Uneven pulses: capering (goat-like [caprizans]), trembling (dicrotus). Values of the notes: squares, 4 counts; semi-circles, 2 counts; circle with a stick, one count. From *Medicina nov-antiqua* by Michael Bernhard Valentini (Frankfurt 1713). Reprinted from Lüderitz 1996[14].

In 1708, Adam Christian Thebesius described the cardiac veins that emptied into the cardiac chambers, now known as Thebessian veins, and the coronary sinus valve – the Thebesian valve[1]. Then, in 1749, Jean-Baptiste de Senac published the first textbook on heart disease. He described the mitral subvalvular apparatus and the chordae[1]. He also recommended chinchona bark for heart fluttering[14]. Cinchona bark and its derivatives quinine, chinchonidine, and quinidin were all developed and applied in the 18th and 19th century, especially in atrial fibrillations, and are important predecessors of modern antiarrhythmic medicine[14]. As a last major 18th-century achievement, Antonio Scarpa discovered the innervation of the heart in 1794[1].

Functionally, great advances were made by Reverend Stephan Hales, describing in *Haemastaticks* blood pressure and volume, and heart work measurements in a mare, in 1773[38]. Also, Luigi Galvani laid the groundwork for the discovery of muscle – and, by extension, cardiac – excitability as he discovered that an electric spark can cause the leg muscles of a dead frog to contract[39].

#### 1.2.2.4 Nineteenth century

In the nineteenth century, the advancements that proved most valuable for cardiac physiology were made in muscle and nerve physiology. The most notable progress specifically in the cardiac field was the discovery of the conduction system. Johann Evangelista Purkinje discovered fibers connecting the atria and ventricles in 1839, and Wilhelm His d.J. described in 1893 fibers in the interventricular septum. The relationship between anatomy and function of these fibers was identified by Sunao Tawara and Ludwig Aschoff in 1906, who also discovered the atrioventricular (AV) node, followed by the discovery of the sinus node in 1907 by Arthur Keith and Martin William Flack: the conduction system was established[1,14].

Since the 19th-century advancements in the neuro-muscular field are so vast and relatively well-known by scientists today, it will suffice to mention the key findings. In 1842, Carlo Matteucci extended Galvani's work by showing that the contraction of one frog leg excited the sciatic nerve of another

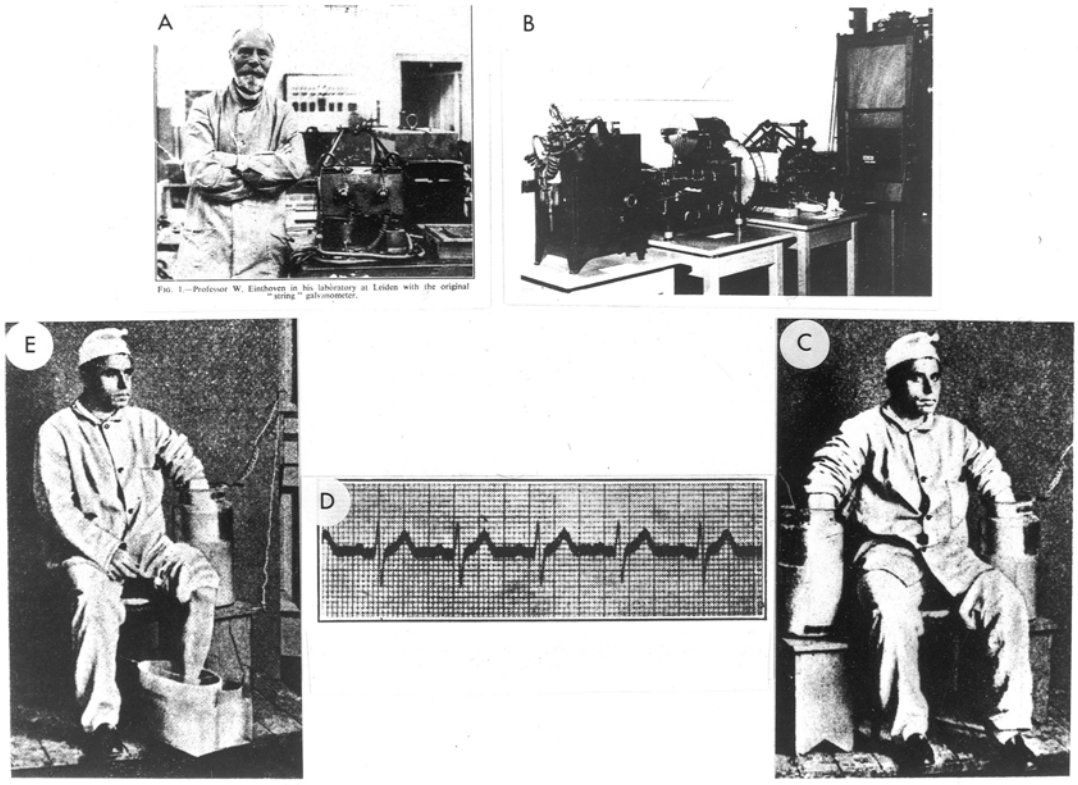


**Figure 5. Einthoven's electrocardiogram.** (**A**) Einthoven and his string galvanometer. (**B**) String galvanometer, from left to right: arc lamp, water-cooled electromagnet, timer, lenses, and falling-glass-plate camera. (**C, E**) Recording leads I and II by immersing extremities in saline. (**D**) An ECG recorded by Einthoven. Reprinted from Fisch 2000[12].

frog that was in contact with the muscle[40]. In 1856, Rudolf Albert von Kölliker and Heinrich Müller repeated this experiment on a beating heart, and observed twitches of the frog's muscle with each ventricular contraction[41].

In 1850, Hermann von Helmholz determined that the conduction speed of excitation in a nerve-muscle preparation was about 30 m/s[42]. In 1852, Emil du Bois-Reymond coined the term "injury current", which was based on Matteucci's observation of the same phenomenon and described the potential difference between the outer and inner surface of the muscle. Eventually, this led to the discovery of the resting membrane potential[42].

Julius Bernstein, in turn, followed up with Helmholz's findings and showed in 1868 that the propagation of the "negative variation" (now called action potential) was as fast as the conduction velocity of a nerve impulse. He also recorded this negative variation in a frog nerve[42].

Then, in 1872 Ludimar Herrmann proposed a model to explain the conduction of the negative variation: at the junction of active and resting regions of a nerve, the differences in electrical potential resulted in local electrical currents that excited adjacent resting areas of the nerve. Hodgkin confirmed this hypothesis in 1939 in giant squid axon[43].

In a series of publications from the 1880s, Sidney Ringer showed that a frog heart keeps beating if the solution with which it is perfused contains sodium, potassium, and calcium ions in given concentrations[44].

Crucial for advancing the understanding of cardiac arrhythmias was the development of the electrocardiogram (ECG). In 1887, the first human ECG was recorded by Augustus Waller with a mercury capillary electrometer, although he recognized no clinical consequences. Willem Einthoven then optimized this technique and identified the P, Q, R, S, and T waves in 1895. In 1903 and 1906, he published a further improved ECG technique using the string galvanometer and introduced the first three ECG leads (**Figure 5**)[12,14,45].

Concerning the membrane potential, Wilhelm Ostwald proposed in 1890 that a potential difference arises across semipermeable membranes if the concentration of permeable ions between the two opposing fluid compartments differ[46]. This was further developed by Bernstein, who published his membrane theory in 1902, the first plausible physico-chemical explanation of bioelectric events. He elegantly combined Oswald's hypothesis with the Nernst equation to predict electrical potentials from ionic concentration gradients. He proposed that excitable cells are surrounded by a membrane selectively permeable to potassium ions at rest, and the negative potential arises from the tendency of potassium ions diffusing down their electrochemical gradient from the intracellular to the extracellular compartment. Bernstein's theory could be considered the foundation of ion channel research as we know it today[42,47].

For a history of cardiac electrophysiology covering the twentieth century, I refer to two excellent and entertaining reviews by Professor Edward Carmeliet[42,48], and for an overview of twentieth-century work on cardiac arrhythmias, to a thorough review by Professor Lüderitz[14].

This thesis will proceed with a discussion of cardiac physiology as we understand it today.

## 1.3 Cell types in the heart

The adult mammalian heart contains several cell types, mainly cardiomyocytes, fibroblasts, endothelial cells, and perivascular cells[49]. Cardiomyocytes make up ~70-85% of the cardiac volume, but constitute ~30-40% of the cell number in mice[49]. A recent study found that endothelial cells make up more than 60% of non-myocytes, hematopoietic-derived cells 5-10%, and fibroblasts less than 20%[50]. These non-myocytes are essential for the extracellular matrix, intercellular communication, and maintaining the cardiac vasculature. Other notable non-myocytes involved in cardiac function include macrophages that assist electrical conduction in the AV node[51], neurons for (para)sympathetic modulation of cardiomyocyte function[22], and epicardial adipocytes involved in paracrine regulation of cardiomyocytes and vascular endothelium[52].

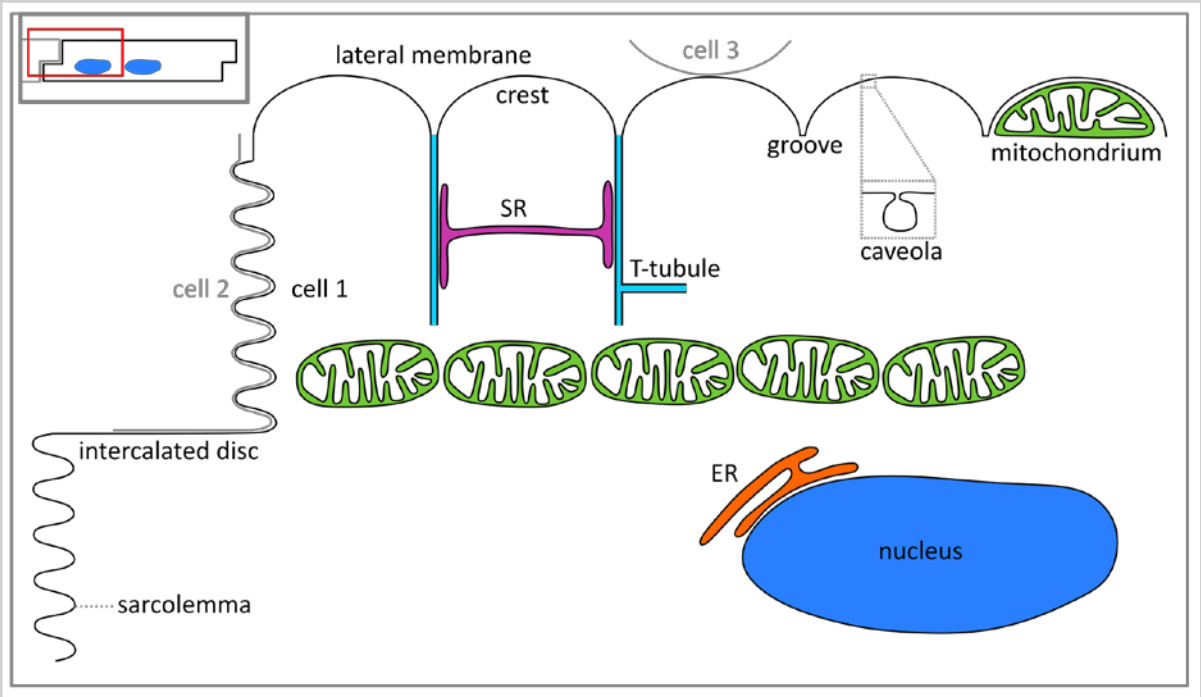


**Figure 6. Main membrane structures of ventricular cardiomyoyctes**. Inset top left: schematic outline of a cardiomyocyte (typically 60-140 µm long) with neighboring cell in grey. Red box indicates area that is shown in detail (schematic and not to scale) in the large image with intercalated disc (intercalated disc of the neighboring cell in grey)[3], lateral membrane with crest and groove (detail of groove of neighboring cell in grey)[6], and T-tubules (blue) opening to the groove[15]. Mitochondria (green) reside under the groove[7] as well as deeper in the cell where they aggregate into columns[17]. Caveolae (in dotted box) are found throughout the sarcolemma[18,19], here depicted on the crest. The endoplasmic reticulum (ER, orange) is mainly found around the nucleus (blue)[20,21], and the sarcoplasmic reticulum (SR, purple) forms a network between T-tubules[21].

### 1.3.1 The ventricular cardiomyocyte

Cardiomyocytes are rod-shaped cells of about 60-140 µm long and and 17-25 µm wide in humans[53]. Dimensions of rodent cardiomyocytes fall within the same range[54]. Cardiomyocytes differ from a skeletal muscle cells: they are shorter, have branches, do not form fibers surrounded by connective tissue, and lack a motor end plate, yet resemble skeletal myocytes in the high degree of sarcomeric organization[22] (**Figure 6**). Sarcomeres are the functional unit of all muscle cells as they enable the contraction of the myocyte when their long protein filaments slide over each other[22]. Cardiac and skeletal myocytes both have multiple nuclei, but due to different mechanisms: individual skeletal myocytes fuse to form a syncytium, but cardiac myocytes reach their mature state when they exit the cell cycle after karyokinesis without cytokinesis, with two nuclei as a result[55]. Murine cardiomyocytes can count up to four nuclei, and a higher number of nuclei correlates with a higher cell volume[56]. In binucleate cardiomyocytes, one nucleus appears to be dormant[57], but the functions of individual nuclei in polynucleated cells remains to be elucidated.

Cardiac muscle is unique as its cells form a functional syncytium due to a high degree of electrical coupling at the intercalated disc[3], which means that the propagation of action potentials through a strand of cardiomyocytes can be described by cable theory[22,58,59] (see **Sections 1.4** and **1.7.3**). The

organization and morphology of cardiomyocytes differs slightly between atria, ventricles, and the conduction system[22,60,61]. This thesis focuses entirely on ventricular cardiomyocytes of the mouse.

The cardiomyocyte sarcolemma can be subdivided in multiple domains (**Figure 6**), which will be discussed extensively in different sections of this thesis. Firstly, the intercalated disc is the primary site of contact between two cardiomyocytes and is specialized in mechanical and electrical coupling (see **Section 1.7.2**). Secondly, the lateral membrane runs along the long axis of the cell and can be further subdivided in a hilly crest and a valley-like groove; the latter coinciding with the sarcomeric Z-disc (see **Section 1.7.1**). Thirdly, the T-tubules are narrow invaginations of the lateral membrane, opening to the groove, and mainly running along Z-discs, although many T-tubular branches run along the long axis of the cell (see **Section 1.7.3**).

In the sarcolemma, many caveolae reside (**Figure 6**), defined as cholesterol- and sphingolipid-rich flask-shaped membrane invaginations of about 50-100 nm in diameter and coated in caveolin and cavin proteins[18]. Caveolae belong to the class of lipid rafts, which are ordered domains of phospholipids with long acyl chains and cholesterol[18,62]. They host many signaling molecules and ion channels[18] – indeed, the ion channel central to this thesis, $Na_v1.5$, has been shown to interact with caveolin-3[63,64].

Mitochondria (**Figure 6**, green) in the cardiomyocyte form two populations: those residing under the crest[7] (see **Section 1.7.1.1**) and those deeper in the cell forming columns[7]. Loss of mitochondria under the crest has been associated with heart failure (see **Section 1.7.1.1**)[65]. The deeper mitochondria are functionally and electrically coupled through intermitochondrial junctions[17,66]. They exchange metabolites, proteins, and even DNA, and enable rapid distribution of ATP throughout the cell[17,66]. The outer mitochondrial membrane also connects with the endoplasmic reticulum (ER), sarcoplasmic reticulum (SR), and T-tubuli[67].

The SR (**Figure 6**, purple) functions as a calcium store and is crucial for excitation-contraction coupling[68]. Ryanodine receptors (RyR2) in the SR membrane form dyads with L-type voltage-gated calcium channels ($Ca_v1.2$) in the T-tubular membrane. Once the cell is excited, calcium ions that enter through $Ca_v1.2$ activate Ryr2 in the SR, which leads to massive calcium release from the SR and concomitant sarcomere shortening. SERCA (sarcoplasmic/endoplasmic reticulum calcium ATPase 2) in turn is responsible for calcium re-uptake into the SR[22,68].

Besides excitation-contraction coupling, the SR also hosts proteins involved in store-operated calcium entry. This process is relatively well described in smooth muscle and some non-excitable cells[22,69], while its relevance for the heart has only recently started to emerge. It mainly occurs in neonatal cardiomyocytes and seems to re-activate in chronic cardiac disease[69]. Store-operated calcium entry is voltage independent and occurs when the SR is depleted of calcium, which induces multimerization of Stim (stromal interaction molecule) in the SR membrane. This multimer then activates Orai and

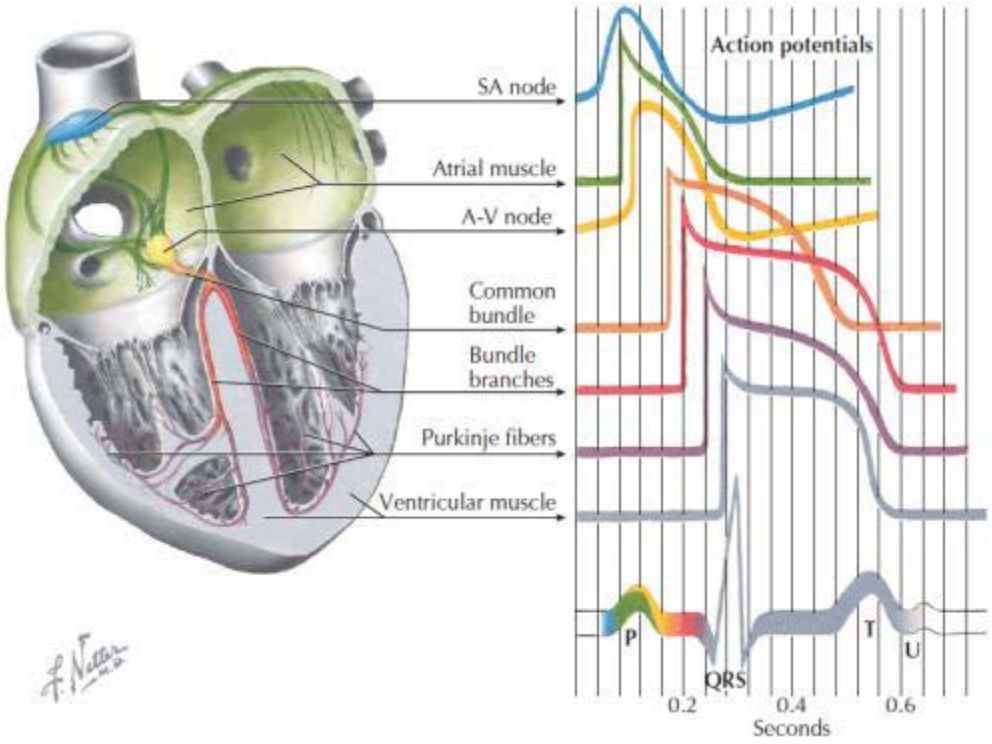


**Figure 7. The cardiac conduction system and respective action potentials.** Note the ECG on the bottom right. Reprinted from Conti 2014[11].

transient receptor potential C (TRPC) channels in the plasma membrane, which in turn conduct calcium from the extracellular compartment into the cell[69].

The rough ER (**Figure 6**, orange) is classically thought to be confined to the perinuclear region and is functionally distinct from the SR as it is the primary site for protein synthesis, among other canonical functions[21]. In cardiomyocytes, however, at least some of the ER seems to be continuous with the SR, and protein synthesis in the SR has been reported[20].

## 1.4 Cardiac conduction

Proper cardiac function relies on the orchestrated contraction of the atria and ventricles enabling blood flow into and out of the heart. The conduction system is crucial in this process (**Figure 7**). Firstly, cells in the sinoatrial (SA) node in the right atrial roof between the two venae cavae generate spontaneous electrical signals called action potentials. Action potentials excite the cell and trigger muscle contraction, and are conducted first through the atrial muscle. Once they reach the AV node, conduction is slightly delayed allowing the blood to move from the atria to the ventricles before the ventricles contract. Then, action potentials propagate through the bundle of His, into the right and left bundle branches in the interventricular septum, and into the Purkinje fibers, spreading the signal through the two ventricles[22,70].

The heart rate is dictated by the firing rate of the sinoatrial (SA) node, which is about 100 beats per minute if it's not tuned up or down by the sympathetic or parasympathetic nerves, respectively[22].

Conduction from cell to cell relies on electrotonic coupling through gap junctions[71,72], and, possibly, on a process called ephaptic coupling (see **Section 1.4.2**)[73]. A gap junction consists of two connexin 43 hexamers from opposing cells that together form a channel, and allows the passage of ions and small molecules (<1.2 kD) to pass from one cell to the next[48]. Gap junctions are highly prevalent at the intercalated disc, where two cardiomyocytes are tightly joined together. This thesis includes a detailed discussion of the intercalated disc in **Section 1.7.2**, and a description of current flow from one cell to its neighbor in **Section 1.7.3** (figure 2 in the respective publication).

Conduction velocity through cardiac tissue varies greatly: it is slowest in the SA and AV nodes, slow through the atrial and ventricular muscle, and fastest in the Purkinje fibers. Conduction is moreover anisotropic: it is slower in the transversal direction than in the longitudinal direction. This can be explained by the anisotropic structure of the cell and by the intercalated discs facilitating longitudinal conduction[48].

### 1.4.1 The cardiac action potential

The action potential is the hallmark of cardiac excitability, and originates from the tightly orchestrated opening and closing (inactivation) of voltage-gated ion channels that selectively conduct sodium, potassium, or calcium ions. When these channels open, ions pass through down their electrochemical gradient, thereby depolarizing or repolarizing (or hyperpolarizing) the membrane[74]. Action potentials have different shapes in different regions of the heart (**Figure 7**), and in different species, depending on the voltage-gated ion channels that are expressed[70] (**Figure 8**).

The action potential of human ventricular cardiomyocytes can be subdivided in five phases[13,75] (**Figure 8**). Phase 0 starts as soon as the membrane potential depolarizes through electrotonic and/or ephaptic coupling and reaches the activation threshold of voltage-gated sodium channels (**Sections 1.4** and **1.4.2**). Once activated, voltage-gated sodium channels conduct a large inward sodium current, depolarizing the membrane from ~-85 to +20 mV within 1 ms, and quickly inactivate after that. The potassium-calcium exchanger NCX works in reverse mode during this phase, extruding sodium ions from the cytoplasm and exchanging them for calcium ions in a 3:1 ratio, resulting in a net efflux of positive charge[70,75].

Phase 1 is the initial repolarization phase where the sodium channels have closed, transient outward potassium current ($I_{To,1}$) is activated, and $Ca_v1.2$ channels have started to activate. The "notch" arises from a short period where $I_{To,1}$ is stronger than the calcium current ($I_{Ca}$). Cardiomyocytes in the

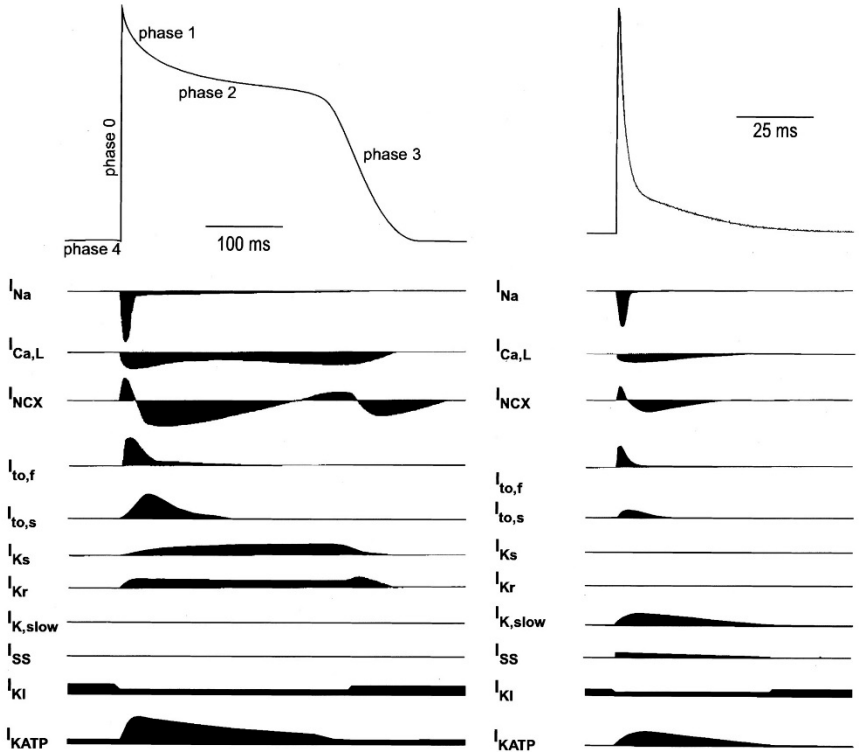


**Figure 8. Shapes and currents of the action potential.** Human (left) and murine (right) ventricular action potentials are shown. Reprinted from Nerbonne 2001[13].

epicardial layer show a more pronounced nudge than those in the endocardial layer due to a larger $I_{To}$[70,75].

Phase 2 forms the plateau of the action potential at around +10-20 mV, as the depolarizing calcium current through $Ca_v1.2$ and the repolarizing rapid and slow potassium currents ($I_{Kr}$ and $I_{Ks}$) balance out. NCX works in forward mode at this time, removing calcium from the cytoplasm while generating a net depolarizing sodium current[70,75].

Phase 3 is the rapid repolarization phase as calcium channels are inactivated and the potassium currents are maximally activated, bringing back the membrane potential to its resting value[70,75].

During phase 4, the resting membrane potential stabilizes while the sodium-potassium ATPase and NCX restore the original electrochemical gradients of sodium, potassium, and calcium[70,75].

The voltage-gated sodium, potassium, and calcium channels that shape the action potential differ in composition and expression level between species and cardiac regions. Of the 350 known genes encoding ion channels, 152 encode pore-forming α-subunits of voltage-gated ion channels, and of those, 41 are significantly expressed in murine Black6/J cardiomyocytes[76] (see **Section 3.2**).

### 1.4.2 Electrotonic versus ephaptic conduction

Measurements of macroscopic conduction velocity and the discovery of electrotonic coupling through gap junctions have led to the assumption that cardiac muscle forms a functional syncytium[58,59].

However, theoretically, ephaptic coupling is also expected, not in the least because avian ventricular myocardium only expresses very little connexins, and connexins are entirely absent in invertebrate hearts[77]. In connexin-deficient hearts, propagation of the action potential should rely on electric field interactions between neighboring cells that are very close (<30 nm[78]) together. Such close opposition occurs at the intercalated disc[79]. In mammalian connexin-rich hearts, ephaptic coupling has been proposed as a back-up mechanism when gap junctions are uncoupled[77].

Ephaptic coupling works as follows. When one cell is depolarized, sodium channels open. At the intercalated disc, where the concentration of sodium channels is very high and the intercellular cleft very narrow, this leads to depletion of sodium ions from the cleft. This depletion reduces the potential difference of the neighboring cell to an extent that the opening threshold of sodium channels is reached. A substantial sodium current can also lead to depletion of sodium from the cleft and sodium current self-attenuation as the driving force decreases[73].

Experimentally, electric field interactions have been demonstrated by bringing axons and cylindrical preparations of heart muscle very close together (reviewed in[48]); however, ephaptic coupling *in vivo* is very hard to prove. In the heart, the perinexus is the most likely stage for ephaptic coupling[77,79,80]. The perinexus surrounds the gap junction plaque in the intercalated disc, and is rich in connexin 43 hemichannels, sodium channel $\beta_1$-, and pore-forming α-subunits. *In silico,* ephaptic coupling has been modeled in different ways and with increasing complexity[73,78,81-83]. Hichri *et al.* showed that when a human embryonic kidney (HEK) cell stably expressing $Na_v1.5$ is brought very close to a non-conducting obstacle, sodium current increased when a voltage step close to threshold was applied, indicating that a small intercellular cleft can increase sodium current. On the other hand, sodium current decreased when voltage steps far above threshold were applied, indicating that the sodium current self-attenuates as sodium efflux from the cleft reduces the driving force of the channels[73].

Taken together, it is increasingly likely that electrotonic and ephaptic conduction both facilitate the propagation of the action potential in mammalian myocardium, also called mixed-mode conduction[77].

## 1.5 Cardiac arrhythmias

A cardiac arrhythmia is defined as improper beating of the heart, whether irregular, too fast, or too slow, and are typically diagnosed based on an ECG. Arrhythmias can be caused by drugs, aging, and heart disease, among others, and many are of genetic origin (see *www.omim.org*).

Of the congenital cardiac arrhythmias, hundreds of mutations in approximately 27 genes encoding ion channels have been described (see *www.omim.org*). The most prevalent cardiac channelopathy is congenital long-QT syndrome (LQTS), which is associated with loss-of-function mutations in potassium channels or gain-of-function mutations in sodium channels, among other mechanisms[8] (see

**Section 1.6.5**). Ion channel mutations can also affect multiple organs, such as in Timothy syndrome, where a mutation in *CACNA1C* encoding $Ca_v1.2$ affects the heart, the brain, and fingers and toes, among other organs[84].

## 1.6 $Na_v1.5$

$Na_v1.5$ is the pore-forming or α-subunit of the cardiac voltage-gated sodium channel. It is highly expressed in myocardium and the conductive system, and less in SA and AV nodes[85]. Within a cardiomyocyte, $Na_v1.5$ is found at the intercalated disc[3,86,87], at the lateral membrane[87-89], and, as this thesis will show, in the T-tubules (see **Section 3.1**). Several central nervous system regions[90], intestinal smooth muscle, certain cancer cells, astrocytes, endothelial cells, microglia, T-lymphocytes,

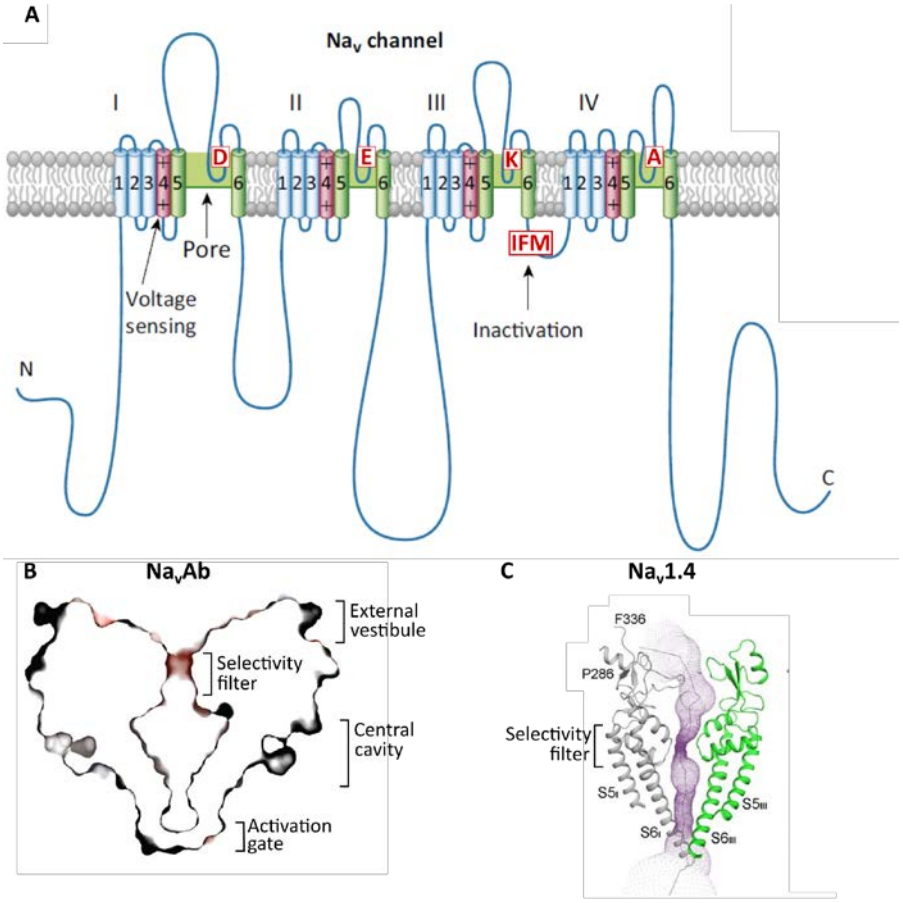


**Figure 9. Structure of voltage-gated sodium ($Na_v$) channels**. (**A**) Eukaryotic $Na_v$ channels consist of four transmembrane domains with six transmembrane segments. Voltage-sensing (red) and pore-forming (green) domains are indicated. Key amino acids are shown in bright red: the DEKA motif forms the sensitivity filter and the IFM motif is responsible for fast inactivation. (**B**) Cross-section of the pore of an *Arcobacter butzleri* $Na_v$ ($Na_vAb$) channel with a closed activation gate. A vestibule opening to the extracellular side, the selectivity filter, a water-filled inner chamber, and the activation gate can be recognized. (**C**) Pore of human $Na_v1.4$. Note that the shape of the pore is similar to that of $Na_vAb$. Permeation path is shown in purple. Adapted from Catterall & Zheng 2015[9] (**A**, **B**) and Pan 2018[10] (**C**).

and macrophages also express $Na_v1.5$[91,92]. The gene *SCN5A* encodes $Na_v1.5$, and many *SCN5A* mutations have been associated with cardiac arrhythmias (see **Section 1.6.5**). $Na_v1.5$ has a molecular weight of about 220 kD[8], and the most prevalent splice variants count 2016 or 2015 amino acids[93-95]. The 2016-amino-acid variant has an extra glutamine residue in the DII-III linker[93-95]. Other less prevalent splice variants and different amino acid composition are reviewed by Rook[93].

$Na_v1.5$ consists of four transmembrane domains (DI-DIV) of six transmembrane segments (S1-S6) each (**Figure 9A**). Once properly folded, segments S5 and S6 form a pore, in which the selectivity filter is formed by the DEKA (Asp-Glu-Lys-Ala) motif[47,96] (**Figure 9A**). This filter allows a 50-fold selectivity over calcium ions and a tenfold selectivity over potassium ions[9,47]. The activation gate is formed by the inner ends of the S6 segments, which physically close the pore[97] (**Figure 9B**). The S4 segments contain positively charged amino acids (mainly arginine and lysine) and serve as a voltage sensor[47]. When the membrane depolarizes, the S4 segments move outward and induce a conformational change in the activation gate, allowing the channel to open[9,47]. The DIII-IV linker in turn contains the IFM (Iso-Phe-Met) motif that enables fast inactivation of the channel by acting as a "hinged lid"[98,99].

A high-resolution three-dimensional structure of $Na_v1.5$ has not yet been resolved, but much insight has been gained from the structures of related proteins. Although prokaryotic sodium channels only have one transmembrane domain of six segments, the tetramer closely resembles the pseudo-tetramer from more complex organisms. The first crystal structure of the prokaryotic voltage-gated sodium channel $Na_vAb$ (or NaChBac) from *Arcobacter butzleri* was published in 2011[97], and described the closed pore structure in detail[97] (**Figure 9B**). Recently, the high-resolution crystal structure of a prokaryotic sodium channel in the open state was resolved, which revealed a heretofore unknown interaction motif between S3 (W77), the S4-5 linker, and the C-terminus[100]. This sodium channel was isolated from the prokaryote *Magnetococcus marinus* and resembles eukaryotic orthologs[100]. Also in 2017, the cryo-electron microscopy (cryo-EM) structure of the putative sodium channel $Na_vPaS$ from the American cockroach has been resolved[101], which reveals disulfide bonds between extracellular loops and between one of the pore helices and S6. The first human voltage-gated sodium channel was resolved in 2018 by cryo-EM, and showed $Na_v1.4$ in complex with its $\beta_1$-subunit[10]. The pore structure resembles that of NaChBac (**Figure 9C**). Moreover, the authors revealed the mechanism of fast inactivation as the IFM motif inserts into a cavity enclosed by S4-5 and S6 in DIII and DIV[10].

### 1.6.1 $Na_v1.5$ states

$Na_v1.5$ – like other voltage-gated channels – has three main operating states: closed, when the channel can be opened by an appropriate stimulus; opened, when ions pass through the channel; and inactivated, when the channel is closed and cannot be opened[47]. The inactivated state is characterized by the IFM motif closing the pore from the outside, whereas the closed state is characterized by the

inner ends of the S6 segments physically sealing the pore[97]. Kinetic states and the gating between those states – which not necessarily correspond to the structural states – can be schematically represented in a Markov model (**Figure 10**). For voltage-gated sodium channels, several elaborate Markov models have been proposed by Hodgkin & Huxley, Clancy & Rudy, and others[16]. All of these models include multiple closed, inactivated, and/or open states. Asfaw & Bondarenko recently proposed a 10-state model for human $Na_v1.5$ that best fits the experimental evidence collected to date and would overcome shortcomings of the aforementioned models[16]. It includes three closed states, three closed inactivated states, and a slow, fast, and intermediate inactivated state (**Figure 10B**). Transitions between these states can be voltage dependent or independent[16].

### 1.6.2 $Na_v1.5$ regulation

$Na_v1.5$ is a member of a macromolecular complex that includes proteins, lipids, and carbohydrates, some of which are covalently linked to $Na_v1.5$. They are involved in the "transcription, translation, trafficking, membrane retention, glycosylation, post-translational modification, turnover, function, and degradation"[8] of $Na_v1.5$, and, by extension, of all cardiac ion channels. Many of these regulators are confined to a specific cardiomyocyte domain, such as the intercalated disc or the lateral membrane[8]. This implies that $Na_v1.5$ is regulated differently at different locations.

The following sections discuss the major regulators of $Na_v1.5$: post-translational modifications, β-subunits, and interacting proteins.

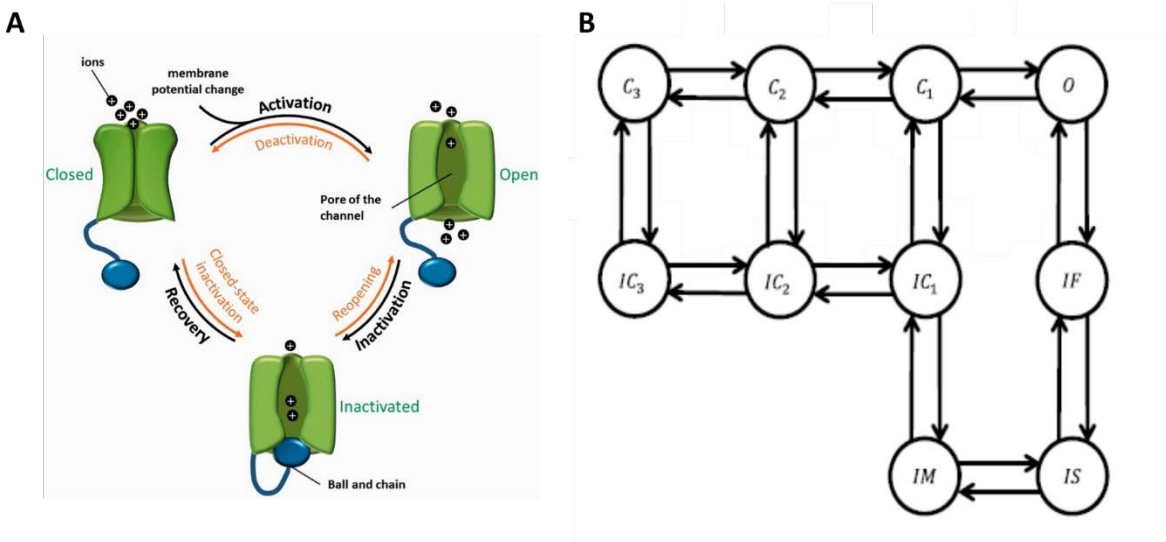


**Figure 10. Markov models of $Na_v1.5$.** (**A**) A simple three-state model showing closed, open, and inactivated states with corresponding transitions. Adapted from Hinard *et al.* 2016[2]. (**B**) According to a recent study, this ten-state model best explains for human $Na_v1.5$ the experimental values of peak current-voltage relationships, voltage dependence of sodium conductance, steady-state activation, inactivation, and de-activation, fast and slow inactivation, and recovery from inactivation. Closed ($C_i$), closed inactivated ($IC_i$), open (O), fast inactivated (IF), slow inactivated (IS), and intermediate inactivated (IM). Adapted from Asfaw & Bondarenko 2018[16].

### 1.6.3 $Na_v1.5$ post-translational modifications

Post-translational regulation of $Na_v1.5$ occurs through covalent binding of several different molecules to amino acids, including but not limited to phosphorylation, N-glycosylation, sumoylation, ubiquitination, and N-nitrosylation. This section concisely addresses phosphorylation, glycosylation, and ubiquitination.

Many kinases have been shown to phosphorylate $Na_v1.5$ at many different amino acids, including protein kinase A and C (PKA and PKC), calcium/calmodulin-dependent protein kinase II (CaMKII), protein tyrosine phosphatase (PTPH1), phosphatidylinositol 3-kinase (PI3K), Fyn, serum- and glucocorticoid-inducible kinases (SGK), and adenosine monophosphate-activated protein kinase (AMPK) (reviewed by[102]). The effects of phosphorylation on $Na_v1.5$ function depend on the kinase and phosphorylation sites, and include changes in biophysical properties (voltage-dependence of inactivation, speed of fast inactivation, recovery from inactivation), $Na_v1.5$ trafficking and sarcolemma expression, whole-cell sodium current, and late sodium current, among others. Consequently, mutations in kinases have been associated with many cardiomyopathies, including LQTS3, Brugada syndrome, sudden infant death syndrome (SIDS), and heart failure (reviewed by[102]).

N-glycosylation is the covalent binding of oligosaccharides, or glycans, to a nitrogen atom of an asparagine[93]. The glycosylated state in $Na_v1.5$ appears to affect activation and inactivation properties of the sodium current[103,104]. Two states have been identified: the fully glycosylated state and the core-glycosylated state. In HEK293T cells, core-glycosylated $Na_v1.5$ seems to be transported to the membrane through a Golgi-independent mechanism[105].

Ubiquitination of $Na_v1.5$ is executed by the ubiquitin ligase Nedd4-2 (neuronal precursor cell expressed developmentally downregulated 4-like), which has been demonstrated in HEK-293 cells[106]. The WW domain of Nedd4-2 interacts with the C-terminal PY-motif of $Na_v1.5$. Ubiquitination leads to internalization of $Na_v1.5$ and degradation by the proteasome[106]. As a result, $Na_v1.5$ expression at the sarcolemma decreases. Interestingly, an increase in intracellular calcium as seen in heart failure increases Nedd4-2 activity though its C2 domain, which increases $Na_v1.5$ internalization[107]. Mice in which the C2 domain of Nedd4-2 was deleted showed increased QRS and QT intervals and shorter PR intervals compared to wild types, suggesting that inhibition of ubiquitination leads to a *de facto* gain of function of the sodium current[108].

### 1.6.4 $Na_v1.5$ interacting proteins

**Figure 11** gives an overview of $Na_v1.5$ regulatory proteins, of which a selection is discussed below. $\alpha_1$-syntrophin, dystrophin, synapse-associated protein 97 (SAP97), and calcium/calmodulin-dependent serine protein kinase (CASK) are especially relevant for this thesis. Note that several proteins interact

with the same motif, e.g., $\alpha_1$-syntrophin, SAP97, and PTPH1 with the SIV motif. This indicates that the composition of $Na_v1.5$ protein complexes depends on time and/or location.

### 1.6.4.1 Sodium channel β-subunits

$Na_v1.5$ can interact with four auxiliary β-subunits ($\beta_1$- $\beta_4$), while $\beta_1$ has two splice variants, $\beta_1$ and $\beta_1B$. Except for $\beta_1B$, which is a secreted protein[109], β-subunits are 30-40 kD proteins with a single transmembrane segment, a short extracellular N-terminal domain, and a long intracellular C-terminal domain that contains immunoglobulin-like domains[110]. In murine cardiomyocytes, we found only $\beta_1$- and $\beta_4$-encoding mRNA[76] (see **Section 3.2**). Functionally, β-subunits modulate the biophysical properties and/or surface expression of $Na_v1.5$, although findings greatly vary depending on experimental conditions and model systems (reviewed by [93,109,111,112]).

The immunoglobulin loop in the β-subunit extracellular domain allows cell-cell adhesion[113]. This is especially interesting in light of the findings that $\beta_1$ seems to be mainly expressed at the intercalated disc[80] and possibly at the T-tubules (reviewed in[109]). At the intercalated disc, $\beta_1$ is specifically expressed at the perinexus, where ephaptic coupling might occur[77,79,80]. $\beta_1$-subunits from opposing cells might therefore regulate the width of the intercellular cleft[80,109].

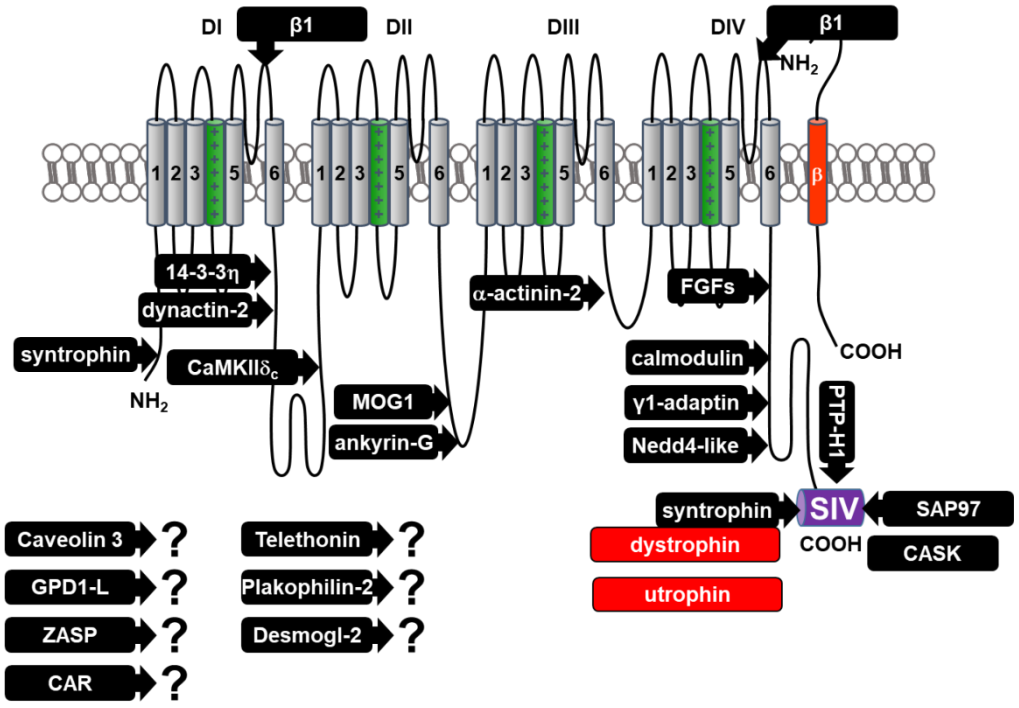


**Figure 11. $Na_v1.5$ and interacting proteins.** Interaction sites are indicated if known. Purple box represents the three C-terminal amino acids of $Na_v1.5$, SIV (Ser-Iso-Val). β1, $\beta_1$-subunit. Red column: β-subunit. GPD1-L, glycerol-3-phosphate dehydrogenase 1-like. ZASP, zona occludens 2-associated speckle protein. CAR, coxsackie and adenovirus receptor. Desmogl-2, desmoglein 2. CaMKII$\delta_c$, calmodulin-dependent protein kinase II δ-c. MOG1, multicopy suppressor of gsp1. FGFs, fibroblast growth factor-like. Nedd4-like, neural precursor cell expressed developmentally downregulated 4-2-like ubiquitin ligases. PTPH1, protein tyrosine phosphatase H1. SAP97, synapse-associated protein 97. CASK, calcium/calmodulin-dependent serine protein kinase. Adapted from Abriel 2015[8].

### 1.6.4.2 $\alpha_1$-syntrophin

$\alpha_1$-syntrophin binds with the C-terminal SIV and around the N-terminal Ser20 of $Na_v1.5$ via its PDZ (PSD95, Dlg1, and ZO-1) domain[87,114]. Its C-terminal domain interacts with dystrophin, dystrobrevin, and utrophin[115]. In cardiomyocytes, it is exclusively expressed at the lateral membrane[87,116]. By bridging $Na_v1.5$ to the actin cytoskeleton via dystrophin, it is crucial for sodium channel stability at the lateral membrane[116,117]. Some of these mutations increased late sodium current, which was associated with an increase in $Na_v1.5$ nitrosylation, while another mutation increased peak sodium current and slowed fast inactivation (reviewed in[8]).

While five syntrophin isoforms have been described ($\alpha_1$, $\beta_1$, $\beta_2$, $\gamma_1$, and $\gamma_2$), we identified only $\alpha_1$-, $\beta_1$-, and $\beta_2$-encoding mRNA in mouse cardiomyocytes, while the expression levels of $\beta_1$- and $\beta_2$-syntrophin are much lower than that of $\alpha_1$-syntrophin[76] (see **Section 3.2**).

### 1.6.4.3 SAP97

SAP97, like $\alpha_1$-syntrophin, interacts with the SIV motif of $Na_v1.5$ via its PDZ domain. It is involved in trafficking and anchoring $Na_v1.5$ and several potassium channels to the plasma membrane; however, SAP97 knock-out cardiomyocytes exhibit reduced $I_{to}$, $I_{Kr}$, and inward-rectifier potassium current ($I_{K1}$), but normal sodium current[118]. SAP97 is involved in clustering of $K_v1.5$ and $K_v4.2/3$ in cardiomyocytes [119-121], but its functional effect on $Na_v1.5$ is less well understood.

SAP97 belongs to the MAGUK (membrane-associated guanylate kinase) protein family characterized by multiple protein-binding domains: three PDZ domains, one GUK, one SH3 (scr homology 3), and the SAP97-specific L27 (Lin-2 and Lin-7) domain. The GUK domain can interact with SH3 domain of other MAGUK proteins, forming dimers. This may support ion channel cluster forming at the membrane[122]. Immunofluorescence data regarding SAP97 localization have shown conflicting results about its localization within a cardiomyocyte[116,118].

### 1.6.4.4 Dystrophin

Dystrophin is a 427-kD protein encoded by *DMD,* the largest gene in the human genome. It is a crucial protein for the costamere, which links the cytoskeleton to the extracellular matrix at the cardiomyocyte lateral membrane, and interacts directly with many costameric proteins and indirectly with many ion channels[123]. Its main domains are (1) the N-terminal actin-binding domain, (2) a large rod-shaped domain, (3) a WW-domain interacting with dystroglycan and other PY-motif-containing proteins, (4) a cysteine-rich region that can interact with calmodulin, and (4) the C-terminal domain that interacts with two syntrophins and dystrobrevin[124].

*DMD* mutations can cause Duchenne muscular dystrophy, an X-linked progressive neuromuscular disease characterized by long-term muscle deterioration and pulmonary and cardiac dysfunction[125].

Mice with dystrophin deletion (*mdx*) show a reduction in $Na_v1.5$ protein expression, both overall and specifically at the lateral membrane, and a reduction in whole-cell sodium current [116,126]. Moreover, the cardiomyocyte lateral membrane is markedly flattened[127], costameres are disintegrated, and the sarcolemma is fragile and leaky[27]. This leads to an increase in intracellular calcium levels, proteolysis, and apoptosis and necrosis[128,129]. These processes compromise both skeletal and cardiac muscle function. Mice without dystrophin show a much milder phenotype than human Duchenne patients due to compensatory utrophin expression[130]. Research efforts have aimed to re-introduce utrophin expression in human tissue, although utrophin expression alone cannot fully rescue a wildtype-like phenotype[131].

#### 1.6.4.5 CASK

CASK is a MAGUK protein like SAP97, and can interact with SAP97. In cardiomyocytes, it is expressed exclusively at the lateral membrane[132]. CASK appears to play a role in the trafficking of $Na_v1.5$, and knock-out or silencing of CASK leads to an upregulation of the sodium current[132], which appears to be mediated by the CASK-binding protein calcineurin[133,134]. CASK silencing may also lead to an increase in the sodium current as it translocates to the nucleus and regulates transcription of genes with T- or E-box elements[135,136]. The promotor of *SCN5A* contains an E-box sequence[137], which seems to be a transcriptional repressor for *SCN5A*, since deletion of the E-box increases the sodium current[137]. Interestingly, CASK silencing also leads to increase in the calcium current in a calcineurin-dependent manner[133,134].

Mutations in the *CASK* gene have been associated with X-linked mental retardation. No cardiac phenotype has yet been described[138], although a combination of a *CASK* and *MYBPC3* (myosin-binding protein C, cardiac) mutation has been described in a patient with dilated cardiomyopathy[139].

### 1.6.5 $Na_v1.5$-related cardiac arrhythmias

Mutations in *SCN5A* have been associated with a wide range of cardiac arrhythmias, including LQTS type 3, Brugada syndrome, sick-sinus syndrome, atrial fibrillation, progressive cardiac conduction defect (PCCD), sudden infant death syndrome, and dilated cardiomyopathy[140]. For cases in which phenotypes overlap, the term *SCN5A* overlap syndrome has been coined[141,142]. PCCD, LQTS, and Brugada syndrome will be concisely elucidated below.

A *SCN5A* mutation can lead to a gain or loss of function of the channel. Loss-of-function mutations typically reduce the upstroke velocity of the action potential, which slows conduction. In PCCD, also known as Lenègre-Lev disease, *SCN5A* loss-of-function mutations or haploinsufficiency cause slow conduction in Purkinje fibers, which can lead to bundle branch block, heart failure, and sudden death[140,143]. Brugada syndrome is also associated with loss-of-function mutations in *SCN5A* that lead to a decrease of $Na_v1.5$ sarcolemma expression and changes in biophysical properties[140,144-146]. Brugada

syndrome patients typically show an ST-segment elevation at the ECG and a T-wave inversion in the right precordial leads and have a high risk of sudden cardiac death[144,146].

Gain-of-function mutations often increase the late sodium current ($I_{Na,late}$) and concomitantly increase action potential duration and QT interval on the ECG[111,147]. These effects may increase the risk of torsades de pointes and sudden cardiac death[147]. Alternatively, $I_{Na,late}$ can induce early or delayed afterdepolarizations (EAD and DAD, respectively) during or after the action potential, respectively[147-149]. EADs lead to $Ca_v1.2$ reactivation, which extends the duration of the action potential plateau, and are associated with LQTS. DADs occur when the $I_{Na,late}$-mediated increase in sodium loading reduces the gradient for calcium efflux through NCX[149]. This in turn causes intracellular calcium overload. DADs underlie arrhythmias in catecholaminergic polymorphic ventricular tachycardia (CPVT), among other diseases[148,149].

Interestingly, neuronal sodium channel isoforms have been implicated in the generation of the arrhythmogenic late sodium current in cardiomyocytes, including $Na_v1.1$, $Na_v1.6$ and $Na_v1.8$[150-153]. Mutations in *SCN10A*, encoding $Na_v1.8$, have been associated with conduction defects in humans[154], and *SCN1A* mutations have been shown to contribute to arrhythmias in dogs[153]. Radwański *et al.* have implicated a pro-arrhythmic role for $Na_v1.6$ in the T-tubules[155]. However, our next-generation RNA sequencing (RNA-seq) data show that expression of the corresponding murine genes *Scn1a*, *Scn8a* and *Scn10a* is negligible in our Black6/J mice[76], which is confirmed by a proteomics approach in mice with unspecified genetic background[156]. Taken together, sodium channel isoform expression seems to differ greatly between models.

Of note, the aforementioned diseases are also associated with mutations in other genes. In Brugada syndrome patients for instance variants in *CACNA1C* encoding $Ca_v1.2$ and *GDP1L* (glycerol phosphate dehydrogenase 1-like) have been identified, and for LQTS, variants in the $Na_v$ $\beta_4$-subunit, caveolin 3, calmodulin, and $\alpha_1$-syntrophin are known[140,157-160]. Moreover, more than 20 mutations in all four β-subunit genes have been associated with sudden cardiac death, LQTS, Brugada syndrome, SIDS, cardiac conduction disease, atrial fibrillation, and idiopathic VF, among others. Most of these mutations decreased sodium current, some however conferred a gain of function (reviewed by [8,111,112]).

#### 1.6.5.1 No straight line from mutation to arrhythmia

The relationship between a mutation and arrhythmia is not straightforward in many cases. Mutations in *SCN5A* have a limited penetrance, and family members carrying the same mutation can show different clinical manifestations, indicating that environmental or other genetic factors are at play[161]. Moreover, gain- or loss-of-function mutations in *SCN5A* can cause many different phenotypes, as mentioned in **Section 1.6.5**, and mutations in some $Na_v1.5$-interacting proteins are associated with the same syndromes as *SCN5A* mutations are[140]. This phenotypic variability remains largely unexplained.

Mutations may have different effects in different pathophysiological environments. For instance, the effect of mutations that affect the calcium sensitivity of $Na_v1.5$ may depend on calcium homeostasis, which is disturbed in heart failure[162]. Conversely, an increase in late sodium current due to a gain-of-function mutation in *SCN5A* can disrupt calcium homeostasis (reviewed by[147]).

Secondly, mutations may have location-specific effects, although no experimental data support this hypothesis yet. Biophysical properties differ between sodium channels at the lateral membrane and intercalated disc[88]. Affecting the intercalated disc pool of $Na_v1.5$ may not only reduce conduction velocity in general, but also disturb ephaptic coupling. Also, the whole-cell biophysical properties of the total $Na_v1.5$ population shifts in the direction of the properties of the lateral membrane pool, which may increase the threshold for cardiac excitation[88].

Interestingly, the perinexus may prevent arrhythmias in a specific *SCN5A* gain-of-function mutation associated with LQTS type 3 (Y1975C). This mutation leads to EADs in single cells, but only rarely in tissue. A computer model showed that sodium current self-attenuation in the intercellular cleft quenched the late sodium current in tissue, showing that ephaptic effects can mask the arrhythmogenic effects of the mutated channel[163].

The $Na_v1.5$ macromolecular complex may also underlie location-specific effects of mutations. Firstly, some $Na_v1.5$ interacting proteins are specific to the intercalated disc (ankyrin G, $\beta_1$-subunit) or the lateral membrane ($\alpha_1$-syntrophin, CASK (see **Section 1.6.4**)); therefore, mutations in those proteins or in the respective interaction sites of $Na_v1.5$ may affect $Na_v1.5$ function differently at different locations. Secondly, a mutation may specifically affect $Na_v1.5$ in caveolae when it occurs in caveolin 3 or in the $Na_v1.5$ motif that interacts with caveolin.

Mutations may also have cell-type-specific effects as cardiomyocyte morphology, ion channel expression, and interacting protein composition differ between ventricular, atrial, nodal, and Purkinje/conducting system cardiomyocytes[164].

Taken together, many factors affect the function of mutated $Na_v1.5$, and linking a phenotype to a mutation requires a deep understanding of cardiac function, on a molecular, cellular and tissue level.

## 1.7 A closer look at cardiomyocyte membrane domains

This section takes a close look at the three main membrane domains of the cardiomyocytes: the lateral membrane (**Section 1.7.1**), the intercalated disc (**Section 1.7.2**), and the T-tubules (**Section 1.7.3**).

### 1.7.1 The cardiomyocyte lateral membrane

Although this thesis has briefly addressed the lateral membrane in **Section 1.3.1** and **Figure 6**, this section discusses the lateral membrane in more detail, including some salient new insights.

Firstly, it must be noted that the groove of the lateral membrane does not only host the openings of T-tubules, but also costameres. Costameres are multiprotein complexes that connect the cytoskeleton to the extracellular matrix[123] (see **Figure 1A,B** in **Section 3.1**). Dystrophin is a major component of the costamere, and the disintegration of the costamere in dystrophin deficiency may be partially responsible for the loss of $Na_v1.5$ at the lateral membrane[126,130].

The crest moreover contains the tight-junction protein claudin. Very recently, tight-junction-like structures joining lateral membranes of two neighboring cells have been identified[7] (**Figure 12 A,B**). These structures could further support tissue cohesion. We may even hypothesize that these structures may enable ephaptic coupling if enough sodium channels are present. This finding also challenges the textbook paradigm that only the intercalated disc contains cell-cell junctions[22,75]. Guilbeau-Frugier *et al.* note that lateral membrane structures are very easily lost when preparing samples for microscopy, which might explain the delayed discovery of lateral membrane tight junctions[7].

Interestingly, like costameres, claudin also partly depends on dystrophin expression[165]. Correspondingly, dystrophin is found over the entire lateral membrane[116]. Claudin expression is also reduced in human end-stage cardiomyopathy[166]. The functional implications are still unknown, but lateral membrane instability and reduced conduction velocity in hearts from dystrophin-deficient *mdx*

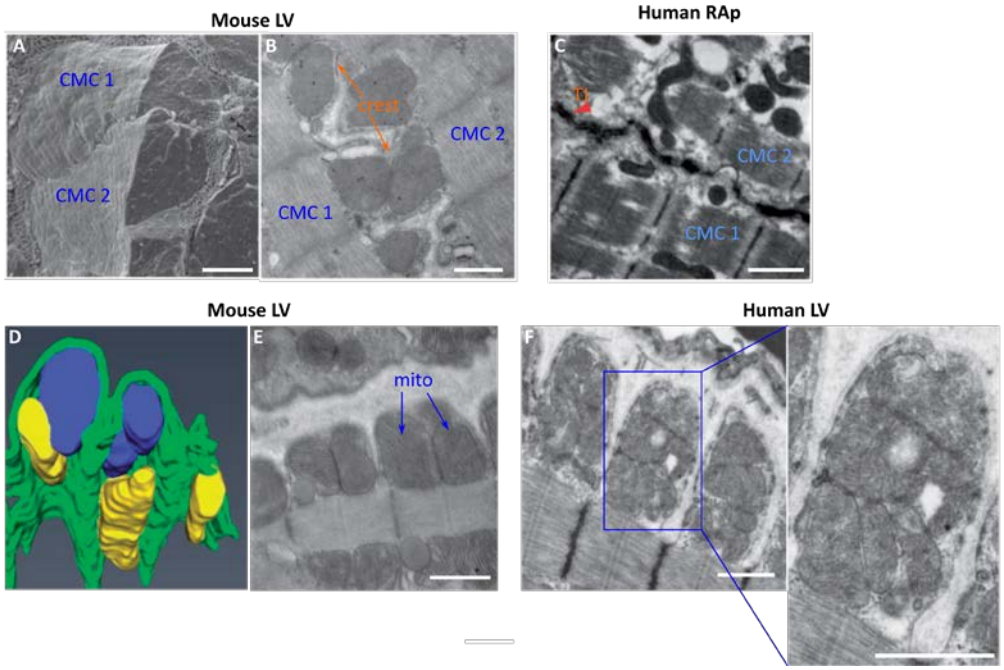


**Figure 12. Crest structures.** (**A-B**) Neighboring murine left ventricular (LV) cardiomyocytes show close proximity of lateral membranes. (**A**) cryo-scanning EM (SEM); (**B**) transmission EM (TEM) images. (**C**) TEM image of human right appendage showing tight junction-like structures at the lateral membrane. Note that mitochondria have disappeared due to suboptimal tissue preparation. (**D**) 3D-reconstruction of dual-beam SEM images showing sausage-like shapes of mitochondria in mouse tissue. (**E**) TEM image showing mitochondria anchored to Z-lines of sarcomeres in a murine cardiomyocyte. (**F**) Crest relief of human LV sample, showing a large number of mitochondria. Scale bars: (**A**) 10 µm, (**B**) 0.5 µm, (**C**) 1 µm, (**E-F**) 1 µm. Adapted from Guilbeau-Frugier *et al.*, 2019[7].

mice and Duchenne patients may not only be caused by a loss of costameres, but also by a loss of these tight-junction-like structures[7,125,126,130].

#### 1.7.1.1 Mitochondria at the lateral membrane

Mitochondria under the crest are arranged end to end and have an elongated shape, but are highly prone to shrinking as soon as cardiomyocytes are isolated from tissue[7]. In mice, the crest usually hosts only one mitochondrion, and is about 1 µm high relative to the groove (for a sense of scale, sarcomeres are typically 2 µm wide). Humans have higher crests and more mitochondria than mice: most crests contain a stack of two or three mitochondria[7]. (**Figure 12 C,D**)

Crest mitochondria tend to disappear or cluster into heaps under the lateral membrane during heart failure[65,127]. In cardiomyocytes from *mdx* mice, functional communication between $Ca_v1.2$ and mitochondria is lost, but this interaction is more likely to occur at the T-tubules[167]. The flattening of the lateral membrane in *mdx* mice is likely a consequence of the loss of mitochondria at the crest[167]. Whether the loss of crest mitochondria contributes to the phenotypes of failing and dystrophin-deficient hearts remains unknown.

#### 1.7.1.2 Voltage-gated ion channels at the lateral membrane

Most voltage-gated ion channels that are expressed in a cardiomyocyte are at least present at the lateral membrane (reviewed by[168]). The distribution of some of these channels over the crest and the groove of lateral membrane has been investigated with scanning ion conductance microscopy. Firstly, calcium currents were recorded in the mouth of T-tubules and very little in other regions of the groove[6,169] or on the crest[169,170]. Sodium currents were recorded at the crest, groove, and T-tubule mouth, but the sodium current amplitude differed: small currents were found in the T-tubular mouth (median: 1-5 channels; no current in ~25% of recordings), slightly larger in the groove (median 6-10 channels; no current in ~40% of recordings), and largest on the crest (more than 20 channels; no current in ~55% of recordings)[170]. Lastly, chloride (likely ClC) channels were found in the T-tubular mouth and in the groove, but not on the crest[169]. These channels are voltage sensitive and may modulate the action potential[169]. However, little is known about their function in cardiomyocytes[171]. Scanning ion conductance microscopy data on potassium channels are to my best knowledge not yet available.

Interestingly, channel distribution over the crest and groove can change in disease conditions. Rivaud *et al.* showed that sodium current decreases on the crest, not in the groove, in a mouse model for cardiac pressure overload by transient aortic constriction[89]. Biophysical properties between crest and groove sodium current were the same[89].

Considering calcium channels, partial mechanical unloading has been shown to reduce functional calcium channel expression at T-tubule mouth[172]. Partial mechanical unloading is achieved by left-

ventricular assist devices, which are implanted in end-stage heart failure patients, in which T-tubules and the lateral membrane are already expected to be highly remodeled[65,89,127,172]. Therapies in these patients may be fine-tuned to limit the negative effects of partial mechanical unloading[172].

Lastly, although gap junctions are not voltage gated, it deserves mentioning that gap junction remodeling in ischemic heart disease and heart failure leads to the expression of connexons (connexin 43 hemichannels, constituting gap junctions at the intercalated disc[3]) at the lateral membrane. These hemichannels are implicated in cell swelling, loss of membrane potential, and ATP release (reviewed by [173]).

#### 1.7.1.3 Lateral membrane interacting proteins of $Na_v1.5$

As mentioned previously (**Section 1.6.4**), some interacting proteins of $Na_v1.5$ are specific to the lateral membrane, including syntrophin, dystrophin, and CASK. However, whether the composition of the $Na_v1.5$ macromolecular complex differs between the crest and at the groove has not yet been investigated.

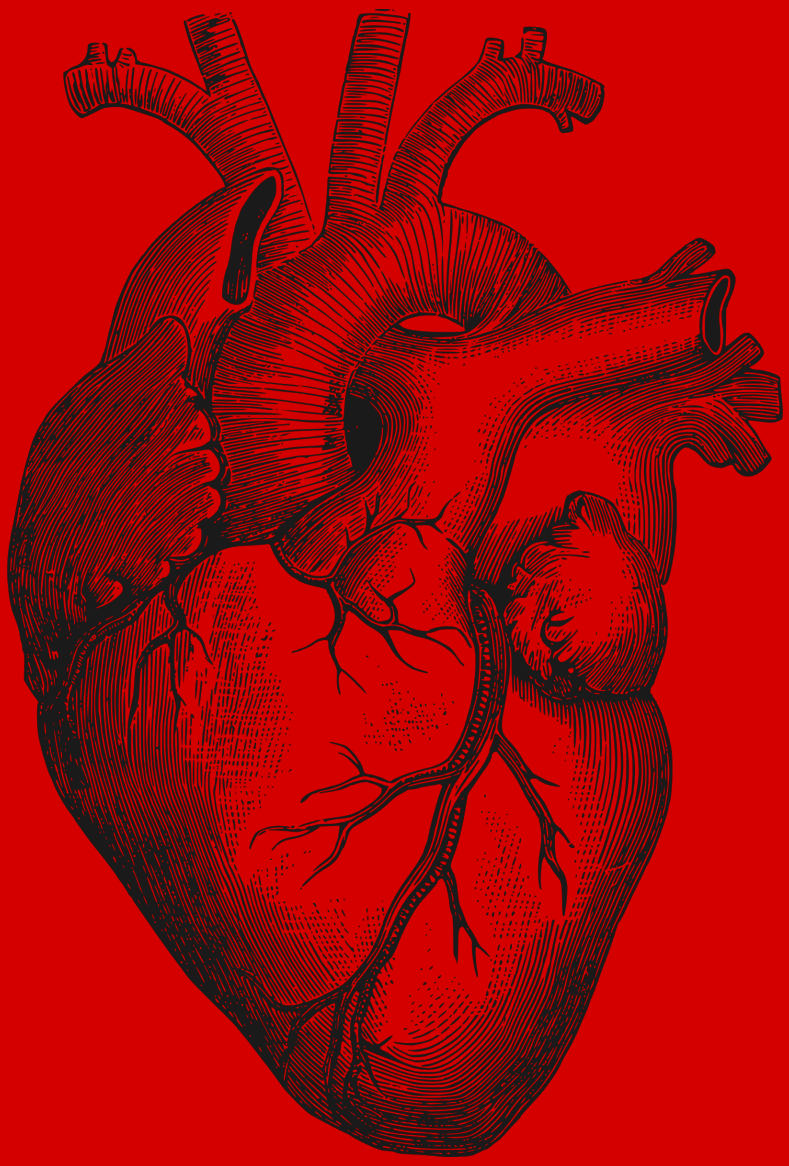

# INTRODUCTION PUBLICATION #1

### 1.7.2 Publication 1: Refining the molecular organization of the cardiac intercalated disc

This publication reconstructs the molecular composition of the cardiac intercalated disc.

I wrote the first draft of this manuscript during my master's degree under the supervision of Dr Toon van Veen (Utrecht University), and edited it for publication during my PhD.

This manuscript was published in *Cardiovascular Research* in 2017[3].

Cardiovascular Research (2017) **113**, 259–275
doi:10.1093/cvr/cvw259

REVIEW

# Refining the molecular organization of the cardiac intercalated disc

**Sarah H. Vermij[1,2], Hugues Abriel[2], and Toon A. B. van Veen[1]***

[1]Department of Medical Physiology, Division of Heart & Lungs, University Medical Center Utrecht, Utrecht, the Netherlands; and [2]Department of Clinical Research, University of Bern, Bern, Switzerland

*Received 30 May 2016; revised 29 September 2016; editorial decision 12 November 2016; accepted 4 January 2017; online publish-ahead-of-print 9 January 2017*

**Abstract** This review presents an extensively integrated model of the cardiac intercalated disc (ID), a highly orchestrated structure that connects adjacent cardiomyocytes. Classically, three main structures are distinguished: gap junctions (GJs) metabolically and electrically connect cytoplasm of adjacent cardiomyocytes; adherens junctions (AJs) connect the actin cytoskeleton of adjacent cells; and desmosomes function as cell anchors and connect intermediate filaments. Furthermore, ion channels reside in the ID. Mutations in ID proteins have been associated with cardiac arrhythmias such as Brugada syndrome and arrhythmogenic cardiomyopathy. However, rather than being independent, all ID components work together intensively by multifunctional proteins such as ZO-1, Ankyrin G, and β-catenin, integrating mechanical and electrical functions. GJs form a plaque surrounded by the perinexus in which free connexons reside; the connexome integrates $Na_V$ channels, the desmosome and GJs; and the area composita hosts AJs and desmosomes, also integrated as adhering junctions. Furthermore, the transitional junction connects sarcomeres to the plasma membrane. Lastly, this review integrates all these findings in comprehensible figures, illustrating the interdependencies of ID proteins.

**Keywords** Intercalated disc • Cardiac arrhythmia • Brugada syndrome • Arrhythmogenic cardiomyopathy • Wnt signaling

## 1. Introduction

The cardiac intercalated disc (ID) is a tightly regulated and complex structure joining together adjacent cardiomyocytes in the heart (*Figure 1*). It ensures fast propagation of the electrical signal that initiates contraction throughout the heart, and allows the cardiomyocytes to withstand the strong mechanical forces imposed by the beating of the heart (reviewed in e.g.[1]). It is because of the ID that cardiomyocytes collectively act as a functional syncytium, both electrically and mechanically. This makes the ID indispensable for the normal functioning of the heart. Moreover, the ID is closely connected to the cytoskeleton and plays a role in signaling cascades.

As opposed to the ID, the lateral membrane (LM) of cardiomyocytes has a different makeup. It hosts, among others, costamers and focal adhesions, linking sarcomeres to the extracellular matrix (ECM).[2] Although the ID and LM have several proteins in common, such as vinculin and α-actinin, and ion channels,[3,4] discussing the LM exceeds the scope of this review.

The classic definition of the ID includes three main structures: the desmosome, which functions as a cell anchor, the adherens junction (AJ), which provides cell strength, and the gap junction (GJ), which couples cells electrically and metabolically. AJs and desmosomes are tightly connected to the cytoskeleton (*Figure 1*). Furthermore, several proteins that are not involved in direct cell-cell contact reside in the ID, such as ion channels,[5] while some membrane areas do not carry proteins, mostly at the apex of a plasma membrane fold, where the transitional junction is located.[6]

Due to the major role of the ID, it is no surprise that mutations in ID proteins cause a range of diseases, including arrhythmogenic cardiomyopathy (AC; until recently known as arrhythmogenic right ventricular cardiomyopathy/dysplasia (ARVC/D)), Carvajal disease, Naxos disease and Brugada syndrome.[7]

The notion that the ID is one functional unit rather than a collection of individual structures has increasingly found its way into the common knowledge of ID researchers. Interacting ID components have been collectively renamed into adhering junction, area composita[8] or connexome,[9] which integrate electrical and mechanical functions.[10] Moreover, mutations in ID proteins and cardiac disease often lead to severe ID remodelling. Still, research articles have focused mainly on one component of the ID. An integrated approach concerning the interplay between all ID components was still lacking. This review aims to fill this gap.

Firstly, this review will discuss in detail the molecular composition of the ID and the interactions between its components. This includes both

* Corresponding author. Tel: +31 30 2538908; fax: +31 30 2539039, E-mail: a.a.b.vanveen@umcutrecht.nl

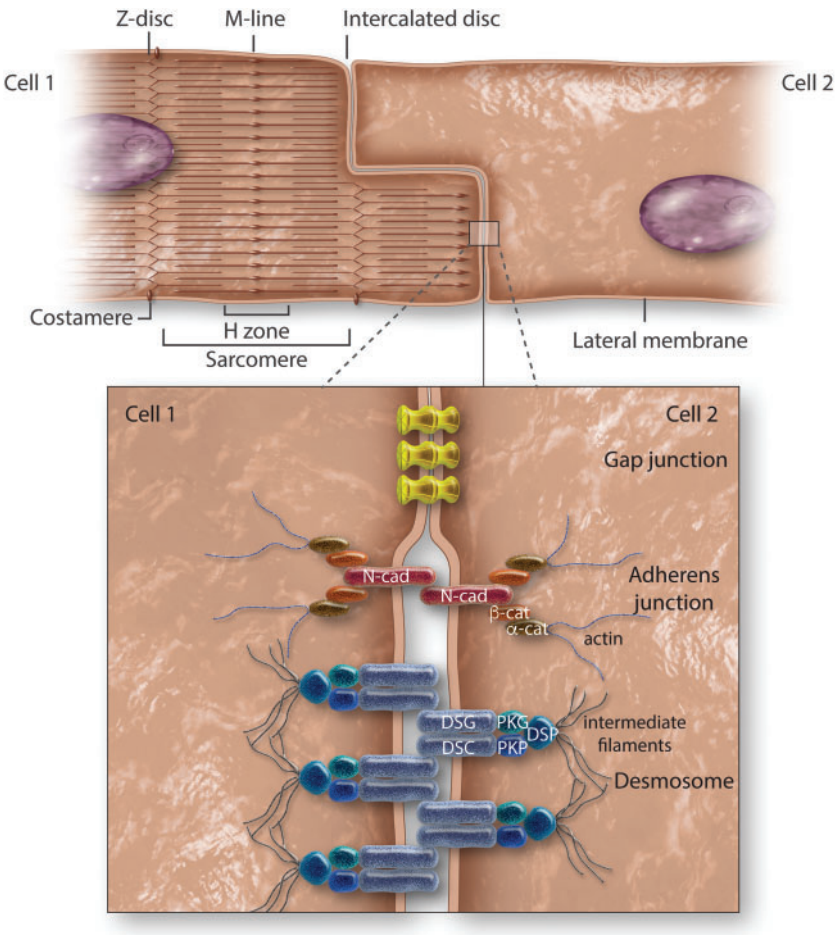


**Figure 1** Old model of the cardiac intercalated disc, in which adherens junctions, desmosomes, and gap junctions are independent structures. Please note that these structures do not anchor the sarcomeres to the ID, although the steps of the ID correspond to the length of a sarcomere. At the lateral membrane, costameres ensure the anchoring of sarcomeric Z-discs to the extracellular matrix. Gap junctions bring the adjacent sarcolemmas close together, whereas desmosomes are visible at electron micrographs as relatively large electron-dense structures compared to adherens junctions.

its structural and its accessory proteins. Furthermore, mechanical and electrical insights will be integrated. Research in this field mainly concerns either mechanical or electrical changes caused by mutations in ID proteins as if these changes were independent; however, mutations in certain ID proteins can result in both mechanical and electrical changes. This indicates a cross-talk between mechanical and electrical players, possibly by common accessory proteins. Where possible, the relationship between mutations, the development of arrhythmias and ID remodelling will be made as well. Signaling pathways in which ID components are involved will be addressed. Finally, a comprehensive picture is given of the new insights in ID organization.

## 2. Adherens junction

*Figure 2* illustrates the composition of the adherens junction (AJ), alternatively named fascia adherens. The AJ is the primary anchor for myofibrils and connects actin filaments from adjacent cells, which allows the cell to retain shape upon mechanical stress.[4] Furthermore, it transduces signals concerning the actin cytoskeleton and it senses mechanical forces on the cell. (reviewed in Ref. 3).

The transmembrane protein N-cadherin (N-Cad) is the main constituent of AJs. It homodimerizes with N-Cads from adjacent cells in the extracellular space, as an intercellular zipper. This provides tissue specificity during development, allowing cells to interact only with cells expressing the same cadherin. Calcium ions ensure the rod shape of N-Cad. The intracellular domain of N-Cad primarily binds β-cat.[1] N-Cad also possesses regulatory functions: see its role in mechanosensing later in this review.

β-catenin directly interacts with the C-terminal cytoplasmic domain of N-Cad. By associating with α-cat and Vcl, it connects AJs to the actin cytoskeleton. Also, β-cat plays a central role in cadherin-mediated signaling. (reviewed in Ref. 3) Moreover, β-cat can activate the canonical Wnt signaling pathway. It translocates to the nucleus when Wnt binds its Frizzled receptor, to initiate transcription of transcription factors of the TCF/LEF family. The canonical Wnt pathway is crucial in cardiac development but also has been proposed as the key mechanism in certain cardiomyopathies: activation induces cardiac hypertrophy. Therefore, N-Cad has been thought to sequester β-cat to prevent Wnt

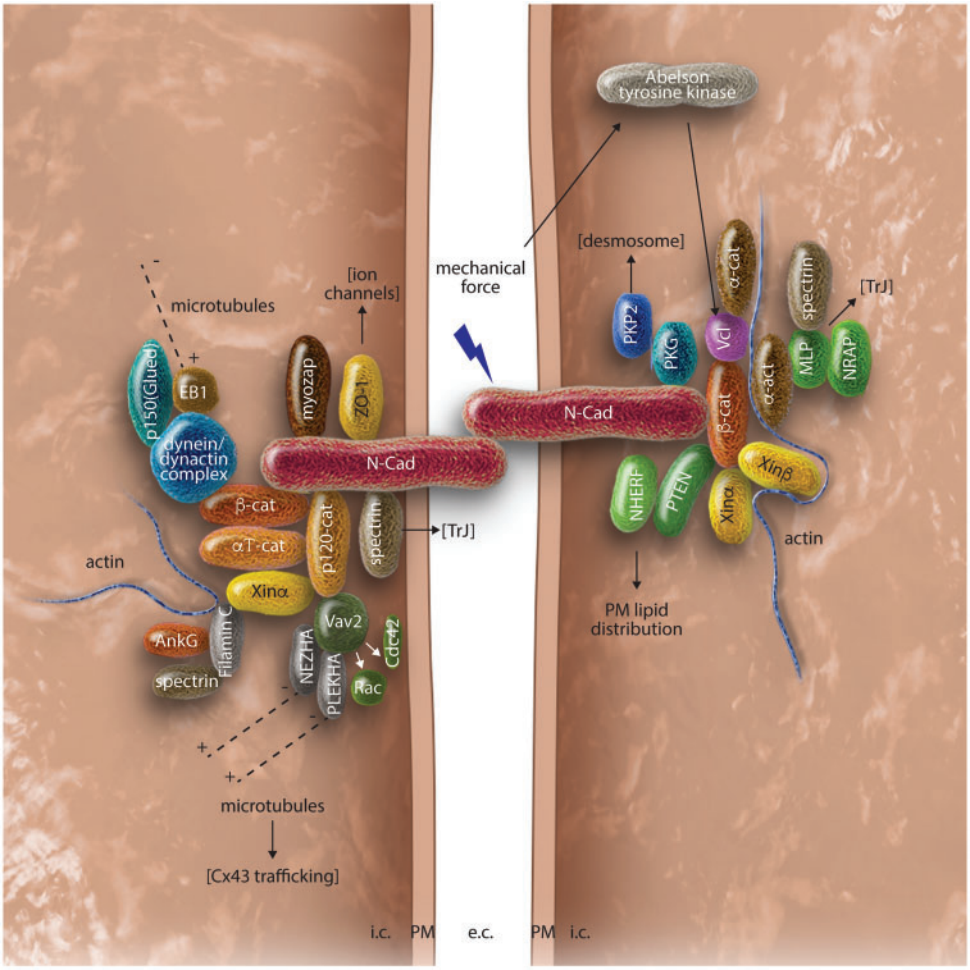


**Figure 2** Structural and associated proteins of the adherens junction. Pathways are depicted with arrows. Connections to other ID components are shown in dotted lines and between brackets. Please note that exact interaction sites are not specified to prevent unnecessary complexity.

activation.[11] Interestingly, activation of the Wnt pathway increases expression of the GJ protein Cx43, and the C-terminus of Cx43 can interact with β-cat. Although increased Cx43 expression seems to contradict conduction slowing in cardiac disease, defective trafficking and the remodelling of GJs to the LM may explain this.[12] When Wnt is not present, cytoplasmic β-cat is targeted for degradation by the proteasome.[3,13,14] Moreover, instead of β-cat, α-actinin and plakoglobin (PKG)—alternatively named γ-catenin—can bridge N-Cad to actin.[15] Note that desmosomes also contain PKG, indicating interplay between AJ and desmosomes.[16] Interestingly, Garcia-Gras *et al.* proposed a model in which PKG, as a functional and structural β-cat homologue, can compete with β-cat at the APC/Axin/GST complex, which facilitates the degradation of cytoplasmic β-cat. The observation that DSP deficiency increases nuclear PKG concentration and the transcription of adipogenic genes underlines this notion.[17,18]

p120-catenin (p120-cat) binds the cytoplasmic domain of N-Cad close to the membrane. There, it regulates adhesion and cell shape by binding to the guanine nucleotide exchange factor Vav2, which activates the Rho family GTPases Rac1 and Cdc42.[3] Also, p120-cat binds to PLEKHA7 and Nezha, two proteins that mediate the binding of the minus end of microtubules, thereby ensuring the connection of AJ to microtubules.[15]

## 2.1 Associated proteins

Vinculin is spread evenly over the ID membrane and resides at the edge of the ID plaque proteins, in contrast to β-catenin that is found at the membrane.[6] Vcl links β-cat to actin via α-act, while β-cat primarily binds N-Cad. At the LM, Vcl links costameres to actin via integrins. Its crystal structure reveals a globular head, hinge region and a C-terminal flexible tail.[19] Vcl may however also insert into the plasma membrane in acidic phospholipid-rich areas where its tail associates with the acidic phospholipid $PIP_2$ (phosphatidylinositol-4,5-biphosphate), which recruits actin regulatory proteins. The tight interaction between Vcl and $PIP_2$ discloses a role of Vcl in pathways that are initiated by PI3Ks (class I phosphoinositide 3-kinases), a scaffolding adapter protein that phosphorylates $PIP_2$ and generates $PIP_3$, which traditionally leads to Akt phosphorylation. This pathway plays many roles, for instance in apoptosis and mechanosensing. Indeed, a small reduction in Vcl induces rapid cell death, although the pathway by which Vcl affects PI3K is unclear.[19]

Other important accessory AJ proteins are PTEN, spectrin and cortactin. PTEN (phosphatase and tensin homologue deleted on chromosome ten) associates with AJ-associated β-cat and with the sodium-proton exchanger regulatory factor NHERF. Hereby, PTEN contributes to the polarized distribution of lipids in the inner leaflet of

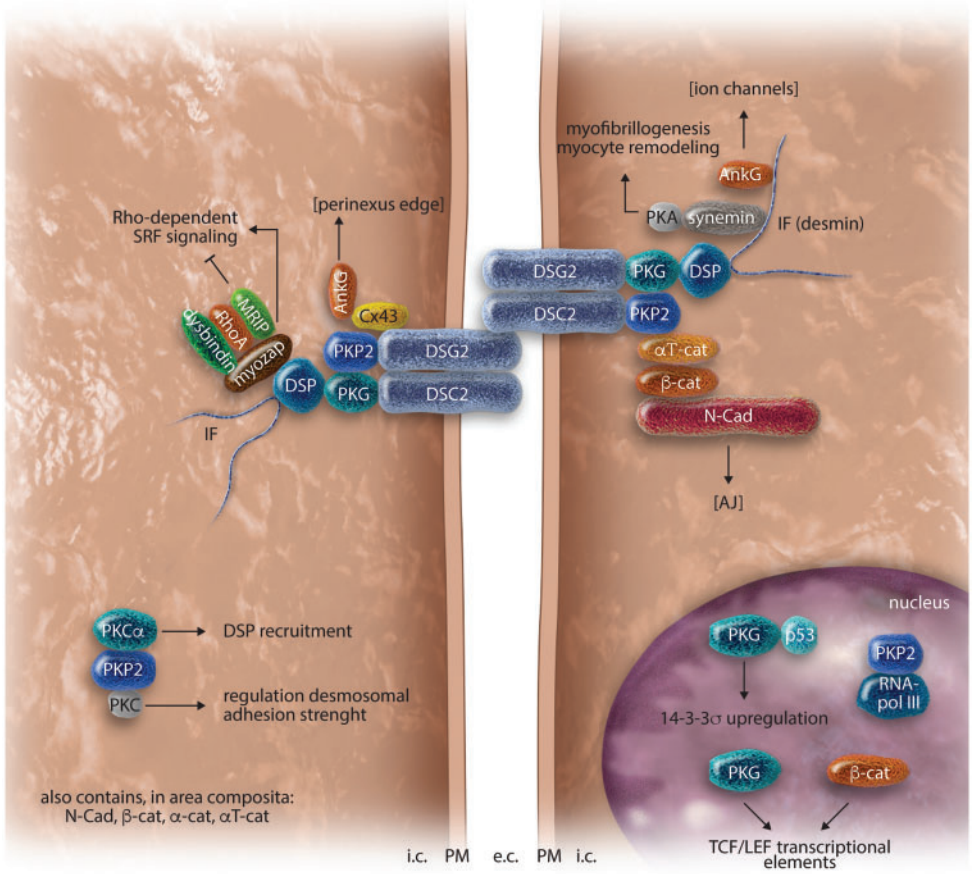


**Figure 3** Structural and associated proteins of the desmosome. Interestingly, PKP2, β-cat, and PKG also play a role in the nucleus.

the plasma membrane.[20] Spectrin however binds N-Cad,[21] and its heterodimers form tetramers to bind actin filaments at their distal ends. At the ID, spectrin probably occurs in the most stable tetramer form $(\alpha II\beta II)_2$, whereas αII spectrin is found at the distal Z-discs of myofibrils, closest to the ID. Moreover, spectrin is predominantly found at the axial extremes of the ID, the transitional junction (see later chapter), whereas Vcl and β-catenin are spread more evenly over the ID surface.[6] Lastly, cortactin is an actin-binding protein that cooperates with N-Cad to regulate actin reorganization and adhesion strength. Its binding protein Arp2 (actin-related protein 2) ensures proper function, which, in turn, forms a complex with Arp3 and thereby regulates actin polymerization and the formation of actin branches.[22] hXinα and hXinβ are Xin proteins named after the Chinese word for heart, alternatively named cardiomyopathy-associated 1 resp. 3 (CMYA1 and -3). Their respective mouse orthologues mXinα and mXinβ have been studied extensively. They associate with AJs: the Xin repeats characteristically bind actin and they contain a β-cat binding domain, whereas mXinα also contains a p120-cat binding domain. Therefore, mXinα and mXinβ have been thought to form predominantly a stable link between AJs and actin. Also, mXinα interacts with filamin, the crosslinker protein of actin, and recruits p0071, a member of the p120-cat subfamily of armadillo proteins. Interactions between mXinα and p120-cat and p0071 might influence Vav2 and Ect2, regulators of the Rho family small GTPases Rac1 and Rho that play an important role in cardiac development. Lastly, GJ remodelling seen in mXinα deficient hearts might be explained by direct interactions of mXinα and ZO-1 and/or Cx43.[3,23] Interestingly, mXinβ is predominantly found in the left ventricle, interventricular septum and apex. Expression is especially strong at the base of the aorta and pulmonary artery, where the tissue undergoes relatively high stress. The distribution of mXinα is not known. Moreover, mXinβ deficient hearts lack mature IDs, suggesting that Xin proteins are involved in N-Cad-mediated signaling. Also, mXinβ is thought to function downstream of angiotensin II (AngII) signaling, modulating hypertrophic responses in disease (reviewed in Ref. 3).

Several proteins that are associated with AJs in other tissues, such as epithelia, are not yet investigated in the context of the heart. This might be an interesting venue for future research. For instance, Bitesize, a synaptotagmin-like protein, is involved in the stabilization of epithelial AJs via E-Cadherin.[24] Furthermore, the intercellular adhesion molecule ICAM-1 regulates N-Cad localization in endothelium through ERM (ezrin-radixin-moesin) proteins. Although ICAM-1 is expressed in the heart, its ID involvement is unclear.[25]

## 3. Desmosome

The desmosome, also known as macula adherens, is a robust, dense and symmetrical cell anchor that provides structural support to

cardiomyocytes and other tissues that are subjected to strong mechanical forces, such as epithelia. Its composition is illustrated in *Figure 3*. While AJs also transduce forces to the cytoskeleton, desmosomes are more robust, thanks to their connection to mechanically resilient IFs.[18] The intercellular part of the cardiac desmosome is built up by the cadherins desmoglein-2 (DSG2) and desmocollin-2 (DSC2), that bind in a heterologous way. DSG2 and DSC2 are, like other cadherins, single-pass transmembrane proteins. The armadillo proteins PKG and plakophilin-2 (PKP2), and desmoplakin (DSP), member of the plakin superfamily, connect desmin to the desmosome. The hyperadhesive state of the desmosome, when DSC2 and DSG2 are bound, depends on the presence of calcium ions. During wound healing and embryogenesis, desmosomes can adopt a lower-affinity state.[5] Also, desmosomal proteins can participate in signaling pathways, influencing the expression of genes involved in proliferation and differentiation, tissue morphogenesis and wound healing.[1]

Considering the major desmosomal proteins, firstly, plakophilin-2 is associated with GJs, (reviewed in Ref. 3) and is required for the organization of ID and desmosomal function (reviewed in Ref. 1). Together with PKG, PKP2 mediates attachment to IFs. PKP2 knockdown causes a decrease in conduction velocity and an increased propensity to develop re-entry arrhythmias,[5] while *PKP2* mutations are most common in hereditary AC. Moreover, like β-cat is a PKG homologue, p120-cat is a PKP2 homologue, indicating that PKP2 may also play a role in signaling.[3,5] Moreover, PKP2 has been associated with RNA polymerase III, suggesting a role in transcriptional regulation.[5,26] Secondly, plakoglobin is present in both desmosomes and AJs. As described in the AJ chapter, PKG plays an important role in Wnt signaling, indicating desmosome-to-nucleus crosstalk. Furthermore, nuclear PKG was shown to bind p53 and upregulate expression of the tumor suppressor 14-3-3σ by interacting with its promotor.[18] Thirdly, desmoplakin is characterized by its plakin domain: a globular head with many α-helices and multiple spectrin repeats that are separated by a Src-homology-3 domain. DSP connects the desmosomes to the type III IF protein desmin. It's a large protein: its N- and C-terminal domains and the α-helical domain in between are each almost 1000 amino acids long. Interaction with PKP2 occurs at their N-terminal domains.[1,5] Lastly, *DSG2* mutations are, like all other cardiac desmosomal proteins, associated with AC. In other tissues, knockout of DSG2 is often compensated by higher expression of DSG1. Although desmosomal integrity is thus restored, cellular signaling is significantly altered since different subtypes of DSG are involved in different pathways. However, since DSG2 is the only cardiac DSG, the lack of compensatory options may explain the AC phenotype.[18]

## 3.1 Associated proteins

Protein kinase Cα (PKCα) can bind PKP2. PKCα is thought to hereby regulate desmosome adhesion when dynamic cell-cell adhesion is required.[20,27] Moreover, PKCα recruits and phosphorylates DSP during desmosome genesis.[5] αT-catenin (αT-cat) is a member of the α-cat family that interacts with PKP2 and β-cat, thereby linking the desmosome and AJ. αT-catenin plays therefore an important role in the area composita, which is the junction in which desmosomes and AJs are tightly linked by sharing structural proteins (see later chapter).[8,28] Possibly, 120-catenin is involved in cardiac desmosomes as well, because it is an interaction partner of DSG1 and DSG3, linking AJs to desmosomes.[3,29] However, DSG1 and DSG3 are not present in cardiac desmosomes, and this interaction only occurs in high calcium concentrations. It is therefore questionable if p120-cat can also bind the cardiac variant DSG2.

## 3.2 Intermediate filaments

Several IF proteins reside in the heart, although desmin is the most prevalent, as a constituent of the sarcomeric Z line. Impairment of the PKG-desmin interaction in transgenic mice impairs delivery of Cx43, DSP, DSC, N-Cad and PKG to the ID, followed by conduction slowing.[1] Furthermore, synemin is clearly located at the ID and binds to protein kinase A (PKA), thereby regulating myofibrillogenesis and myocyte remodelling, although synemin is predominantly expressed during heart disease.[30] It is suspected to interact with desmin.[31] Please note that desmosome-associated desmin is not directly associated to Z-discs, since mature Z-discs are absent at the ID. Immature Z-discs, in turn, are connected to the transitional junction region of the ID (see chapter 6.3).

## 3.3 Adhesion junction–bringing the desmosome and adherens junction together

The classical definition of the desmosome is based on electron microscopy images that reveal the inner dense plaque (IDP), outer dense plaque (ODP) and electron dense midline (EDM) or membrane core. The EDM comprises of the interacting domains of DSG and DSC. The ODP contains the transmembrane proteins DSG, DSC and intracellular PKG and PKP. Furthermore, to the ODP, the intermediate filaments (IFs) are connected.[18] However, this a rather old-fashioned model. Rather, the AJ and desmosomes together are named 'adhesion junctions' or 'adhering junctions' because cadherins make up the intercellular contact proteins of both junctions, and AJs and desmosomes both connect cells to the cytoskeleton of adjacent cells, albeit through different cytoskeletal proteins.[13,32] PKG is thought to be the most important factor in the adhesion junction, since it is a structural element of both AJs and desmosomes.[16] Also, p120-cat is a common constituent,[3] and PKP2 interacts with multiple AJ proteins.[33]

Observations in PKG-deficient mice give another clear example of AJ and desmosome interdependency: they lack desmosomes and instead have extended AJs with desmosomal proteins. Their hearts have increased right ventricular volume and spontaneous right ventricular ectopic activity.[1] Furthermore, DSP-deficient mice have normal GJs and AJs but lack desmosomes, indicating that DSP is essential for desmosome function and development, proposedly because DSP is essential for desmin binding. DSP also regulates actin assembly and organization via RhoA signaling.[1,5] However, the concept of adhesion junction can be extended to include GJs and ion channels, in which case it is called area composita, which will be discussed in detail later.

# 4. Gap junction

The gap junction (GJ) is an agglomeration of multiple individual gap junction channels with associated proteins (*Figure 4*). The GJ enables electro-metabolic coupling, allowing propagation of action potentials and passage of small solutes between cells.[1] In general, GJs are composed of twelve connexin molecules: six molecules form a connexon in the membrane and connect with a connexon of the opposing membrane.[1] In ventricular myocytes, connexin43 (Cx43) is the most prevalent. GJ development, regulation and degradation seems to be a highly orchestrated process with a fast turnover[1,2]: the half-life of Cx43 is as short as 1–3 h.[34]

Cx43 also has noncanonical roles, independent of connexons and GJs. It is necessary for sodium channel function for instance (see later

chapter), and loss of the GJ-independent functions of Cx43 causes severe arrhythmias and death. (reviewed in Ref. 9) Interestingly, Cx43 is also found in mitochondria, while ischaemic preconditioning increases mitochondrial Cx43 localization.[35] Moreover, GJs can have direct physical contact with mitochondria.[36] However, the functional consequences of these phenomena are still unknown. Moreover, GJs between myocytes and fibroblasts also exist, although they are very hard to find. A fibroblast-specific small GJ subtype that is normally found between fibroblasts may also occur in IDs. This field is however still in its infancy (reviewed in Ref. 37).

## 4.1 Associated proteins

Mena (mammalian Enabled) is a member of the Ena/VASP (Enabled/vasodilator-stimulated phosphoprotein) family, which interacts with Cx43 and Vcl via its EVH1 domain. It regulates the actin cytoskeleton and microfilaments, both at the ID as well as at focal adhesions. Mena and VASP also exert actin polymerase and anti-capping activities and thereby increase actin filament assembly.[38] Mena is proposedly an important cardioprotective protein: by binding Rac1, it prevents the activation of Rac1-associated pathways. In fact, Mena knockout cardiomyocytes show an increase in Rac1 activity, leading to GJ remodelling, cardiomyocyte apoptosis, cardiac dysfunction and ID destabilization, while Cx43 expression is increased.[39]

Caveolin-1 (Cav-1) colocalizes and co-immunoprecipitates with Cx43. Caveolins are cholesterol-binding integral membrane proteins that do not span the membrane. Together with cholesterol and sphingolipids, they are important constituents of caveolae. Caveolae are the best characterized type of lipid rafts and recognizable as flask-shaped invaginations of the plasma membrane of 60–80 nm with a 10–50 nm neck.[3] Furthermore, caveolae are involved in endocytosis, transcytosis and outside-in signaling.[40,41] The Cx43-Cav-1 interaction implies a relation between GJs and caveolae.[40] The experimental evidence for Cav localization at the ID is however thin. Undoubtedly, caveolins and caveolae play a role at the ID, but the exact role remains to be determined.

## 4.2 Linking adhering/adhesion junctions to gap junctions

In development, GJs only appear at the ID when the adhering junctions are already formed, or in other words, mechanical coupling precedes electrical coupling.[2,13,42] GJ stability depends on the 'strong state' of AJs.[19,20] This shows that mechanical and electrical coupling of cardiomyocytes are tightly linked. Cx43 connexons are transported in vesicles

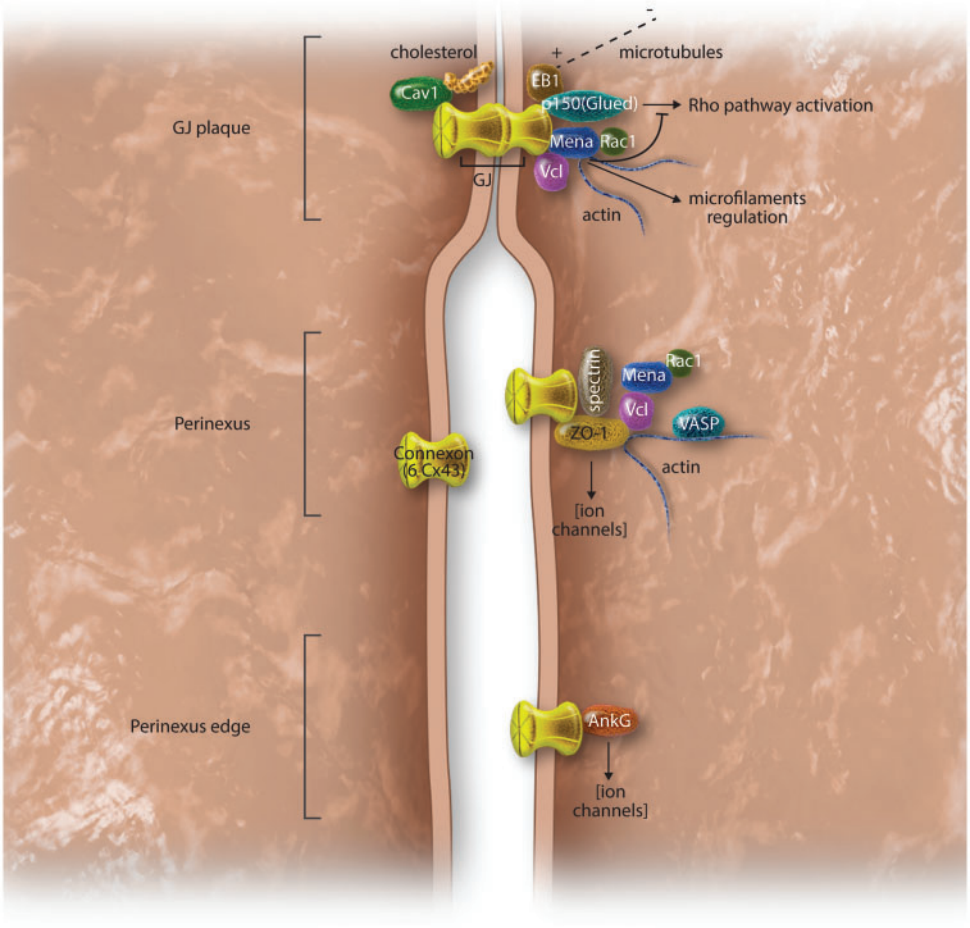


**Figure 4** Structural and associated proteins of the gap junction. Please note that connexin43 binds different partners at the gap junction plaque, perinexus and perinexus edge.

from the Golgi system to the ID via microtubules that are tethered to AJs via N-Cad, β-cat and the dynein/dynactin complex. Hereby, Cx43 interacts with the +TIP EB1 and p150(Glued). Although EB1-capped microtubuli can also bind mature GJ plaques,[43] N-Cad-knockout mice are not able to form GJs, and blocking the intercellular binding of N-Cad inhibits GJ formation. Interestingly, this connexon delivery system assures that GJs only form between homologous cells, since cadherins only connect to the homologous cadherins.[43] When adhesion junctions function improperly, for instance due to PKP2 deficiency, GJs remodel: Cx43 lateralizes and its signal at the ID decreases. This may be an arrhythmogenic substrate.[1,13] Furthermore, GJ remodelling due to Xin deficiency is thought to occur through interaction with ZO-1 and/or Cx43. (reviewed in Ref. 3).

Since GJs are sensitive to mechanical stress, they locate in the vicinity of AJs and desmosomes. (reviewed in Ref. 2), while PKP2 and Cx43 also co-immunoprecipitate.[13] Desmosomal mutations that cause AC are associated with loss of GJ plaques at the ID, which illustrates the importance of this organization. However, a complete loss of PKP2 only causes a 50% reduction in functional GJs, which surprisingly does not affect conduction velocity.[9,44] Also in Carvajal and Naxos disease, the decrease of Cx43 at the ID is obvious. Conversely, it is disputed whether Cx43 is essential for AJ or desmosome functioning. In cell lines, loss of Cx43 expression preceded a loss of intercellular adhesion strength,[9] whereas other reports show the opposite.[1,2] Importantly, Cx43 expression is aberrant in several cardiac diseases: relocalization of dephosphorylated, unfunctional Cx43 to the LM is seen in atrial fibrillation (AF), overloaded human atria, and in CMC of a rat myocardial infarction (MI) model. This notably impairs ID coupling and may lead to conduction block.[45] In an aged mouse model, Cx43 expression was decreased, many IDs were disrupted, and the intercellular space was widened at AJ regions.[46] The phenomenon of ID remodelling is however, although interesting, too complex to be covered in this review as well; therefore, we refer to other reviews.[1,47] Interestingly, delocalized connexons are not phosphorylated, contrary to their ID counterparts, indicating that phosphorylation is important for the regulation of GJ function.[9] Lateralized connexons may however still be functional in action potential propagation.[48] However, it is clear that GJs are a vulnerable structure, which is illustrated by the observation that during cardiac disease, GJs are the first structures to delocalize from the ID. A cardiac specific N-Cad knockout mouse model showed for instance reduced levels of Cx43, which lead to a reduced conduction velocity and ventricular arrhythmias, although also α-, β- and p120-cat were reduced. This indicates that N-Cad and Cx43 are tightly related, probably via ZO-1.[1] CamKII-mediated signaling is probably involved in this Cx43 lateralization, illustrated by the observation that CaMKII inhibition enhances conduction and Cx43 localization at the ID at baseline, and preserves this localization under conditions of heart failure.[49]

The MAGUK ZO-1 is thought to connect AJs to GJs by means of its scaffolding properties. ZO-1 consist of three domains, the non-functional GUK domain, the SH3 domain that interacts with proline-rich PXXP sequences, and the PDZ domain. This PDZ domain interacts with N-Cad, which stabilizes both AJs and GJs, and with Cx43. Also, ZO-1 anchors actin to the cytoskeleton. Generally, MAGUKs localize close to the plasma membrane to regulate surface expression of certain specialized domains in a variety of tissues.[19,20] ZO-1 can also connect AJs to GJs by interacting with α-cat via its N-terminal fragment, and with actin via its C terminus (reviewed in Ref. 3). Furthermore, afadin might link actin and N-Cad in this interaction chain, since afadin bridges actin to E-cad in epithelia.[50] However, although afadin is present in cardiomyocytes,[51] we do not know its cardiac function.

In cardiomyocytes and cell lines without ZO-1, normal organization of Cx43 and N-Cad was lost, and GJs lateralized. This lateralization is thought to occur through microtubule-dependent mechanisms.[48] The effect of ZO-1 on GJ localization occurs however via the interaction between ZO-1 and AJ. This interaction ensures the strong state of the AJ, on which the GJ depends.[52] In cardiac disease, the function of ZO-1 in relation to AJs and GJs can change. In healthy hearts, ZO-1 colocalizes to a greater extent with N-Cad than with Cx43. In ventricles from patients with heart failure however, ZO-1 expression is increased, and Cx43 and ZO-1 colocalize stronger, which could imply that ZO-1 prevents the increase in functional GJs.[53] (reviewed in Ref. 3) Lastly, ZO-1 also links AJs to $K_v$1.5 ion channels, and interacts with PKG, APC (adenomatous polyposis coli), an important player in the Wnt pathway, and claudin, a protein generally associated with tight junctions, while its role at the ID is unknown.[19,20,54]

As described before, vinculin anchors actin filaments to the AJ via β-cat. Its head domain also interacts with the third PDZ domain of ZO-1, thereby stabilizing GJs, either directly or via α-cat. The notion that Cx43, ZO-1, and Vcl form a complex implies that Vcl is an important anchoring point between AJs and GJs. Indeed, GJs were destabilized when the interaction between Vcl and ZO-1 was impaired, and GJ function and even cardiomyocyte integrity was lost. Loss of GJ function was demonstrated in a Vcl-deficient cell line. Moreover, in a Vcl-deficient mouse model, Cx43 and ZO-1 signals were decreased at the ID. The hearts showed excessive replacement fibrosis and cardiomyocyte loss, which could be attributed to PI3K signaling. Additionally, Vcl plays an important role in the assembly and alignment of myofibrils and in regulation of cell shape.[19]

Muscle LIM protein (MLP) may also play a role at the intersection of GJ and AJ, while MLP mutations are a suggested cause of dilated cardiomyopathy (DCM). MLP is thought to form a ternary complex with the nebulin-related anchoring protein (NRAP) and α-actinin,[55] and also interacts with actin and spectrin. In DCM patients, *MLP* mutations inhibit the interactions with NRAP and α-actinin, and compromise its zinc finger domain. In MLP knockout mice, the expression of N-Cad, β-cat, PKG, α-catenin, Vcl and NRAP is upregulated, while Cx43 was downregulated. Furthermore, Vcl distribution at the ID was disturbed,[56] which might point to a structural disruption of the transitional junction, where sarcomeres are attached to the sarcolemma.[55]

## 4.3 Perinexus

The perinexus is a newly identified functional region in the ID (*Figure 5*), in which ZO-1 plays a crucial role.[34,57] The perinexus is defined as the area around the plaque of functional GJs, in which free connexons interact with ZO-1 via its PDZ-2 domain. Here, ZO-1 regulates size, number and localization of GJs: (reviewed in Ref. 3) first, new connexons appear at the periphery of the GJ aggregate, after which ZO-1 binds. Connexons are unable to associate with connexons of neighboring cells as long as ZO-1 is bound. Two ZO-1-free connexons are able to form a GJ, thereby increasing intercellular communication.[34] Indeed, in a ZO-1 knockout model, GJ plaques were larger.[52] Lastly, ZO-1 is thought to mediate Cx43 delivery from lipid raft domains to GJs in the ID.[19] Ankyrin G (AnkG) is also found at the perinexus; it binds the outer connexons and thereby probably determines the perinexus size, and the traffic between perinexus and GJ plaque (see *Figure 5*).[9] Concomitantly, the Cx43 plaque size and Cx43-mediated electrical coupling are inversely related.[58] Also, in super-resolution fluorescence microscopy, PKP2 is

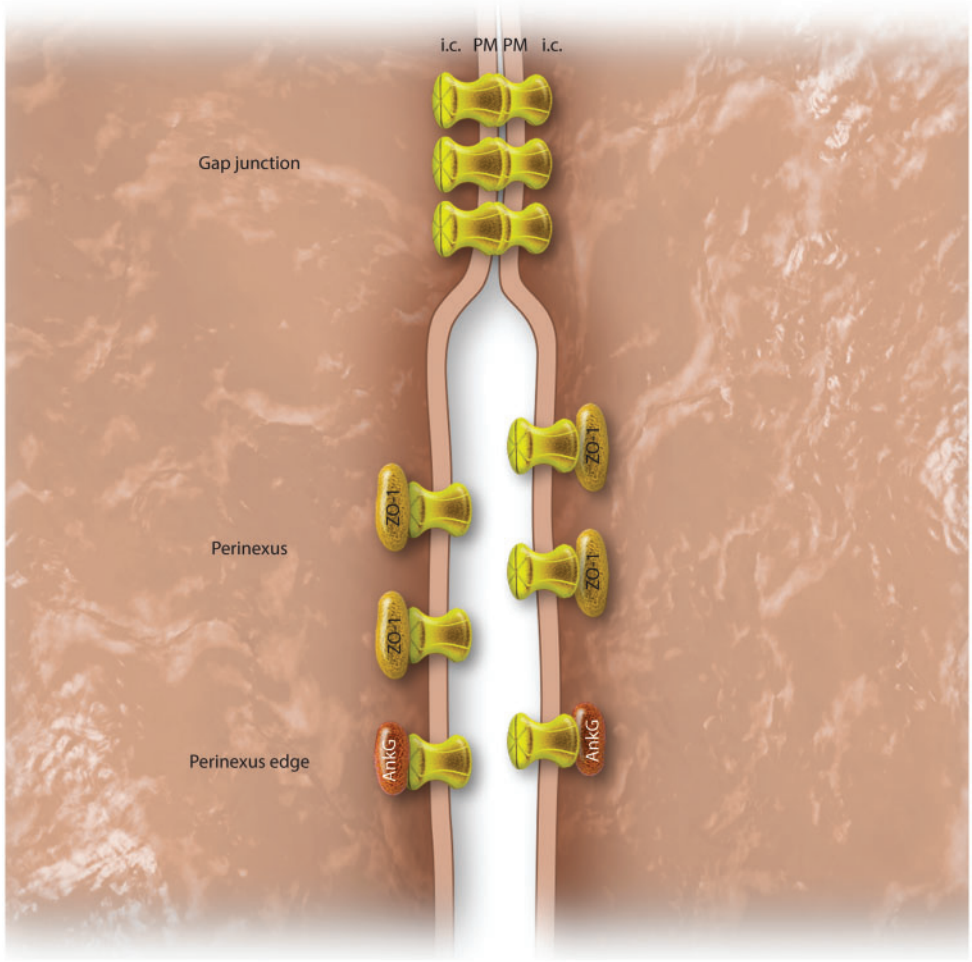


**Figure 5** Model of the perinexus, in which ZO-1 binds connexons around the gap junction plaque. AnkG binding determines the perinexus edge.

seen at the edge of the perinexus.[9] AnkG is thought to scaffold the interaction between PKP2 and Cx43. When AnkG was silenced by means of siRNA interference, the GJ-PKP2 interacting areas increased in size, as did the GJ plaques, in accordance with the perinexus model as described before.[9] Other AnkG silencing effects include decreased reduced electrical coupling and intercellular adhesion strength in cardiomyocytes.

# 5. Ion channels

Ion channels in the sarcolemma are critical for the creation and propagation of action potentials throughout the heart and for excitation-contraction coupling. They are found at three main membrane areas of the cardiomyocyte: at the ID, in the LM, and in t-tubuli. The composition of ion channels is different in each area.[2,40] Ion channels at the ID (*Figure 6*) can be classified in three main categories: $K_V$ channels ($K_V$1.4, –1.5, –4.2, –7.1, and 11.1), Kir channels (Kir2.1, –2.2, –2.3, –6.2, and SUR2a) and $Na_V$ channels ($Na_v$1.5 and –1.3). Moreover, the stretch-activated channels TRPV2 and TREK-1 are expressed at the ID, which will be discussed in the mechanosensing section. Lastly, $Na^+/K^+$-ATPase is present at the ID.[2,59]

## 5.1 Potassium channels

Potassium channels control the resting membrane potential and the repolarization phase of the action potential. Although these channels are known to reside in the well-studied ID for a long time, their interaction partners remain underexposed.[60]

$K_V$ channels are voltage-gated. Its α-subunits make up the actual channel, whereas accessory β-subunits ensure proper $K_V$ function. $K_V$1.x channels, members of the shaker family, are essential for the repolarizing currents. $K_V$1.4 for instance underlies the rapidly activating, slowly inactivating 'slow transient' current, whereas $K_V$1.5 is responsible for a rapidly activating, very slowly inactivating current.[40,60] On the other hand, the Kir (inward rectifying) channels in the heart are ATP-dependent and generally regulate the action potential duration when heart rates rise. Furthermore, they have a stress-protective role. Kir2.x channels facilitate the primary inward-rectifying currents, also regulating the resting membrane potential.[40,60] Lastly, Kir6.2 ion channels are supported by SUR2A subunits, and the $Na^+/K^+$ pump interacts with $K_{ATP}$ channels in the heart.[61]

### 5.1.1 Associated proteins

The actin cytoskeleton appears to associate with α- and β-subunits of $K_V$ channels. The actin cytoskeleton probably determines ion channel

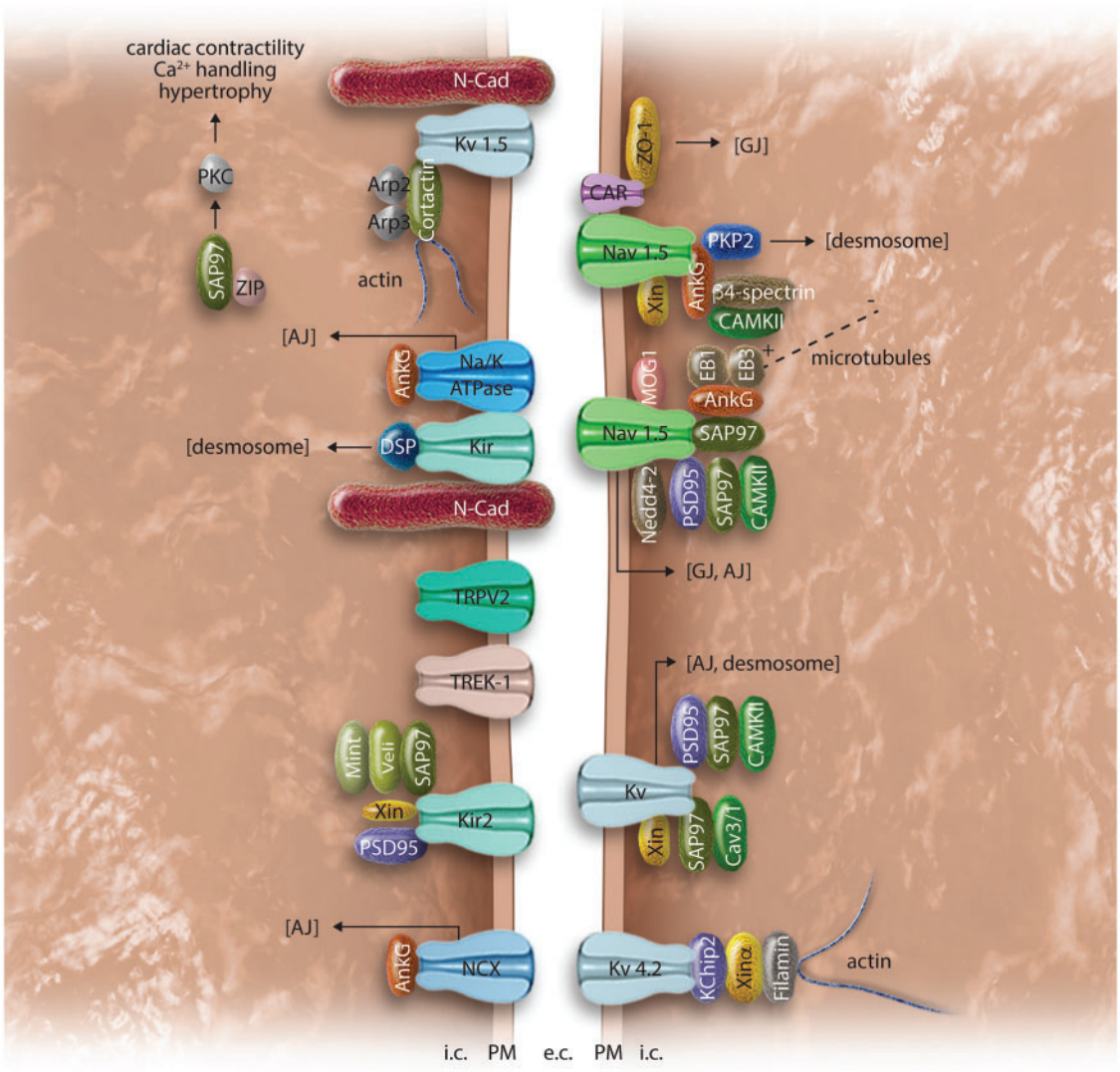


**Figure 6** This model sums up the large variety of ion channels found at the ID, of which Nav1.5 is the most important, and their interaction partners for as far these are known.

stability and surface distribution, and has been associated with $K_V1.5$ channel endocytosis. Cortactin thereby links between actin to $K_V1.5$.[60] Moreover, PSD-95–post-synaptic density protein 95, alternatively named SAP90–is a member of the MAGUK family and associates with $K_V1.4$, $K_V1.5$, and Kir2.x, supposedly to ensure localization to lipid rafts. SAP97 is also present in lipid rafts to scaffold the interaction between $K_V1.5$ and its cytosolic subunit $K_V\beta$. Furthermore, SAP97 interacts with PDCζ-interacting protein (ZIP) to recruit PKC, which is involved in a variety of pathways, including the regulation of cardiac contractility, $Ca^{2+}$ handling and hypertrophic response.[40,62] $K_V1.5$ and $Na_V1.5$ are also regulated by type-II $Ca^{2+}$ activated calmodulin kinase (CAMKII), when it is bound to SAP97 and PSD95.[40] mXinα, the mouse homologue of hXinα that has been discussed in the AJ chapter, also regulates ion channels. mXinα-deficient mice presented with a prolonged AP due to delayed inward-rectifier $K^+$ currents. This, together with changes $Ca^{2+}$ metabolism, increased the risk for arrhythmias. mXinα was shown to regulate the transient outward potassium ($I_{To}$) current by interacting with the $K_V4.2$ auxiliary subunit KChIP2 ($K_V$ channel interacting protein 2) and the actin-crosslinking protein filamin.[63] However, the conclusions regarding conduction slowing and arrhythmias may be confounded since expression of Cx43 and N-Cad is also reduced in mXinα deficient mice (reviewed in Ref. 3). Because mXinα and mXinβ can interact with ion channels, actin, β-cat and p120-cat, these proteins may scaffold N-Cad-mediated adhesion and surface expression of ion channels, of which a recent study reported.[63] In fact, the role of mXinα in regulating function and expression of ion channels has been thought to be analogous to that of AnkG (reviewed in Ref. 3).

## 5.2 Sodium channels

Whereas both $Na_V1.3$ as $Na_V1.5$ localize at the ID,[2] most is known about $Na_V1.5$, while interaction partners of $Na_V1.3$ are still unknown. Furthermore, it is noteworthy that the β-subunits of $Na_V$ channels are of unknown composition and function–although they participate in cell–cell adhesion in other cell systems than the heart.[5] The functional

complex of α- and β-subunits is called VGSC (voltage-gated sodium channel complex).

The cardiac voltage-gated sodium channel $Na_V1.5$ is responsible for the rapid upstroke of the cardiac action potential. It consists of one α-subunit of 220 kDa that forms the functional channel and β-subunits of 30 kDa each. Its essential function is illustrated by many pathologies associated with mutations in its gene *SCN5A*, such as Brugada syndrome, long-QT syndrome and familial ventricular fibrillation.[64] However, interestingly, the channel can function differently at different locations in the cells. At the ID, $Na_V1.5$ is more dependent on voltage to reach its steady-state inactivation than at the LM.[65,66]

Interestingly, $Na_V1.5$ is suggested to be enriched in the perinexus. AnkG might be a mediator between $Na_v1.5$ and Cx43.[57] The idea has emerged that GJs are not the only mediators of intercellular action potential propagation. At the perinexus, $Na_V1.5$ is potentially involved in ephaptic coupling. This term is derived from the neuronal synapse and is defined as cell-to-cell transfer of electrical activation via ion accumulation/depletion or transient extracellular electric fields within a confined interstitial space between closely apposed cells.[67] Interstitial oedema, which widens the cleft, would reduce conduction velocity, contrary to more common belief that interstitial oedema would increase conduction velocity due to a reduction in resistance. Indeed, inhibiting sodium channels with flecainide slowed conduction, but even more in an interstitial oedema model, which findings moreover follow the outcomes of a mathematical model.[67] Therefore, the interstitial volume could be an important determinant in arrhythmogenesis.[57] However, this mathematical model assumed all Nav1.5 at the perinexus, which is contrary to more recent findings which also describe Nav1.5 associated with N-Cad at excitation-excitability nodes.[68] A mathematical model considering these two pools of Nav1.5 is still awaited.

### 5.2.1 Associated proteins

$Na_V1.5$ has many cytoplasmic interacting proteins. Via its PDZ-domain-binding motif consisting of its three distal amino acids SIV, for instance, it binds the syntrophin-dystrophin complex. However, this interaction only occurs at the lateral sarcolemma. At the ID, SAP97 can bind the SIV motif of $Na_V1.5$, which implies a regulatory relation between the two.[64] SAP97 interacts also with Kir2.x, $K_V4.x$, and $K_V1.5$. Silencing of SAP97 has elucidated its essential role as an enhancer of the number of functional ion channels and potassium currents.[69] The underlying mechanism is however not yet understood. It is thought that SAP97 stabilizes the ion channel. Furthermore, SAP97 has the propensity to multimerize, and this SAP97 network may function as a scaffold for ion channels and accessory proteins. Regulation of multimerization is exerted by changing from its open to its closed state, the latter exposing protein binding sites.Regulation of multimerization is exerted by changing from its open to its closed state, the latter exposing protein binding sites (reviewed in Ref. 2).

In addition, MOG1 increases $Na_V1.5$ transport and thereby sodium-current density in ventricular myocytes,[70] and it interacts with Nav1.5 at the linker sequence between intramembrane region II and III. Immunostainings show that MOG1 mainly localizes at the ID[71]; however, these results require cautious interpretation, since a proper control for these stainings are missing. Thirdly, the α-subunit of the stimulatory heterotrimeric G-protein $G\alpha_s$ promotes the localization of $Na_V1.5$ at the sarcolemma. Hereby, β-adrenergic pathways indirectly control the number of $Na_V1.5$ channels and its current density.[40,72] Furthermore, Nedd4-2 (neural precursor cell expressed, developmentally down-regulated 4-2) is an E3 ubiquitin-protein ligase that binds $Na_V1.5$. This interaction promotes internalization of the channel, effectively decreasing the sodium current. Nedd4-2 is therefore an important player in the life cycle of $Na_V1.5$.[64] CAR (coxsackie and adenovirus receptor) is a single-pass transmembrane protein that interacts with Nav1.5 at the ID. CAR heterozygous myocytes showed reduced sodium current magnitude at the ID, which is associated with ventricular conduction slowing and earlier onset of ventricular arrhythmias during myocardial infarction.[73]

The most notable interaction partner for Nav1.5 however is Ankyrin G, whose members predominantly anchor ion transporters. AnkG resides at the ID as well as in at the LM (reviewed in Ref. 2). At the ID, AnkG primarily binds and regulates $Na_V1.5$.[74,75] Interaction partners of AnkG are the +TIPs EB1 and EB3, which link AnkG to microtubules. Knockdown of these proteins leads to a decrease of AnkG and $Na_V1.5$ channels.[65] AnkG also plays a role in the regulation of the $Na^{\pm}/K^{\pm}$-ATPase and the $Na^{2+}/Ca^{2+}$ exchanger NCX1.[76] Furthermore, AnkG forms a 'signaling platform', linking CaMKIIδ to $Na_V1.5$.[75]

Interestingly, the spectrin network at the ID resembles the spectrin network in erythrocytes. Firstly, while AnkG anchors spectrin-actin complexes to the lipid bilayer and controls localization of ion channels, the cytoskeletal adaptor protein 4.1R does the same in the erythrocytes. However, not 4.1R but its family member 4.1N is present at the ID. Interestingly, Bennet *et al.* also found the anion exchanger Band 3 at the ID, which stabilizes the interaction between actin and spectrin in erythrocytes. However, no other source confirms the presence of this protein.[6,74]

# 6. Integrating ID components

Over the last years, the idea that the ID components AJs, GJs, desmosomes and ion channels are individual structures has been challenged. Components appear to work together and share many accessory proteins. This section aims to give a complete overview of the associations and interdependencies of the ID components AJ, GJ, desmosome and ion channels, and their related proteins. Furthermore, this chapter covers the transitional junction, junction-free stretches of the ID membrane as an anchor point of sarcomeres.

## 6.1 Area composita

### 6.1.1 Linking AJ to desmosome

The AJ and desmosome together are also named area composita, which definition has been expanded to include ion channels and GJs as well, to distinct the term from adhesion junction. Less common names for the area composita include hybrid adherens junction and composite junction.[77] The term area composita initially arose on the notion that in electron microscopy, AJs and desmosomes were detected as one electron-dense structure.[5] AJs contain desmosomal cadherins and cytoplasmic plaque proteins, whereas desmosomes also contain N-Cad, β-cat, and α-cat. An early analysis of the composition of the area composita listed the following cardiac proteins: cadherins, DSP, α- and β-cat, Vcl, p120-cat and ZO-1, and afadin, of which cardiac localization is still speculative.[51] Interestingly, mice hearts lose their regenerative capacity at 1 week of gestation, which exactly corresponds to the development of the area composita.[3] Moreover, in a ewe heart failure model, N-Cad/catenin complexes, desmin, and Cx43 were all upregulated, which suggests that HF affects the entire area composita. A 3D-reconstruction of the HF IDs revealed that both plicate and interplicate domains are more extended in

HF than in controls, more intercellular vacuoles are seen, and GJs are reduced in plicate regions.[78]

The important role of catenins in the area composita is illustrated by mutations in *CTNNA3* encoding αT-cat: these perturb the assembly and function of AJs and desmosomes. Interestingly, αT-cat is only found in desmosomes that are part of areae compositae.[8] Furthermore, the recently described protein myozap (myocardium-enriched zona occludens-1-associated protein) binds and colocalizes with β-cat, N-Cad, PKP2, DSP, and ZO-1.[11] It is involved in Rho-dependent SRF (serum response factor) signaling, which is antagonized by MRIP (myosin phosphatase-RhoA interacting protein), a binding partner of myozap. SRF-dependent genes include natriuretic peptides and c-fos.[79] Dysbindin is a binding partner of myozap that can also interact with RhoA.[11] The notion that myozap also influences the AJ is strengthened by the fact that myozap contains an ezrin, radixin, and moesin (ERM)-like domain, since ERM proteins are known to influence the function of AJs via binding and regulating the actin cytoskeleton.[79] In certain other tissues, ezrin, radixin, and moesin connect the actin cytoskeleton to the plasma membrane and regulate actin-related cell-cell junctions such as AJs.[24] However, ERM proteins have not yet been studied specifically in cardiomyocytes.

### 6.1.2 Linking GJ to ion channels

Later, the GJ and ion channels were included in the area composita model as well, although GJs are not continuous with the AJ and desmosome plaque.[32] Multifunctional proteins like AnkG, ZO-1 and SAP97, however, connect all four components, directly or indirectly (reviewed in Ref. 9). This implies that the ID is actually one functional unit in which all components depend on each other to ensure intercellular mechanical strength and communication. Furthermore, cell–cell junctions, such the ID, are proposed to form a 'protein-binding hotspot' to which modulators of gene transcription are sequestered, while also regulating contact inhibition. The observation that ZO-1 is found in the nucleus of non-contacted cells, but at the ID of contacted cells, and the notion that N-Cad sequesters β-cat, illustrate this.[20]

Considering the major multifunctional proteins, firstly, AnkG interacts with GJs, AJs and the VGSC complex. However, mutations in *ANK3* encoding AnkG seem to play a minor role in cardiac disease, although Brugada syndrome may be caused by mutations in the $Na_V1.5$ domain that interacts with AnkG (reviewed in Ref. 2). Brugada syndrome is a familial channelopathy characterized by life-threatening ventricular arrhythmias and a high risk on sudden cardiac death, but without structural cardiomyopathy.[80] Secondly, the PKG homologue β-cat is an important linker between AJs, GJs, and desmosomes. Its role in AJs and signaling pathways and interaction with Cx43 have been discussed previously. β-cat is however not essential for mechanical junction integrity, probably because PKG can compensate for β-cat deficiency. Conversely, PKG deficiency cannot be compensated by β-cat despite β-cat upregulation, leading to abnormal desmosome structure. Cardiac-specific double knockout mouse models for β-cat and PKG show disassembly of the ID structure, reduction of Cx43 phosphorylation and of functional GJs, and lethal arrhythmias. This phenotype is remarkably similar to N-Cad deficient mice, although replacement fibrosis was missing.[7]

Regarding less pivotal proteins, the transmembrane protein CAR that associates with $Na_V1.5$ seems also to be involved in GJ regulation, since cardiomyocytes of CAR knockout mice show reduced Cx43 expression and, surprisingly, increased dye coupling.[81] ZO-1 might modulate this, since it binds both Cx43 and CAR, although the ZO-1-CAR interaction only has been shown *in vitro*.[82,83] Moreover, the gene *Pitx2* (paired-like homeodomain 2) has been identified to play a role at the ID. Micro-array analysis revealed that many target genes of Pitx2 are involved in cell junction assembly, ion channels and transcriptional regulation. Target genes include genes encoding β-cat, DSP, Cx43, and Kir6.2. This diversity implies a role for Pitx2 on area composita level. Its precise function is unknown, but its chromosomal location is close to the 4q25 familial atrial fibrillation locus. Indeed, Pitx2 haploinsufficiency in mice show pacing-induced arrhythmias. Furthermore, the atrial IDs of mice that were conditionally deficient for atrial Pitx2 were remodelled, and spaces between cardiomyocytes were increased. Interestingly, mitochondria were swollen and dysfunctional. Identifying the function of the Pitx protein would therefore be very interesting.[84]

### 6.1.3 Linking ion channels to other ID components

Recently, super-resolution microscopy data revealed that Nav1.5 occurs in two distinct pools at the ID: one at the perinexus, which is described in a previous section, and one at AJs.[85] A connection between $Na_V1.5$ and the AJ at the ID is indicated by co-immunoprecipitation of N-Cad and $Na_V1.5$.[33] Moreover, a recent paper showed that clusters of $Na_V1.5$ and N-Cad preferentially localize in each other's close vicinity, illustrating that both proteins depend on each other, suggesting the presence of adhesion/excitability nodes rather than independent structures.[68] N-Cad is also related to potassium channels, since decreased N-Cad affected $K_V1.5$ channels.[86] Presumably, N-Cad is associated with $K_V1.5$ via cortactin, which specifically regulates the interactions between N-Cad and $K_V1.5$ and is required for proper $K_V1.5$ activity. However, N-Cad does not coprecipitate with $K_V1.5$. N-Cad knockout mice show a decrease in cortactin levels, actin skeleton disruption, and decreased expression of $K_V1.5$. This means that N-Cad deficiency leads to prolonged action potentials, conduction slowing, and an increase in arrhythmia incidence.[60]

$K_{ATP}$ channel subunits Kir6.2 and SUR2A co-localize with PKP2 and PKG at the ID. Moreover, super-resolution microscopy shows that $K_{ATP}$ channels are at interacting distance from the junctional proteins N-Cad, AnkG and DSP. Colocalization with Cx43 was weak, so a tight relationship with GJs is not expected.[61]

Desmosomal integrity is important to ensure sodium current, in which espec ially PKP2 plays a crucial role. Cardiomyocytes without PKP2 showed a decreased sodium current and reduced abundance of $Na_V1.5$ at the ID. This led to reentry activity and decreased conduction velocity. In a PKP2-haploinsufficient mouse model, desmosomal integrity was lost, sodium current amplitude decreased and conduction velocity reduced.[9,10,60] $Na_V1.5$ was remodelled, but unlike Cx43 remodelling, this process was not mediated by microtubules.[48] AnkG has been proposed to be an important modulator of the interactions between PKP2 and $Na_V1.5$, (reviewed in Ref. 9) also regarding the notion that PKP2 and $Na_V1.5$ occur in the same protein complex with β4-spectrin and CAMKIIδ. The desmosome is thought to anchor AnkG to the membrane, which stabilizes the spectrin-AnkG complex,[5,33] and desmosomal proteins might be involved in the targeting of Na channels to the ID. Indeed, *in vivo* AnkG loss results in PKP2 remodelling,[75] and PKP2 haploinsufficiency in mice reduced potassium current, but the mechanisms behind this reduction remain unclear.[61]

### 6.1.4 Noncanonical roles for Cx43

Classically, sodium channels are thought to be responsible for cell excitability, while GJs gate the transduction of charge between cells. However, noncanonical roles of Cx43 have emerged: Cx43 maintains the complex that generates the action potential, which means that Cx43

is needed for both charge transduction and cell excitability. (reviewed in Ref. 9) It is therefore noteworthy that Cx43 and $Na_V1.5$ co-immunoprecipitate[33] and Cx43 deficiency leads to a reduced $Na_V1.5$ expression and conduction delay. Cx43 insufficiency is deleterious in two ways: the actual GJ between cells is compromised, but also the charge generated by cells is diminished. Cx43 deficiency reduced the expression of $Na_V1.5$, leading to a reduced sodium current and increased vulnerability for arrhythmias.[87] Furthermore, truncating Cx43 by its five C-terminal amino acid residues confirms its noncanonical roles. Truncated Cx43 cannot bind ZO-1, while GJs remain functional. Mice expressing this truncated form die from ventricular arrhythmias, which were explained by decreased sodium and potassium current densities. The arrhythmias are therefore independent of GJ function. The changes in current density might however be not the only cause. Cx43 truncation may also affect the function of mitochondrial Cx43. Still, ZO-1 appears essential in linking GJ to ion channel function.[86] Depletion of AnkG also leads to a decrease in Cx43 abundance, GJ plaques, and intercellular conductance.[9,33] These effects are probably caused by a disruption of microtubule-mediated delivery of Cx43.[65]

## 6.2 Connexome

The VGSC, Cx43 and desmosomes–interestingly, without AJ–are together distinguished as one functional unit, named the connexome, regulating excitability, cell-cell adhesion, and intercellular contact.[80] Interestingly, the connexome is thought to include the outer connexons and Nav1.5 of the perinexus, and the adjacent PKP2.[58] How the perinexus, connexome and area composita relate to each other, is not described yet. However, it is probable that the connexome is a border zone between perinexus and area composita. According to the connexome hypothesis, Cx43 exerts GJ-independent functions in the connexome, ensuring normal sodium current density. Specifically, the C-terminus of Cx43 ensures functional surface expression of $Na_V1.5$ at the ID, probably by regulating microtubule-mediated vesicle delivery.[88] The VGSC is essential for proper cell-cell adhesion,[9,33] and desmosomal integrity is a requirement for proper VGSC function. In a mouse model with an AC-related mutation in *PKP2*, $Na_V1.5$ abundance was not affected, but sodium current amplitude was decreased, comparable to the results of PKP2 deficiency. PKP2 might be required to ensure proper microtubule capping that is needed for $Na_V1.5$ delivery at the ID. Brugada syndrome has been mentioned as a disease of the connexome, in which mutations in *PKP2* and the subsequent deficit in $Na_V1.5$ at the ID cause the arrhythmogenic phenotype and fibrosis, even in the absence of structural cardiomyopathy.[80]

AnkG is also thought to be crucial in the connexome, linking the VGSC complex, GJs, and desmosomes. It ensures for instance mechanical continuity and electrical coupling between cardiomyocytes, which makes it indispensable for action potential propagation. Moreover, AnkG integrates GJ and desmosome function. Also, it influences the subcellular localization of PKP2, but this association might be indirect. AnkG deficiency did not influence PKG or N-Cad distribution, which implies that the AJ and AnkG do not interact, although it might be a false-negative result.[33]

Recently, the ultrastructure of the connexome has been investigated. Lateral edges of GJs and desmosomes are shown to form a triad, with rough budding vesicles in between. Budding vesicles were also seen at the edge of the GJ plaque and in the intercellular space. The mechanisms behind these vesicles and its contents remain unclear.[36]

## 6.3 Transitional junction

The ID membrane is not completely studded with transmembrane proteins. The apex of membrane interdigitations appears to be junction-free, and there, sarcomeres are connected to the membrane. This region is called the transitional junction (TrJ).[6] Although typical Z-disc structures are not recognizable and actin filaments apparently seamlessly integrate into the membrane, typical Z-disc proteins such as α-actinin, titin, ZASP, non-muscle myosin IIB and NRAP (nebulin-related anchoring protein) are identified. Furthermore, the terminal thin filaments at the ID are composed of β-actin instead of the ID-specific α-actin (reviewed in Ref. 3). It has been proposed that α-actinin crosslinks sarcomeric α-actin, whereby Z-disc-associated protein ZASP supports α-act. Titin then binds to actin and α-actinin, linking the sarcomere to the ID.[6] The TrJ is the proposed site for sarcomerogenesis, where myofibrils are elongated and the cardiomyocyte grows longitudinally. In this respect, the TrJ is thought to function as a proto-Z-disc for sarcomeric addition. Interestingly, during cardiac growth, the membrane fold amplitude varies between 0.2 and 2 μm. The largest amplitude is equivalent to sarcomere length and at that stage, the TrJ hosts the development of the Z-disc. The TrJ is then an anchor for new filaments, incorporating titin and subsequently maturing into a Z-disc.[77]

Also, αII-Spectrin and Mena/VASP are crucial elements of the TrJ: in fact, their complexes protect the terminal sarcomeric filaments and connect them to the sarcolemma, thereby forming the TrJ. At the ID, the SH3*i* splice variant of αII-Spectrin is found, with an extra C-terminal 20 amino acid insertion in the SH3 domain.[38] Other spectrin-binding proteins at the TrJ include MLP and filamins.[56] The SH3 domain of spectrin is crucial for the direct interaction with Mena/VASP. This direct interaction ensures β-actin filament assembly and stabilization of intercellular contact. PKA-mediated VASP phosphorylation inhibits this binding. Also, Mena complexes with β-actin, sarcomeric α-actinin and Cx43. Although Mena and VASP both bind β-actin, it is unknown how they distinguish between different actin isoforms.[38] Mice deficient in αII-spectrin, and Mena/VASP double-knockout mice all suffer from severe cardiac abnormalities. These similarities indicate that both proteins are essential for connecting the sarcomeres to the ID, or in other words, for the transitional junctions.[38]

Furthermore, AnkG contains an obscurin/titin-binding-related domain (OTBD), which means that AnkG could also be involved in the transitional junction, since obscurin is a Z-disc-associated protein. The OTBD can also bind plectin and filamin C, factors that organize the cytoskeleton and regulate myogenesis.[76] The enormous protein plectin has not been reported in association with the ID before. It might be interesting to search for the role of plectin at the ID, since it anchors IFs to desmosomes in other tissues than the heart.[89] And as a last TrJ-related protein, filamin C is the cardiac-specific variant of filamin, which has been mentioned before in this review as an interaction partner of AnkG, spectrin, and mXinα. Mutations in *FLNC* encoding filamin *C* cause myopathy with cardiac involvement in humans. In medaka fish, the filamin C mutant *zac* caused similar symptoms. In the heart, this mutant protein localized at IDs, where myofibrils failed to attach to the sarcolemma, which made the hearts more vulnerable to mechanical stress. However, it remains to be seen if these results can be extrapolated to mice or humans.[90]

# 7. Role of focal adhesions

Although focal adhesions function primarily as cell-matrix junctions in the LM of cardiomyocytes, they also fulfill a role in mechanically

stabilizing IDs in development and disease. They stabilize cells in which IDs are assembled and which undergo myofibrillogenesis. When the ID is mature, the focal adhesions disassemble due to intercellular mechanical force transduction. In cardiac disease, fibrosis challenges cell-cell junctions because of increased mechanical forces. Then, focal adhesions are found around the ID again to ensure mechanical stability. Since GJs form relatively late in development when focal adhesions have already dissociated from the ID, it is interesting to note that remodelling of GJs during disease correlates with the renewed presence of focal adhesions of GJs. Unraveling the mechanism behind this observation might be crucial in understanding GJ remodelling during disease.[91]

# 8. ID mutations and disease

Mutations in desmosomal proteins, such as DSP and the cutaneous variant PKP1, have been associated with diverse diseases, including the blistering skin disease pemphigus, palmoplantar keratoderma, and inherited hypotrichosis. Desmosomal mutations may perturb cell-cell adhesion, IF adhesion, or both. These diseases illustrate the importance of desmosomes in other tissues than the heart, and are caused by mutations in or autoimmune reactions to non-cardiac homologues of desmosomal proteins. However, how *DSP* mutations can specifically cause a cutaneous phenotype while leaving the heart unaffected remains unclear.[5]

Cardiac desmosomal mutations are strongly associated with arrhythmogenic cardiomyopathy (AC), characterized by syncope and sudden death in young athletes or sustained ventricular tachycardia. *PKP2* mutations are most prevalent in AC patients, but mutations affecting the desmosomal cadherins, DSP, and PKG also have been associated with this disease.[1,5] These mutations distort proper desmosome structure, which might cause dissociation of PKG from the desmosome. PKG is then able to compete with β-cat at the AJ, which suppresses the Wnt pathway. This might lead to the fibrofatty replacement and apoptosis of the myocardium, characteristic of AC. Surprisingly, mutations affecting the AJ proteins N-Cad, α-cat, mXinα, and β-cat lead to dilated cardiomyopathy without myocyte loss and inflammation, unlike the AC phenotype. Therefore, desmosomes are thought to be involved in different signaling pathways than AJs.[3] Overall, a decrease in desmosomal protein expression has an effect on multiple levels. Firstly, it causes GJ remodelling. Secondly, nuclear PKG levels increase, the expression of Wnt/β-cat signaling genes c-Myc and Cyclin D1 decreases, and expression of several adipogenic genes increases. This might lead to a transdifferentiation of cardiomyocytes into adipocytes.[5]

Interestingly, cardiocutaneous diseases in which cardiac and skin abnormalities are combined are often caused by desmosomal mutations. Naxos disease is a type of AC combined with woolly hear and palmoplantar keratoderma, which is associated with mutations in *JUP* encoding PKG. Carvajal disease, symptomatically very similar to Naxos disease, is associated with *DSP* mutations. In AC, Naxos and Carvajal disease patients, GJs are also remodelled.[1,5]

Brugada syndrome, Carvajal disease and AC are also associated with mutations affecting the proteins desmin, titin, lamins A and C, transmembrane protein (TMEM) 43, striatin, and transforming growth factor β3. Desmin and titin play a role at the ID, but this is not the case for the other proteins listed here. Lamins for instance are a class of intermediate filaments at the nuclear membrane. Striatins have a caveolin-binding domain, implying a role at the ID.[92,93] Lastly, muations in *CTNNA3* are associated with AC. Although the mutated protein impairs the association with β-cat, this does not completely explain the perturbation of AJ and desmosome assembly.[8]

# 9. The ID as mechanosensor

Beyond mechanical and electrical coupling, the ID also exerts mechanosensing roles, which are realized via N-Cad, Cx43, and the ion channels TRPV2 and TREK-1. The roles of these elements only have been described individually, so a very interesting question is whether and how these mechanosensors influence each other. Considering the known connections between mechanics and electrics, this crosstalk very likely occurs.

## 9.1 Area composita

AJs don't just glue cells together. By means of mechanosensing cadherins, they affect the stiffness of neighboring CMCs. This is of great importance for the structural integrity of the heart: after all, a chain is as strong as its weakest link. Mechanical force on cadherins leads to changes in sarcomeric organization, cell shape, and stiffness. The force is transduced to α-actinin, which changes its conformation, thereby recruiting Vcl from costameric areas.[94] Another study showed that mechanical force on cadherins leads to activation of Abelson tyrosine kinase, which phosphorylates Vcl. This correlates with the finding that Vcl phosphorylation at position Y822 leads to higher Vcl concentrations at the AJ than at the costameres.[4] Further downstream, common global cytoskeleton regulators such as RhoA are probably responsible for the observed effects at the cytoskeleton level: changes in sarcomeric organization, cell shape, and stiffness.[95–97] Furthermore, mechanical stretch increases N-Cad protein expression.[98] Please note that integrins at the LM are also mechanosensitive, but they have different effects on the cytoskeleton.[95] Interestingly, stretch on ECM-integrin complexes induce upregulation of N-Cad, PKG, DSP, and Cx43 expression (reviewed in Ref. 99).

## 9.2 Gap junctions

GJs seem to be mechanodependent as well. Cyclic mechanical stress (CMS), representing the forces arising from cardiomyocyte contractions, increases GJ number and size,[98] as well as Cx43 protein and mRNA levels, which is similar to the effect of α- or β-adrenergic stimulation. Moreover, Cx43 phosphorylation is increased under CMS conditions.[100] These processes are probably mediated by vascular endothelial growth factor (reviewed in Ref. 99).

## 9.3 Ion channels

Mechanically gated channels (MGCs) are sensors and effectors in mechano-electric feedback (MEF), an excellent example of the integration of mechanical and electrical properties. The concept of MEF was coined after the discovery of the Bainbridge effect, which entails that stretch of the right atrium increases the spontaneous beating rate of the SA node. At the ID, two MGCs are described: transient receptor potential cation subfamily V member 2 (TRPV2) and the two-pore $K^+$ channel TREK-1. Firstly, TRPV2 is cell volume-activated, allowing $K^+$ efflux when cell volume increases. However, TRPV2 only translocates to the ID upon osmotic shock or insulin-like growth factor 1 (IGF-1) stimulation. TRPV2 also seems pivotal for ID integrity: cardiomyocytes of neonatal TRPV2 KO mice show impaired excitation-contraction coupling, and no ID formation. Concomitantly, induced cardiac-specific TRPV2 KO mice show disorganized ID structures, and impaired cardiac pump function. IGF-1 administration partly prevented chamber dilation and improved cardiac pump function.[101–103] Secondly, TREK-1 is a stretch-activated

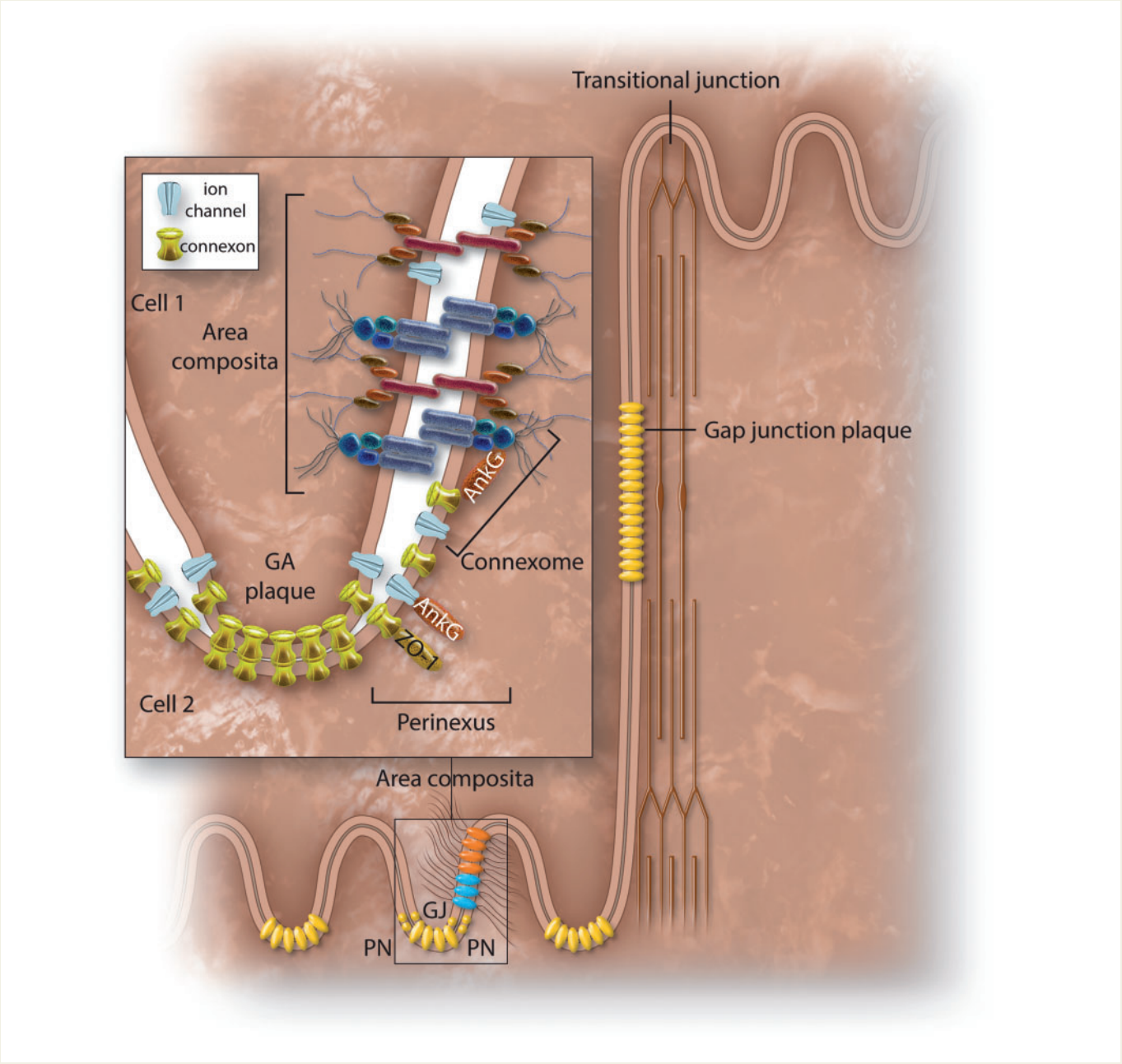


**Figure 7** Spatial distribution of ID components. Large GJ plaques occur at the interplicate region, whereas smaller GJs are found in the apex of plicae of the plicate region. These GJs are surrounded by the perinexus and connexome. The connexome seems to be continuous with the area composita. Ion channels reside in the perinexus and area composita.

channel (SAC) that aids normal repolarization of the AP, while increased current shortens the AP. In mouse heart, TREK-1 interacts with βIV-spectrin, which ensures its membrane targeting and activity. However, it hasn't been found (yet) in human heart.[103,104] Lastly, it must be noted that Kir channels and Nav1.5 are, although mainly activated by other stimuli, also mechanically affected–at least in human embryonic kidney cells (reviewed in Ref. 103).

## 10. An integrated model of the ID

The data presented in this review together result in the detailed molecular models as expressed in the *Figures 3–6*, which summarize protein interaction data for all 'separate' ID structures. *Figure 7*, in turn, enhances our understanding by linking the molecular models of individual structures into a refined, spatially integrated model of the ID.

The ID can be viewed as a stair-like structure with several steps, with the 'tread' perpendicular to the longitudinal axis of the myocytes and the 'riser' in parallel. The membrane area in the longitudinal axis of the cell is called the interplicate region and is one or more sarcomere units long. Only GJs, and no other structures, have been reported in this part of the membrane.[68,105,106] The plicate region, perpendicular to the long axis of the cell, is heavily folded. TrJs are located at the transition between plicate and interplicate regions, gluing the sarcomere to the sarcolemma. Nesting on the innermost ends of these plicate folds are GJs[78]–but the

plaques are smaller than those in the interplicate region.[105] Although no report on the perinexus mentions whether it's located in either the plicate or interplicate region,[57] it resides most likely in the plicate regions. We deduce this from the findings that perinexi host sodium channels,[107] and are neighbored by desmosomes[34]–both structures are not found in interplicate regions.[68,105] This raises the question how GJs at interplicate regions look like, and if these also have perinexus-like structures. The outer connexons and sodium channels of the perinexus and the neighboring desmosomes together form the connexome, linked by AnkG.[36,58] These desmosomal proteins most probably continue into the area composita, which spans a large part of the plicate region.[78] In this relatively large area composita area, sodium channels–and likely potassium channels too–form adhesion/excitability nodes with N-Cad.[68] Whether there is a relationship between the area composita and TrJ remains however unknown.

# 11. Conclusion

AJs, desmosomes, GJs, and ion channels are not individually operating structures, but form one functional unit as the area composita; they work together in many different ways, for instance via scaffolding proteins such as ZO-1 and AnkG. Some structural components of cell-cell junctions can also interact with other ID proteins or function in signaling pathways, such as Cx43 and β-cat. GJs and ion channels together comprise the perinexus; VGSC complexes, GJs and desmosomes are together named the connexome; whereas AJs, desmosomes, GJs and ion channels together form the area composita. Moreover, not every stretch of ID membrane is covered with junctional proteins: certain parts of the membrane are involved in the connection of myofibrils to the membrane, which is called the transitional junction. Furthermore, GJs and ion channels likely create and propagate action potentials together. The model in which GJs solely transport charge and small solutes whereas ion channels only produce and propagate action potentials, appears to be outdated. Protein deficiencies may lastly lead to mechanical dysfunction of for instance the AJ, but also to arrhythmias, often via GJ remodelling. This illustrates the interdependency of the ID components and the coupling of mechanical and electrical elements.

## 11.1 Future perspectives

The introduction of the term area composita is an important step forward in ID research. However, the definition of the area composita is still unclear: do all AJs and desmosomes fuse into an adhering junction? To what extent are GJs involved? And does the area composita include ion channels? Furthermore, the relationship between the perinexus, the connexome, and the area composita remains to be determined, as well as the regulation, development and specific properties of these structures. Advances in mathematical modelling, and novel techniques, such as super-resolution microscopy, and scanning ion-conductance microscopy (SICM), should help to address these open questions in the near future.

To summarize, the ID is a very complex structure, which we are only starting to understand. New proteins and processes are continuously discovered, and they deserve to be investigated since their apparent roles in cardiac disease. The role of the ID far exceeds the ensuring of mechanical strength and electrical coupling; many components are involved in intracellular signaling pathways. The observation that mutations in one ID protein may have a wide range of effects in cardiac diseases like AC and Brugada syndrome illustrate that ID components strongly rely on each other for their proper function.


## Funding

We acknowledge the support from the Netherlands CardioVascular Research Initiative: the Dutch Heart Foundation, Dutch Federation of University Medical Centres, the Netherlands Organisation for Health Research and Development and the Royal Netherlands Academy of Sciences (CVON-PREDICT to TABvV).

**Conflict of interest:** none declared.


## References


1. Noorman M, van der Heyden MA, van Veen TA, Cox MG, Hauer RN, de Bakker JM, van Rijen HV. Cardiac cell-cell junctions in health and disease: electrical versus mechanical coupling. *J Mol Cell Cardiol* 2009;**47**:23–31.
2. Balse E, Steele DF, Abriel H, Coulombe A, Fedida D, Hatem SN. Dynamic of ion channel expression at the plasma membrane of cardiomyocytes. *Physiol Rev* 2012;**92**:1317–1358.
3. Wang Q, Lin JL, Wu KH, Wang DZ, Reiter RS, Sinn HW, Lin CI, Lin CJ. Xin proteins and intercalated disc maturation, signaling and diseases. *Front Biosci (Landmark Ed)* 2012;**17**:2566–2593.
4. Bays JL, Peng X, Tolbert CE, Guilluy C, Angell AE, Pan Y, Superfine R, Burridge K, DeMali KA. Vinculin phosphorylation differentially regulates mechanotransduction at cell-cell and cell-matrix adhesions. *J Cell Biol* 2014;**205**:251–263.
5. Delmar M, McKenna WJ. The cardiac desmosome and arrhythmogenic cardiomyopathies: from gene to disease. *Circ Res* 2010;**107**:700–714.
6. Bennett PM, Maggs AM, Baines AJ, Pinder JC. The transitional junction: a new functional subcellular domain at the intercalated disc. *Mol Biol Cell* 2006;**17**:2091–2100.
7. Swope D, Cheng L, Gao E, Li J, Radice GL. Loss of cadherin-binding proteins beta-catenin and plakoglobin in the heart leads to gap junction remodeling and arrhythmogenesis. *Mol Cell Biol* 2012;**32**:1056–1067.
8. van Hengel J, Calore M, Bauce B, Dazzo E, Mazzotti E, De Bortoli M, Lorenzon A, Li Mura IE, Beffagna G, Rigato I, Vleeschouwers M, Tyberghein K, Hulpiau P, van Hamme E, Zaglia T, Corrado D, Basso C, Thiene G, Daliento L, Nava A, van Roy F, Rampazzo A. Mutations in the area composita protein alphaT-catenin are associated with arrhythmogenic right ventricular cardiomyopathy. *Eur Heart J* 2013;**34**:201–210.
9. Agullo-Pascual E, Cerrone M, Delmar M. Arrhythmogenic cardiomyopathy and Brugada syndrome: diseases of the connexome. *FEBS Lett* 2014;**588**:1322–1330.
10. Cerrone M, Delmar M. Desmosomes and the sodium channel complex: implications for arrhythmogenic cardiomyopathy and Brugada syndrome. *Trends Cardiovasc Med* 2014;**24**:184–190.
11. Frank D, Rangrez AY, Poyanmehr R, Seeger TS, Kuhn C, Eden M, Stiebeling K, Bernt A, Grund C, Franke WW, Frey N. Mice with cardiac-restricted overexpression of Myozap are sensitized to biomechanical stress and develop a protein-aggregate-associated cardiomyopathy. *J Mol Cell Cardiol* 2014;**72**:196–207.
12. Ai Z, Fischer A, Spray DC, Brown AM, Fishman GI. Wnt-1 regulation of connexin43 in cardiac myocytes. *J Clin Invest* 2000;**105**:161–171.
13. Yoshida M, Ohkusa T, Nakashima T, Takanari H, Yano M, Takemura G, Honjo H, Kodama I, Mizukami Y, Matsuzaki M. Alterations in adhesion junction precede gap junction remodelling during the development of heart failure in cardiomyopathic hamsters. *Cardiovasc Res* 2011;**92**:95–105.
14. GeneCards. CTNNB1 gene; GCID: GC03P041236 Weizmann Institute of Science, 2015.
15. Kaufmann U, Zuppinger C, Waibler Z, Rudiger M, Urbich C, Martin B, Jockusch BM, Eppenberger H, Starzinski-Powitz A. The armadillo repeat region targets ARVCF to cadherin-based cellular junctions. *J Cell Sci* 2000;**113** (Pt 22):4121–4135.
16. Geisler SB, Green KJ, Isom LL, Meshinchi S, Martens JR, Delmar M, Russell MW. Ordered assembly of the adhesive and electrochemical connections within newly formed intercalated disks in primary cultures of adult rat cardiomyocytes. *J Biomed Biotechnol* 2010;**2010**:624719.
17. Garcia-Gras E, Lombardi R, Giocondo MJ, Willerson JT, Schneider MD, Khoury DS, Marian AJ. Suppression of canonical Wnt/beta-catenin signaling by nuclear plakoglobin recapitulates phenotype of arrhythmogenic right ventricular cardiomyopathy. *J Clin Invest* 2006;**116**:2012–2021.
18. Harmon RM, Green KJ. Structural and functional diversity of desmosomes. *Cell Commun Adhes* 2013;**20**:171–187.
19. Zemljic-Harpf AE, Godoy JC, Platoshyn O, Asfaw EK, Busija AR, Domenighetti AA, Ross RS. Vinculin directly binds zonula occludens-1 and is essential for stabilizing connexin-43-containing gap junctions in cardiac myocytes. *J Cell Sci* 2014;**127**:1104–1116.

20. Giepmans BN, van Ijzendoorn SC. Epithelial cell-cell junctions and plasma membrane domains. *Biochim Biophys Acta* 2009;**1788**:820–831.
21. BioGrid3.4. CDH2 Homo sapiens. In: TylersLab.com, ed., 2015.
22. Welch MD, DePace AH, Verma S, Iwamatsu A, Mitchison TJ. The human Arp2/3 complex is composed of evolutionarily conserved subunits and is localized to cellular regions of dynamic actin filament assembly. *J Cell Biol* 1997;**138**:375–384.
23. Wang Q, Lin JL, Erives AJ, Lin CI, Lin JJ. New insights into the roles of Xin repeat-containing proteins in cardiac development, function, and disease. *Int Rev Cell Mol Biol* 2014;**310**:89–128.
24. Arpin M, Chirivino D, Naba A, Zwaenepoel I. Emerging role for ERM proteins in cell adhesion and migration. *Cell Adh Migr* 2011;**5**:199–206.
25. Amsellem V, Dryden NH, Martinelli R, Gavins F, Almagro LO, Birdsey GM, Haskard DO, Mason JC, Turowski P, Randi AM. ICAM-2 regulates vascular permeability and N-cadherin localization through ezrin-radixin-moesin (ERM) proteins and Rac-1 signalling. *Cell Commun Signal* 2014;**12**:12.
26. Mertens C, Hofmann I, Wang Z, Teichmann M, Sepehri Chong S, Schnolzer M, Franke WW. Nuclear particles containing RNA polymerase III complexes associated with the junctional plaque protein plakophilin 2. *Proc Natl Acad Sci USA* 2001;**98**:7795–7800.
27. Wallis S, Lloyd S, Wise I, Ireland G, Fleming TP, Garrod D. The alpha isoform of protein kinase C is involved in signaling the response of desmosomes to wounding in cultured epithelial cells. *Mol Biol Cell* 2000;**11**:1077–1092.
28. Li J, Radice GL. A new perspective on intercalated disc organization: implications for heart disease. *Dermatol Res Pract* 2010;**2010**:207835.
29. Kanno M, Aoyama Y, Isa Y, Yamamoto Y, Kitajima Y. P120 catenin is associated with desmogleins when desmosomes are assembled in high-Ca2+ medium but not when disassembled in low-Ca2+ medium in DJM-1 cells. *J Dermatol* 2008;**35**:317–324.
30. Russell MA, Lund LM, Haber R, McKeegan K, Cianciola N, Bond M. The intermediate filament protein, synemin, is an AKAP in the heart. *Arch Biochem Biophys* 2006;**456**:204–215.
31. BioGrid3.4. SYNM Homo sapiens. In: TylersLab.com, ed., 2015.
32. Franke WW, Borrmann CM, Grund C, Pieperhoff S. The area composita of adhering junctions connecting heart muscle cells of vertebrates. I. Molecular definition in intercalated disks of cardiomyocytes by immunoelectron microscopy of desmosomal proteins. *Eur J Cell Biol* 2006;**85**:69–82.
33. Sato PY, Coombs W, Lin X, Nekrasova O, Green KJ, Isom LL, Taffet SM, Delmar M. Interactions between ankyrin-G, Plakophilin-2, and Connexin43 at the cardiac intercalated disc. *Circ Res* 2011;**109**:193–201.
34. Rhett JM, Jourdan J, Gourdie RG. Connexin 43 connexon to gap junction transition is regulated by zonula occludens-1. *Mol Biol Cell* 2011;**22**:1516–1528.
35. Boengler K, Dodoni G, Rodriguez-Sinovas A, Cabestrero A, Ruiz-Meana M, Gres P, Konietzka I, Lopez-Iglesias C, Garcia-Dorado D, Di Lisa F, Heusch G, Schulz R. Connexin 43 in cardiomyocyte mitochondria and its increase by ischemic preconditioning. *Cardiovasc Res* 2005;**67**:234–244.
36. Leo-Macias A, Liang M, Delmar M. 3D Tomographic segmentation of adult cardiac ventricle reveals a complex tubular and vesicular network surrounding the gap junction plaque. Ultrastructure of the connexome. *Heart Rhythm* 2013;**10**:1749–1750.
37. Kohl P, Gourdie RG. Fibroblast-myocyte electrotonic coupling: does it occur in native cardiac tissue? *J Mol Cell Cardiol* 2014;**70**:37–46.
38. Benz PM, Merkel CJ, Offner K, Abesser M, Ullrich M, Fischer T, Bayer B, Wagner H, Gambaryan S, Ursitti JA, Adham IM, Linke WA, Feller SM, Fleming I, Renne T, Frantz S, Unger A, Schuh K. Mena/VASP and alphaII-Spectrin complexes regulate cytoplasmic actin networks in cardiomyocytes and protect from conduction abnormalities and dilated cardiomyopathy. *Cell Commun Signal* 2013;**11**:56.
39. Ram R, Wescott AP, Varandas K, Dirksen RT, Blaxall BC. Mena associates with Rac1 and modulates connexin 43 remodeling in cardiomyocytes. *Am J Physiol Heart Circ Physiol* 2014;**306**:H154–H159.
40. Maguy A, Hebert TE, Nattel S. Involvement of lipid rafts and caveolae in cardiac ion channel function. *Cardiovasc Res* 2006;**69**:798–807.
41. Pelkmans L, Helenius A. Endocytosis via caveolae. *Traffic* 2002;**3**:311–320.
42. Vreeker A, van Stuijvenberg L, Hund TJ, Mohler PJ, Nikkels PG, van Veen TA. Assembly of the cardiac intercalated disk during pre- and postnatal development of the human heart. *PLoS One* 2014;**9**:e94722.
43. Shaw RM, Fay AJ, Puthenveedu MA, von Zastrow M, Jan YN, Jan LY. Microtubule plus-end-tracking proteins target gap junctions directly from the cell interior to adherens junctions. *Cell* 2007;**128**:547–560.
44. Oxford EM, Musa H, Maass K, Coombs W, Taffet SM, Delmar M. Connexin43 remodeling caused by inhibition of plakophilin-2 expression in cardiac cells. *Circ Res* 2007;**101**:703–711.
45. Rucker-Martin C, Milliez P, Tan S, Decrouy X, Recouvreur M, Vranckx R, Delcayre C, Renaud JF, Dunia I, Segretain D, Hatem SN. Chronic hemodynamic overload of the atria is an important factor for gap junction remodeling in human and rat hearts. *Cardiovasc Res* 2006;**72**:69–79.
46. Bonda TA, Szynaka B, Sokolowska M, Dziemidowicz M, Winnicka MM, Chyczewski L, Kaminski KA. Remodeling of the intercalated disc related to aging in the mouse heart. *J Cardiol* 2016;**68**:261–268.
47. Lyon RC, Zanella F, Omens JH, Sheikh F. Mechanotransduction in cardiac hypertrophy and failure. *Circ Res* 2015;**116**:1462–1476.
48. Chkourko HS, Guerrero-Serna G, Lin X, Darwish N, Pohlmann JR, Cook KE, Martens JR, Rothenberg E, Musa H, Delmar M. Remodeling of mechanical junctions and of microtubule-associated proteins accompany cardiac connexin43 lateralization. *Heart Rhythm* 2012;**9**:1133–1140 e1136.
49. Takanari H, Bourgonje VJ, Fontes MS, Raaijmakers AJ, Driessen H, Jansen JA, van der Nagel R, Kok B, van Stuijvenberg L, Boulaksil M, Takemoto Y, Yamazaki M, Tsuji Y, Honjo H, Kamiya K, Kodama I, Anderson ME, van der Heyden MA, van Rijen HV, van Veen TA, Vos MA. Calmodulin/CaMKII inhibition improves intercellular communication and impulse propagation in the heart and is antiarrhythmic under conditions when fibrosis is absent. *Cardiovasc Res* 2016;**111**:410–421.
50. GeneCards. MLLT4 Gene; GCID: GC06P167826 2015.
51. Borrmann CM, Grund C, Kuhn C, Hofmann I, Pieperhoff S, Franke WW. The area composita of adhering junctions connecting heart muscle cells of vertebrates. II. Colocalizations of desmosomal and fascia adhaerens molecules in the intercalated disk. *Eur J Cell Biol* 2006;**85**:469–485.
52. Palatinus JA, O'Quinn MP, Barker RJ, Harris BS, Jourdan J, Gourdie RG. ZO-1 determines adherens and gap junction localization at intercalated disks. *Am J Physiol Heart Circ Physiol* 2011;**300**:H583–H594.
53. Bruce AF, Rothery S, Dupont E, Severs NJ. Gap junction remodelling in human heart failure is associated with increased interaction of connexin43 with ZO-1. *Cardiovasc Res* 2008;**77**:757–765.
54. GeneCards. CLDN10 Gene; GCID: GC13P095433 2015.
55. Gehmlich K, Geier C, Osterziel KJ, Van der Ven PF, Furst DO. Decreased interactions of mutant muscle LIM protein (MLP) with N-RAP and alpha-actinin and their implication for hypertrophic cardiomyopathy. *Cell Tissue Res* 2004;**317**:129–136.
56. Ehler E, Horowits R, Zuppinger C, Price RL, Perriard E, Leu M, Caroni P, Sussman M, Eppenberger HM, Perriard JC. Alterations at the intercalated disk associated with the absence of muscle LIM protein. *J Cell Biol* 2001;**153**:763–772.
57. Rhett JM, Veeraraghavan R, Poelzing S, Gourdie RG. The perinexus: sign-post on the path to a new model of cardiac conduction? *Trends Cardiovasc Med* 2013;**23**:222–228.
58. Agullo-Pascual E, Reid DA, Keegan S, Sidhu M, Fenyo D, Rothenberg E, Delmar M. Super-resolution fluorescence microscopy of the cardiac connexome reveals plakophilin-2 inside the connexin43 plaque. *Cardiovasc Res* 2013;**100**:231–240.
59. TheHumanProteinAtlas. ATP1B1. 2015.
60. Cheng L, Yung A, Covarrubias M, Radice GL. Cortactin is required for N-cadherin regulation of Kv1.5 channel function. *J Biol Chem* 2011;**286**:20478–20489.
61. Hong M, Bao L, Kefaloyianni E, Agullo-Pascual E, Chkourko H, Foster M, Taskin E, Zhandre M, Reid DA, Rothenberg E, Delmar M, Coetzee WA. Heterogeneity of ATP-sensitive K+ channels in cardiac myocytes: enrichment at the intercalated disk. *J Biol Chem* 2012;**287**:41258–41267.
62. GeneCards. PRKCA Gene; GCID: GC17P066302 2015.
63. Chan FC, Cheng CP, Wu KH, Chen YC, Hsu CH, Gustafson-Wagner EA, Lin JL, Wang Q, Lin JJ, Lin CI. Intercalated disc-associated protein, mXin-alpha, influences surface expression of ITO currents in ventricular myocytes. *Front Biosci (Elite Ed)* 2011;**3**:1425–1442.
64. Petitprez S, Zmoos AF, Ogrodnik J, Balse E, Raad N, El-Haou S, Albesa M, Bittihn P, Luther S, Lehnart SE, Hatem SN, Coulombe A, Abriel H. SAP97 and dystrophin macromolecular complexes determine two pools of cardiac sodium channels Nav1.5 in cardiomyocytes. *Circ Res* 2011;**108**:294–304.
65. Delmar M. Connexin43 regulates sodium current; ankyrin-G modulates gap junctions: the intercalated disc exchanger. *Cardiovasc Res* 2012;**93**:220–222.
66. Shy D, Gillet L, Abriel H. Cardiac sodium channel NaV1.5 distribution in myocytes via interacting proteins: the multiple pool model. *Biochim Biophys Acta* 2013;**1833**:886–894.
67. Veeraraghavan R, Lin J, Hoeker GS, Keener JP, Gourdie RG, Poelzing S. Sodium channels in the Cx43 gap junction perinexus may constitute a cardiac ephapse: an experimental and modeling study. *Pflugers Arch* 2015;**467**:2093–2105.
68. Leo-Macias A, Agullo-Pascual E, Sanchez-Alonso JL, Keegan S, Lin X, Arcos T, Feng Xia L, Korchev YE, Gorelik J, Fenyo D, Rothenberg E, Delmar M. Nanoscale visualization of functional adhesion/excitability nodes at the intercalated disc. *Nat Commun* 2016;**7**:10342.
69. Gillet L, Rougier JS, Shy D, Sonntag S, Mougenot N, Essers M, Shmerling D, Balse E, Hatem SN, Abriel H. Cardiac-specific ablation of synapse-associated protein SAP97 in mice decreases potassium currents but not sodium current. *Heart Rhythm* 2015;**12**:181–192.
70. Chakrabarti S, Wu X, Yang Z, Wu L, Yong SL, Zhang C, Hu K, Wang QK, Chen Q. MOG1 rescues defective trafficking of Na(v)1.5 mutations in Brugada syndrome and sick sinus syndrome. *Circ Arrhythm Electrophysiol* 2013;**6**:392–401.
71. Wu L, Yong SL, Fan C, Ni Y, Yoo S, Zhang T, Zhang X, Obejero-Paz CA, Rho HJ, Ke T, Szafranski P, Jones SW, Chen Q, Wang QK. Identification of a new co-factor, MOG1, required for the full function of cardiac sodium channel Nav 1.5. *J Biol Chem* 2008;**283**:6968–6978.
72. Yarbrough TL, Lu T, Lee HC, Shibata EF. Localization of cardiac sodium channels in caveolin-rich membrane domains: regulation of sodium current amplitude. *Circ Res* 2002;**90**:443–449.
73. Marsman RF, Bezzina CR, Freiberg F, Verkerk AO, Adriaens ME, Podliesna S, Chen C, Purfurst B, Spallek B, Koopmann TT, Baczko I, Dos Remedios CG, George AL Jr, Bishopric NH, Lodder EM, de Bakker JM, Fischer R, Coronel R, Wilde AA,

Gotthardt M, Remme CA. Coxsackie and adenovirus receptor is a modifier of cardiac conduction and arrhythmia vulnerability in the setting of myocardial ischemia. *J Am Coll Cardiol* 2014;**63**:549–559.
74. Pinder JC, Taylor-Harris PM, Bennett PM, Carter E, Hayes NV, King MD, Holt MR, Maggs AM, Gascard P, Baines AJ. Isoforms of protein 4.1 are differentially distributed in heart muscle cells: relation of 4.1R and 4.1G to components of the Ca2+ homeostasis system. *Exp Cell Res* 2012;**318**:1467–1479.
75. Makara MA, Curran J, Little SC, Musa H, Polina I, Smith SA, Wright PJ, Unudurthi SD, Snyder J, Bennett V, Hund TJ, Mohler PJ. Ankyrin-G coordinates intercalated disc signaling platform to regulate cardiac excitability in vivo. *Circ Res* 2014;**115**:929–938.
76. Maiweilidan Y, Klauza I, Kordeli E. Novel interactions of ankyrins-G at the costameres: the muscle-specific Obscurin/Titin-Binding-related Domain (OTBD) binds plectin and filamin C. *Exp Cell Res* 2011;**317**:724–736.
77. Wilson AJ, Schoenauer R, Ehler E, Agarkova I, Bennett PM. Cardiomyocyte growth and sarcomerogenesis at the intercalated disc. *Cell Mol Life Sci* 2014;**71**:165–181.
78. Pinali C, Bennett HJ, Davenport JB, Caldwell JL, Starborg T, Trafford AW, Kitmitto A. Three-dimensional structure of the intercalated disc reveals plicate domain and gap junction remodeling in heart failure. *Biophys J* 2015;**108**:498–507.
79. Seeger TS, Frank D, Rohr C, Will R, Just S, Grund C, Lyon R, Luedde M, Koegl M, Sheikh F, Rottbauer W, Franke WW, Katus HA, Olson EN, Frey N. Myozap, a novel intercalated disc protein, activates serum response factor-dependent signaling and is required to maintain cardiac function in vivo. *Circ Res* 2010;**106**:880–890.
80. Cerrone M, Lin X, Zhang M, Agullo-Pascual E, Pfenniger A, Chkourko Gusky H, Novelli V, Kim C, Tirasawadichai T, Judge DP, Rothenberg E, Chen HS, Napolitano C, Priori SG, Delmar M. Missense mutations in plakophilin-2 cause sodium current deficit and associate with a Brugada syndrome phenotype. *Circulation* 2014;**129**:1092–1103.
81. Lisewski U, Shi Y, Wrackmeyer U, Fischer R, Chen C, Schirdewan A, Juttner R, Rathjen F, Poller W, Radke MH, Gotthardt M. The tight junction protein CAR regulates cardiac conduction and cell-cell communication. *J Exp Med* 2008;**205**:2369–2379.
82. Toyofuku T, Yabuki M, Otsu K, Kuzuya T, Hori M, Tada M. Direct association of the gap junction protein connexin-43 with ZO-1 in cardiac myocytes. *J Biol Chem* 1998;**273**:12725–12731.
83. Cohen CJ, Shieh JT, Pickles RJ, Okegawa T, Hsieh JT, Bergelson JM. The coxsackievirus and adenovirus receptor is a transmembrane component of the tight junction. *Proc Natl Acad Sci USA* 2001;**98**:15191–15196.
84. Tao Y, Zhang M, Li L, Bai Y, Zhou Y, Moon AM, Kaminski HJ, Martin JF. Pitx2, an atrial fibrillation predisposition gene, directly regulates ion transport and intercalated disc genes. *Circ Cardiovasc Genet* 2014;**7**:23–32.
85. Veeraraghavan R, Gourdie RG. STORM-based quantitative assessment of sodium channel localization relative to junctional proteins within the cardiac intercalated disc. *Microscopy and Microanalysis* 2016;**22**(S3):1032–1033.
86. Lubkemeier I, Requardt RP, Lin X, Sasse P, Andrie R, Schrickel JW, Chkourko H, Bukauskas FF, Kim JS, Frank M, Malan D, Zhang J, Wirth A, Dobrowolski R, Mohler PJ, Offermanns S, Fleischmann BK, Delmar M, Willecke K. Deletion of the last five C-terminal amino acid residues of connexin43 leads to lethal ventricular arrhythmias in mice without affecting coupling via gap junction channels. *Basic Res Cardiol* 2013;**108**:348.
87. Jansen JA, Noorman M, Musa H, Stein M, de Jong S, van der Nagel R, Hund TJ, Mohler PJ, Vos MA, van Veen TA, de Bakker JM, Delmar M, van Rijen HV. Reduced heterogeneous expression of Cx43 results in decreased Nav1.5 expression and reduced sodium current that accounts for arrhythmia vulnerability in conditional Cx43 knockout mice. *Heart Rhythm* 2012;**9**:600–607.
88. Agullo-Pascual E, Lin X, Pfenniger A, Lübkemeier I, Willecke K, Rothenberg E, Delmar M. A novel noncanonical role of Cx43 in the heart: ensuring the arrival of Nav1.5 to the intercalated disk. *Heart Rhythm* 2013;**10**:1742.
89. GeneCards. PLEC Gene; GCID: GC08M143916 2015.
90. Fujita M, Mitsuhashi H, Isogai S, Nakata T, Kawakami A, Nonaka I, Noguchi S, Hayashi YK, Nishino I, Kudo A. Filamin C plays an essential role in the maintenance of the structural integrity of cardiac and skeletal muscles, revealed by the medaka mutant zacro. *Dev Biol* 2012;**361**:79–89.
91. McCain ML, Lee H, Aratyn-Schaus Y, Kleber AG, Parker KK. Cooperative coupling of cell-matrix and cell-cell adhesions in cardiac muscle. *Proc Natl Acad Sci USA* 2012;**109**:9881–9886.
92. Rickelt S, Pieperhoff S. Mutations with pathogenic potential in proteins located in or at the composite junctions of the intercalated disk connecting mammalian cardiomyocytes: a reference thesaurus for arrhythmogenic cardiomyopathies and for Naxos and Carvajal diseases. *Cell Tissue Res* 2012;**348**:325–333.
93. Hartz PA. Striatin, calmodulin-binding protein; STRN. 2012.
94. Yonemura S, Wada Y, Watanabe T, Nagafuchi A, Shibata M. alpha-Catenin as a tension transducer that induces adherens junction development. *Nat Cell Biol* 2010;**12**:533–542.
95. Chopra A, Tabdanov E, Patel H, Janmey PA, Kresh JY. Cardiac myocyte remodeling mediated by N-cadherin-dependent mechanosensing. *Am J Physiol Heart Circ Physiol* 2011;**300**:H1252–H1266.
96. le Duc Q, Shi Q, Blonk I, Sonnenberg A, Wang N, Leckband D, de Rooij J. Vinculin potentiates E-cadherin mechanosensing and is recruited to actin-anchored sites within adherens junctions in a myosin II-dependent manner. *J Cell Biol* 2010;**189**:1107–1115.
97. Smutny M, Yap AS. Neighborly relations: cadherins and mechanotransduction. *J Cell Biol* 2010;**189**:1075–1077.
98. Zhuang J, Yamada KA, Saffitz JE, Kleber AG. Pulsatile stretch remodels cell-to-cell communication in cultured myocytes. *Circ Res* 2000;**87**:316–322.
99. Salameh A, Dhein S. Effects of mechanical forces and stretch on intercellular gap junction coupling. *Biochim Biophys Acta* 2013;**1828**:147–156.
100. Salameh A, Karl S, Djilali H, Dhein S, Janousek J, Daehnert I. Opposing and synergistic effects of cyclic mechanical stretch and alpha- or beta-adrenergic stimulation on the cardiac gap junction protein Cx43. *Pharmacol Res* 2010;**62**:506–513.
101. Katanosaka Y, Iwasaki K, Ujihara Y, Takatsu S, Nishitsuji K, Kanagawa M, Sudo A, Toda T, Katanosaka K, Mohri S, Naruse K. TRPV2 is critical for the maintenance of cardiac structure and function in mice. *Nat Commun* 2014;**5**:3932.
102. Iwata Y, Katanosaka Y, Arai Y, Komamura K, Miyatake K, Shigekawa M. A novel mechanism of myocyte degeneration involving the Ca2+-permeable growth factor-regulated channel. *J Cell Biol* 2003;**161**:957–967.
103. Peyronnet R, Nerbonne JM, Kohl P. Cardiac mechano-gated ion channels and arrhythmias. *Circ Res* 2016;**118**:311–329.
104. Hund TJ, Snyder JS, Wu X, Glynn P, Koval OM, Onal B, Leymaster ND, Unudurthi SD, Curran J, Camardo C, Wright PJ, Binkley PF, Anderson ME, Mohler PJ. beta(IV)-Spectrin regulates TREK-1 membrane targeting in the heart. *Cardiovasc Res* 2014;**102**:166–175.
105. Hoyt RH, Cohen ML, Saffitz JE. Distribution and three-dimensional structure of intercellular junctions in canine myocardium. *Circ Res* 1989;**64**:563–574.
106. Severs NJ. Gap junction shape and orientation at the cardiac intercalated disk. *Circ Res* 1989;**65**:1458–1462.
107. Rhett JM, Ongstad EL, Jourdan J, Gourdie RG. Cx43 associates with Na(v)1.5 in the cardiomyocyte perinexus. *J Membr Biol* 2012;**245**:411–422.

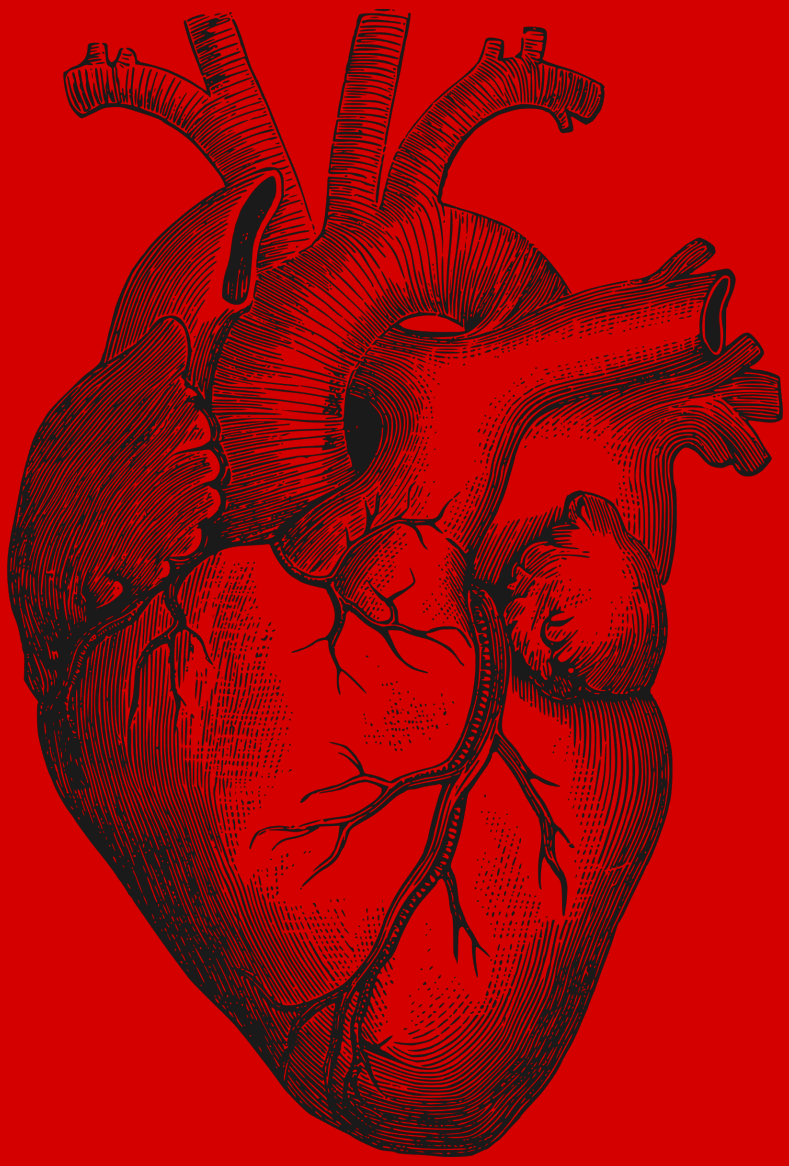

# INTRODUCTION PUBLICATION #2

### 1.7.3 Publication 2: A fundamental evaluation of the electrical properties and function of cardiac transverse tubules

I conceptualized and wrote this review article under the supervision of Prof Hugues Abriel and Prof Jan Kucera. Prof Kucera contributed greatly to the biophysical chapters.

This manuscript is in press at *BBA Molecular Cell Research*[174].

BBA - Molecular Cell Research xxx (xxxx) xxx–xxx

Contents lists available at ScienceDirect

BBA - Molecular Cell Research

journal homepage: www.elsevier.com/locate/bbamcr

# A fundamental evaluation of the electrical properties and function of cardiac transverse tubules☆

S.H. Vermij[a,*], H. Abriel[a], J.P. Kucera[b]

[a] Institute of Biochemistry and Molecular Medicine, University of Bern, Bühlstrasse 28, 3012 Bern, Switzerland
[b] Department of Physiology, University of Bern, Bühlplatz 5, 3012 Bern, Switzerland

ARTICLE INFO

*Keywords:*
Myocytes
Cardiac
Transverse tubules
Cardiac conduction
Action potential
Voltage-gated sodium channels

ABSTRACT

This work discusses active and passive electrical properties of transverse (T-)tubules in ventricular cardiomyocytes to understand the physiological roles of T-tubules. T-tubules are invaginations of the lateral membrane that provide a large surface for calcium-handling proteins to facilitate sarcomere shortening. Higher heart rates correlate with higher T-tubular densities in mammalian ventricular cardiomyocytes. We assess ion dynamics in T-tubules and the effects of sodium current in T-tubules on the extracellular potential, which leads to a partial reduction of the sodium current in deep segments of a T-tubule. We moreover reflect on the impact of T-tubules on macroscopic conduction velocity, integrating fundamental principles of action potential propagation and conduction. We also theoretically assess how the conduction velocity is affected by different T-tubular sodium current densities. Lastly, we critically assess literature on ion channel expression to determine whether action potentials can be initiated in T-tubules.

This article is part of a Special Issue entitled: Cardiomyocyte biology: new pathways of differentiation and regeneration edited by Marijke Brinkm, Marcus C. Schaub, and Christian Zuppinger.

## 1. Introduction

Transverse tubules are deep membrane invaginations of the lateral sarcolemma found in all striated muscle cells. In cardiomyocytes from mammalian cardiac ventricles, T-tubules form a particularly complex network throughout the cell [3,4] (see Fig. 1), and are rich in ion channels and many regulatory proteins (reviewed in [5–7]). In atrial cells, the T-tubular network is dense, half-dense, or absent [8]. From the classic dictum “form follows function”, it is easy to formulate hypotheses about the function of T-tubules without becoming teleologic. Given that the T-tubular network protrudes deep into the cell, the increase in sarcolemmal surface functions as a platform for signaling and calcium handling [5]. Through T-tubules, signals from extra- to intracellular domains – both electrical and biochemical – can be conducted relatively fast. Indeed, T-tubules are the stage for many different processes (reviewed in [6]).

This work is dedicated to the question what the functional roles of T-tubules are. We discuss the depolarization delay of T-tubular membrane, and the effects of sodium current on membrane potential and electrical potentials in T-tubules. We also discuss principles of physiology in the context of T-tubules, and experimental data in the context of these physiological principles. Since the remodeling of T-tubules is observed in many cardiac diseases [9,10], it is crucial to understand the roles of T-tubules in healthy cells before we can address the consequences of T-tubular remodeling.

We will only concisely discuss T-tubular structure (Section 2.2), signaling (Section 2.3), and remodeling in disease (Section 3.6), since excellent reviews have already been published on these topics [5–7,9–11]. Rather, our work will focus on the electrical properties of T-tubules. Firstly, we will discuss the passive properties of T-tubules (Section 3.1), that is, the process by which initial depolarization of the cell membrane propagates into T-tubules without considering voltage-gated ion channels. This includes the discussion of relevant aspects of cable theory [12–16]. Special attention will go out to the capacitive current, which charges the membrane during cell excitation, whereby a larger membrane surface requires more time to charge. To this end, we discuss the delay of T-tubular membrane depolarization. We then assess extracellular potential along the T-tubules and its effect on sodium current amplitude (Section 3.2).

Section 3.3 is dedicated to conduction, since conduction velocity is

☆ This article is part of a Special Issue entitled: Cardiomyocyte biology: new pathways of differentiation and regeneration edited by Marijke Brinkm, Marcus C. Schaub, and Christian Zuppinger.

* Corresponding author.
*E-mail addresses:* sarah.vermij@ibmm.unibe.ch (S.H. Vermij), hugues.abriel@ibmm.unibe.ch (H. Abriel), kucera@pyl.unibe.ch (J.P. Kucera).

https://doi.org/10.1016/j.bbamcr.2019.06.016
Received 30 November 2018; Received in revised form 7 June 2019; Accepted 28 June 2019

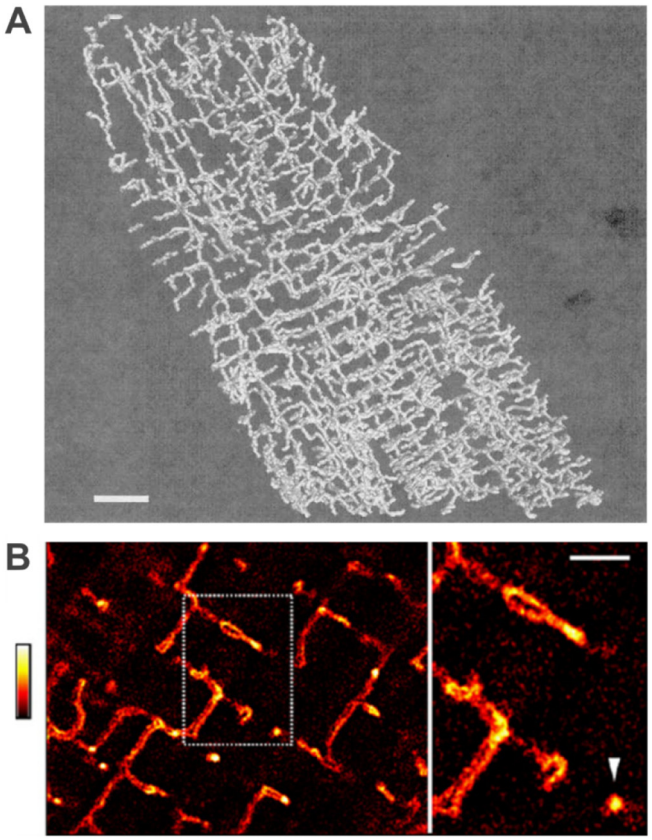


**Fig. 1.** T-tubular structure. (A) Two-photon image of T-tubular network in rat ventricular cardiomyocyte. Scale bar: 5 µm. Reprinted from Soeller & Cannell [1] with authorization of the publisher. (B) Transverse and axial elements of the T-tubular network in murine ventricular cardiomyocyte stained with the membrane dye di-8-ANEPPS imaged by stimulated emission depletion (STED) microscopy. Dotted rectangle indicates location of magnified region on the right. White arrowhead indicates a cross-section of a T-tubule. Scale bar: 1 µm; fluorescence intensity given by look-up table on the left. Reprinted from Wagner et al. 2012 [2] with authorization of the publisher.

an important parameter in arrhythmogenesis [17] and is affected by the presence of T-tubular membrane and ion channels. Over the course of the upstroke of an action potential, we describe the capacitive current, transmembrane current, and membrane potential changes for a cell. We will then assess theoretically how conduction velocity may differ between tissues with three different densities of T-tubular voltage-gated sodium channels: (1) no or few channels in T-tubules; (2) same channel density in T-tubules as in surface membrane; and (3) higher channel density in T-tubules than in surface sarcolemma.

In Section 3.4, we critically review published data on the expression of voltage-gated ion channels and ion pumps, because the data quality is at times unsatisfactory, yet often cited without critical connotations. This will elucidate whether T-tubules contain the necessary collection of ion handling proteins to generate an action potential. Although Section 3.1 and 3.2 will illustrate that theoretically passive conduction suffices to depolarize the T-tubular membrane quickly enough, action potentials may still be evoked.

Ion dynamics in the T-tubular lumen will be concisely discussed in Section 3.5. The small and tortuous T-tubular lumen restricts diffusion and affects driving force of voltage-gated ion channels [18,19]. Lastly, we will discuss T-tubule heterogeneity in atrial cardiomyocytes in Section 4. Atrial cells contract as often as ventricular cells, yet have less T-tubules than ventricular cells or none at all [20].

Taken together, this work will thoroughly assess the electrical properties and roles of T-tubules and a better fundamental understanding of T-tubules will contribute to a better understanding of the implications of T-tubular remodeling in disease.

## 2. T-tubules – the basics

### 2.1. T-tubules in cardiac excitability

The benchmark role of T-tubules is to facilitate excitation-contraction coupling [7], the process that couples the action potential with muscle contraction. The cardiac action potential is triggered when gap junctions at the intercalated disc, where two cardiomyocytes are connected [21], conduct a depolarizing current from an excited to a resting cell. Once the membrane potential reaches the activation threshold of voltage-gated sodium channels, these channels open quickly and conduct a large inward sodium current, further depolarizing the membrane (see Fig. 2). Sodium channels at the intercalated disc may also be activated by ephaptic interactions [22–24], a process relying on interactions between sodium current and extracellular potential. Besides the intercalated disc, sodium channels are also expressed in the lateral membrane [25]. Whether sodium channels are present in the T-tubules will be discussed in a later chapter. As soon as the membrane has depolarized further, the L-type voltage-gated calcium channels, which are mainly located in the T-tubules [26], also open and conduct an inward calcium current. Voltage-gated calcium channels are close to (~15 nm) ryanodine receptors (isoform RyR2 in the heart) in the sarcoplasmic reticulum (SR) [7], together forming dyads. Calcium influx through T-tubular channels therefore quickly leads to calcium efflux from the SR conducted by RyR2, a process called calcium-induced calcium release [7]. The increased intracellular calcium concentration then induces sarcomere shortening [7]. By bringing voltage-gated calcium channels close to sarcomeres at the periphery as well as in the core of the cell, T-tubules provide a large stage for calcium handling proteins, promoting synchronous contraction of the whole depth of the cell [27]. Later during the action potential, voltage-gated potassium channels also open. The opposing potassium and calcium currents create the plateau of the action potential, where the membrane stays depolarized for a while, after which calcium channels close and the potassium current repolarizes the sarcolemma. Then, the sodium-potassium ATPase and the sodium-calcium exchanger among others restore ion concentrations at both sides of the membrane, while SERCA (sarco/endoplasmic reticulum $Ca^{2+}$ ATPase) takes up calcium from the myoplasm back into the SR.

T-tubules also serve as hubs for signaling molecules. Catecholamines for instance bind to β-adrenergic receptors in the T-tubules, modifying cardiac contraction and relaxation [6].

### 2.2. Structure

T-tubules can be subdivided in transversal tubules, perpendicular to the lateral sarcolemma and running along the z-discs of sarcomeres, and longitudinal or axial tubules that link transversal tubules to each other (Fig. 1B). T-tubules however do not form a continuous network throughout the cell. The mean length for a T-tubular segment in rats is about 6.8 µm [1]. Of note, T-tubular structure differs considerably between species. For instance, in sheep, axial segments make up 9% of total T-tubular volume, but 60% in rat [1]. Described T-tubular luminal diameters range from 20 to 450 nm, with an average of 200–300 nm in rat [1] (reviewed in [5]). For the sake of comparison, T-tubules of skeletal muscle are only 30 nm in diameter [28]. When considering cardiac T-tubular openings, those in rabbit are wider than in mouse [29]. As a rule, mammals with a high heart rate, such as mice, have a much denser T-tubular network with smaller diameters than low-heart rate species, such as human [3,27]. Possibly, the higher the heart rate, the faster and more efficient excitation-contraction coupling must occur, and the more membrane surface is required to accommodate more calcium-handling structures such as dyads.

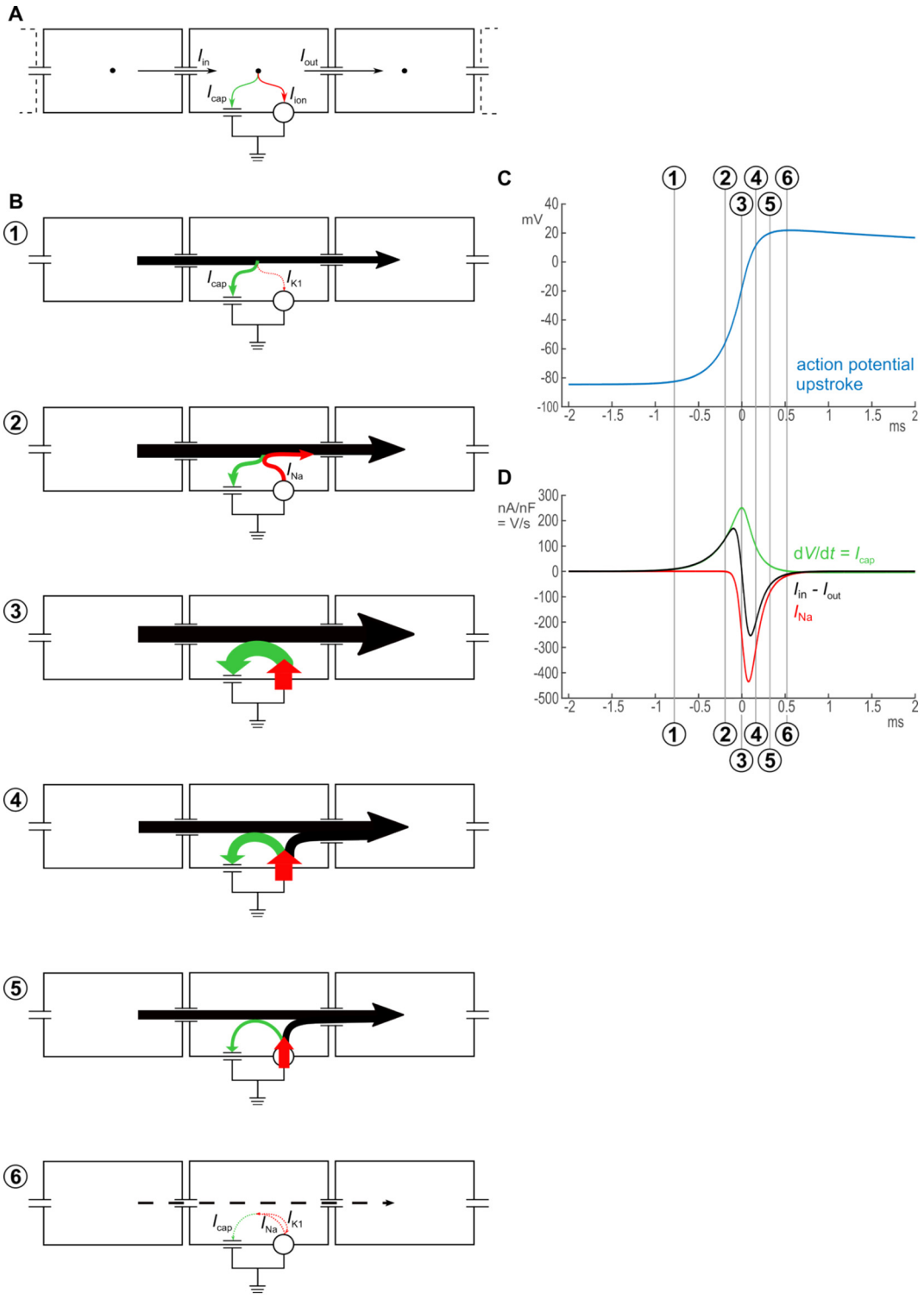


*(caption on next page)*

As for membrane area, the measurements differ depending on the applied method, even within one species. For rats, T-tubular membrane area estimations range from 21 to 64% of total sarcolemma [30]. Causes and implications of these differences will be discussed extensively in Section 3.3.

On a nanoscale, T-tubules connect with the flat ends of SR, known as terminal cisternae, where dyads are located. Connections of T-tubules with the nuclear envelope, endoplasmic reticulum (ER), and mitochondria have also been described [5,31]. Nuclear envelope-T-tubule connections are likely to facilitate a process called excitation-translation coupling [32]. Moreover, the T-tubular membrane forms microfolds. Their folding is mediated by the BAR-domain protein Bin1 [33].

T-tubules also contain caveolae, 50–100 nm-wide flask-shaped invaginations of the membrane. Their coating of caveolin and cavin sets them apart from other lipid rafts. The density of caveolae seems to be equally high in the T-tubular and other sarcolemma [34,35].

Considering that T-tubules associate with many proteins and have tortuous membrane folds, T-tubules are complex structures that still can

**Fig. 2.** Principles of conduction and current flow during the upstroke of the action potential. Panel (A) depicts a strand of cardiac cells. During action potential propagation, current will enter a given cell through gap junctions at one end of the cell ($I_{in}$) and leave through gap junctions at the other end ($I_{out}$). The cell membrane is represented by a capacitance connected in parallel to all ion currents. The membrane current is thus the sum of the capacitive and ionic currents ($I_{cap}$ and $I_{ion}$, respectively). Panel (B) describes currents in the middle cell at different stages (1–6) of the action potential upstroke, corresponding to numbers 1–6 in panels (C) and (D). Stage 1: at the foot of the upstroke, a part of $I_{in}$ will charge the membrane ($I_{cap}$, green), while a very small outward current ($I_{K1}$ and $I_{leak}$, red) will leak through the membrane. $I_{K1}$ and $I_{leak}$ are very small and are not depicted in stages 2–5. Stage 2: a fraction of $I_{in}$ is transferred to the membrane as $I_{cap}$ while the first sodium channels open (red) and contribute to $I_{out}$ and $I_{cap}$. Stage 3: at the time of $dV/dt_{max}$, $I_{in}$ equals $I_{out}$. Therefore, at this time point, the large inward sodium current serves to depolarize the membrane. Stage 4: now, $I_{out}$ is larger than $I_{in}$. The sodium current contributes to $I_{out}$ as well as to $I_{cap}$. Stage 5: $I_{in}$ further decreases. $I_{Na}$ is also smaller, yet still contributes to $I_{cap}$ and $I_{out}$. Stage 6: end of the upstroke. Most sodium channels are inactivated, very little current is flowing. Panel (C) and (D) depict the relationship between action potential upstroke and ion currents. (C) The blue curve represents the upstroke of the action potential. (D) The green curve depicts $dV/dt$, which reflects the capacitive current. The red curve represents the sodium current normalized to cell capacitance, which is at its maximum just after the $dV/dt_{max}$. Note that during the upstroke, the sodium current prevails largely over the other ion currents. The difference between current entering and exiting the cell ($I_{in}$ - $I_{out}$), also normalized to cell capacitance, is given by the black curve. This curve is directly following the sum of capacitive and transmembrane ion currents (in this case, only the sodium current is relevant).

be dynamic under certain circumstances, for instance in disease [9,36].

### 2.3. Regulation and signaling

Many factors regulate T-tubules biochemically or biophysically, a few of which will be mentioned in this section (reviewed in [5,6,27]). Caveolae for instance compartmentalize specific signaling proteins, such as the $\beta_2$-adrenergic receptor ($\beta_2$-AR), which forms signaling clusters with the G protein $G_s$ and $G_i$. $G_s$ activates the adenylyl cyclases AC5 and AC6 and PKA. AC5 and AC6 in turn produce cAMP, which has a wide range of downstream effects. Targets of PKA include calcium-handling proteins such as the voltage-gated calcium channel and RyR2, and the sarcomeric proteins troponin I and C. $\beta_1$-AR on the other hand is not confined to caveolae and couples exclusively to the stimulatory $G_s$ pathway (reviewed in [6]). The L-type voltage-gated calcium channel is expressed both inside and outside of caveolae. The caveolar channels appear to be cAMP-activated and affect hypertrophy instead of excitation-contraction coupling [37]. Other noteworthy regulators of T-tubules are: (1) Tcap, which regulates the formation of T-tubules under influence of load and stretch of the cell [38]; (2) junctophilin-2, which stabilizes dyads [39,40]; and (3) Bin1, which folds the T-tubular membrane and recruits calcium channels [41,42].

## 3. Electrical properties of T-tubules

### 3.1. Passive properties

In this section, we will address the electrical properties of T-tubules, and how they affect cardiomyocyte excitability.

During the propagation of the depolarizing wavefront, the voltage difference between neighboring cells is the driving force for intercellular current. This current is conducted by gap junctions and depolarizes the membrane of the neighboring cell. Once a membrane depolarizes at the surface of a myocyte, the change in voltage induces passive electrotonic responses of the T-tubular membrane for which ion channel openings are not required. To assess whether passive conduction suffices to depolarize the entire T-tubular system, cable theory comes into play [43,44]. If we consider a passive T-tubular membrane, when the cell is excited by an action potential, the T-tubular transmembrane voltage drops due to current leaking across the membrane resistance ($r_m$) and flowing outwards down the T-tubules through their longitudinal resistance ($r_{TT}$). These effects limit the extent of electrotonic responses. To assess the decay of action potential propagation, the length constant for guinea pig T-tubules was theoretically estimated at $\lambda = 240\,\mu m$ [10,45]. Kong et al. also calculated the length constant based on optical measurements in mouse cardiomyocytes at $\lambda \approx 240\,\mu m$ [46].

To assess passive electrical properties experimentally, Scardigli et al. [47] were inspired by an experimental geology study, in which conductivity of a porous rock was determined to assess the diffusive properties. In isolated cardiomyocytes, the apparent diffusion coefficient $D'$ of fluorescent dextran was determined by fluorescence recovery after photobleaching (FRAP) microscopy. The cardiomyocytes were modeled as porous cylinders and Fick's second law of diffusion was applied to calculate $D'$ from the time to recovery after photobleaching and the cellular radius ($D' \approx 1.4\,\mu m^2 \cdot s^{-1}$). Based on the analogies between Fick's first law of diffusion and the electrical current density law, the electrical conductivity of T-tubules was determined at $K' = (5.3 \pm 0.5)\ 10^{-4}\,\Omega^{-1} \cdot cm^{-1}$. Lastly, the length constant was calculated from the diffusion rate and the previously measured T-tubular surface area per unit cell volume: $\lambda = 290 \pm 90\,\mu m$. This is very similar to the aforementioned values.

Scardigli et al. however did not properly consider that the analogy between conductivity and diffusion depends on the detailed porous structure, which in geology is described by the so-called “formation factor”. This factor describes the ratio of the resistivity of a porous rock filled with water to the resistivity of water and must be empirically measured or defined for different rock types. For cardiac myocytes, the actual factor is unknown. Scardigli et al.'s estimate of the diffusion coefficient may therefore be subject to uncertainty and thus differ from values reported by for instance Kong et al. ($D' \approx 23\,\mu m^2 \cdot s^{-1}$) [29]. The obtained length constant however resembled that found by Kong et al. because the formation factor offsets diffusion [29].

For a rat T-tubule with a mean length of 6.84 μm [1], Scardigli et al. calculated a voltage drop from the surface sarcolemma to the cell core of $\sim -4\,mV$ assuming an infinite cable, and thus an exponential decay of potential along the T-tubule. The voltage drop in an infinite cable can be described by [48,49].

$$\Delta V(x) = \Delta V_0 \left(e^{-\frac{x}{\lambda}}\right) \tag{1}$$

where $\Delta V_0 = 100\,mV$ and λ is the length constant, which can be described by the following cable-theory-derived equation [49].

$$\lambda = \sqrt{\frac{r}{2 g_m \rho_e}} \tag{2}$$

where $r$ is the T-tubular lumen radius, $g_m$ the conductance of resting membrane per unit area, and $\rho_e$ the resistivity of extracellular space. A sealed-end cable however approaches a T-tubule more closely than an infinite cable does. Voltage drop in a sealed-end cable at depth $x$ can be described by [48,49].

$$\Delta V(x) = \Delta V_0 \frac{\cosh\left(\frac{L-x}{\lambda}\right)}{\cosh(L/\lambda)} \tag{3}$$

where $L$ is the T-tubule length [48]. Eq. (3) decreases less steeply with $x$ than Eq. 1, and if $L \ll \lambda$, $\Delta V(x)$ hardly decays at all as described by Eq. (3). For the T-tubular properties described by Scardigli, Eq. (3) yields a much smaller voltage drop of $-0.028\,mV$ [50].

Uchida and Lopatin [51] recently showed that a length constant of ~290 μm is probably a significant overestimation, because the previously discussed publications [45,47] did not take the dilations and constrictions of T-tubules into account. In addition, T-tubules form

branching networks, and can also form loops. In neuroscience, much effort was invested in deriving simplifying formulas to describe the decay of the electrotonic potential in neuritic trees with changing neurite diameters (e.g., flaring, tapering) and branches [49,52–55]. For example, Rall has shown that a branching dendritic tree can be collapsed to a cylinder model under certain stringent constraints such as defined relationships between the diameters of parent and daughter branches [54–56]. While certain neurons may exhibit parent and daughter branch diameters compatible with such constraints, these constraints certainly do not pertain to T-tubules. The morphological heterogeneity of T-tubules disqualifies the straightforward application of classic cable theory.

Uchida and Lopatin determined the diffusion coefficient $D'_{TT} \approx 4\,\mu m^2 \cdot s^{-1}$ in murine cardiomyocytes. This is comparable to the findings of Scardigli et al. ($D'_{TT} \approx 1.4\,\mu m^2 \cdot s^{-1}$ as mentioned previously) [47], but not to the findings from Kong et al. who calculate a much higher diffusion coefficient in murine T-tubules of $\sim 23\,\mu m^2 \cdot s^{-1}$ for 1 kDa solutes [29]. The diffusion coefficient found by Kong et al. corresponds to a $\sim$ 12 times reduction of free diffusion rate, which is comparable to the $\sim$ 8 times reduction of calcium ion diffusion estimated based on electrophysiological experiments [57]. This finding from Kong et al. likely approximates the in vivo diffusion coefficient better since their model is not confounded by cell and illumination beam geometries, which might have affected the results from Scardigli and Uchida [47,51]. Interestingly, the diffusion coefficient in rabbit T-tubules is only $\sim$ 5 times slower than free diffusion rate compared to the $\sim$ 12 times reduction in mice [29]. This difference can be explained by the structural differences between murine and rabbit T-tubules: murine T-tubules are more tortuous close to the surface than rabbit T-tubules, and the luminal "ground substance" identified by electron microscopy – potentially representing the glycocalyx – forms a stronger diffusion barrier in murine T-tubules [29].

Uchida and Lopatin furthermore illustrate the importance of T-tubular structure in determining the diffusion time [51]. The in vivo diffusion time constant of 3.9 s could only be approached in an in silico 3D cell model of murine T-tubules by introducing 20-nm-wide constrictions and 600-nm-wide dilations in the model (values represent luminal diameters; $\tau_{dilations} = 2.2$ s and $\tau_{constrictions} = 2.5$ s) [51]. Extrapolating this to electrical properties under standard conditions for specific membrane capacitance, extracellular and membrane resistivity, the time constant for cylindrical T-tubules would be $\tau_{Vm} = 10.1\,\mu s$ and for T-tubules with dilations or constrictions $\tau_{Vm} = 102\,\mu s$ [51]. The latter time constant approaches the experimental finding $\tau_{Vm} \approx 200\,\mu s$ in murine T-tubules [58]. Uchida and Lopatin however do not consider microfolds [33]. This membrane tortuosity could be corrected for by increasing the specific capacitance from 1 to 2 $\mu F/cm^2$, which would double the time constant $\tau_{Vm}$ from $\sim 100\,\mu s$ to $\sim 200\,\mu s$, which is even closer to the experimental finding [58].

Constrictions and dilations considerably affect the length constant. For a 200-nm-wide T-tubule with short 20-nm-wide constrictions every 2 µm, $\lambda_{TT} \approx 68\,\mu m$ [51]. This is considerably smaller than the $\lambda_{TT} \approx 240$–$290\,\mu m$ reported before [45,47]. To transition from the steady state to the non-steady state, the length constant needs to be corrected for the characteristic frequencies ($f$) of the action potential (during the upstroke, $f \approx 150$ Hz) [46], and $\lambda_{AP}$ will be $\sim 34\,\mu m$ [51]. Since the length constant also depends on membrane resistance $R_m$, the length constant will decrease further when voltage-channels are open.

This implies that, in an average murine T-tubule of 9 µm long [42], the voltage drop will be $\sim -13$ mV from the surface to the end of the T-tubule when assuming an infinite cable as described by Eq. (1). When assuming a sealed-end cable, the applicable equation is Eq. (3), which gives a voltage drop of only 0.87 mV. In any case, this voltage drop is small enough to allow voltage-gated calcium channels to open, assuming that the surface sarcolemma depolarizes to +20 mV and the threshold of calcium channels lies near −40 mV. The question whether the entire T-tubular membrane depolarizes quickly enough to open calcium channels once a cell is excited is discussed in Section 3.2. To conclude, we have to keep in mind that passive electrical parameters will differ significantly between species. Whereas rabbit T-tubules openings are relatively accessible and easy to follow, openings of murine T-tubules are relatively tortuous and filled with glycocalyx, which considerably limits diffusion [29].

### 3.2. Delay of T-tubular membrane depolarization

T-tubules greatly increase membrane surface, so charging the capacitance of the membrane of a tubulated cell will take longer. The time it takes to charge the membrane as a capacitor and depolarize T-tubules was assumed to be negligible [45,59], but recent results indicate this is incorrect [50,60]. Quantifying the capacitance charging time of T-tubules would give important insight into the delay between the opening of voltage-gated channels at the sarcolemma and those deep in the T-tubules. This section addresses this depolarization delay and the effect of voltage-gated sodium channels on tubular depolarization.

We developed a simple computational model of a murine T-tubule, represented as a 9-µm-long cylinder with a diameter of 98.5 nm and a specific capacitance of 2 $\mu F/cm^2$ to simulate microfolds (normal specific capacitance is considered 1 $\mu F/cm^2$), subdivided in 100 segments. This model revealed a depolarization delay of 10 µs in the innermost segment in the absence of inward currents in the T-tubules [50]. This value is expected to greatly increase in the presence of T-tubular branches and frequent 20-nm-diameter constrictions. Conversely, sodium currents may facilitate T-tubular depolarization. Although Uchida and Lopatin determined that these structural changes increase the time constant of depolarization from ~10 to ~100 µs for this model (see Section 3.1) [51], they did not determine the delay of membrane depolarization of a deep T-tubular segment. Of note, linear cable theory assuming a passive linear membrane has limited applicability to a T-tubule given their non-linear current-voltage relationships. It is expected that the depolarization delay of a deep segment of a T-tubule with constrictions and dilatation is considerably greater because each dilatation poses a large capacitive load, in addition to the depolarization delay due to the higher resistance in each constriction. To quantitatively assess the delay of depolarization deep in a T-tubule, we incorporated constrictions into our model of an unbranched cylindrical T-tubule [50]. We used the parameters for the healthy mouse T-tubule (9 µm long, 197 nm in diameter) [50], as these parameters lead to the longest depolarization delay (10 µs to depolarize the innermost T-tubule segment to −40 mV). We introduced five 450-nm-long constrictions with a tenfold diameter reduction to 19.7 nm, its centers spaced 1.8 µm apart. This is similar to the model of Uchida and Lopatin [51], which included 20-nm-wide constrictions every 2 µm. With the constrictions in our model, the threshold for $Ca_v$ channels (−40 mV) in the deepest tubular segment was reached 200 µs later than at the surface. This is 20 times later than in the simpler model without constrictions, where the threshold was reached after 10 µs [50]. This delay of 200 µs is not expected to affect excitation-contraction coupling too much considering the relatively slow kinetics of the calcium current. Regarding the sodium current, the delay is still within the range of the upstroke of the action potential. Also considering that the conduction time for a 100 µm-long cell with a macroscopic conduction velocity of 50 cm/s is 0.2 ms, the T-tubular delay represents no major latency for the sodium current. However, the delay is also expected to be modulated by the exact location of the constrictions and by branching of the T-tubules. A detailed investigation would require a full-scale modeling study. Taken together, the question remains open how much later voltage-gated calcium channels open deep inside the T-tubules when the surface sarcolemma is excited.

The effect of a voltage-gated sodium current on the depolarization of T-tubules and the effects of intratubular potentials on the sodium current have been simulated by Hatano et al. [60] in an elaborate 3D model with structurally simple T-tubules without branches, constrictions and dilations. The T-tubular sodium current density was set at

30 mS/μF according to experimental results from [45] (see Section 3.4.2 for a critical evaluation of these results). In the deepest segments of the modeled T-tubule (5 μm from the surface), the extracellular potential was slightly negative (−1 mV) because of the flow of current along the narrow tubule. Due to this negative potential, the sodium current was ~8% smaller in the deep segment than the segment at the cell surface [60]. A similar result was obtained with our simpler model [50] with a slightly smaller T-tubular sodium current density of 23 mS/μF.

The mechanism underlying this sodium current reduction in the deep portions of the T-tubules resides in the notion that an ion current $I_X$ carried by ion species X can be described by $I_X = g_X \cdot P_O \cdot (V_m - E_X)$, where $g_X$ is the maximal conductance of that current, $P_O$ is the open probability of the corresponding channels, $V_m$ is membrane potential, and $E_X$ is the reversal potential of $I_X$. The term $V_m - E_X$ is called the driving force. For the case of the sodium current, the driving force becomes smaller (in absolute value) when the extracellular potential becomes negative, thus decreasing the current (in absolute value). A comparable mechanism, called “self-attenuation”, has been proposed to occur in intercalated discs due to ephaptic interactions [22–24]. Thus, we postulate that the sodium current is slightly self-attenuating deep inside the T-tubules. Additionally, the tubular lumen can be transiently depleted from sodium if the T-tubular sodium current is substantial. Sodium depletion decreases $E_{Na}$, the Nernst potential of sodium and thus the driving force, representing an additional mechanism reducing the sodium current. This was specifically addressed in a modeling study by Mori et al. who showed that sodium depletion in the intercalated disc contributes to self-attenuation of the sodium current [61]. In addition, a recent study by Greer-Short et al. indicates that sodium depletion in intercalated discs and the resulting decreased driving force for sodium ions are also important in shaping repolarization as they attenuate the late sodium current. Interestingly, this phenomenon can mask the phenotype of long-QT syndrome type 3 [62].

### 3.3. Influence of T-tubules on macroscopic conduction velocity

In this chapter, we will assess theoretically how macroscopic conduction velocity (i.e., conduction along the surface membrane and throughout cardiac tissue) is influenced by T-tubular ion channels and membrane. To do so, one has to take a closer look at the propagation of action potentials through cardiac tissue. Much insight has been gained from the ground-breaking work of Hodgkin and Huxley and others [12–16,63].

Firstly, one has to understand the dynamics of current flow into, out of, and within a cell during the propagation of the depolarizing wavefront as detailed and illustrated in Fig. 2. The dynamics of various currents during the upstroke of the action potential are crucial determinants of conduction.

During the passage of a wavefront, electrotonic current enters the cell from upstream ($I_{in}$) and exits the cell downstream ($I_{out}$) (Fig. 2B,D, in black). According to Kirchhof's current law [64], the difference $I_{in} - I_{out}$ must be transferred to the membrane in the form of capacitive current ($I_{cap}$; Fig. 2B,D, in green) or flow through membrane ion channels and transporters ($I_{ion}$; Fig. 2B,D, in red).

The capacitive current $I_{cap}$ directly follows the upstroke velocity of the action potential (Fig. 2C), i.e., the rate of change of membrane potential $V$, expressed as $\partial V/\partial t$. Assuming that cell capacitance $C$ is constant, $I_{cap}$ is indeed defined as:

$$I_{cap} = C \cdot \frac{\partial V}{\partial t} \tag{4}$$

thus

$$I_{in} - I_{out} = C\frac{\partial V}{\partial t} + I_{ion} \tag{5}$$

Assuming that the cell is much smaller than the length constant of the tissue and the spatial extent of the upstroke (which is the case for well-coupled cardiac tissue), then the tissue can be considered as a continuous syncytium [17,64]. In one dimension, Eqs. (4) and (5) can be written in a spatially continuous form as:

$$\sigma\frac{\partial^2 V}{\partial x^2} = c\frac{\partial V}{\partial t} + i_{ion} \tag{6}$$

where $x$ is position, $\sigma$ is the lumped conductivity (normalized by surface-to-volume ratio) of the gap junctions, the intracellular space, and the extracellular space; $c$ is the membrane capacitance per unit area; and $i_{ion}$ is the total ion current per unit area. This equation is known as the cable equation [12,13], or in the cardiac community as the monodomain equation, which is valid for cardiac tissue when assuming that the anisotropy ratios of intra- and extracellular resistivities are equal [64].

When conductivity ($\sigma$) changes, conduction velocity ($\theta$) follows a square-root relationship [13,49,64]:

$$\theta \propto \sigma^{1/2} \tag{7}$$

Now, we will consider three possible scenarios to assess the influence of T-tubular membrane and channels on conduction (Fig. 3). In the first (Fig. 3A), T-tubules contain a low density of channels, especially of voltage-gated sodium ($Na_v$) channels (or an absence of $Na_v$ channels in the extreme case). In the second scenario (Fig. 3B), we will consider that the composition of $Na_v$ channels in the T-tubular membrane is the same as in the surface sarcolemma. In the third (Fig. 3C), we will consider that the density of $Na_v$ channels is higher in the T-tubular membrane than in surface sarcolemma. We initially assume that the axial resistance of the T-tubules and the intratubular potential gradient are negligible. This is equivalent to assuming a homogeneous membrane potential throughout the cell surface and T-tubular membranes. Thus, we assume that the T-tubular membrane potential quickly follows the lateral membrane potential, and that extracellular potentials in the T-tubular lumen are small [50,60]. These three scenarios therefore correspond to changing the total capacitance and/or the number of channels in the membrane.

The first scenario (few or no $Na_v$ channels in the T-tubules, Fig. 3A) corresponds to scaling the specific membrane capacitance $c$ in the cable equation (Eq. (6)). Intuitively, adding capacitance would increase the load to excite the tissue and slow conduction. This scenario is however difficult to assess theoretically in a quantitative manner. It is reminiscent of myofibroblasts connected to myocytes with a high level of gap junctional coupling, although myofibroblasts will render the resting membrane potential of the myocytes less negative. The effects of such an additional capacitive load have been studied by Jacquemet and Henriquez [65].

Huxley [66] as well as Jack, Noble and Tsien [49] have addressed our first scenario theoretically in detail, and showed that the kinetic properties of the voltage-gated ion currents also determine the exact relationship between conduction velocity ($\theta$) and capacitance ($c$). Nevertheless, $\theta$ is expected to decrease when c increases. The relationship between $\theta$ and $c$ lies between

$$\theta \propto c^{-1/2} \tag{8}$$

and

$$\theta \propto c^{-1} \tag{9}$$

These relationships are illustrated in Fig. 3D. Thus, in the extreme case of this first scenario and assuming that T-tubules contribute 50% to cell capacitance, $\theta$ may be decreased by an amount between 29% (Eq. (8)) and 50% (Eq. (9)).

The second scenario (same ion channel composition of the T-tubular membrane as the surface sarcolemma; Fig. 3B) corresponds to changing $I_{ion}$ and $I_{cap}$ by the same factor. If the two summands of the right hand side of the cable equation (Eq. (6)) are scaled by a factor $n$, we can observe that the cable equation remains the same if $\sigma$ is also scaled by $n$.

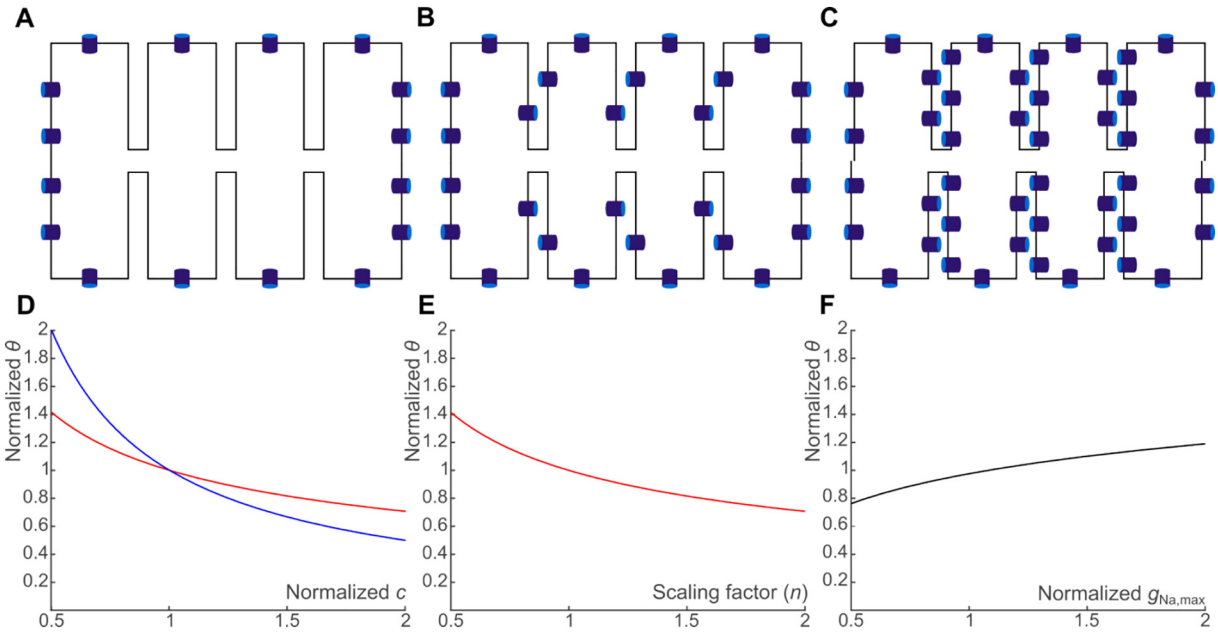


**Fig. 3.** Scenarios in assessing the influence of T-tubule composition on macroscopic conduction velocity (along the surface membrane and throughout cardiac tissue). (A) First scenario: T-tubules contain no (or very few) voltage-gated sodium channels. (B) Second scenario: density of voltage-gated sodium channels is similar inside and outside of T-tubules. (C) Third scenario: T-tubules contain a higher voltage-gated sodium channel density than surface sarcolemma. (D) Relationship (pertaining to the first scenario, A) between normalized conduction velocity ($\theta$) and normalized capacitance ($c$) as defined by inverse square root (red) and inverse (blue) functions, corresponding to Eqs. (8) and (9), respectively. (E) Relationship (pertaining to the second scenario, B) between normalized $\theta$ and the scaling factor $n$, described by the inverse square root function corresponding to Eq. (10). (F) Relationship (pertaining to the third scenario, C) between normalized $\theta$ and the normalized $g_{Na,max}$ as described by the logarithmic dependence given in Eq. (11), with $k = 0.308$. (For interpretation of the references to colour in this figure legend, the reader is referred to the web version of this article.)

Thus, in terms of effects on $\theta$, scaling $I_{ion}$ and $I_{cap}$ by $n$ is equivalent to scaling $\sigma$ by $1/n$ and we can expect that $\theta$ will behave as

$$\theta \propto n^{-1/2} \tag{10}$$

Therefore, if T-tubules contribute 50% to cell capacitance, $\theta$ may be decreased by up to 29% (Fig. 3E).

Finally, the third scenario corresponds to adding relatively more $Na_v$ channels than membrane (Fig. 3C). In the extreme situation of adding $Na_v$ channels only, $\theta$ is expected to increase [63]. In a computer model of conduction, King and Fraser [44] have shown empirically that $\theta$ is linearly related to the logarithm of $g_{Na,max}$, i.e.,

$$\frac{\theta}{\theta_{ref}} = 1 + k \log\left(\frac{g_{Na,max}}{g_{Na,max,ref}}\right) \tag{11}$$

where $\theta_{ref}$ is the reference control velocity, $g_{Na,max}$ is the maximal conductance of $Na_v$ channels, $g_{Na,max,ref}$ is the reference control $g_{Na,max}$, and $k$ is a model-dependent constant that must be determined empirically. For conduction in the Luo-Rudy dynamic model as investigated by Shaw and Rudy [63], we estimated $k$ to be 0.308. The function given by Eq. (11) is illustrated in Fig. 3F. Thus, $\theta$ may increase due to the larger $Na_v$ channel density, but this effect may be opposed by the increase of $c$. The net effect will depend on the exact change of $g_{Na,max}$ and $c$. This scenario however appears unlikely in the light of recent experimental data, since studies addressing $Na_v$ expression in the T-tubules have suggested that at most 29% of $Na_v$ channels are present in the T-tubules [67], which may be an overestimation (see Section 3.4.2 for a detailed discussion).

Next, we conjecture about the additional effects of T-tubular exit resistance and associated large T-tubular potential gradients on macroscopic conduction velocity (along the surface membrane and throughout cardiac tissue). On the one hand, a substantial exit resistance would tend to decouple the capacitive load of the T-tubules, thereby accelerating macroscopic conduction. In the limit of a very large resistance, the load of the T-tubules would be fully decoupled, corresponding to a detubulated situation. However, the experimentally observed time constants in the range of 100–200 μs [51,58] and the small potential gradients reported in modeling studies [50,60] suggest that the exit resistance is small. The reported time constants of 100–200 μs are moreover much shorter than the typical timescale of the upstroke of the action potential (~1 ms), suggesting that the capacitive load only has small effects on the action potential upstroke. These considerations are in line with those of Jacquemet and Henriquez [65], who studied the effects of the capacitive load of fibroblasts in various myocyte-fibroblast coupling regimes. Of note, a large exit resistance would slow conduction along the T-tubules.

On the other hand, we note that the exit resistance of the T-tubules will directly influence the level of self-attenuation. If the exit resistance is small, self-attenuation will be negligible, and we expect no influence on conduction velocity. If the exit resistance is sufficiently large, self-attenuation of the sodium current will appear because of the large negative tubular potential, which would tend to slow conduction. Current results of computer simulations suggest that self-attenuation is in the range of a few percent [50,60], and the resulting conduction slowing would also be in the percent range. An increase in the tubular resistance would however also decrease the capacitive load (see above), which may compensate the conduction slowing. In the extreme case of a very large exit resistance, we would retrieve once more the detubulated situation. Since there is no experimental proof of sodium current self-attenuation in the T-tubules for the moment, we must limit ourselves to speculation.

In summary, the reality most likely lies somewhere between the first two scenarios, so the presence of T-tubules will decrease $\theta$. Conversely, loss of T-tubules may accelerate conduction. To explicitly investigate all these factors, including T-tubule resistance, intratubular potential gradients, and self-attenuation of the sodium current, specific modeling approaches need to be developed.

### 3.4. Action potentials in T-tubules?

A logical follow-up question to the passive conductive properties of T-tubules is: are action potentials generated in T-tubules? To generate an action potential, the right collection of depolarizing currents (conducted by voltage-gated sodium and calcium channels) and repolarizing current (conducted by potassium channels) must be present. This section discusses evidence regarding the presence or absence of ion channels in the T-tubules.

Firstly, it must be noted that data regarding T-tubular action potentials and ion channel expression require careful interpretation. In functional experiments, the cell capacitance is used to calculate membrane surface area, often assuming that 1 μF corresponds to 1 $cm^2$ membrane area [35]; thus, dividing whole-cell current by capacitance gives current density. Any difference in current density between normal and detubulated cells should indicate that the density of ion channels differs between T-tubular and non-T-tubular sarcolemma [26,67]. A caveat of this assumption is that measuring the capacitance underestimates the T-tubular membrane surface, since optical measurements give much higher fractions of T-tubular membrane (65% versus 32% from capacitance-based measurements [30]). One partial explanation for this discrepancy is the fact that capacitance is often determined too straightforwardly when the current transient evoked by a voltage-clamp step is simply integrated and divided by the commanded voltage step [68]. This method underestimates the capacitance if the opening of the cell at the pipette is imperfect, yielding a higher access resistance and a concomitant increase in capacitance charging time, and if the cell cannot be approximated as a single resistance in parallel with a single capacitor, which is the case for structurally complex cells such as cardiomyocytes. As a result, the apparent time constant of the current transient charging the capacitor increases, and from a certain time constant value, the “tail” of the current transient is usually excluded from the integration. The resistance that certain structural obstacles pose to the capacitive current may moreover be so high that the membrane depolarizes too late for the ion channels in this region to be activated. The ability to depolarize the entire cell membrane on a satisfactorily short time scale is called space clamp. In other words, in a voltage-clamped cell, the transmembrane potentials will differ between different portions of the membrane due to electric field interactions with geometric barriers.

Taken together, these pitfalls lead to an underestimation of membrane area of normal (non-detubulated) cells and an overestimation of current density. Therefore, the fraction of T-tubular current density must be lower than the capacitance-based measurements implicate, and ion channel density in T-tubules will be overestimated.

Indeed, when ion channel densities are determined from functional experiments, only rarely the results are corrected for cell surface [30]. Pásek et al. [30] reconcile the discrepancy between membrane area estimations by assuming a lower specific capacitance of T-tubules due to the relatively high cholesterol concentration in T-tubular membranes, and correcting for incomplete detubulation, setting T-tubular membrane surface at 49% instead of 32%. This reconciliation should lead to a decrease in current attributed to the T-tubules, even after correcting for the fact that formamide treatment leaves about 7% of T-tubules unaffected. A recent study however invalidated the hypothesis that cholesterol reduces the specific capacitance [69]. The discrepancy between electrophysiological and optical surface measurements may also be sought in difficulties in obtaining a complete space clamp in cardiomyocytes.

Comparing currents between whole-cell and detubulated cells may be complicated by more factors. Firstly, applying an osmotic shock to a cell may elicit unwanted effects which have not yet been investigated. The sudden internalization of membrane proteins may result in other acute membrane remodeling responses; the remodeling of structural proteins may affect protein expression at the membrane. Secondly, the sodium current in deep T-tubular segments may self-attenuate (see Section 3.2) [50,60], so whole-cell peak sodium current may not reflect the full available sodium current. Taken together, it is crucial to keep in mind that ion current densities between normal and detubulated cardiomyocytes should not be compared without taking into account the limitations mentioned above.

Immunohistochemistry data also require careful interpretation. Ideally, any staining for T-tubular proteins should be combined with a fiducial T-tubular marker and a knock-out model to assess the specificity of the antibody. Most publications addressing ion channel expression in T-tubules miss one or both of these quality controls. As a good example, Eichel et al. [70] show that the staining for the ion channel regulator CASK follows a regular striated pattern in cardiomyocytes, which may indicate T-tubular localization. The signal however did not colocalize with RyR2 and $Ca_v1.2$, so the authors concluded that CASK was not expressed at the T-tubules [70]. We will therefore interpret published data on ion channel expression in T-tubules carefully.

#### 3.4.1. Calcium-handling proteins

The voltage-gated calcium channel consists of an α-subunit with multiple auxiliary β-, $\alpha_2\delta$- and γ-subunits [71]. The predominant cardiac splice variant of the α-subunit is $Ca_v1.2$ (reviewed in [5]). Electrophysiological studies in detubulated and normal rat cardiomyocytes have determined that 60–75% of calcium current is conducted by calcium channels in the T-tubules [26,72]. The authors did not normalize the calcium influx [26] or whole-cell calcium peak current [72] to the cell capacitance; the difference in calcium influx or peak current between control and detubulated cardiomyocytes already indicated which fraction of calcium channels was localized in the T-tubules. The previously stated problems with normalizing whole-cell currents by capacitance (Section 3.4) do therefore not apply to these studies.

Most calcium channels in the T-tubular membrane are close (~ 15 nm) to RyR2 in the SR, forming dyads [73]. This close proximity allows calcium ions entering the cell through $Ca_v1.2$ to quickly and efficiently bind RyR2, followed by calcium-induced calcium release from the SR and subsequent sarcomere shortening. RyR2 and $Ca_v1.2$ stay so close together because junctophilin-2 bridges the membranes of the SR and T-tubule to stabilize the dyad [39]. RyR2 and $Ca_v1.2$ both bind Bin1, a banana-shaped protein that assists in trafficking and clustering of calcium channels [41].

The sodium-calcium exchanger NCX is predominantly expressed in the T-tubules. With detubulation experiments in rat cardiomyocytes, 60% of total NCX current – both outward an inward – was determined to originate from the T-tubules, corresponding to a ratio NCX current carried by the T-tubules/surface membrane of 1.5 [74]. Another study stated on the basis of similar detubulation experiments that the ratio of NCX-carried current in T-tubular to that carried in surface membrane varies from 1.7 to 25 [75]. Both aforementioned publications determine T-tubular NCX currents by comparing current densities, which methodological problems have been outlined extensively in Section 3.4. It is therefore likely that T-tubular NCX currents make up less than 60% of total. When we assume that T-tubules account for 50% of membrane surface [30], while the T-tubular membrane surface measured in [74] only was 32% of total, the T-tubular NCX current may be overestimated twofold. In other words, T-tubular NCX current may make up 30% rather than 60% of total current. Still, this does not necessarily conflict with the generally accepted idea that NCX plays an important role in calcium handling in T-tubules.

T-tubular NCX expression correlates with the function of T-tubules as the main stage for calcium handling: a relatively high concentration of $Ca_v1.2$ and RyR2 at the T-tubules facilitates a higher calcium conduction at the T-tubules than at the surface sarcolemma. This also requires more NCX activity to remove cytoplasmic calcium again. Indeed, NCX seems to be close to dyads, as well as SERCA, which pumps calcium ions back into the SR (reviewed in [27]), facilitating fast contraction as well as fast relaxation of the sarcomeres. $Ca_v1.2$ and the NCX isoform NCX1 are both reported inside and outside of caveolae [37,76].

Dyadic $Ca_v1.2$ and NCX1 however most likely occur outside of caveolae, since caveolar $Ca_v1.2$ seems to play a role in the hypertrophy pathway and not to participate in contraction [37].

$Ca^{2+}$ ATPase also extrudes calcium ions from the cytoplasm. Its activity is reported to be confined to the T-tubules in rat cardiomyocytes based on recordings in cardiomyocytes with the $Ca^{2+}$ ATPase blocker carboxyeosin [77].

### 3.4.2. Sodium-handling proteins

The cardiac voltage-gated sodium channel $Na_v1.5$ is crucial for generating the rapid upstroke of the action potential in cardiac cells. It is the first channel to open when the membrane depolarizes. It is unclear whether voltage-gated sodium channels are required in T-tubules, since the T-tubular membrane will depolarize quickly due to passive conduction alone, yet T-tubular $Na_v$ channels would support conduction (see Section 3.3). Data regarding T-tubular sodium channel expression are multi-interpretable or inconclusive. Brette et al. concluded that 29% of sodium current is present in T-tubules because sodium current density in detubulated cardiomyocytes and normal cells were similar while cell capacitance decreased by 29% after detubulation [67]. After correcting for the larger T-tubular membrane area in untreated cells, however, current density would decrease. As a result, the calculated T-tubular sodium current fraction would be lower. We may also conclude that T-tubules do not contain $Na_v$ channels because the same study showed that whole-cell sodium current did not differ between normal and detubulated cells [67].

When we consider immunohistochemistry data for $Na_v1.5$, we have to conclude that a reliable co-staining of $Na_v1.5$ and a T-tubular marker is still missing. Only a striated pattern of $Na_v1.5$ has supported the in our view premature conclusion that $Na_v1.5$ would be expressed in T-tubules [78–80].

Although $Na_v1.5$ is the main cardiac isoform of the voltage-gated sodium channel family, other isoforms have been reported in the heart [81]. It is important to keep in mind however that the expression of neuronal isoforms remains controversial. A recent report reported only $Na_v1.5$ and $Na_v1.4$ expression using next-generation RNA sequencing data from murine cardiomyocytes [82], yet other reports suggest that the neuronal isoforms $Na_v1.1$, $Na_v1.3$ and $Na_v1.6$ may be enriched in T-tubules [83–85] and even contribute to arrhythmias [86]. These neuronal channels have a lower activation threshold and inactivate more rapidly, which may facilitate action potential propagation into the T-tubules [5] – yet the fast passive propagation of depolarization renders T-tubular sodium channels relatively unessential. The immunohistochemistry data showing $Na_v1.1$, $-1.3$, and $-1.6$ in T-tubules of murine cardiomyocytes need careful interpretation because no knock-out control is presented for the antibodies [84,86]. Another publication presents striated patterns of neuronal isoforms in immunohistochemistry data [85], whereas pre-absorbing the antibodies with peptides inhibits any staining, suggesting specificity of the antibodies [85]. Westenbroek et al. quantified the relative expression of $Na_v1.1$–6 in murine cardiomyocytes [87]. $Na_v1.5$ was only found at the intercalated disc and lateral membrane. $Na_v1.1$ and $-1.3$ showed a striated pattern, but compared to $Na_v1.5$, the signal intensity was relatively low, as was expected from protein expression data [88]. A T-tubular marker was however missing [87].

On a functional level, current conducted by neuronal channels was recorded in murine ventricular cardiomyocytes treated with β-scorpion toxin, a specific activator of neuronal sodium channels [85]. $Na_v1.6$-deficient mice moreover showed prolonged calcium transients in cardiomyocytes, suggesting a functional link between $Na_v1.6$ and excitation-contraction coupling [89]. In wild type mice, $Na_v1.6$ staining showed a striated pattern that weakly colocalized with α-actinin, but we have to consider that α-actinin is not an ideal T-tubular marker. $Na_v1.6$-deficient mice did not show any striated pattern, which suggests the anti-$Na_v1.6$ antibody binds specifically. In a model for CPVT (catecholaminergic polymorphic ventricular tachycardia), an arrhythmic persistent sodium current seemed to be conducted by neuronal $Na_v$ isoforms [90]. The immunofluorescence data from this paper however show too high background signals to allow any conclusions on $Na_v$ isoform expression.

Taken together, despite many reports on the expression of sodium channels in T-tubules, T-tubular $Na_v$ expression remains debatable. A de facto inward sodium current by NCX should be expected in any case because of the high electrochemical gradient.

Lastly, NKA is expressed in T-tubules [91]. Especially the $\alpha_3$-subunit is enriched in T-tubules, whereas the $\alpha_1$-subunit is more uniformly expressed over the sarcolemma [91].

### 3.4.3. Potassium-handling proteins

Although the subcellular localization of potassium channels is less studied, several potassium currents seem to be conducted in the T-tubular systems of mice and rats. These include the inward rectifier current $I_{K1}$ [58] (conducted by $K_{ir}2.1$, 2.2, and/or 2.3), the steady-state current $I_{ss}$ ($K_v1.2$ and/or $-2.1$), the transient outward current $I_{to}$ ($K_v4.2$ and/or $-4.3$), the slow delayed rectifier current $I_{K,s}$ ($K_v7.1$), and the rapid delayed rectifier current $I_{K,r}$ ($K_v11.1$/hERG) [30]. Based on detubulation experiments, $I_{K1}$, $I_{to}$, $I_{K,r}$, and $I_{K,s}$ seem to be divided equally over T-tubular and surface sarcolemma [92]. The inward-rectifying current $I_{K1}$ is especially high in T-tubules because potassium accumulates in the small extracellular space during the repolarization phase of the action potential, increasing its driving force [58]. Other currents were found to be enriched in rat T-tubules, including $I_{ss}$ [92]. Interestingly, only $K_v2.1$-encoding mRNAs were detected in isolated murine cardiomyocytes [82], suggesting $K_v1.2$ may not contribute to $I_{ss}$ in these cells.

The T-tubular fraction of $I_{KATP}$ has, to our knowledge, not yet been determined. It is however likely that at least one of the $I_{KATP}$-conducting channels $K_{ir}6.1$ and $-6.2$ is expressed in T-tubules, since $I_{KATP}$, as well as $I_{K1}$, decreases along with the loss of T-tubules in cardiomyocytes that have been taken in culture (reviewed in [5]). $K_{ir}6.2$ has been associated with the T-tubular protein ankyrin-B, although these immunohistochemistry data lack a fiducial T-tubular marker [93].

Considering immunohistochemistry data, T-tubular expression has been shown relatively convincingly for $K_v11.1$ by co-staining with myosin-binding protein C [94]. A thorough live-cell imaging study for $K_v2.1$ and $K_v1.4$ in rat cardiomyocytes shows a T-tubular-like pattern, including axial elements, but unfortunately lacks a T-tubular marker [95]. $K_{ir}2.1$, $-2.3$, $-4.2$ and TASK-1 show clear co-localization with the membrane marker wheat germ agglutinin in murine ($K_{ir}2.1$), canine ($K_{ir}2.1$ and $-2.3$) and rat ($K_v4.2$ and TASK-1) ventricular cardiomyocytes [96–99]. For $K_v4.3$ only a striated pattern was shown without T-tubular marker in canine cells [100]. Note that potassium channel composition probably differs between species, since $K_{ir}2.3$ mRNA was not detected in isolated murine cardiomyocytes [82] while $K_{ir}2.3$ protein was found in in canine cells [97]. Interestingly, TASK-1 has been recently defined as an atrial-specific current [101], which seems to contradict these immunohistochemistry and mRNA expression data – although it must be noted that we did not find any recordings of ventricular TASK-1 currents in the literature.

### 3.4.4. Other ion-handling proteins

Chloride channels are not well researched in T-tubules. Scanning ion conductance microscopy (SICM) experiments revealed that these channels are close to the openings of T-tubules at the lateral membrane [102]. mRNA data show that the voltage-sensitive chloride channels CLCN4, $-7$, $-3$, $-6$ and $-1$ are expressed in murine ventricular myocytes (in order of expression level) [82], but their roles in cardiac physiology remain to be investigated.

Another ion channel family which roles in cardiac physiology are just emerging is the transient receptor potential (TRP) superfamily of non-selective cation channels. The vanilloid subfamily member TRPV4 is expressed in T-tubules of aged mice and human cardiomyocytes

[103]. This is based on immunohistochemistry data in which TRPV4 and the membrane marker caveolin-3 are co-stained. TRPV4 seems to play a role in calcium cycling, but in the aged heart it may contribute to stress-induced cell damage. Of note, TRPV4-encoding mRNA is not found in murine cardiomyocytes [82], which illustrates that even among mouse models, ion channel composition may differ.

### 3.5. Ion dynamics in T-tubules

The small luminal space of T-tubules can affect the ion diffusion and therefore the driving force of ion channels (discussed in Section 3.2). Diffusion rates of ions are slower in T-tubules than in other extracellular spaces, with a markedly higher delay for divalent than monovalent ions [18,19]. Functionally, an extracellular change in calcium concentration reaches the T-tubules 2.3 s later in guinea pig cardiomyocytes, indicating a “fuzzy space” [104]. This diffusion delay is related to the membrane microfolds that are shaped by Bin1 [42]. These microfolds are proposed to protect against arrhythmias, since excitability of the cell would increase when ions can diffuse faster (reviewed in [5]). The finding that T-tubules of animals with higher heart rates are narrower than in low-heart-rate animals [5] might indicate that the relatively high calcium depletion and potassium accumulation rates in the narrow tubules of high-heart-rate animals are of evolutionary benefit.

Theoretically, calcium influx during an action potential may deplete the T-tubular lumen of calcium and reduce the driving force of the calcium channel. This may cause self-attenuation of the calcium current and thus shorten the action potential [45], in a manner similar to what was proposed in the context of intercalated discs for the late sodium current during the plateau phase (see Section 3.2) [62]: the sooner the calcium channels close, the sooner the potassium current repolarizes the membrane. A strong depletion of calcium and accumulation of potassium in the T-tubular lumen is however unlikely due to the physiological need for significant electrochemical gradients of calcium and potassium, which will be secured by NCX and NKA [74]. An important general remark is that we cannot speak of a shorter or longer action potential in T-tubules compared to the rest of the sarcolemma as one might think from the finding that detubulated rat cells show shorter action potentials due to the lost calcium current [26]. The membrane domains of the cell are electrically too tightly coupled [105,106]. Detubulation may however affect action potential duration of other species differently as rat cardiomyocytes show a relatively unique calcium handling profile compared to other mammals, which is partly explained by a reduced NCX/SERCA2a ratio [67].

### 3.6. T-tubular remodeling in disease

Heart failure has been associated with T-tubular remodeling, characterized by T-tubular widening and an increase in tortuosity [107], the loss of the microfold regulator Bin1 [42], collagen deposition in T-tubules [11,51], dyad uncoupling [108], physical obstruction of T-tubules [47], and sheet-like T-tubular remodeling in end-stage heart failure [36].

The loss of Bin1 observed in human heart failure has been suggested to be arrhythmogenic as Bin1 knockout mice show a loss of microfolds and are more vulnerable to arrhythmias due to changes in ion dynamics as discussed in Section 3.5 [42]. Sheet-like remodeling is similarly expected to be arrhythmogenic [36]. On the other hand, collagen deposition in T-tubules, which is also seen in human heart failure, and physical obstruction of T-tubules would again slow ion diffusion [10,11,51]. Understanding the interplay of these effects will need further investigation.

T-tubular remodeling likely disturbs optimal excitation-contraction coupling as calcium dynamics greatly depend on T-tubular microstructure [109] and on the association and membrane expression of voltage-gated calcium channels and the sodium-calcium exchanger [110]. Indeed, a hallmark of T-tubular dysfunction is the increase in orphaned RyR2 at the *Z*-lines [108]. This causes a dysregulation of calcium release as diffusion distances for calcium increase, and the calcium transient slows and broadens. In turn, contraction of the cell desynchronizes and slows. Expectedly, detubulated cardiomyocytes show comparable contraction kinetics as failing cells (reviewed in [10]). Interestingly, in end-stage heart failure patients, relieving the mechanical load with a left-ventricular assist device (LVAD) improves cardiac function but only if the T-tubular system is intact, suggesting that calcium handling deficits may be reversible whereas sheet-like T-tubular remodeling is not [36].

It may be valuable to compare depolarization delays in T-tubules from healthy and diseased cells to assess the passive electrical effects of T-tubular remodeling, although other processes associated with T-tubular remodeling may play greater roles in pathophysiology. Since heart failure is also associated with a reduction of Bin1 expression, and Bin1 is important for voltage-gated calcium channel trafficking to the T-tubules [33], the resulting dysregulation of this trafficking may further impair calcium dynamics. In summary, the T-tubular remodeling associated with heart failure probably affects cardiomyocyte function via different pathways, yet the effects of T-tubular remodeling on T-tubular depolarization remains to be determined.

## 4. T-tubules in atrial cardiomyocytes

Although T-tubules support a high heart rate in mammalian ventricular cardiomyocytes, heart rates of atrial cells are just as high with a far less dense T-tubular system [20]. Atrial cells in many species can be subdivided in three sub-populations based on their T-tubular network: dense, semi-dense and disorganized, or absent [8]. In pig and rat atria, cardiomyocytes with a well-organized T-tubular network populated the epicardial layer, whereas the endocardial layer mostly contained empty cardiomyocytes [111]. The degree of tubulation furthermore correlated well with synchronicity of calcium release. This may suggest that T-tubules at the epicardial layer are involved in synchronizing the contraction across the atrial wall [111], and that β-adrenergic stimulation has a faster and greater effect on cells close to the epicardium. Interestingly, one recent study [112] reports that human and murine atrial cardiomyocytes contain relatively many axial tubules, which run over the long axis of the cell. The sparse transverse tubules conduct the excitation of the cell from the surface sarcolemma to the axial tubules, while axial tubules contain much more dyads than transverse tubules, thus allowing quick excitation-contraction coupling around these axial tubules [112].

## 5. Discussion

This work assessed passive and active electrical properties of T-tubules from which we distilled the physiological function of T-tubules. Generally, the roles of T-tubules are twofold: firstly, T-tubules provide a large calcium-handling stage to allow the cardiomyocyte to generate a relatively high force, and secondly, the relatively large membrane surface facilitates the cell to respond faster to signaling molecules than non-tubulated cells. Importantly, T-tubules are not crucial to sustain a high heart rate – atrial cardiomyocytes contract just as fast [20], and non-tubulated cardiomyocytes from certain avian species even faster [113,114]. Within mammalian ventricular cardiomyocytes however there is a relationship between heart rate and T-tubular density.

The publications discussed in this review strengthen the hypothesis that T-tubules facilitate rapid and efficient excitation-contraction coupling throughout the entire volume of the cell [26]. The length constant of ~ 68 μm [51] and time constant of ~ 200 μs [58] indicate that electrotonic responses allow depolarization of the entire T-tubular membrane within physiological timescales.

When assessing conduction velocity in cardiac tissue, T-tubules most likely slow conduction from a theoretical point of view. Since a tubulated cardiomyocyte has a greater membrane surface, this

additional capacitive load may slow down and delay depolarization. Ion channels in T-tubules, especially $Na_v$ channels, will mitigate this delay. Given that the concentration of $Na_v$ channels in the T-tubule is most likely lower than that in the surface sarcolemma, and assuming T-tubular membrane accounts for 50% of the membrane (which is the case at least in mice and rats [30]), T-tubules will slow down conduction velocity by 29–50%, while loss of T-tubules may accelerate conduction.

Next, we evaluated evidence regarding the expression of voltage-gated sodium channels in the T-tubules. Some neuronal isoforms seem to be expressed in low levels; especially $Na_v1.6$ seems to be expressed in the T-tubules of a mouse model [89]. It remains unclear if these low levels could carry enough current to initiate an action potential. The expression of neuronal channels moreover varies greatly between species and even mouse strains. Concerning the cardiac isoform $Na_v1.5$, T-tubular expression remains debatable, despite several reports pointing in that direction. Generally, it is important to keep in mind that sodium channels are not required to depolarize T-tubular membranes. The often-used term “action potential propagation” in T-tubules therefore should be interpreted as “either passive or active”.

In terms of repolarizing currents, the expression of voltage-gated potassium channels differs greatly between species and mouse models. It is probable that the expression levels suffice to repolarize the membrane to balance the high expression level of voltage-gated calcium channels. Considering ion channel expression data in general, the authors would like to stress that critical evaluation of research data is pivotal, especially when functional detubulation experiments and immunohistochemistry data are concerned.

In cardiac disease, T-tubules often remodel [9]. As a result, T-tubules widen, the tortuous membrane microfolds disappear, dyads uncouple, T-tubules close off to the extracellular space, calcium transient weakens, and T-tubules may take on a sheet-like shape while collagen content in the lumen is increased.

## Financial statement

This work was supported by the Swiss National Science Foundation [grant no. 310030_165741; HA group].

## Author contributions

Sarah Vermij: conceptualization, methodology, visualization, writing- original draft preparation, reviewing and editing.

Hugues Abriel: supervision, writing- reviewing and editing.

Jan Kucera: visualization, writing- reviewing and editing.

## Transparency document

The Transparency document associated with this article can be found, in online version.

## Acknowledgments

The authors express their gratitude to Prof Stephan Rohr and Prof Ernst Niggli for helpful discussions on physiology; Dr. Jean-Sébastien Rougier for thorough feedback on the manuscript; and Diana Gamborino Uzcanga and Michaela Gazzetto for assistance with basic physics.

## References

[1] C. Soeller, M.B. Cannell, Examination of the transverse tubular system in living cardiac rat myocytes by 2-photon microscopy and digital image-processing techniques, Circ. Res. 84 (1999) 266–275.

[2] E. Wagner, M.A. Lauterbach, T. Kohl, V. Westphal, G.S. Williams, J.H. Steinbrecher, J.H. Streich, B. Korff, H.T. Tuan, B. Hagen, S. Luther, G. Hasenfuss, U. Parlitz, M.S. Jafri, S.W. Hell, W.J. Lederer, S.E. Lehnart, Stimulated emission depletion live-cell super-resolution imaging shows proliferative remodeling of T-tubule membrane structures after myocardial infarction, Circ. Res. 111 (2012) 402–414, https://doi.org/10.1161/circresaha.112.274530.

[3] I.D. Jayasinghe, A.H. Clowsley, M. Munro, Y. Hou, D.J. Crossman, C. Soeller, Revealing T-tubules in striated muscle with new optical super-resolution microscopy techniquess, Eur. J. Trans. Myol. 25 (2015) 4747, https://doi.org/10.4081/ejtm.2015.4747.

[4] C. Pinali, H. Bennett, J.B. Davenport, A.W. Trafford, A. Kitmitto, Three-dimensional reconstruction of cardiac sarcoplasmic reticulum reveals a continuous network linking transverse-tubules: this organization is perturbed in heart failure, Circ. Res. 113 (2013) 1219–1230, https://doi.org/10.1161/CIRCRESAHA.113.301348.

[5] T. Hong, R.M. Shaw, Cardiac T-tubule microanatomy and function, Physiol. Rev. 97 (2017) 227–252, https://doi.org/10.1152/physrev.00037.2015.

[6] N.K. Bhogal, A. Hasan, J. Gorelik, The development of compartmentation of cAMP signaling in cardiomyocytes: the role of T-tubules and caveolae microdomains, J. Cardiovasc. Dev. Dis. 5 (2018), https://doi.org/10.3390/jcdd5020025.

[7] D.M. Bers, Cardiac excitation-contraction coupling, Nature 415 (2002) 198–205, https://doi.org/10.1038/415198a.

[8] M.A. Richards, J.D. Clarke, P. Saravanan, N. Voigt, D. Dobrev, D.A. Eisner, A.W. Trafford, K.M. Dibb, Transverse tubules are a common feature in large mammalian atrial myocytes including human, Am. J. Physiol. Heart Circ. Physiol. 301 (2011) H1996–H2005, https://doi.org/10.1152/ajpheart.00284.2011.

[9] D.J. Crossman, I.D. Jayasinghe, C. Soeller, Transverse tubule remodelling: a cellular pathology driven by both sides of the plasmalemma? Biophys. Rev. 9 (2017) 919–929, https://doi.org/10.1007/s12551-017-0273-7.

[10] C. Crocini, C. Ferrantini, R. Coppini, L. Sacconi, Electrical defects of the transverse-axial tubular system in cardiac diseases, J. Physiol. 595 (2017) 3815–3822, https://doi.org/10.1113/JP273042.

[11] D.J. Crossman, X. Shen, M. Jullig, M. Munro, Y. Hou, M. Middleditch, D. Shrestha, A. Li, S. Lal, C.G. Dos Remedios, D. Baddeley, P.N. Ruygrok, C. Soeller, Increased collagen within the transverse tubules in human heart failure, Cardiovasc. Res. 113 (2017) 879–891, https://doi.org/10.1093/cvr/cvx055.

[12] A.L. Hodgkin, A.F. Huxley, Propagation of electrical signals along giant nerve fibers, Proc R Soc Soc Lond, Ser B: Biol Sci 140 (1952) 177–183.

[13] A.L. Hodgkin, A.F. Huxley, A quantitative description of membrane current and its application to conduction and excitation in nerve, J. Physiol. 117 (1952) 500–544.

[14] D. Noble, Cardiac action and pacemaker potentials based on the Hodgkin-Huxley equations, Nature 188 (1960) 495–497.

[15] D. Noble, The voltage dependence of the cardiac membrane conductance, Biophys. J. 2 (1962) 381–393.

[16] R.W. Joyner, Effects of the discrete pattern of electrical coupling on propagation through an electrical syncytium, Circ. Res. 50 (1982) 192–200.

[17] A.G. Kleber, Y. Rudy, Basic mechanisms of cardiac impulse propagation and associated arrhythmias, Physiol. Rev. 84 (2004) 431–488, https://doi.org/10.1152/physrev.00025.2003.

[18] W.J. Lederer, E. Niggli, R.W. Hadley, Sodium-calcium exchange in excitable cells: fuzzy space, Science 248 (1990) 283.

[19] F. Swift, T.A. Stromme, B. Amundsen, O.M. Sejersted, I. Sjaastad, Slow diffusion of K+ in the T tubules of rat cardiomyocytes, J. Appl. Physiol. 101 (2006) 1170–1176, https://doi.org/10.1152/japplphysiol.00297.2006.

[20] S. Brandenburg, E.C. Arakel, B. Schwappach, S.E. Lehnart, The molecular and functional identities of atrial cardiomyocytes in health and disease, Biochim. Biophys. Acta 1863 (2016) 1882–1893, https://doi.org/10.1016/j.bbamcr.2015.11.025.

[21] S.H. Vermij, H. Abriel, T.A. van Veen, Refining the molecular organization of the cardiac intercalated disc, Cardiovasc. Res. 113 (2017) 259–275, https://doi.org/10.1093/cvr/cvw259.

[22] E. Hichri, H. Abriel, J.P. Kucera, Distribution of cardiac sodium channels in clusters potentiates ephaptic interactions in the intercalated disc, J. Physiol. 596 (2018) 563–589, https://doi.org/10.1113/JP275351.

[23] J.M. Rhett, R. Veeraraghavan, S. Poelzing, R.G. Gourdie, The perinexus: sign-post on the path to a new model of cardiac conduction? Trends Cardiovasc. Med. 23 (2013) 222–228, https://doi.org/10.1016/j.tcm.2012.12.005.

[24] R. Veeraraghavan, J. Lin, G.S. Hoeker, J.P. Keener, R.G. Gourdie, S. Poelzing, Sodium channels in the Cx43 gap junction perinexus may constitute a cardiac ephapse: an experimental and modeling study, Pfluegers Arch./Eur. J. Physiol. 467 (2015) 2093–2105, https://doi.org/10.1007/s00424-014-1675-z.

[25] D. Shy, L. Gillet, J. Ogrodnik, M. Albesa, A.O. Verkerk, R. Wolswinkel, J.S. Rougier, J. Barc, M.C. Essers, N. Syam, R.F. Marsman, A.M. van Mil, S. Rotman, R. Redon, C.R. Bezzina, C.A. Remme, H. Abriel, PDZ domain-binding motif regulates cardiomyocyte compartment-specific NaV1.5 channel expression and function, Circulation 130 (2014) 147–160, https://doi.org/10.1161/circulationaha.113.007852.

[26] F. Brette, L. Salle, C.H. Orchard, Quantification of calcium entry at the T-tubules and surface membrane in rat ventricular myocytes, Biophys. J. 90 (2006) 381–389, https://doi.org/10.1529/biophysj.105.069013.

[27] M. Ibrahim, J. Gorelik, M.H. Yacoub, C.M. Terracciano, The structure and function of cardiac t-tubules in health and disease, Proc R Soc Soc Lond, Ser B: Biol Sci 278 (2011) 2714–2723, https://doi.org/10.1098/rspb.2011.0624.

[28] A. Sandow, Excitation-contraction coupling in skeletal muscle, Pharmacol. Rev. 17 (1965) 265–320.

[29] C.H.T. Kong, E.A. Rog-Zielinska, P. Kohl, C.H. Orchard, M.B. Cannell, Solute movement in the t-tubule system of rabbit and mouse cardiomyocytes, Proc. Natl. Acad. Sci. U. S. A. 115 (2018) E7073–E7080, https://doi.org/10.1073/pnas.1805979115.

[30] M. Pasek, F. Brette, A. Nelson, C. Pearce, A. Qaiser, G. Christe, C.H. Orchard, Quantification of t-tubule area and protein distribution in rat cardiac ventricular myocytes, Prog. Biophys. Mol. Biol. 96 (2008) 244–257, https://doi.org/10.1016/j.pbiomolbio.2007.07.016.
[31] T. Hayashi, M.E. Martone, Z. Yu, A. Thor, M. Doi, M.J. Holst, M.H. Ellisman, M. Hoshijima, Three-dimensional electron microscopy reveals new details of membrane systems for Ca2+ signaling in the heart, J. Cell Sci. 122 (2009) 1005–1013, https://doi.org/10.1242/jcs.028175.
[32] M. Escobar, C. Cardenas, K. Colavita, N.B. Petrenko, C. Franzini-Armstrong, Structural evidence for perinuclear calcium microdomains in cardiac myocytes, J. Mol. Cell. Cardiol. 50 (2011) 451–459, https://doi.org/10.1016/j.yjmcc.2010.11.021.
[33] Y. Fu, T. Hong, BIN1 regulates dynamic t-tubule membrane, Biochim. Biophys. Acta 1863 ( (2016) 1839–1847, https://doi.org/10.1016/j.bbamcr.2015.11.004.
[34] K.R. Levin, E. Page, Quantitative studies on plasmalemmal folds and caveolae of rabbit ventricular myocardial cells, Circ. Res. 46 (1980) 244–255.
[35] E. Page, Quantitative ultrastructural analysis in cardiac membrane physiology, Am. J. Physiol. Cell Physiol. 235 (1978) C147–C158, https://doi.org/10.1152/ajpcell.1978.235.5.C147.
[36] T. Seidel, S. Navankasattusas, A. Ahmad, N.A. Diakos, W.D. Xu, M. Tristani-Firouzi, M.J. Bonios, I. Taleb, D.Y. Li, C.H. Selzman, S.G. Drakos, F.B. Sachse, Sheet-like remodeling of the transverse tubular system in human heart failure impairs excitation-contraction coupling and functional recovery by mechanical unloading, Circulation 135 (2017) 1632–1645, https://doi.org/10.1161/circulationaha.116.024470.
[37] C.A. Makarewich, R.N. Correll, H. Gao, H. Zhang, B. Yang, R.M. Berretta, V. Rizzo, J.D. Molkentin, S.R. Houser, A caveolae-targeted L-type ca(2)+ channel antagonist inhibits hypertrophic signaling without reducing cardiac contractility, Circ. Res. 110 (2012) 669–674, https://doi.org/10.1161/circresaha.111.264028.
[38] M. Ibrahim, A. Nader, M.H. Yacoub, C. Terracciano, Manipulation of sarcoplasmic reticulum Ca2+ release in heart failure through mechanical intervention, J. Physiol. Lond. 593 (2015) 3253–3259, https://doi.org/10.1113/Jp270446.
[39] R.J. van Oort, A. Garbino, W. Wang, S.S. Dixit, A.P. Landstrom, N. Gaur, A.C. De Almeida, D.G. Skapura, Y. Rudy, A.R. Burns, M.J. Ackerman, X.H. Wehrens, Disrupted junctional membrane complexes and hyperactive ryanodine receptors after acute junctophilin knockdown in mice, Circulation 123 (2011) 979–988, https://doi.org/10.1161/circulationaha.110.006437.
[40] I. Jayasinghe, A.H. Clowsley, R. Lin, T. Lutz, C. Harrison, E. Green, D. Baddeley, L. Di Michele, C. Soeller, True molecular scale visualization of variable clustering properties of ryanodine receptors, Cell Rep. 22 (2018) 557–567, https://doi.org/10.1016/j.celrep.2017.12.045.
[41] T.T. Hong, J.W. Smyth, D. Gao, K.Y. Chu, J.M. Vogan, T.S. Fong, B.C. Jensen, H.M. Colecraft, R.M. Shaw, BIN1 localizes the L-type calcium channel to cardiac T-tubules, PLoS Biol. 8 (2010) e1000312, , https://doi.org/10.1371/journal.pbio.1000312.
[42] T. Hong, H. Yang, S.S. Zhang, H.C. Cho, M. Kalashnikova, B. Sun, H. Zhang, A. Bhargava, M. Grabe, J. Olgin, J. Gorelik, E. Marban, L.Y. Jan, R.M. Shaw, Cardiac BIN1 folds T-tubule membrane, controlling ion flux and limiting arrhythmia, Nat. Med. 20 (2014) 624–632, https://doi.org/10.1038/nm.3543.
[43] S. Dhein, T. Seidel, A. Salameh, J. Jozwiak, A. Hagen, M. Kostelka, G. Hindricks, F.W. Mohr, Remodeling of cardiac passive electrical properties and susceptibility to ventricular and atrial arrhythmias, Front. Physiol. 5 (2014) 424, , https://doi.org/10.3389/fphys.2014.00424.
[44] J.H. King, C.L. Huang, J.A. Fraser, Determinants of myocardial conduction velocity: implications for arrhythmogenesis, Front. Physiol. 4 (2013) 154, , https://doi.org/10.3389/fphys.2013.00154.
[45] M. Pasek, J. Simurda, C.H. Orchard, G. Christe, A model of the Guinea-pig ventricular cardiac myocyte incorporating a transverse-axial tubular system, Prog. Biophys. Mol. Biol. 96 (2008) 258–280, https://doi.org/10.1016/j.pbiomolbio.2007.07.022.
[46] C.H.T. Kong, E.A. Rog-Zielinska, C.H. Orchard, P. Kohl, M.B. Cannell, Sub-microscopic analysis of t-tubule geometry in living cardiac ventricular myocytes using a shape-based analysis method, J. Mol. Cell. Cardiol. 108 (2017) 1–7, https://doi.org/10.1016/j.yjmcc.2017.05.003.
[47] M. Scardigli, C. Crocini, C. Ferrantini, T. Gabbrielli, L. Silvestri, R. Coppini, C. Tesi, E.A. Rog-Zielinska, P. Kohl, E. Cerbai, C. Poggesi, F.S. Pavone, L. Sacconi, Quantitative assessment of passive electrical properties of the cardiac T-tubular system by FRAP microscopy, Proc. Natl. Acad. Sci. U. S. A. 114 (2017) 5737–5742, https://doi.org/10.1073/pnas.1702188114.
[48] S. Weidmann, The electrical constants of Purkinje fibres, J. Physiol. 118 (1952) 348–360.
[49] J.J.B. Jack, D. Noble, R.W. Tsien, Chapter 10 in: Electric Current Flow in Excitable Cells, Clarendon Press, Oxford, 1975, pp. 292–296.
[50] S.H. Vermij, H. Abriel, J.P. Kucera, Modelling depolarization delay, sodium currents, and electrical potentials in cardiac transverse tubules, bioRxiv (2019) 611558, , https://doi.org/10.1101/611558.
[51] K. Uchida, A.N. Lopatin, Diffusional and electrical properties of T-tubules are governed by their constrictions and dilations, Biophys. J. 114 (2018) 437–449, https://doi.org/10.1016/j.bpj.2017.11.3742.
[52] R.R. Poznanski, A generalized tapering equivalent cable model for dendritic neurons, Bull. Math. Biol. 53 (1991) 457–467.
[53] S.S. Goldstein, W. Rall, Changes of action potential shape and velocity for changing core conductor geometry, Biophys. J. 14 (1974) 731–757, https://doi.org/10.1016/S0006-3495(74)85947-3.
[54] W. Rall, Theory of physiological properties of dendrites, Ann. N. Y. Acad. Sci. 96 (1962) 1071–1092.
[55] A. Gopinathan, Neuronal Space Constants in Various Geometries and Physiological Conditions, arXiv, (2013).
[56] W. Rall, Electrophysiology of a dendritic neuron model, Biophys. J. 2 (1962) 145–167.
[57] N. Shepherd, H.B. McDonough, Ionic diffusion in transverse tubules of cardiac ventricular myocytes, Am. J. Phys. 275 (1998) H852–H860.
[58] L.F. Cheng, F. Wang, A.N. Lopatin, Metabolic stress in isolated mouse ventricular myocytes leads to remodeling of t tubules, Am. J. Physiol. Heart Circ. Physiol. 301 (2011) H1984–H1995, https://doi.org/10.1152/ajpheart.00304.2011.
[59] M. Pasek, J. Simurda, G. Christe, The functional role of cardiac T-tubules explored in a model of rat ventricular myocytes, Philos. Trans. A Math. Phys. Eng. Sci. 364 (2006) 1187–1206, https://doi.org/10.1098/rsta.2006.1764.
[60] A. Hatano, J. Okada, T. Washio, T. Hisada, S. Sugiura, An integrated finite element simulation of cardiomyocyte function based on triphasic theory, Front. Physiol. 6 (2015) 287, , https://doi.org/10.3389/fphys.2015.00287.
[61] Y. Mori, G.I. Fishman, C.S. Peskin, Ephaptic conduction in a cardiac strand model with 3D electrodiffusion, Proc. Natl. Acad. Sci. U. S. A. 105 (2008) 6463–6468, https://doi.org/10.1073/pnas.0801089105.
[62] A. Greer-Short, S.A. George, S. Poelzing, S.H. Weinberg, Revealing the concealed nature of long-QT type 3 syndrome, Circ. Arrhythm. Electrophysiol. 10 (2017) e004400, , https://doi.org/10.1161/CIRCEP.116.004400.
[63] R.M. Shaw, Y. Rudy, Ionic mechanisms of propagation in cardiac tissue. Roles of the sodium and L-type calcium currents during reduced excitability and decreased gap junction coupling, Circ. Res. 81 (1997) 727–741.
[64] R. Plonsey, R.C. Barr, Chapter 9 in: Bioelectricity, a Quantitative Approach, Springer, New York, 2007, pp. 267–323.
[65] V. Jacquemet, C.S. Henriquez, Loading effect of fibroblast-myocyte coupling on resting potential, impulse propagation, and repolarization: insights from a microstructure model, Am. J. Physiol. Heart Circ. Physiol. 294 (2008) H2040–H2052, https://doi.org/10.1152/ajpheart.01298.2007.
[66] A.F. Huxley, Ion movements during nerve activity, Ann. N. Y. Acad. Sci. 81 (1959) 221–246.
[67] F. Brette, C.H. Orchard, Density and sub-cellular distribution of cardiac and neuronal sodium channel isoforms in rat ventricular myocytes, Biochem. Biophys. Res. Commun. 348 (2006) 1163–1166, https://doi.org/10.1016/j.bbrc.2006.07.189.
[68] D. Platzer, K. Zorn-Pauly, Letter to the editor: accurate cell capacitance determination from a single voltage step: a reminder to avoid unnecessary pitfalls, Am. J. Physiol. Heart Circ. Physiol. 311 (2016) H1072–H1073, https://doi.org/10.1152/ajpheart.00503.2016.
[69] H.C. Gadeberg, C.H.T. Kong, S.M. Bryant, A.F. James, C.H. Orchard, Cholesterol depletion does not alter the capacitance or Ca handling of the surface or t-tubule membranes in mouse ventricular myocytes, Physiol Rep 5 (2017), https://doi.org/10.14814/phy2.13500.
[70] C.A. Eichel, A. Beuriot, M.Y. Chevalier, J.S. Rougier, F. Louault, G. Dilanian, J. Amour, A. Coulombe, H. Abriel, S.N. Hatem, E. Balse, Lateral membrane-specific MAGUK CASK down-regulates NaV1.5 channel in cardiac myocytes, Circ. Res. 119 (2016) 544–556, https://doi.org/10.1161/circresaha.116.309254.
[71] S. Dai, D.D. Hall, J.W. Hell, Supramolecular assemblies and localized regulation of voltage-gated ion channels, Physiol. Rev. 89 (2009) 411–452, https://doi.org/10.1152/physrev.00029.2007.
[72] M. Kawai, M. Hussain, C.H. Orchard, Excitation-contraction coupling in rat ventricular myocytes after formamide-induced detubulation, Am. J. Phys. 277 (1999) H603–H609, https://doi.org/10.1152/ajpheart.1999.277.2.H603.
[73] D.R. Scriven, P. Dan, E.D. Moore, Distribution of proteins implicated in excitation-contraction coupling in rat ventricular myocytes, Biophys. J. 79 (2000) 2682–2691, https://doi.org/10.1016/S0006-3495(00)76506-4.
[74] S. Despa, F. Brette, C.H. Orchard, D.M. Bers, Na/Ca exchange and Na/K-ATPase function are equally concentrated in transverse tubules of rat ventricular myocytes, Biophys. J. 85 (2003) 3388–3396, https://doi.org/10.1016/S0006-3495(03)74758-4.
[75] M. Pasek, J. Simurda, G. Christe, Different densities of Na-Ca exchange current in T-tubular and surface membranes and their impact on cellular activity in a model of rat ventricular cardiomyocyte, Biomed. Res. Int. 2017 (2017) 6343821, , https://doi.org/10.1155/2017/6343821.
[76] E. Lin, V.H. Hung, H. Kashihara, P. Dan, G.F. Tibbits, Distribution patterns of the Na+-Ca2+ exchanger and caveolin-3 in developing rabbit cardiomyocytes, Cell Calcium 45 (2009) 369–383, https://doi.org/10.1016/j.ceca.2009.01.001.
[77] A. Chase, C.H. Orchard, Ca efflux via the sarcolemmal Ca ATPase occurs only in the t-tubules of rat ventricular myocytes, J. Mol. Cell. Cardiol. 50 (2011) 187–193, https://doi.org/10.1016/j.yjmcc.2010.10.012.
[78] P.J. Mohler, I. Rivolta, C. Napolitano, G. LeMaillet, S. Lambert, S.G. Priori, V. Bennett, Nav1.5 E1053K mutation causing Brugada syndrome blocks binding to ankyrin-G and expression of Nav1.5 on the surface of cardiomyocytes, Proc. Natl. Acad. Sci. U. S. A. 101 (2004) 17533–17538, https://doi.org/10.1073/pnas.0403711101.
[79] J.N. Dominguez, A. de la Rosa, F. Navarro, D. Franco, A.E. Aranega, Tissue distribution and subcellular localization of the cardiac sodium channel during mouse heart development, Cardiovasc. Res. 78 (2008) 45–52, https://doi.org/10.1093/cvr/cvm118.
[80] D. Ponce-Balbuena, G. Guerrero-Serna, C.R. Valdivia, R. Caballero, F.J. Diez-Guerra, E.N. Jimenez-Vazquez, R.J. Ramirez, A. Monteiro da Rocha, T.J. Herron, K.F. Campbell, B.C. Willis, F.J. Alvarado, M. Zarzoso, K. Kaur, M. Perez-Hernandez, M. Matamoros, H.H. Valdivia, E. Delpon, J. Jalife, Cardiac Kir2.1 and NaV1.5 channels traffic together to the sarcolemma to control excitability, Circ. Res. 122 (2018) 1501–1516, https://doi.org/10.1161/circresaha.117.311872.

[81] J.S. Rougier, H. Abriel, Role of "non-cardiac" voltage-gated sodium channels in cardiac cells, J. Mol. Cell. Cardiol. 53 (2012) 589–590, https://doi.org/10.1016/j.yjmcc.2012.08.011.
[82] M. Chevalier, S.H. Vermij, K. Wyler, L. Gillet, I. Keller, H. Abriel, Transcriptomic analyses of murine ventricular cardiomyocytes, Sci. Data 5 (2018) 180170, , https://doi.org/10.1038/sdata.2018.170.
[83] F. Brette, C.H. Orchard, No apparent requirement for neuronal sodium channels in excitation-contraction coupling in rat ventricular myocytes, Circ. Res. 98 (2006) 667–674, https://doi.org/10.1161/01.RES.0000209963.02720.70.
[84] S.K. Maier, R.E. Westenbroek, K.A. McCormick, R. Curtis, T. Scheuer, W.A. Catterall, Distinct subcellular localization of different sodium channel alpha and beta subunits in single ventricular myocytes from mouse heart, Circulation 109 (2004) 1421–1427, https://doi.org/10.1161/01.CIR.0000121421.61896.24.
[85] S.K. Maier, R.E. Westenbroek, K.A. Schenkman, E.O. Feigl, T. Scheuer, W.A. Catterall, An unexpected role for brain-type sodium channels in coupling of cell surface depolarization to contraction in the heart, Proc. Natl. Acad. Sci. U. S. A. 99 (2002) 4073–4078, https://doi.org/10.1073/pnas.261705699.
[86] M. Koleske, I. Bonilla, J. Thomas, N. Zaman, S. Baine, B.C. Knollmann, R. Veeraraghavan, S. Gyorke, P.B. Radwanski, Tetrodotoxin-sensitive Navs contribute to early and delayed afterdepolarizations in long QT arrhythmia models, J. Gen. Physiol. 150 (2018) 991–1002, https://doi.org/10.1085/jgp.201711909.
[87] R.E. Westenbroek, S. Bischoff, Y. Fu, S.K. Maier, W.A. Catterall, T. Scheuer, Localization of sodium channel subtypes in mouse ventricular myocytes using quantitative immunocytochemistry, J. Mol. Cell. Cardiol. 64 (2013) 69–78, https://doi.org/10.1016/j.yjmcc.2013.08.004.
[88] C. Marionneau, C.F. Lichti, P. Lindenbaum, F. Charpentier, J.M. Nerbonne, R.R. Townsend, J. Merot, Mass spectrometry-based identification of native cardiac Nav1.5 channel alpha subunit phosphorylation sites, J. Proteome Res. 11 (2012) 5994–6007, https://doi.org/10.1021/pr300702c.
[89] S.F. Noujaim, K. Kaur, M. Milstein, J.M. Jones, P. Furspan, D. Jiang, D.S. Auerbach, T. Herron, M.H. Meisler, J. Jalife, A null mutation of the neuronal sodium channel NaV1.6 disrupts action potential propagation and excitation-contraction coupling in the mouse heart, FASEB J. 26 (2012) 63–72, https://doi.org/10.1096/fj.10-179770.
[90] P.B. Radwanski, H.T. Ho, R. Veeraraghavan, L. Brunello, B. Liu, A.E. Belevych, S.D. Unudurthi, M.A. Makara, S.G. Priori, P. Volpe, A.A. Armoundas, W.H. Dillmann, B.C. Knollmann, P.J. Mohler, T.J. Hund, S. Gyorke, Neuronal Na(+) channels are integral components of pro-arrhythmic Na(+)/ca(2+) signaling nanodomain that promotes cardiac arrhythmias during beta-adrenergic stimulation, JACC Basic Transl. Sci. 1 (2016) 251–266, https://doi.org/10.1016/j.jacbts.2016.04.004.
[91] G.K. Yuen, S. Galice, D.M. Bers, Subcellular localization of Na/K-ATPase isoforms in ventricular myocytes, J. Mol. Cell. Cardiol. 108 (2017) 158–169, https://doi.org/10.1016/j.yjmcc.2017.05.013.
[92] K. Komukai, F. Brette, T.T. Yamanushi, C.H. Orchard, K+ current distribution in rat sub-epicardial ventricular myocytes, Pfluegers arch./Eur, J. Physiol. 444 (2002) 532–538, https://doi.org/10.1007/s00424-002-0851-8.
[93] J. Li, C.F. Kline, T.J. Hund, M.E. Anderson, P.J. Mohler, Ankyrin-B regulates Kir6.2 membrane expression and function in heart, J. Biol. Chem. 285 (2010) 28723–28730, https://doi.org/10.1074/jbc.M110.147868.
[94] E.M. Jones, E.C. Roti Roti, J. Wang, S.A. Delfosse, G.A. Robertson, Cardiac IKr channels minimally comprise hERG 1a and 1b subunits, J. Biol. Chem. 279 (2004) 44690–44694, https://doi.org/10.1074/jbc.M408344200.
[95] K.M. O'Connell, J.D. Whitesell, M.M. Tamkun, Localization and mobility of the delayed-rectifer K+ channel Kv2.1 in adult cardiomyocytes, Am. J. Physiol. Heart Circ. Physiol. 294 (2008) H229–H237, https://doi.org/10.1152/ajpheart.01038.2007.
[96] R.B. Clark, A. Tremblay, P. Melnyk, B.G. Allen, W.R. Giles, C. Fiset, T-tubule localization of the inward-rectifier K(+) channel in mouse ventricular myocytes: a role in K(+) accumulation, J. Physiol. 537 (2001) 979–992.
[97] P. Melnyk, L. Zhang, A. Shrier, S. Nattel, Differential distribution of Kir2.1 and Kir2.3 subunits in canine atrium and ventricle, Am. J. Physiol. Heart Circ. Physiol. 283 (2002) H1123–H1133, https://doi.org/10.1152/ajpheart.00934.2001.
[98] S. Takeuchi, Y. Takagishi, K. Yasui, Y. Murata, J. Toyama, I. Kodama, Voltage-gated K(+) channel, Kv4.2, localizes predominantly to the transverse-axial tubular system of the rat myocyte, J. Mol. Cell. Cardiol. 32 (2000) 1361–1369, https://doi.org/10.1006/jmcc.2000.1172.
[99] S.A. Jones, M.J. Morton, M. Hunter, M.R. Boyett, Expression of TASK-1, a pH-sensitive twin-pore domain K(+) channel, in rat myocytes, Am. J. Physiol. Heart Circ. Physiol. 283 (2002) H181–H185, https://doi.org/10.1152/ajpheart.00963.2001.
[100] I. Deschenes, D. DiSilvestre, G.J. Juang, R.C. Wu, W.F. An, G.F. Tomaselli, Regulation of Kv4.3 current by KChIP2 splice variants: a component of native cardiac I(to)?, Circulation, 106 (2002) 423–429.
[101] C. Schmidt, F. Wiedmann, A.R. Gaubatz, A. Ratte, H.A. Katus, D. Thomas, New targets for old drugs: cardiac glycosides inhibit atrial-specific K2P3.1 (TASK-1) channels, J. Pharmacol. Exp. Ther. 365 (2018) 614–623, https://doi.org/10.1124/jpet.118.247692.
[102] Y. Gu, J. Gorelik, H.A. Spohr, A. Shevchuk, M.J. Lab, S.E. Harding, I. Vodyanoy, D. Klenerman, Y.E. Korchev, High-resolution scanning patch-clamp: new insights into cell function, FASEB J. 16 (2002) 748–750, https://doi.org/10.1096/fj.01-1024fje.
[103] J.L. Jones, D. Peana, A.B. Veteto, M.D. Lambert, Z. Nourian, N.G. Karasseva, M.A. Hill, B.R. Lindman, C.P. Baines, M. Krenz, T.L. Domeier, TRPV4 increases cardiomyocyte calcium cycling and contractility yet contributes to damage in the aged heart following hypoosmotic stress, Cardiovasc. Res. (2018), https://doi.org/10.1093/cvr/cvy156.
[104] L.A. Blatter, E. Niggli, Confocal near-membrane detection of calcium in cardiac myocytes, Cell Calcium 23 (1998) 269–279.
[105] G. Bu, H. Adams, E.J. Berbari, M. Rubart, Uniform action potential repolarization within the sarcolemma of in situ ventricular cardiomyocytes, Biophys. J. 96 (2009) 2532–2546, https://doi.org/10.1016/j.bpj.2008.12.3896.
[106] L. Sacconi, C. Ferrantini, J. Lotti, R. Coppini, P. Yan, L.M. Loew, C. Tesi, E. Cerbai, C. Poggesi, F.S. Pavone, Action potential propagation in transverse-axial tubular system is impaired in heart failure, Proc. Natl. Acad. Sci. U. S. A. 109 (2012) 5815–5819, https://doi.org/10.1073/pnas.1120188109.
[107] D.J. Crossman, A.A. Young, P.N. Ruygrok, G.P. Nason, D. Baddelely, C. Soeller, M.B. Cannell, T-tubule disease: relationship between t-tubule organization and regional contractile performance in human dilated cardiomyopathy, J. Mol. Cell. Cardiol. 84 (2015) 170–178, https://doi.org/10.1016/j.yjmcc.2015.04.022.
[108] L.S. Song, E.A. Sobie, S. McCulle, W.J. Lederer, C.W. Balke, H. Cheng, Orphaned ryanodine receptors in the failing heart, Proc. Natl. Acad. Sci. U. S. A. 103 (2006) 4305–4310, https://doi.org/10.1073/pnas.0509324103.
[109] P.M. Kekenes-Huskey, Y. Cheng, J.E. Hake, F.B. Sachse, J.H. Bridge, M.J. Holst, J.A. McCammon, A.D. McCulloch, A.P. Michailova, Modeling effects of L-type ca(2+) current and na(+)-ca(2+) exchanger on ca(2+) trigger flux in rabbit myocytes with realistic T-tubule geometries, Front. Physiol. 3 (2012) 351, , https://doi.org/10.3389/fphys.2012.00351.
[110] P. Neco, B. Rose, N. Huynh, R. Zhang, J.H. Bridge, K.D. Philipson, J.I. Goldhaber, Sodium-calcium exchange is essential for effective triggering of calcium release in mouse heart, Biophys. J. 99 (2010) 755–764, https://doi.org/10.1016/j.bpj.2010.04.071.
[111] M. Frisk, J.T. Koivumaki, P.A. Norseng, M.M. Maleckar, O.M. Sejersted, W.E. Louch, Variable t-tubule organization and Ca2+ homeostasis across the atria, Am. J. Physiol. Heart Circ. Physiol. 307 (2014) H609–H620, https://doi.org/10.1152/ajpheart.00295.2014.
[112] S. Brandenburg, J. Pawlowitz, F.E. Fakuade, D. Kownatzki-Danger, T. Kohl, G.Y. Mitronova, M. Scardigli, J. Neef, C. Schmidt, F. Wiedmann, F.S. Pavone, L. Sacconi, I. Kutschka, S. Sossalla, T. Moser, N. Voigt, S.E. Lehnart, Axial tubule junctions activate atrial ca(2+) release across species, Front. Physiol. 9 (2018) 1227, , https://doi.org/10.3389/fphys.2018.01227.
[113] S. Perni, V.R. Iyer, C. Franzini-Armstrong, Ultrastructure of cardiac muscle in reptiles and birds: optimizing and/or reducing the probability of transmission between calcium release units, J. Muscle Res. Cell Motil. 33 (2012) 145–152, https://doi.org/10.1007/s10974-012-9297-6.
[114] E.P. Odum, Variations in the heart rate of birds: a study in physiological ecology, Ecol. Monogr. 11 (1941) 299–326.

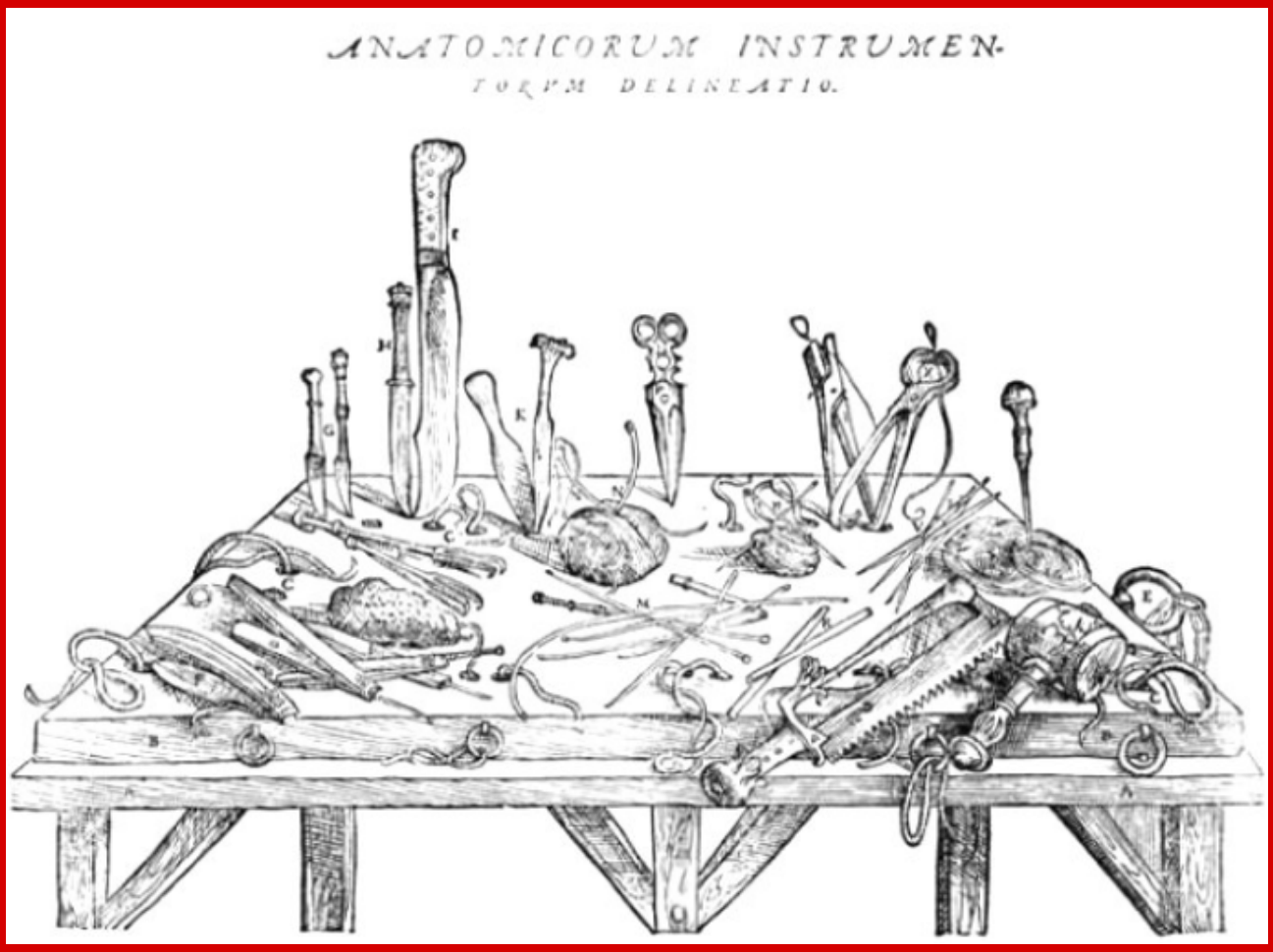


# AIMS & HYPOTHESES

# 2. AIMS AND HYPOTHESES

This thesis aims to contribute to the fundamental understanding of cardiac arrhythmias by the study of voltage-gated ion channels and electrical properties of cardiomyocytes. The specific aims and hypotheses are the following:

## 2.1 To characterize single-molecule organization of $Na_v1.5$ clusters at the lateral membrane and T-tubules in cardiomyocytes from mice with different genetic backgrounds

The aims of this project are twofold. Firstly, $Na_v1.5$ expression at the T-tubules has not been shown convincingly, and we aimed to answer this question by single-molecule localization microscopy. We hypothesize a small but significant proportion of $Na_v1.5$ is present in the T-tubules.

Secondly, dystrophin deficiency and C-terminal $Na_v1.5$ truncation (ΔSIV) have been shown to lead to an overall reduction in lateral membrane $Na_v1.5$ expression[87,116,126]. This project aimed to address the changes in $Na_v1.5$ clusters at the lateral membrane crest and groove and at the T-tubules of dystrophin-deficient and ΔSIV mice compared to wild type. We hypothesize that dystrophin deficiency and $Na_v1.5$ truncation affect $Na_v1.5$ cluster organization.

This project pertains to **Section 3.1**.

## 2.2 To characterize ion channel mRNA expression in isolated ventricular murine cardiomyocytes

This project aimed to precisely characterize mRNA expression by attaining high-throughput next-generation RNA-seq data from isolated murine cardiomyocytes. We especially aimed to determine the expression profile of voltage-gated ion channels since the cardiac field has disagreed on the fundamental question which ion channels are expressed in cardiomyocytes. Moreover, comparing RNA-seq data from wild-type mice with mice in which ion channel regulators are absent (SAP97 knock-down[118], CASK knock-down, and *mdx*[116,126]) will provide a wealth of information on potential arrhythmogenic mechanisms.

We hypothesized that non-muscle sodium channels isoforms ($Na_v1.1$-3, $Na_v1.7$-9) are largely absent in murine cardiomyocytes because data suggesting neuronal sodium channel expression in these cells are often of low quality (see **Section 1.7.3**).

This project pertains to **Section 3.2**.

## 2.3 To characterize electrical properties of T-tubules

This project is closely related to Publication 2 (**Section 1.7.3**) on electrical properties of T-tubules. Since the electrical behavior of T-tubules is not completely understood, we aimed to model the depolarization delay of deep T-tubular membrane segments, and the effect of a hypothetical large sodium current on extracellular potentials. We hypothesized (1) that depolarization delay would be very fast, within the sub-millisecond range, allowing timely excitation-contraction coupling; and (2) that a large sodium current would show a slight degree of self-attenuation due to the small extracellular space, reminiscent of the self-attenuation that has been proposed to occur at the intercalated disc[73,163].

This project pertains to **Section 3.3**.

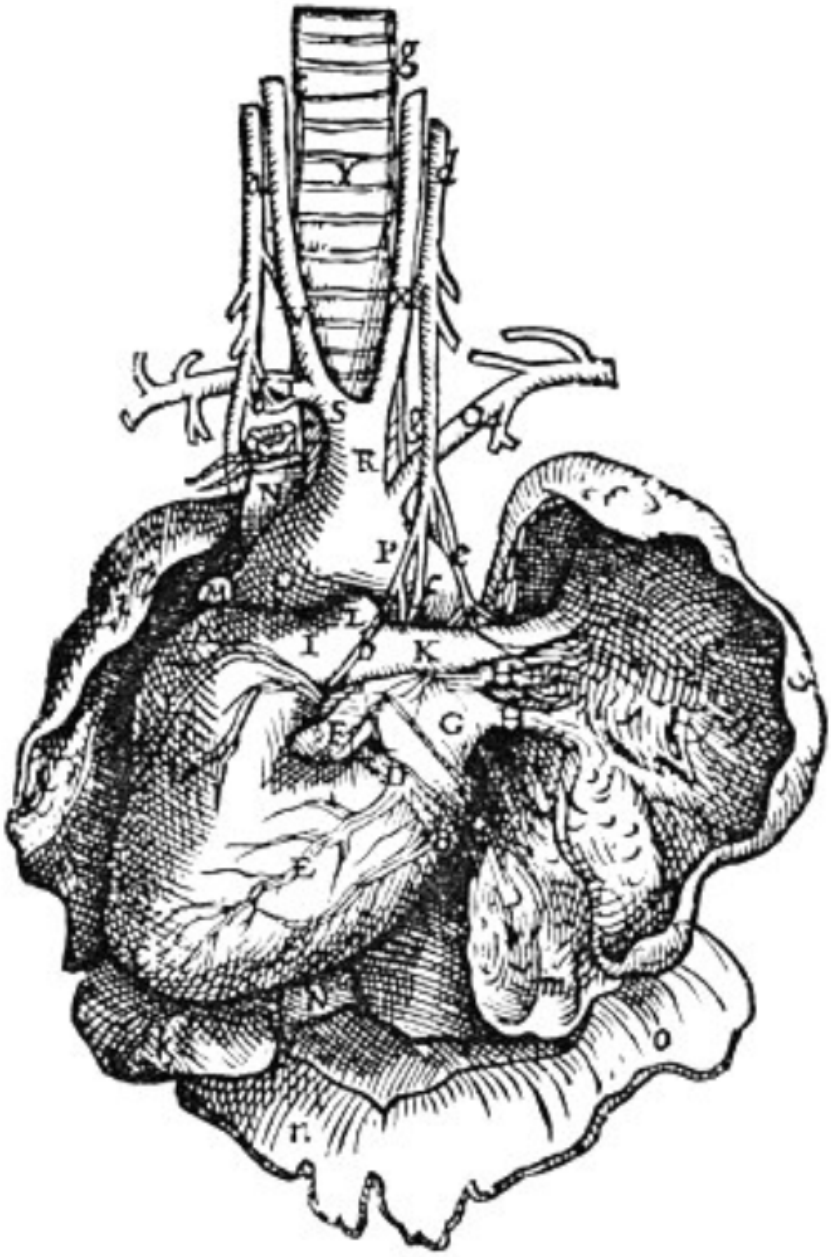

# RESULTS
# PUBLICATION #3

# 3. RESULTS

## 3.1 Publication 3: Single-molecule localization of $Na_v1.5$ reveals different modes of reorganization at cardiomyocyte lateral membrane and T-tubules

I performed single-molecule imaging experiments, simulations, and image analyses in the labs of Prof Mario Delmar and Eli Rothenberg, PhD, at New York University School of Medicine. In Bern, I performed confocal imaging. Jean-Sébastien Rougier, PD PhD, performed electrophysiological experiments. I wrote the manuscript and made the figures.

This manuscript is at the time of writing submitted, and can be found at bioRxiv[175].

# Single-molecule localization of $Na_v1.5$ reveals different modes of reorganization at cardiomyocyte membrane domains

Sarah H. Vermij[1], Jean-Sébastien Rougier[1], Esperanza Agulló-Pascual[2], Eli Rothenberg[3], Mario Delmar[4], and Hugues Abriel[1*]

**ABSTRACT**

Mutations in the gene encoding the sodium channel $Na_v1.5$ cause various cardiac arrhythmias. This variety may arise from different determinants of $Na_v1.5$ expression between cardiomyocyte domains. At the lateral membrane and T-tubules, $Na_v1.5$ localization and function remain insufficiently characterized. We used novel single-molecule localization microscopy (SMLM) and modeling to define nanoscale features of $Na_v1.5$ localization and distribution at the lateral membrane, groove, and T-tubules in wild-type, dystrophin-deficient (*mdx*) mice, and mice expressing C-terminally truncated $Na_v1.5$ (ΔSIV). We show that $Na_v1.5$ organizes as distinct clusters in the groove and T-tubules which density and distribution partially depend on SIV and dystrophin. We found that overall reduction in $Na_v1.5$ expression in *mdx* and ΔSIV cells results in a non-uniform re-distribution with $Na_v1.5$ being specifically reduced at the groove of ΔSIV and increased in T-tubules of *mdx* cardiomyocytes. $Na_v1.5$ mutations may therefore site-specifically affect $Na_v1.5$ localization and distribution depending on site-specific interacting proteins.

**AFFILIATIONS**

**1,** Institute of Biochemistry and Molecular Medicine, University of Bern, Bern, Switzerland

**2,** Microscopy Core, Icahn School of Medicine at Mount Sinai, New York City, USA

**3,** Department of Biochemistry and Pharmacology, New York University School of Medicine, New York City, USA

**4,** Department of Cardiology, New York University School of Medicine, New York City, NY, USA

*** CORRESPONDENCE**
hugues.abriel@ibmm.unibe.ch

This article was submitted to BioRxiv.org on 18 June 2019 (BIORXIV/2019/674275)

## INTRODUCTION

Proper function of the heart heavily relies on the cardiac sodium channel $Na_v1.5$. $Na_v1.5$ generates the rapid upstroke of the cardiac action potential; thus, it is pivotal for cardiac excitability, conduction, and muscle contraction[1,2]. Mutations in its gene *SCN5A* have been associated with many cardiac arrhythmias, such as long-QT syndrome type 3, Brugada syndrome, and sick-sinus syndrome[3]. Mutations can cause loss or gain of function of $Na_v1.5$, but the wide diversity in cardiac arrhythmias remains unexplained. The key may lie in the distribution of $Na_v1.5$ over specific membrane domains – "pools" – of the cardiomyocyte. $Na_v1.5$ pools are regulated by different proteins, so a given $Na_v1.5$ mutation may affect a specific pool if it disturbs the interaction with a specific protein. $Na_v1.5$ expression at the intercalated disc[4] and at the lateral membrane[5] is well established (**Figure 1**) while a third pool at the T-tubules is still disputed[6]. At the intercalated disc, where two cardiomyocytes are tightly coupled electrically and mechanically, $Na_v1.5$ interacts with ankyrin-G, connexin-43, and N-cadherin, among others[4]. At the lateral membrane, where costameres connect the cytoskeleton to the extracellular matrix (**Figure 1a,b**), $Na_v1.5$ interacts with the syntrophin/dystrophin complex, which is important for $Na_v1.5$ stability, and CASK, among others[7-9]. The lateral membrane is shaped distinctly with valley-like grooves and hilly crests[10], and $Na_v1.5$ is expressed at both locations in murine cardiomyocytes (**Figure 1a**)[11,12]. T-tubules are deep invaginations of the lateral membrane that originate in the groove. They mainly provide a large surface for calcium handling, and are crucial for the uniform contraction of ventricular cardiomyocytes[13]. Consequently, the majority of the voltage-gated calcium channels $Ca_v1.2$ is expressed at the T-tubules[14,15]. The claim of a T-tubular $Na_v1.5$ pool has so far only been supported by inconclusive results. By comparing whole-cell $I_{Na}$ densities in detubulated and control cardiomyocytes, T-tubular sodium channels were determined to conduct 30% of total sodium current[16]. This is probably a considerable overestimation as this method relies on the membrane capacitance as a measure for cell membrane area, but underestimates the surface area of cardiomyocytes by about 50%[17]. Therefore, the presence of a T-tubular $Na_v1.5$ pool remains undetermined.

Our current state of knowledge regarding the localization and distribution of $Na_v1.5$ at the lateral membrane and T-tubules is based on standard microscopy methods that are limited in resolution and sensitivity. At the T-tubules, previously published immunofluorescence data on $Na_v1.5$ show an intracellular striated pattern for $Na_v1.5$, but without a T-tubular marker, this pattern cannot be attributed to the T-tubules[18,19]. The respective confocal microscopy techniques moreover lacked resolution to resolve the narrow T-tubular structure[18,19]. At the lateral membrane, cell-attached and scanning ion conductance microscopy (SICM) recordings of the sodium current have provided information on the number of functional channels in a given area at the lateral membrane or specifically at the crest and groove[11,12,20,21], but they did not provide the molecular features needed to characterize $Na_v1.5$ organization at these domains. Moreover, previous studies did not correlate the signal of $Na_v1.5$ with other structural markers such as α-actinin for the groove and Bin1 for the T-tubules[18,19,22]. As such, current models of the roles of

1

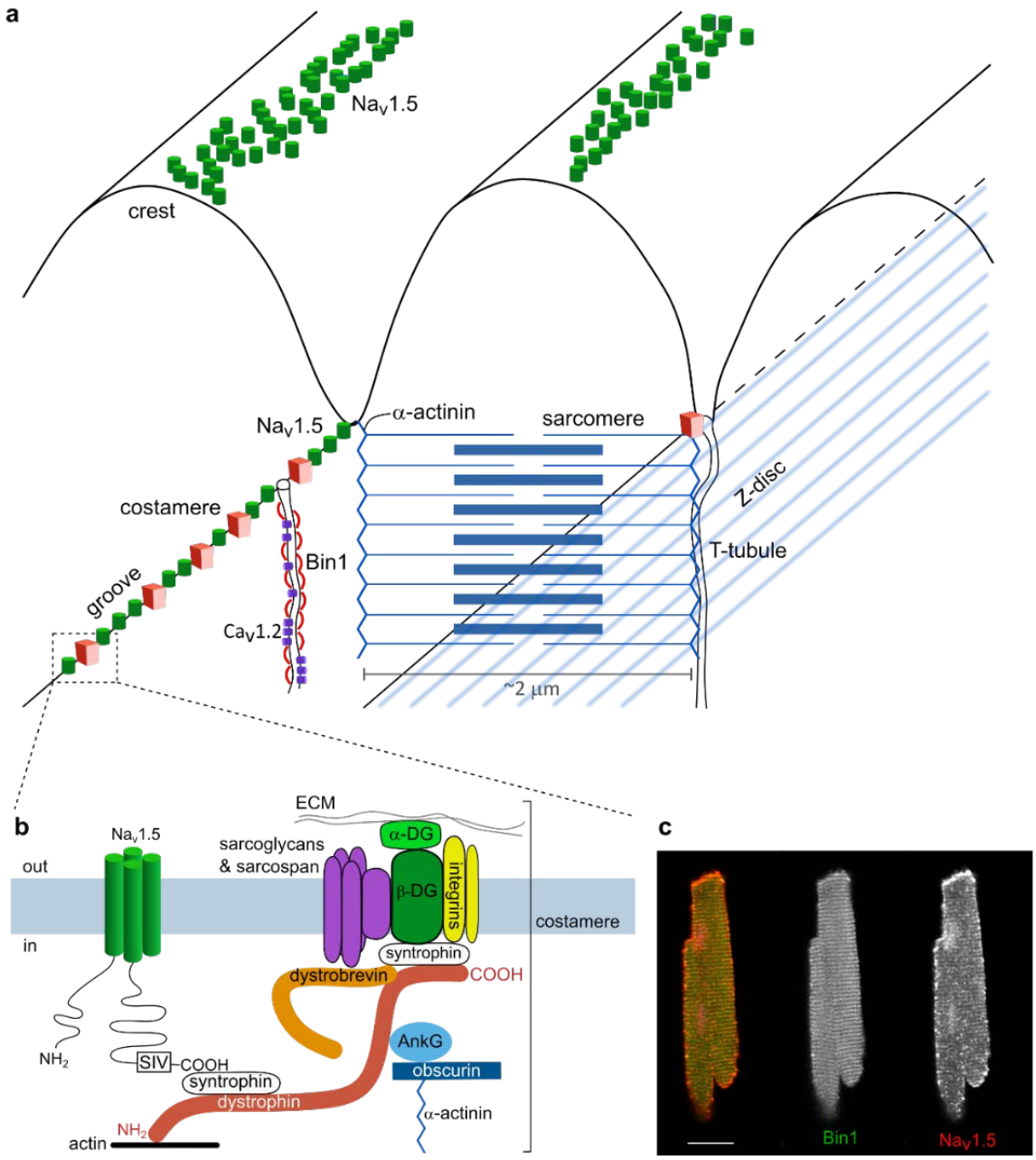


**Figure 1. Pools of $Na_v1.5$ in cardiomyocytes. a**, The lateral membrane has a characteristic profile: at the groove, the membrane is anchored to the sarcomeric Z-line (α-actinin; blue) through costameres (red boxes). T-tubules follow Z-lines and open to the groove. Their membrane is shaped by Bin1 (red curves) and contain, among many other proteins, voltage-gated calcium channels ($Ca_v1.2$; purple). The crest has a dome shape. $Na_v1.5$ is expressed at the crest and the groove. The amount of $Na_v1.5$ in this image serves illustrative purposes only and does not reflect experimental values. **b**, At the groove, $Na_v1.5$ (green; left) is associated with the costamere (right). The C-terminal SIV motif of $Na_v1.5$ binds syntrophin (white), which binds dystrophin (red). Dystrophin also binds syntrophin associated with the costamere, which contains multiple transmembrane proteins, including integrins (yellow), sarcoglycans (purple), and β-dystroglycan (green). β-dystroglycan connects the sarcolemma with the extracellular matrix (ECM) *via* α-dystroglycan. Dystrophin also links the costamere to the cytoskeleton through its association with actin at its N-terminus and with α-actinin via ankyrin-G and obscurin. **c**, Confocal image of murine ventricular cardiomyocyte stained for $Na_v1.5$ (red) and T-tubular marker Bin1 (green), showing $Na_v1.5$ expression at the intercalated disc, lateral membrane, and an intracellular punctate pattern coinciding with Bin1 signal. Scale bar 20 µm.

$Na_v1.5$ at the lateral membrane and T-tubules do not represent the true molecular nature of Nav1.5 expression and organization at these domains. To address these issues, we utilize multi-color single-molecule localization microscopy (SMLM)[23], a super-resolution imaging method, providing the features of $Na_v1.5$ organization and related markers with nanoscale resolution. Using this approach, we addressed $Na_v1.5$ expression and cluster organization at the T-tubules using the T-tubular marker Bin1[24], and $Na_v1.5$ affinity for the groove using the groove marker α-actinin in isolated cardiomyocytes. We also assessed T-tubular $I_{Na}$ by comparing whole-cell $I_{Na,}$, rather than cluster densities, from control and detubulated cardiomyocytes. We then addressed the consequences of dystrophin deficiency (*mdx*) and $Na_v1.5$ C-terminal truncation (ΔSIV) on $Na_v1.5$ expression and organization at the lateral membrane overall, at the groove specifically, and at the T-tubules. ΔSIV resembles the p.V2016M mutation found in a Brugada syndrome patient, replacing the C-terminal valine with a methionine, which results in an apparent reduced expression of $Na_v1.5$[5]. ΔSIV knock-in mice display a loss of sodium current and $Na_v1.5$ expression specifically at the lateral membrane[5], and interaction of $Na_v1.5$-ΔSIV with the syntrophin/dystrophin complex is impaired[5]. In accordance, dystrophin-deficient *mdx* mice display a strong reduction of sodium current and $Na_v1.5$ expression, both overall and specifically at the lateral membrane[7,8].

By characterizing $Na_v1.5$ organization and expression at different pools at a nanoscale and addressing their pool-specific determinants, we come closer to understanding the pathophysiological variety in patients carrying *SCN5A* mutations, as mutations may affect $Na_v1.5$ pools and shape the pathophysiological landscape differently. The two genetic mouse models investigated in this study give insight into pool-specific effects of a $Na_v1.5$ mutation (ΔSIV) and of disturbing $Na_v1.5$ regulation (*mdx*). It appears that (1) $Na_v1.5$ is expressed in T-tubules; (2) dystrophin deficiency increases T-tubular $Na_v1.5$ expression; and (3) $Na_v1.5$ expression is reduced at the lateral membrane of *mdx* and ΔSIV mice overall whereas groove expression is specifically reduced in ΔSIV cells; (4) $Na_v1.5$ cluster organization changes at the lateral membrane of *mdx* cells and in the T-tubules of *mdx* and ΔSIV cells compared to wild type.

## RESULTS

### $NA_v1.5$ OCCURS AT DISTINCT POOLS IN MURINE VENTRICULAR CARDIOMYOCYTES

The main focus of this work is the characterization of $Na_v1.5$ localization and cluster organization in different cardiomyocyte domains with novel quantitative single-molecule localization microscopy (SMLM) and modeling. Technical validation of SMLM is shown in **Supplementary Figure 1**. Firstly, however, we gained a general overview over the $Na_v1.5$ pools with confocal microscopy. To this end, we immunostained isolated murine ventricular cardiomyocytes for $Na_v1.5$ and the T-tubular marker Bin1. $Na_v1.5$ is clearly expressed at the lateral membrane and intercalated disc (**Figure 1c**). Some $Na_v1.5$ seems to co-localize with Bin1, the latter showing a striated pattern that indicates the T-tubular membrane. The limited resolution and sensitivity of the

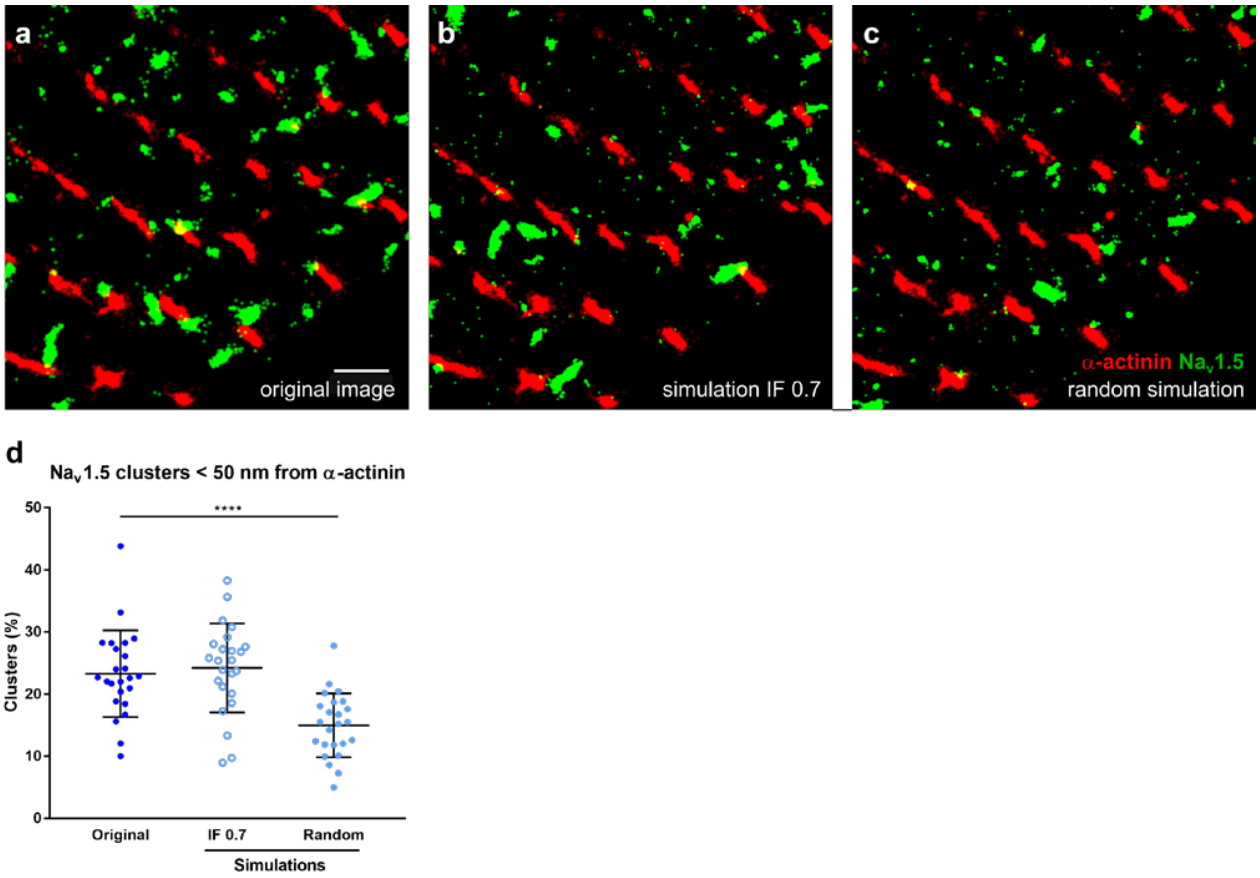


**Figure 2. $Na_v1.5$ has affinity for the groove at the lateral membrane of a cardiomyocyte. a**, Super-resolution image of the lateral membrane of murine ventricular myocyte stained for $Na_v1.5$ (green) and α-actinin (red). $Na_v1.5$ occurs close to α-actinin, indicating the groove; and in between α-actinin lines, indicating the crest. Scale bar 1 µm. **b** and **c** display simulations of the original SMLM image (**a**), in which $Na_v1.5$ clusters were randomly distributed (**b**) or had a high affinity for α-actinin (interaction factor [IF] 0.7 [**c**]). Note that differences in affinity are hard to spot by eye, especially in a small area of a cell. **d**, In original SMLM images of wild-type cells ($N$ = 3, $n$ = 24), the proportion of $Na_v1.5$ within 50 nm of α-actinin is ~30% higher than in simulations in which $Na_v1.5$ clusters of each image are distributed randomly, and similar to images in which a high affinity of $Na_v1.5$ for α-actinin was simulated (IF 0.7). ****, $p < 0.0001$, Mann-Whitney test.

confocal microscope however prevents us from establishing a detailed quantitative analysis of $Na_v1.5$ in the T-tubules (**Figure 1c**).

To determine the molecular characteristics of $Na_v1.5$ expression at the lateral membrane by SMLM, we imaged the lateral membrane of wild-type cardiomyocytes stained for $Na_v1.5$ and α-actinin, which coincides with the groove ($N$ = 3, $n$ = 24; **Figure 2a**). Indeed, $Na_v1.5$ occurred both in close proximity to α-actinin and in between α-actinin clusters, indicating localization at the groove and the crest, respectively (**Figure 1a**, **Figure 2a**). To quantify whether the $Na_v1.5$ clusters have an affinity for the groove, we used a novel analysis approach[25] based on Monte-Carlo simulations for each SMLM image ($N$ = 3, $n$ = 24) in which $Na_v1.5$ clusters were redistributed over the image either randomly or with a high affinity for α-actinin (**Figure 2b,c**). The random simulations were performed by selecting the $Na_v1.5$ clusters and stochastically redistributing them within the boundaries of the

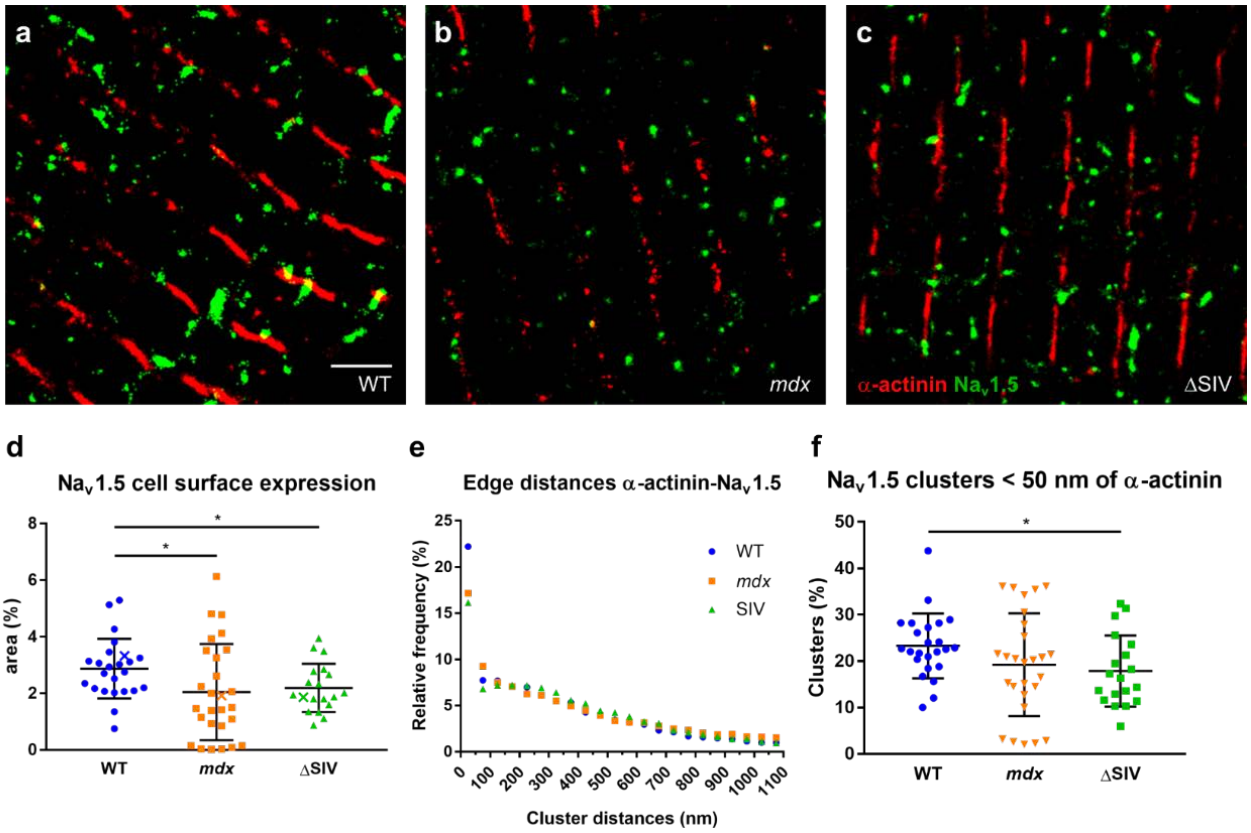


**Figure 3. ΔSIV and *mdx* cardiomyocytes show loss of $Na_v1.5$ expression at the lateral membrane. a-c**, Detail of SMLM images of the lateral membrane from wild-type (WT; **a**), *mdx* (**b**), and ΔSIV (**c**) cells. Scale bar 1.5 µm. **d**, Total $Na_v1.5$ expression at the lateral membrane is reduced by ~30% in *mdx* and ΔSIV compared to wild type. Data points represented by a cross (*X*) correspond to examples from panels **a-c**. **e**, Frequency distribution plot of edge distances from any α-actinin cluster to the closest $Na_v1.5$ cluster, bin size 50 nm. In *mdx* and ΔSIV, a smaller proportion of $Na_v1.5$ resides within 50 nm to α-actinin compared to wild type. Frequency distributions for cluster distances larger than 50 nm are similar between the genotypes. **f**, Groove expression of $Na_v1.5$, defined as $Na_v1.5$ clusters within 50 nm of Bin1, is reduced by ~30% in ΔSIV cardiomyocytes compared to wild type. Note that *mdx* cells display high variability in $Na_v1.5$ cluster expression at the lateral membrane (**d**) and at the groove (**f**). Wild type $N = 3$, $n = 24$; *mdx* $N = 3$, $n = 27$; ΔSIV $N = 3$, $n = 19$. *, $p = 0.024$ (wt vs. *mdx* [**d**]); $p = 0.016$ (wt vs. ΔSIV [**d**]); $p = 0.019$ (wt vs. ΔSIV [**f**]), Mann-Whitney test.

user-defined region of interest (ROI). For high-affinity simulations, an interaction factor of 0.7 was assumed, given that an interaction factor of 0.0 represents random overlap between the two colors, an interaction factor of 1.0 perfect overlap, and an interaction factor equal to or more than 0.5 indicates that one color has significant affinity for the other color[25]. To generate high-affinity simulations with an interaction factor of 0.7, each $Na_v1.5$ cluster was first placed randomly within the region of interest, then the program determined whether one or more pixels of the cluster overlapped with an α-actinin cluster. If this overlap was detected, the cluster was kept in place; if not, the program generated a random number between 0 and 1. If that number was greater than 0.7, the cluster was kept in its position; if not, this process was repeated. Overall, these high-affinity simulations generated an image in which $Na_v1.5$ clusters overlapped with α-actinin clusters to more than a random degree.

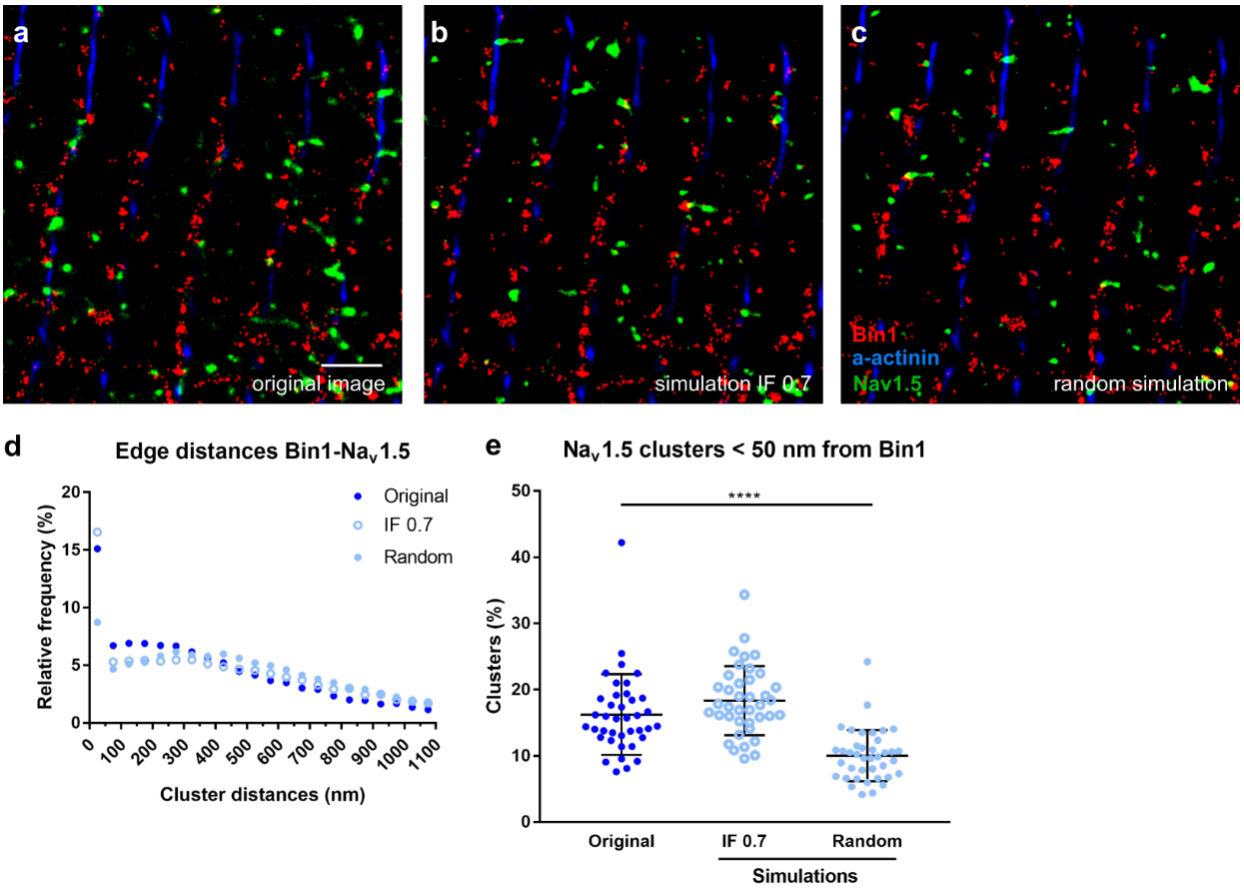


**Figure 4. $Na_v1.5$ is expressed in the T-tubules. a**, Detail of an intracellular recording from a wild-type cardiomyocyte stained for α-actinin (blue), Bin1 (red), and $Na_v1.5$ (green). All $Na_v1.5$ clusters are redistributed over the image either randomly (**b**) or with a high affinity for Bin1 (interaction factor [IF] 0.7 [**c**]). Scale bar 1.5 µm. **d**, For each Bin1 cluster, the closest $Na_v1.5$ cluster is within 50 nm in ~15% of cases, which is significantly more than the ~8% from random simulations and close to ~17% of the high-affinity simulations (IF 0.7) ($N = 3$, $n = 39$). The frequency distributions of $Na_v1.5$ for distances to α-actinin of more than 50 nm does not show any apparent difference between the genotypes. **e**, In experimental SMLM images, a higher proportion (~40%) of $Na_v1.5$ are within 50 nm from the nearest Bin1 cluster than in random simulations, but not as much as in simulations with a high-affinity simulations (IF 0.7). Values for each individual cell/simulation are plotted. ****, $p < 0.0001$, unpaired t-test.

Then, for the original and simulated images, the distance from the edge of each α-actinin cluster to the edge of the closest $Na_v1.5$ cluster was determined. $Na_v1.5$ was considered to be expressed in the groove if it was located within 50 nm from an α-actinin cluster. We found that 25% of $Na_v1.5$ clusters were in the groove in experimental images. This value was close to that of the simulations with high affinity for α-actinin (**Figure 2d**), whereas in random simulations, only 15% of $Na_v1.5$ clusters were within 50 nm from α-actinin. These results strongly suggest that $Na_v1.5$ has an affinity for the groove.

## $NA_V1.5$ EXPRESSION AT THE LATERAL MEMBRANE AND THE GROOVE DEPENDS ON DYSTROPHIN AND THE ΔSIV MOTIF, WHEREAS CLUSTER ORGANIZATION DEPENDS ON DYSTROPHIN ONLY

Our SMLM-derived metrics indicate that $Na_v1.5$ cluster density at the lateral membrane is reduced by about 30% in *mdx* and ΔSIV cardiomyocytes compared to wild-type cells (**Figure 3a-d**; wild type $N = 3$, $n = 24$; *mdx* $N = 3$, $n = 27$; ΔSIV $N = 3$, $n = 19$). Cell size and average $Na_v1.5$ cluster size did not change between the genotypes, although *mdx* cells showed a high variability in $Na_v1.5$ cluster size (**Supplementary Figure 2a**). Interestingly, the solidity and circularity of $Na_v1.5$ clusters was markedly increased in *mdx* cells compared to wild type (**Supplementary Figure 2a**). Given that solidity is defined as the ratio between the particle area and the convex hull area of the particle, and circularity as the roundness of a particle (1.0 indicating a perfect circle), the increased solidity and circularity together indicate that $Na_v1.5$ clusters are of geometrically less complex shapes. The overall reduction of $Na_v1.5$ expression at the lateral membrane in ΔSIV and *mdx* cells additionally confirms the specificity of the anti-$Na_v1.5$ antibody since these findings accord with previously reported results[5,7]. In addition, they show that the reduction in whole-cell $I_{Na}$ in *mdx* cells is at least partly due to reduced $Na_v1.5$ expression at the lateral membrane[8].

To assess the effects of $Na_v1.5$ truncation and dystrophin deficiency on $Na_v1.5$ expression at the crest and the groove, we determined the distances from each α-actinin cluster to the closest $Na_v1.5$ cluster in *mdx* and ΔSIV lateral-membrane images, and compared them to wild-type values. The frequency histogram (**Figure 3e**) shows that the proportion of $Na_v1.5$ clusters within 50 nm of α-actinin is reduced by ~25% in *mdx* and ΔSIV compared to wild-type cells. When the proportion of $Na_v1.5$ within 50 nm of α-actinin is plotted for each individual cell (**Figure 3f**), only ΔSIV cardiomyocytes show a significant ~20% reduction compared to wild type. Although mean $Na_v1.5$ expression in *mdx* cells is reduced by about 17% compared to wild type, the data show high variability (**Figure 3f**), which correlates with the high variability in $Na_v1.5$ expression at the lateral membrane of *mdx* cells (**Figure 3d**). The affinity of $Na_v1.5$ for the groove is however similar in wild-type, *mdx*, and ΔSIV cells when comparing the proportion of $Na_v1.5$ clusters within 50 nm of α-actinin from experimental images, and random and high-affinity simulations for each genotype (**Supplementary Figure 3a**).

Taken together, these results establish that (1) $Na_v1.5$ expression at the groove of the lateral membrane partially depends on the ΔSIV motif and dystrophin expression; (2) in dystrophin-deficient cells, $Na_v1.5$ clusters at the lateral membrane are organized into simpler shapes compared to wild-type cells; and (3) dystrophin deficiency induces high variability in $Na_v1.5$ expression and $Na_v1.5$ cluster size.

## $NA_V1.5$ IS EXPRESSED IN THE T-TUBULAR MEMBRANE

$Na_v1.5$ expression in the T-tubules was assessed by co-staining cardiomyocytes for $Na_v1.5$ and the T-tubular marker Bin1, and imaging an intracellular plane of each cell in highly inclined and laminated optical (HILO)

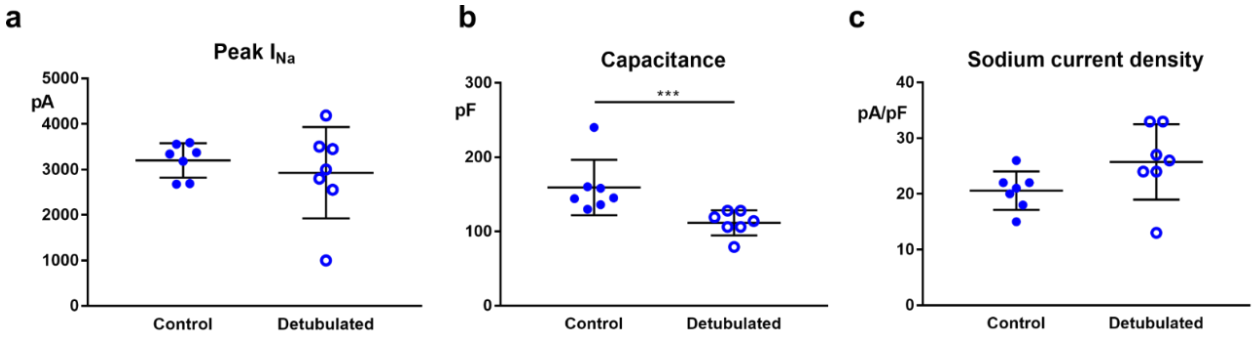


**Figure 5. Whole-cell sodium current recordings in detubulated and normal cardiomyocytes.** Compared to control cells, maximum sodium current (**a**) didn't change, capacitance (**b**) was reduced by about 30%, and sodium current density (**c**) increased by about 25% (non-significant) in detubulated cells. *N* = 5, *n* = 7 for both conditions. ***, *p* = 0.006, Mann-Whitney test.

mode with the TIRF (total internal reflection fluorescence) objective. Bin1 was chosen as a T-tubular marker since it binds and shapes the T-tubular membrane and assists in the trafficking and clustering of the voltage-gated calcium channel $Ca_v1.2$[24,26]. The Bin1 antibody was first validated by confirming that Bin1 stainings are in close proximity to α-actinin, given that T-tubules run in close proximity to the sarcomeric Z-disc (*N* = 3, *n* = 59) (**Supplemental figure 4**)[13]. Then, we assessed whether $Na_v1.5$ and Bin1 associated randomly or not by performing simulations for each SMLM image (*N* = 3, *n* = 39), where $Na_v1.5$ clusters were redistributed either randomly or with high affinity for Bin1 (**Figure 4a-c**). $Na_v1.5$ clusters at the lateral membrane and intercalated disc were excluded. Then, the distance from each Bin1 cluster to the closest $Na_v1.5$ cluster was determined. The frequency histogram shows that about 16-17% of $Na_v1.5$ clusters is within 50 nm of Bin1 in both original images and high-affinity simulations, whereas in random simulations this value was only ~8% (**Figure 4d**). This was confirmed when plotting the proportion of $Na_v1.5$ clusters within 50 nm of Bin1 for each individual image (**Figure 4e**). Together, these findings indicate that a considerable subset of intracellular $Na_v1.5$ is expressed in the T-tubular membrane.

## T-TUBULAR SODIUM CURRENT CANNOT BE ASSESSED BY WHOLE-CELL RECORDINGS

Having shown that $Na_v1.5$ is expressed at the T-tubules (**Figure 4**), we investigated whether we could record a T-tubular sodium current. To this end, we compared whole-cell $I_{Na}$ recordings from normal (*N* = 5, *n* = 7) and detubulated (N = 5, *n* = 7) ventricular cardiomyocytes. Firstly, we concluded that detubulation was successful as the capacitance of detubulated cells was 30% lower than of control cells (**Figure 5b**). Whole-cell $I_{Na}$ did not decrease after detubulation (**Figure 5a**), which indicates that the vast majority of sodium current is conducted by sodium channels at the intercalated disc and lateral membrane. Comparing the current density shows a 25% yet non-significant increase in $I_{Na}$ density after detubulation (**Figure 5c**), further confirming that the majority of sodium channels is outside the T-tubular domain. As discussed in the introduction, current densities of

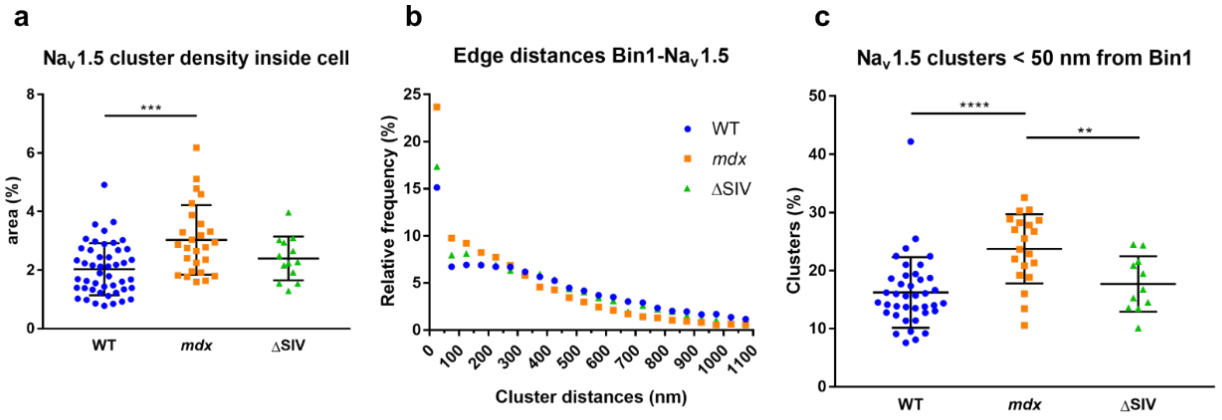


**Figure 6. $Na_v1.5$ expression is increased in T-tubules of *mdx* mice. a**, $Na_v1.5$ cluster density in intracellular membrane compartments and T-tubules is ~30% higher in *mdx* cardiomyocytes than in wild-type cardiomyocytes, but no change was observed in ΔSIV compared to wild-type cells. **b**, For each Bin1 cluster, the distance to the closest $Na_v1.5$ cluster is measured. Cluster distances are plotted in a frequency histogram with bins of 50 nm. The given histogram indicates that $Na_v1.5$ preferentially locates within 50 nm to Bin1, in ΔSIV and *mdx* more so than in wild-type cells. **c**, In *mdx* cells, a higher proportion of $Na_v1.5$ clusters is within 50 nm from Bin1 than in wild-type cells. Together with the increase in overall intracellular $Na_v1.5$ expression in *mdx*, this indicates that T-tubules in *mdx* cells show a higher $Na_v1.5$ expression. ΔSIV cells show a similar T-tubular $Na_v1.5$ expression as WT cells. **a**, Wild type $N = 3$, n = 47; *mdx* $N = 3$, $n = 26$; ΔSIV $N = 3$, $n = 13$. **b,c** Wild type $N = 3$, n = 39; *mdx* $N = 3$, $n = 20$; ΔSIV $N = 3$, $n = 11$. **, $p = 0.0095$; ***, $p = 0.0002$; ****, $p < 0.0001$, Mann Whitney test.

detubulated and control cardiomyocytes cannot be compared directly as capacitance measurements in control cardiomyocytes result in a considerable underestimation of cell membrane area. Thus, our data show that the T-tubular $I_{Na}$ is below the detection limit of the whole-cell patch-clamp technique.

## $Na_v1.5$ EXPRESSION IS INCREASED IN T-TUBULES FROM DYSTROPHIN-DEFICIENT CARDIOMYOCYTES, AND CLUSTER ORGANIZATION DEPENDS ON THE SIV MOTIF AND DYSTROPHIN

We next investigated whether dystrophin deficiency (*mdx*) and deletion of the SIV motif of $Na_v1.5$ affected $Na_v1.5$ expression in the T-tubules. Firstly, we determined that overall $Na_v1.5$ cluster density in intracellular planes was increased in *mdx* compared to wild-type cells, whereas no difference was observed between ΔSIV and wild-type cells (**Figure 6a**; wild type $N = 3$, $n = 47$; *mdx* $N = 3$, $n = 26$; ΔSIV $N = 3$, $n = 13$). We also noted an increase in cluster solidity in *mdx* and an increase in cluster circularity in *mdx* and ΔSIV compared to wild-type cells, while cell size and average $Na_v1.5$ cluster size did not differ between the three genotypes. Similar to what we observed at the lateral membrane, this indicates that intracellular $Na_v1.5$ clusters have geometrically simpler shapes in *mdx* and ΔSIV cells.

The frequency histogram plotting distances between Bin1 and $Na_v1.5$ shows that the proportion of $Na_v1.5$ within 50 nm to Bin1 was ~30% higher in *mdx* and ~4% higher in ΔSIV compared to wild type (**Figure 6b**; wild type $N = 3$, n = 39; *mdx* $N = 3$, $n = 20$; ΔSIV $N = 3$, $n = 11$). Plotting these values from individual cells confirmed this increase of T-tubular $Na_v1.5$ in *mdx* cells, but no difference between ΔSIV and wild type cells was observed

(**Figure 6c**). When comparing T-tubular $Na_v1.5$ expression from original images and random and high-affinity simulations, $Na_v1.5$ displays an affinity for Bin1 in all three genotypes; but in *mdx* cells, $Na_v1.5$ has an even higher affinity for Bin1 than in the high-affinity simulations (**Supplementary figure 3b**).

Taken together, these data indicate that dystrophin deficiency induces a higher $Na_v1.5$ expression associated with intracellular membrane compartments and T-tubules compared to wild type, whereas this effect was not observed in ΔSIV cells. Intracellular $Na_v1.5$ cluster shapes were also markedly simpler in ΔSIV and *mdx* compared to wild-type cardiomyocytes.

## DISCUSSION

This work aimed to surpass the previously published limited-resolution characterization of $Na_v1.5$ expression and cluster organization at the lateral membrane and T-tubules of cardiomyocytes. To this end, we applied novel quantitative single-molecule localization microscopy (SMLM) and modeling techniques to investigate Nav1.5 organization at the crest, groove, and T-tubules in cardiomyocytes from wild-type mice, dystrophin-deficient (*mdx*) mice, and mice expressing C-terminally truncated $Na_v1.5$ (ΔSIV). We showed that (1) $Na_v1.5$ expression in the groove of the lateral membrane partly depends on dystrophin and the SIV motif of $Na_v1.5$; (2) dystrophin is involved in $Na_v1.5$ cluster organization at the lateral membrane; (3) $Na_v1.5$ is expressed in the T-tubules, although we could not assess T-tubular sodium current with our electrophysiological approach; (4) T-tubular $Na_v1.5$ expression is increased in dystrophin-deficient but not in ΔSIV cardiomyocytes; and (5) intracellular $Na_v1.5$ cluster organization depends on dystrophin and the SIV motif. These findings are schematically summarized in **Figure 7**.

We convincingly showed that $Na_v1.5$ is expressed in the T-tubules by co-staining $Na_v1.5$ with the T-tubular marker Bin1 in SMLM recordings, and assessing the robustness of this association by novel *in silico* methods[25,27]. Comparing original images to simulations of these images in which $Na_v1.5$ clusters were redistributed either randomly or with high affinity for Bin1, we observed that the T-tubular population of $Na_v1.5$ in original images is twice as high as in random populations and comparable to that from high-affinity simulations (**Figure 4e**). The function of $Na_v1.5$ at the T-tubules remains elusive, although $Na_v1.5$ in the T-tubules will theoretically increase conduction velocity[28]. Since some Bin1 and $Na_v1.5$ clusters overlapped (**Figure 4a**), we may hypothesize that Bin1 could be involved in the regulation of $Na_v1.5$ in the T-tubules as Bin1 also regulates the trafficking of voltage-gated calcium channel $Ca_v1.2$[29].

We showed that the presence of a T-tubular $I_{Na}$ could not be deducted from whole-cell electrophysiological methods as whole-cell currents between detubulated and control cardiomyocytes were similar (**Figure 5a**). The

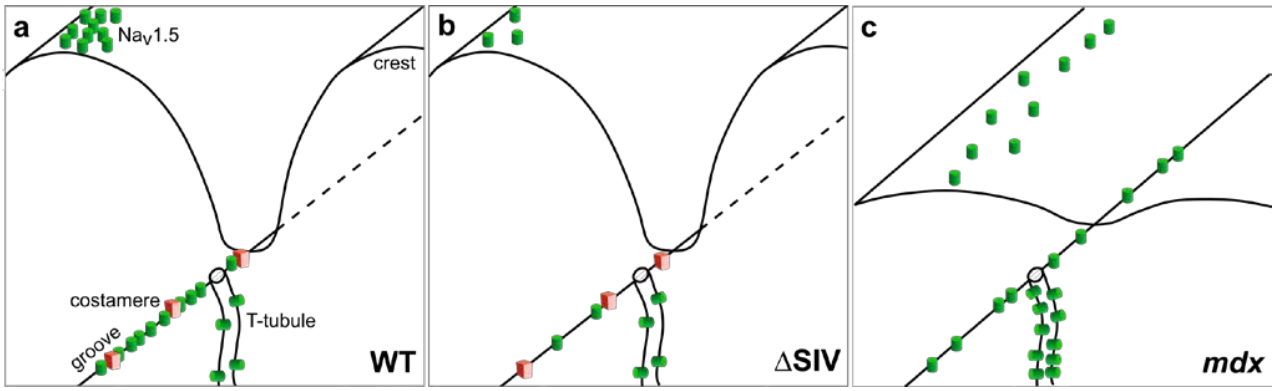


**Figure 7. Model depicting changes at the lateral membrane and T-tubules of ΔSIV and *mdx* cardiomyocytes.** Compared to the wild-type condition (**a**), ΔSIV cells (**b**) show less $Na_v1.5$ at the lateral membrane overall and specifically in the groove, whereas the lateral membrane structure remain intact. In *mdx* cells (**c**), the lateral membrane is flatter than in wild-type and ΔSIV cells, and $Na_v1.5$ expression at the lateral membrane is reduced overall; yet the expression at groove of *mdx* cells is not as affected as that of ΔSIV cells. Costameres are severely compromised in *mdx* cells. In the T-tubules, $Na_v1.5$ expression is similar in wild-type (**a**) and ΔSIV cells (**b**), and increased in *mdx* cardiomyocytes (**c**).

T-tubular $I_{Na}$ may not surpass the noise of whole-cell recordings, or the T-tubular membrane may not be properly voltage clamped in our whole-cell approach, thus a proportion of T-tubular sodium channels may not be activated (space clamp issue). In the past, the T-tubular $I_{Na}$ was suggested to be ~30% of total $I_{Na}$ by comparing current densities from detubulated and control cells[16]. Measuring the capacitance in control cells underestimates cell membrane area, however, which disqualifies the direct comparison of current densities non-detubulated to detubulated cells[17]. Other electrophysiological methods have not been able to record T-tubular currents either: cell-attached[30] and SICM data[11,31] only show currents from a few voltage-gated calcium channels whereas a much stronger calcium current would be expected from the T-tubules. To assess the T-tubular $I_{Na}$, more specific methods need to be developed.

When dystrophin is absent, less $Na_v1.5$ is expressed at the lateral membrane (**Figure 3a**), but more $Na_v1.5$ is expressed in the T-tubules compared to wild-type cells (**Figure 6c**). The reduction $Na_v1.5$ at the lateral membrane of *mdx* cells may be explained by the loss of costamere integrity (**Figure 7**)[32]. We may also hypothesize that dystrophin deficiency causes a partial rerouting of $Na_v1.5$ trafficking to the T-tubules instead of to the lateral membrane by an unknown mechanism. The short dystrophin product Dp71 may be involved since it is present only at the T-tubules[33], and binds ion channels and the cytoskeleton[34]. In light of the overall reduction of Nav1.5 protein expression and $I_{Na}$ in *mdx* hearts[8], the relative increase of T-tubular $Na_v1.5$ expression may make matters worse: due to the restricted space in the T-tubular lumen, the T-tubular sodium current may partially self-attenuate[6,35]. A *de facto* translocation of $Na_v1.5$ from the lateral membrane to the T-tubules of *mdx* cells may quench whole-cell sodium current and contribute to the reduction in ventricular conduction velocity observed in *mdx* mice[6,8]. Whether this effect indeed takes place *in vivo* requires further research.

Interestingly, $Na_v1.5$ cluster shapes in the groove and the intracellular compartment are simpler in *mdx* than in wild-type cells, illustrated by the increased solidity and circularity (**Supplementary Figure 2**). This indicates that dystrophin is involved in scaffolding and shaping of the $Na_v1.5$ clusters, which may be related to the large size (427 kD) of dystrophin, and to the link to the actin cytoskeleton that dystrophin provides[36]. On the other hand, $Na_v1.5$ clusters in ΔSIV cells show an increase in solidity only in intracellular planes (**Supplementary Figure 2b**). This suggests that the interaction of $Na_v1.5$ with the syntrophin-dystrophin plays a role in cluster organization in the intracellular compartment/T-tubules, while at the lateral membrane, the secondary N-terminal syntrophin-binding site of $Na_v1.5$ may support interaction with dystrophin and wild-type-like $Na_v1.5$ cluster organization[37].

The residual $Na_v1.5$ expression at the lateral membrane of *mdx* mice may be explained by the dystrophin homologue utrophin[38]. Utrophin is expressed during the fetal phase and re-expressed in adult tissue when dystrophin is absent in mice, but not in humans[38,39]. Since we found that $Na_v1.5$ cluster density and size at the lateral membrane and at the groove is highly variable in *mdx* cells (**Figure 3a,c, Supplementary Figure 2a**), ventricular cardiomyocytes may display a high variability in compensatory utrophin and Dp71 expression. Utrophin however does not rescue a wild-type-like phenotype: the costameres and sarcolemma of utrophin-expressing *mdx* mice are still weak[40], and the crest-groove profile at the lateral membrane of *mdx* cardiomyocytes is flattened compared to wild type (**Figure 7c**)[41]. The effects of dystrophin deficiency when the aforementioned compensatory mechanisms are not available needs to be assessed in heart samples from Duchenne patients and from dystrophin/utrophin/Dp71 triple knock-out mice.

Like *mdx* mice, ΔSIV mice express less $Na_v1.5$ at the lateral membrane, and the groove pool is specifically affected (**Figure 3d,f**). The ΔSIV truncation reduces the interaction of $Na_v1.5$ with the syntrophin-dystrophin complex[5]. Since ΔSIV mice still express dystrophin, costameres presumably remain intact. Of note, the syntrophin-dystrophin complex may also interact with the N-terminus of $Na_v1.5$[37], possibly explaining the reduction, rather than the abolition, of $Na_v1.5$ localization to the groove and the lateral membrane. Contrary to *mdx* mice, we did not observe an increase of $Na_v1.5$ at the T-tubules in ΔSIV mice, which may be explained by their intact costameres.

A groove-specific reduction of $Na_v1.5$, as shown for ΔSIV and a subset of *mdx* cardiomyocytes, and an increase in T-tubular $Na_v1.5$, as shown for *mdx* cells, may affect conduction and excitability in different ways. However, late openings between the crest and the groove as well as biophysical properties did not differ in murine cardiomyocytes[11]. Future studies should address specific differences in function and regulation of $Na_v1.5$ in the crest, groove, and T-tubules.

Intriguingly, while our data revealed that $Na_v1.5$ is reduced at the groove of *mdx* and ΔSIV mice, Rivaud *et al.* have recently shown in a murine heart failure model (transient aortic constriction) that sodium current is

specifically reduced at the crest, not at the groove, compared to sham-operated animals[11]. Rivaud *et al.* showed that $Na_v1.5$ cluster size, not cluster density, was markedly reduced at the lateral membrane in the heart failure model, whereas our data show that cluster density, not cluster size, was reduced in *mdx* and ΔSIV cells (**Supplementary Figure 2a**). Expression and organization of $Na_v1.5$ at the crest and the groove was however not investigated in this heart failure model. Together, these data suggest that cardiomyocytes respond differently to dystrophin deficiency, $Na_v1.5$ truncation (ΔSIV), and transient aortic constriction[11]. One obvious difference is the hypertrophy observed in the heart failure model but not in *mdx* or ΔSIV mice. These different pathways remain to be elucidated in detail.

The phenotype of Brugada syndrome patients carrying the mutation p.V2016M, which changes the C-terminal motif SIV into SIM, may be partly explained by a reduction in $Na_v1.5$ cluster density in the groove of the lateral membrane and a reduction of dystrophin-$Na_v1.5$ interaction[8]. Indeed, in ΔSIV cardiomyocytes, transversal conduction velocity, total sodium current, and sodium current at the lateral membrane are decreased[5], which may contribute to the Brugada syndrome phenotype. However, the specific effect of groove-specific $Na_v1.5$ reduction remains to be determined.

A limitation of our study is that *mdx* mice display various compensatory mechanisms discussed above that do not allow us to assess the effects of a "pure" dystrophin deficiency. *Mdx* mice moreover do not have the optimal controls, since they were on a Bl6/Ros background while being backcrossed to Bl/6J in the fourth generation, whereas wild-type and ΔSIV mice were littermates on a pure Bl6/J background. The discrepancy in backgrounds may have introduced variability in our data, although the data are consistent with previously published results[7,8]. Lastly, our methods did not allow us to quantify crest expression of $Na_v1.5$.

Taken together, our findings provide important and previously unattainable mechanistic insights on the properties of $Na_v1.5$ organization on the crest, groove, and lateral membrane of cardiomyocytes, and are an important step towards identifying cardiac domain-specific molecular determinants of $Na_v1.5$ and location-specific effects of *SCN5A* mutations. However, pool-specific function and regulation of $Na_v1.5$ at the crest, groove, and T-tubules remains to be studied in more detail.

## METHODS

### ETHICAL STATEMENT

All animal experiments conformed to the *Guide to the Care and Use of Laboratory Animals* (US National Institutes of Health, publication No. 85-23, revised 1996); were approved by the Cantonal Veterinary Administration, Bern, Switzerland; conformed to the New York University guidelines for animal use and care (IACUC Protocol 160726-03 to MD, approved 07/11/2018); and have complied with the Swiss Federal Animal Protection Law.

### MOUSE MODELS

### Dystrophin knock-out (*mdx*$^{5CV}$) mice

The *mdx*$^{5CV}$ mouse strain displays total deletion of dystrophin protein. It was generated as described previously[42], and purchased from the Jackson laboratory (Bar Harbor, Maine; stock #002379). *Mdx* mice were on a mixed background of Bl6/Ros and Bl6/J (fourth generation of backcrossing). Male littermates aged 16 weeks were used.

### ΔSIV knock-in mice

In ΔSIV knock-in mice, the C-terminal SIV motif of $Na_v1.5$ is deleted (*Scn5a*-p.S2017STOP), as described previously[5]. ΔSIV mice and wild-type littermates are on a pure Bl6/J background. All mice (male and female) were 16 weeks old.

## ISOLATION OF MURINE VENTRICULAR MYOCYTES

All experimental steps are performed at room temperature unless specified otherwise.

Cardiomyocytes were isolated based on a previously established enzymatic method[8]. Briefly, mice were euthanized by cervical dislocation. Hearts was excised, cannulated, and mounted on a Langendorff system for retrograde perfusion at 37°C. Hearts were rinsed first with nominally $Ca^{2+}$-free solution containing (in mM) 135 NaCl, 4 KCl, 1.2 $MgCl_2$, 1.2 $NaH_2PO_4$, 10 HEPES, and 11 glucose (pH 7.4, NaOH adjusted), then with digestion solution for 15 minutes, consisting of the aforementioned solution supplemented with 50 μM $Ca^{2+}$ and collagenase type II (1 mg/mL; Worthington, Allschwil, Switzerland). Subsequently, atria were removed. Ventricles were transferred to nominally $Ca^{2+}$-free solution and minced into small pieces. To increase the yield of isolated cells, digested ventricular tissue was triturated gently and filtered through a 100 μm nylon mesh. Before use, cells were subjected to a calcium increase procedure.

## CONFOCAL MICROSCOPY

Isolated cardiomyocytes were fixed with acetone at -20°C for 10 minutes in cell culture chambers. Cells were washed twice with phosphate-buffered saline (PBS), permeabilized with 0.1% saponin in PBS for 2 x 7 minutes, and blocked for 15 minutes with PBS containing 10% normal goat serum, 1% bovine serum albumin (BSA), 0.1% saponin, and 30 μg/mL Fab fragment donkey anti-mouse IgG (H+L) (Jackson Immuno Research, Baltimore, Maryland). All following antibody dilutions and washing steps were performed with incubation buffer (3% normal goat serum, 0.05% saponin, and 1% BSA in PBS) unless specified otherwise. Primary antibodies were diluted and applied onto cells for overnight incubation at 4°C. Afterwards, cells were washed 4 times for 5 minutes, and incubated with secondary antibodies for 2 hours. Cells were washed 3 times for 5 minutes, incubated with DAPI (1 μL in 200 μL PBS) for 20 minutes, washed twice with PBS, and finally embedded in FluorSave reagent (Merck, Burlington, Massachusetts). Cells were imaged on a confocal microscope (LSM710, Zeiss, Oberkochen, Germany).

## SINGLE-MOLECULE LOCALIZATION MICROSCOPY

### Sample preparation

Freshly isolated cardiomyocytes were plated on laminin-coated glass coverslips and allowed to adhere at 37°C for 30 minutes. Cells were fixed with 4% paraformaldehyde for 10 minutes and washed 3 times with PBS. To quench

autofluorescence, cells were placed overnight under 470 nm LED light. Then, cells were permeabilized with 0.1% Triton X-100 in PBS for 10 minutes, and blocked with blocking solution (2% glycine, 2% BSA, and 0.2% gelatin in PBS) for 30 minutes. All following antibody dilutions and washes were performed with blocking solution unless specified otherwise. Unconjugated primary antibodies were applied to the cells for 1 hour, followed by three 5-minute washes. Secondary antibodies were applied for 15 minutes, followed by three 5-minute washes and an optional 15-minute incubation with conjugated primary antibodies. Lastly, cells were washed with PBS for 5 minutes. Coverslips were mounted onto microscope slides in which two small holes were drilled and using double-sided tape as spacers, creating a fluid chamber. Chambers were sealed with epoxy resin.

## Optical setup and image acquisition

SMLM imaging was performed in accordance to a previously described method[23]. To achieve stochastic fluorophore blinking, imaging buffer was added to the cells, containing 200 mM 2-mercaptoethylamine, 10% glucose, 0.04 mg/mL glucose oxidase and 0.08 mg/mL catalase in T50 buffer (10 mM Tris pH 8 and 50 mM NaCl in MilliQ). Samples were imaged on a customized Leica DMI 300 inverse microscope equipped with an HCX PL APO 63X NA = 1.47 OIL CORR TIRF objective (Zeiss), a 2X tube lens (Diagnostic Instruments, Sterling Heights, Michigan) and a chromatic aberration correction lens (AC254-300-A; Thorlabs, Newton, New Jersey). Samples were sequentially excited by a 639 nm laser (, MRL-FN-639-800; UltraLasers, Newmarket, Canada), 561 nm laser (MGL-FN-561-200; UltraLasers), and 488 nm laser (OBIS; Coherent, Santa Clara, California). A 405 nm laser (MDL-III-405-150; CNI, Changchun, China) was used to reactivate AlexaFluor 647 fluorophores. Lasers were aligned by a penta-edged dichroic beam splitter (FF408/504/581/667/762-Di01-22x29). The 488, 561, and 639 laser lines were adjusted to ~0.8, 1.0, and 1.5 $kW/cm^2$, respectively. The emitted fluorescence was filtered by the applicable single-band fluorescence filter (FF01-531/40, FF01-607/36, and FF01-676/37 for AlexaFluor 488, 568, and 647, respectively; Semrock, Rochester, New York) in a filter wheel, and recorded at 33 Hz by a sCMOS camera (Prime95B; Photometrics, Tucson, Arizona) with a minimum of 2000 frames per wavelength. Recordings were controlled by MicroManager software (version 1.4.22; www.micro-manager.com). The readout noise of each camera pixel was pre-calibrated and characterized by a Gaussian distribution[43].

## Alignment of different colors for SMLM images

Different colors were aligned following previously described methods[23]. Briefly, broad-spectrum fluorescent beads (diameter ~100 nm, TetraSpec; Thermo Fisher, Waltham, Massachusetts) were imaged sequentially in the blue (488 nm), green (568 nm), and red (639 nm) channels. The images from the blue and green channels were aligned to the red channel using a second polynomial warping algorithm in Matlab (version R2017b; Mathworks, Natick, Massachusetts).

## Single-molecule localization

Single-molecule localization also followed a previously described method[23]. In short, from each image stack, each frame was box-filtered. Box size was four times the full width at half maximum of a 2D Gaussian point spread function (PSF). Each pixel was weighted by the inverse of its variation during such box-filtering. The low-pass filtered image was extracted from the raw image, and local maxima were identified. Local maxima from all frames of one image stack were subjected to 2D Gaussian multi-PSF fitting[44]. The 2D Gaussian single-PSF fitting was performed using the maximum likelihood estimation (MLE) algorithm on a GPU (GTX 1060, CUDA 8.0; Nvidia, Santa Clara, California). The likelihood function

at each pixel was based on convolving the Poisson distribution of the shot noise, which is governed by the photons emitted from nearby fluorophores, and the Gaussian distribution of the readout noise characterized by the pre-calibrated expectation, variation, and analog-to-digital conversion factor. Fitting accuracy was estimated by Cramér-Rao lower bound.

### Image analysis

Images were processed based on previously described methods[27]. Briefly, images were subjected to a smoothing filter, adjusted for brightness and contrast, and filtered to a threshold to obtain a binary image with ImageJ software (version 1.51j8; https://imagej.net). Regions of interest were drawn, defined as regions with regular α-actinin and/or Bin1 staining, depending on the applied antibodies. We excluded the intercalated disc regions from both surface and intracellular recordings, and the lateral membrane regions from intracellular recordings. Clusters were analyzed in ImageJ. Image simulations were performed using the Interaction Factor plugin in ImageJ[25], and distance between clusters in experimental and simulated images were obtained using the ImageJ function 'Analyze particles' and a script written in Python (version 2.7; www.python.org) that utilized the image processing packages 'scikit-image' and 'mahotas'[27]. Frequency histograms of cluster distances were made in GraphPad Prism (version 7; GraphPad Software, San Diego, CA, USA). The investigator that analyzed the images was ignorant of the corresponding genotypes.

### ANTIBODIES

Primary antibodies were: custom-made rabbit anti-$Na_v1.5$ (epitope: amino acids 493-511 of rat $Na_v1.5$; Pineda Antibody Service, Berlin, Germany; 1:100), mouse anti-Bin1 (amphiphysin-II; epitope: amino acids 179-207 of human Bin1; Santa Cruz Biotechnology, Dallas, Texas; 1:50), mouse anti-α-actinin (raised against rabbit skeletal α-actinin; Sigma-Aldrich, St. Louis, Missouri; 1:400), and the same anti-α-actinin antibody directly conjugated to AlexaFluor 488 or 647 (Thermo Fisher; 1:2000 or 1:5000, respectively). Secondary antibodies were: rabbit AlexaFluor 568 (Life Technologies, Carlsbad, California; SMLM: 1:10,000; confocal: 1:200), mouse AlexaFluor 647 (Life Technologies; SMLM: 1:5000), and mouse AlexaFluor 488 (Life Technologies; confocal: 1:200).

### DETUBULATION

Isolated cardiomyocytes were detubulated by osmotic shock using formamide based on a previously described method[45]. Briefly, cardiomyocytes were resuspended in 2 mL 1.5 M formamide solution for 15 minutes and washed twice with extracellular solution (see "Electrophysiology" section).

### ELECTROPHYSIOLOGY

Whole-cell sodium currents ($I_{Na}$) were recorded at 22-23°C using a VE-2 amplifier (Alembic Instruments Inc., Montréal, Canada). Borosilicate glass pipettes were pulled to a series resistance of ~2 MΩ. Recordings were visualized with pClamp software (version 8, Axon Instruments, Union City, California), and analyzed with pClamp and OriginPro (version 7.5, OriginLab Corp., Northampton, Massachusetts). Current densities (pA/pF) were calculated by dividing the peak current by the cell capacitance. Cells were bathed in extracellular solution containing (in mM) 5 NaCl, 125 NMDG-Cl, 5.6 CsCl, 5 BaCl2, 1 $MgCl_2$, 10 HEPES, and 5 glucose (pH 7.4, CsOH adjusted). Internal solution contained (in mM) 130 KCl, 4 Mg-ATP, 12 NaCl, 1 $MgCl_2$, 1 $CaCl_2$, 10 EGTA, 10 HEPES (pH 7.2, KOH adjusted).

## STATISTICS

Data are presented as means ± standard deviation. Differences between two groups were analyzed in GraphPad Prism by two-tailed T-tests if the data were normally distributed, and Mann-Whitney tests if the data were not. $P < 0.05$ was considered statistically significant. No explicit power analysis was used. Three (SMLM) or five (electrophysiology) mice per genotype were used as biological replicates, providing sufficient statistical power. For SMLM, 47/24 (wild type), 26/27 (*mdx*), and 13/19 (ΔSIV) cells were imaged on intracellular and surface imaging planes, respectively, also providing sufficient statistical power. For individual experiments, cells from different genotypes were always isolated, or stained and imaged side by side. We performed 5/4 (wild type), 3/3 (*mdx*), and 2/3 (ΔSIV) technical replicates for intracellular and surface imaging, respectively. A technical replicate is defined as one round of staining and imaging. For electrophysiology, currents were recorded in seven control and seven detubulated cells from five wild-type mice. Each mouse counts as one technical replicate as data from each mouse were collected on one experiment day.

### Exclusion and inclusion criteria

Regarding SMLM data, cells with irregular Bin1 staining were excluded, as they indicated a technical problem and/or T-tubular remodeling. All other cells were included as α-actinin and $Na_v1.5$ stainings showed consistent results. No outliers were excluded.

Regarding electrophysiology data, we only included recordings with gigaseal and high-quality voltage clamp. Among those, no outliers were excluded.

## ACKNOWLEDGMENTS

The authors express their gratitude to Marta Pérez-Hernández Durán, Alejandra Leo-Macias, and Yandong Yin (NYUMC), and to Maria Essers and Sabrina Guichard (University of Bern) for their stellar technical assistance.

HA and SHV acknowledge funding from the Swiss National Science Foundation (grant no. 310030_165741 [HA] and P1BEP3_172237 [SHV]).

## AUTHOR CONTRIBUTIONS

SHV, HA, and JSR contributed conception of the study; SHV, JSR, EAP, ER, and MD contributed methodology; SHV and JSR performed experiments; SHV contributed validation, data curation, project administration, visualization, and writing–original draft; SHV and JSR performed formal analysis and investigation; EAP, ER, MD, and HA contributed resources; JSR, EAP, ER, MD, and HA supervised; SHV and HA contributed funding acquisition; and all authors contributed writing–review & editing.

## ADDITIONAL INFORMATION

**Competing interest:** The authors declare that the research was conducted in the absence of any commercial or financial relationships that could be construed as a potential conflict of interest.

## REFERENCES


1 Gellens, M. E., George, A. L., Jr., Chen, L. Q., Chahine, M., Horn, R., Barchi, R. L. & Kallen, R. G. Primary structure and functional expression of the human cardiac tetrodotoxin-insensitive voltage-dependent sodium channel. *Proc Natl Acad Sci U S A* **89**, 554-558, doi:10.1073/pnas.89.2.554 (1992).

2 Veerman, C. C., Wilde, A. A. & Lodder, E. M. The cardiac sodium channel gene SCN5A and its gene product NaV1.5: Role in physiology and pathophysiology. *Gene* **573**, 177-187, doi:10.1016/j.gene.2015.08.062 (2015).

3 Wilde, A. A. M. & Amin, A. S. Clinical Spectrum of SCN5A Mutations: Long QT Syndrome, Brugada Syndrome, and Cardiomyopathy. *JACC Clin Electrophysiol* **4**, 569-579, doi:10.1016/j.jacep.2018.03.006 (2018).

4 Vermij, S. H., Abriel, H. & van Veen, T. A. Refining the molecular organization of the cardiac intercalated disc. *Cardiovasc. Res.* **113**, 259-275, doi:10.1093/cvr/cvw259 (2017).

5 Shy, D., Gillet, L., Ogrodnik, J. *et al.* PDZ domain-binding motif regulates cardiomyocyte compartment-specific NaV1.5 channel expression and function. *Circulation* **130**, 147-160, doi:10.1161/circulationaha.113.007852 (2014).

6 Vermij, S. H., Abriel, H. & Kucera, J. P. Modelling depolarization delay, sodium currents, and electrical potentials in cardiac transverse tubules. *bioRxiv*, 611558, doi:10.1101/611558 (2019).

7 Petitprez, S., Zmoos, A. F., Ogrodnik, J. *et al.* SAP97 and dystrophin macromolecular complexes determine two pools of cardiac sodium channels Nav1.5 in cardiomyocytes. *Circ. Res.* **108**, 294-304, doi:10.1161/CIRCRESAHA.110.228312 (2011).

8 Gavillet, B., Rougier, J. S., Domenighetti, A. A. *et al.* Cardiac sodium channel Nav1.5 is regulated by a multiprotein complex composed of syntrophins and dystrophin. *Circ. Res.* **99**, 407-414, doi:10.1161/01.RES.0000237466.13252.5e (2006).

9 Eichel, C. A., Beuriot, A., Chevalier, M. Y. *et al.* Lateral Membrane-Specific MAGUK CASK Down-Regulates NaV1.5 Channel in Cardiac Myocytes. *Circ. Res.* **119**, 544-556, doi:10.1161/CIRCRESAHA.116.309254 (2016).

10 Guilbeau-Frugier, C., Cauquil, M., Karsenty, C. *et al.* Structural evidence for a new elaborate 3D-organization of the cardiomyocyte lateral membrane in adult mammalian cardiac tissues. *Cardiovasc. Res.* **115**, 1078-1091, doi:10.1093/cvr/cvy256 (2019).

11 Rivaud, M. R., Agullo-Pascual, E., Lin, X. *et al.* Sodium Channel Remodeling in Subcellular Microdomains of Murine Failing Cardiomyocytes. *J Am Heart Assoc* **6**, doi:10.1161/JAHA.117.007622 (2017).

12 Bhargava, A., Lin, X., Novak, P., Mehta, K., Korchev, Y., Delmar, M. & Gorelik, J. Super-resolution scanning patch clamp reveals clustering of functional ion channels in adult ventricular myocyte. *Circ. Res.* **112**, 1112-1120, doi:10.1161/CIRCRESAHA.111.300445 (2013).

13 Hong, T. & Shaw, R. M. Cardiac T-tubule microanatomy and function. *Physiol. Rev.* **97**, 227-252, doi:10.1152/physrev.00037.2015 (2017).

14 Bootman, M. D., Higazi, D. R., Coombes, S. & Roderick, H. L. Calcium signalling during excitation-contraction coupling in mammalian atrial myocytes. *J. Cell Sci.* **119**, 3915-3925, doi:10.1242/jcs.03223 (2006).

15 Kawai, M., Hussain, M. & Orchard, C. H. Excitation-contraction coupling in rat ventricular myocytes after formamide-induced detubulation. *Am. J. Physiol.* **277**, H603-609, doi:10.1152/ajpheart.1999.277.2.H603 (1999).

16 Brette, F. & Orchard, C. H. Density and sub-cellular distribution of cardiac and neuronal sodium channel isoforms in rat ventricular myocytes. *Biochem. Biophys. Res. Commun.* **348**, 1163-1166, doi:10.1016/j.bbrc.2006.07.189 (2006).

17 Pasek, M., Brette, F., Nelson, A., Pearce, C., Qaiser, A., Christe, G. & Orchard, C. H. Quantification of t-tubule area and protein distribution in rat cardiac ventricular myocytes. *Prog. Biophys. Mol. Biol.* **96**, 244-257, doi:10.1016/j.pbiomolbio.2007.07.016 (2008).

18 Mohler, P. J., Rivolta, I., Napolitano, C., LeMaillet, G., Lambert, S., Priori, S. G. & Bennett, V. Nav1.5 E1053K mutation causing Brugada syndrome blocks binding to ankyrin-G and expression of Nav1.5 on the surface of cardiomyocytes. *Proc. Natl. Acad. Sci. USA* **101**, 17533-17538, doi:10.1073/pnas.0403711101 (2004).

19 Ponce-Balbuena, D., Guerrero-Serna, G., Valdivia, C. R. *et al.* Cardiac Kir2.1 and NaV1.5 channels traffic together to the sarcolemma to control excitability. *Circ. Res.* **122**, 1501-1516, doi:10.1161/circresaha.117.311872 (2018).

20 Lin, X., Liu, N., Lu, J. *et al.* Subcellular heterogeneity of sodium current properties in adult cardiac ventricular myocytes. *Heart Rhythm* **8**, 1923-1930, doi:10.1016/j.hrthm.2011.07.016 (2011).

21 Rougier, J.-S., Essers, M. C., Gillet, L., Guichard, S., Sonntag, S., Shmerling, D. & Abriel, H. A Distinct Pool of Nav1.5 Channels at the Lateral Membrane of Murine Ventricular Cardiomyocytes. *Front. Physiol.* **10**, doi:10.3389/fphys.2019.00834 (2019).

22 Dominguez, J. N., de la Rosa, A., Navarro, F., Franco, D. & Aranega, A. E. Tissue distribution and subcellular localization of the cardiac sodium channel during mouse heart development. *Cardiovasc. Res.* **78**, 45-52, doi:10.1093/cvr/cvm118 (2008).

23 Yin, Y., Lee, W. T. C. & Rothenberg, E. Ultrafast data mining of molecular assemblies in multiplexed high-density super-resolution images. *Nat Commun* **10**, 119, doi:10.1038/s41467-018-08048-2 (2019).

24 Fu, Y. & Hong, T. BIN1 regulates dynamic t-tubule membrane. *Biochim. Biophys. Acta* **1863**, 1839-1847, doi:10.1016/j.bbamcr.2015.11.004 (2016).

25 Bermudez-Hernandez, K., Keegan, S., Whelan, D. R. *et al.* A Method for Quantifying Molecular Interactions Using Stochastic Modelling and Super-Resolution Microscopy. *Sci Rep* **7**, 14882, doi:10.1038/s41598-017-14922-8 (2017).

26 Hong, T., Yang, H., Zhang, S. S. *et al.* Cardiac BIN1 folds T-tubule membrane, controlling ion flux and limiting arrhythmia. *Nat. Med.* **20**, 624-632, doi:10.1038/nm.3543 (2014).

27 Leo-Macias, A., Agullo-Pascual, E., Sanchez-Alonso, J. L. *et al.* Nanoscale visualization of functional adhesion/excitability nodes at the intercalated disc. *Nat Commun* **7**, 10342, doi:10.1038/ncomms10342 (2016).

28 Jack, J. J. B., Noble, D. & Tsien, R. W. Nonlinear cable theory: conduction. in *Electric current flow in excitable cells* ed. J. J. B. Jack, D. Noble, & R. W. Tsien) Ch. 10, 292-296 (Clarendon Press, Oxford, 1975).

29 Hong, T. T., Smyth, J. W., Gao, D. *et al.* BIN1 localizes the L-type calcium channel to cardiac T-tubules. *PLoS Biol.* **8**, e1000312, doi:10.1371/journal.pbio.1000312 (2010).

30 Rougier, J.-S., Essers, M. C., Gillet, L., Guichard, S., Sonntag, S., Shmerling, D. & Abriel, H. A distinct pool of Nav1.5 channels at the lateral membrane of murine ventricular cardiomyocytes. *bioRxiv*, 572180, doi:10.1101/572180 (2019).

31 Lab, M. J., Bhargava, A., Wright, P. T. & Gorelik, J. The scanning ion conductance microscope for cellular physiology. *Am. J. Physiol. Heart Circ. Physiol.* **304**, H1-11, doi:10.1152/ajpheart.00499.2012 (2013).

32 Bonuccelli, G., Sotgia, F., Schubert, W. *et al.* Proteasome inhibitor (MG-132) treatment of mdx mice rescues the expression and membrane localization of dystrophin and dystrophin-associated proteins. *Am J Pathol* **163**, 1663-1675, doi:10.1016/S0002-9440(10)63523-7 (2003).

33 Masubuchi, N., Shidoh, Y., Kondo, S., Takatoh, J. & Hanaoka, K. Subcellular localization of dystrophin isoforms in cardiomyocytes and phenotypic analysis of dystrophin-deficient mice reveal cardiac myopathy is predominantly caused by a deficiency in full-length dystrophin. *Exp Anim* **62**, 211-217, doi:10.1538/expanim.62.211 (2013).

34 Hernandez-Gonzalez, E. O., Mornet, D., Rendon, A. & Martinez-Rojas, D. Absence of Dp71 in mdx3cv mouse spermatozoa alters flagellar morphology and the distribution of ion channels and nNOS. *J. Cell Sci.* **118**, 137-145, doi:10.1242/jcs.01584 (2005).

35 Hatano, A., Okada, J., Washio, T., Hisada, T. & Sugiura, S. An integrated finite element simulation of cardiomyocyte function based on triphasic theory. *Front. Physiol.* **6**, 287, doi:10.3389/fphys.2015.00287 (2015).

36 Amann, K. J., Renley, B. A. & Ervasti, J. M. A cluster of basic repeats in the dystrophin rod domain binds F-actin through an electrostatic interaction. *J. Biol. Chem.* **273**, 28419-28423, doi:10.1074/jbc.273.43.28419 (1998).

37 Matamoros, M., Perez-Hernandez, M., Guerrero-Serna, G. *et al.* Nav1.5 N-terminal domain binding to alpha1-syntrophin increases membrane density of human Kir2.1, Kir2.2 and Nav1.5 channels. *Cardiovasc. Res.* **110**, 279-290, doi:10.1093/cvr/cvw009 (2016).

38 Albesa, M., Ogrodnik, J., Rougier, J. S. & Abriel, H. Regulation of the cardiac sodium channel Nav1.5 by utrophin in dystrophin-deficient mice. *Cardiovasc. Res.* **89**, 320-328, doi:10.1093/cvr/cvq326 (2011).

39 Liao, H. K., Hatanaka, F., Araoka, T. *et al.* In Vivo Target Gene Activation via CRISPR/Cas9-Mediated Trans-epigenetic Modulation. *Cell* **171**, 1495-1507 e1415, doi:10.1016/j.cell.2017.10.025 (2017).

40 Garcia-Pelagio, K. P., Bloch, R. J., Ortega, A. & Gonzalez-Serratos, H. Biomechanics of the sarcolemma and costameres in single skeletal muscle fibers from normal and dystrophin-null mice. *J. Muscle Res. Cell Motil.* **31**, 323-336, doi:10.1007/s10974-011-9238-9 (2011).

41 Lorin, C., Gueffier, M., Bois, P., Faivre, J. F., Cognard, C. & Sebille, S. Ultrastructural and functional alterations of EC coupling elements in mdx cardiomyocytes: an analysis from membrane surface to depth. *Cell Biochem Biophys* **66**, 723-736, doi:10.1007/s12013-013-9517-8 (2013).

42 Chapman, V. M., Miller, D. R., Armstrong, D. & Caskey, C. T. Recovery of induced mutations for X chromosome-linked muscular dystrophy in mice. *Proc Natl Acad Sci U S A* **86**, 1292-1296, doi:10.1073/pnas.86.4.1292 (1989).

43 Huang, F., Hartwich, T. M., Rivera-Molina, F. E. *et al.* Video-rate nanoscopy using sCMOS camera-specific single-molecule localization algorithms. *Nat. Methods* **10**, 653-658, doi:10.1038/nmeth.2488 (2013).

44 Huang, F., Schwartz, S. L., Byars, J. M. & Lidke, K. A. Simultaneous multiple-emitter fitting for single molecule super-resolution imaging. *Biomed Opt Express* **2**, 1377-1393, doi:10.1364/BOE.2.001377 (2011).

45 Brette, F., Komukai, K. & Orchard, C. H. Validation of formamide as a detubulation agent in isolated rat cardiac cells. *Am. J. Physiol. Heart Circ. Physiol.* **283**, H1720-1728, doi:10.1152/ajpheart.00347.2002 (2002).

## SOURCE DATA

**Figure 2d – Source data 1.** This spreadsheet contains the percentages of $Na_v1.5$ clusters which edges are 50 nm from the edge of the nearest α-actinin cluster at the lateral membrane of wild-type cardiomyocytes, and the corresponding statistical analyses. Values from original images are compared to those from simulations in which $Na_v1.5$ clusters are redistributed over the respective image either randomly or with high affinity for α-actinin.

**Figure 3d-f – Source data 2.** This spreadsheet contains data on $Na_v1.5$ cell surface expression (pertaining to **Fig 3d**), frequency distribution of edge distances from any α-actinin cluster to the closest $Na_v1.5$ cluster (pertaining to **Fig 3e**), and the percentage of $Na_v1.5$ clusters within 50 nm from α-actinin at the lateral membranes of wild-type, *mdx*, and ΔSIV cells. Statistical analyses and descriptive statistics are given where applicable.

**Figure 4d-e – Source data 3.** This spreadsheet contains the values of the frequency distribution of edge distances from any Bin1 cluster to the closest $Na_v1.5$ cluster (pertaining to **Fig 4d**), and the percentages of $Na_v1.5$ clusters within 50 nm from Bin1 (pertaining to **Fig 4e**) in intracellular recordings of wild-type cardiomyocytes. Statistical analyses and descriptive statistics are also given.

**Figure 5 – Source data 4.** This spreadsheet contains values of cell capacitance, maximum sodium current, and sodium current density recorded in normal and detubulated wild-type cardiomyocytes. Statistical analyses are included.

**Figure 6 – Source data 5.** This spreadsheet contains values of $Na_v1.5$ cluster density and frequency distributions of edge distances from any Bin1 cluster to the closest $Na_v1.5$ cluster in intracellular planes in wild-type, *mdx*, and ΔSIV cells. Statistical analyses and descriptive statistics are included.

**Supplemental figure 2 – Source file 6.** This spreadsheet contains values of cell size, average $Na_v1.5$ cluster size, $Na_v1.5$ cluster solidity and circularity of wild-type, *mdx*, and ΔSIV cardiomyocytes at surface (pertaining to **Supplemental Fig 2a**) and intracellular imaging planes (pertaining to **Supplemental Fig 2b**). Statistical analyses are included.

**Supplemental figure 3 – Source file 7.** This spreadsheet contains values of $Na_v1.5$ clusters within 50 nm from α-actinin at the cell surface (pertaining to **Supplemental Fig 3a**) and Bin1 inside the cell (pertaining to **Supplemental Fig 3b**). Values are compared between original images and simulations in which $Na_v1.5$ clusters are redistributed either randomly or with high affinity for α-actinin or Bin1, respectively. Statistical analyses are also given.

## SUPPLEMENTAL FIGURES

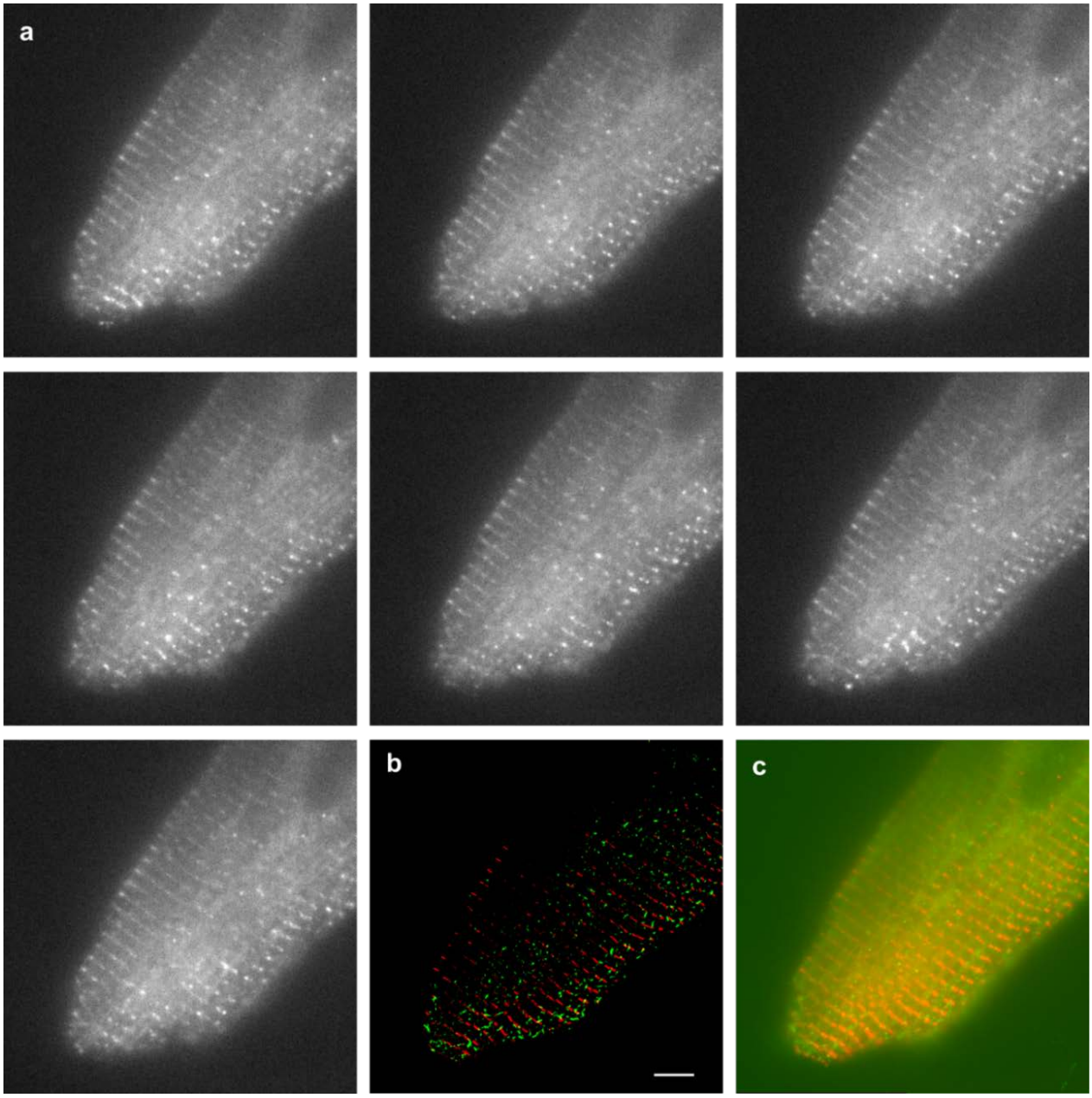


**Supplemental figure 1. Fluorophores blink during SMLM image acquisition. a**, Frames from a recording of a cardiomyocyte stained with anti-α-actinin antibodies directly conjugated to AlexaFluor 647 fluorophores and excited with a 639 nm laser. The fluorophores release photons intermittently – "blink" – due to the oxygen scavenging imaging buffer (see Methods). **b**, Reconstructed image depicting α-actinin in red and $Na_v1.5$ in green. Note that the fluorophores on the left side of the cell that did not blink, characterized by a faint striated pattern in all panels of (**a**), are not reconstructed in the final SMLM image (**b**). Scale bar 5 µm.

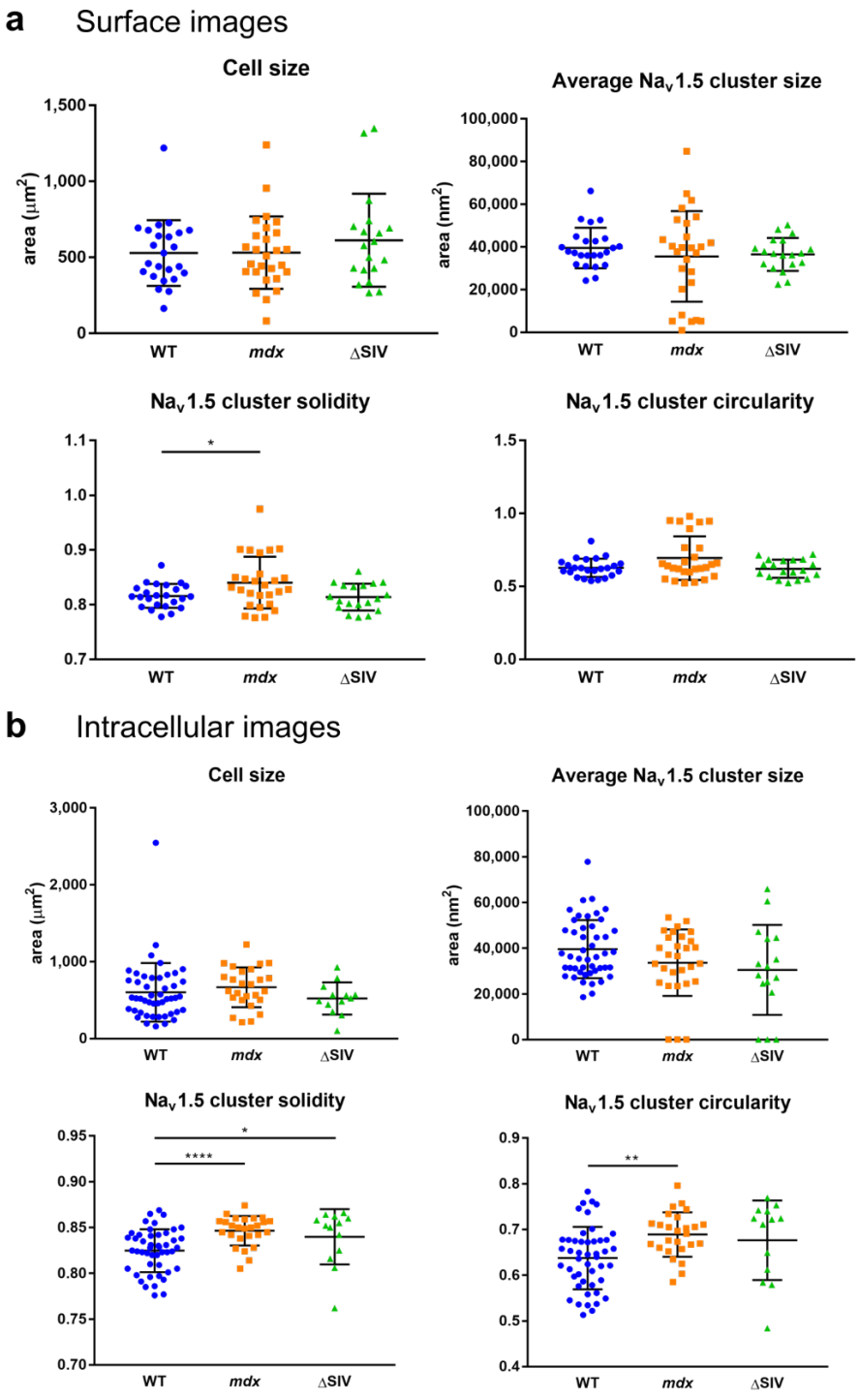


**Supplemental figure 2. Cell and $Na_v1.5$ cluster properties of SMLM images.** For all images from wild-type, *mdx,* and ΔSIV cells at the lateral membrane (**a**) and inside the cell (**b**), this figure shows cell size, and cluster size, circularity, and solidity of $Na_v1.5$ clusters per cell. Perfectly circular and solid clusters give value 1. Solidity indicates the ratio of the particle area to the area of the convex hull of the particle. **a**, Wild type $N = 3$, $n = 24$; *mdx* $N = 3$, $n = 27$; ΔSIV $N = 3$, $n = 19$. **b**, Wild type $N = 3$, $n = 39$; *mdx* $N = 3$, $n = 20$; ΔSIV $N = 3$, $n = 11$. *, $p = 0.041$ (**a**, solidity); $p = 0.021$ (**b**, solidity); **, $p = 0.001$; ****, $p < 0.0001$, Mann Whitney test.

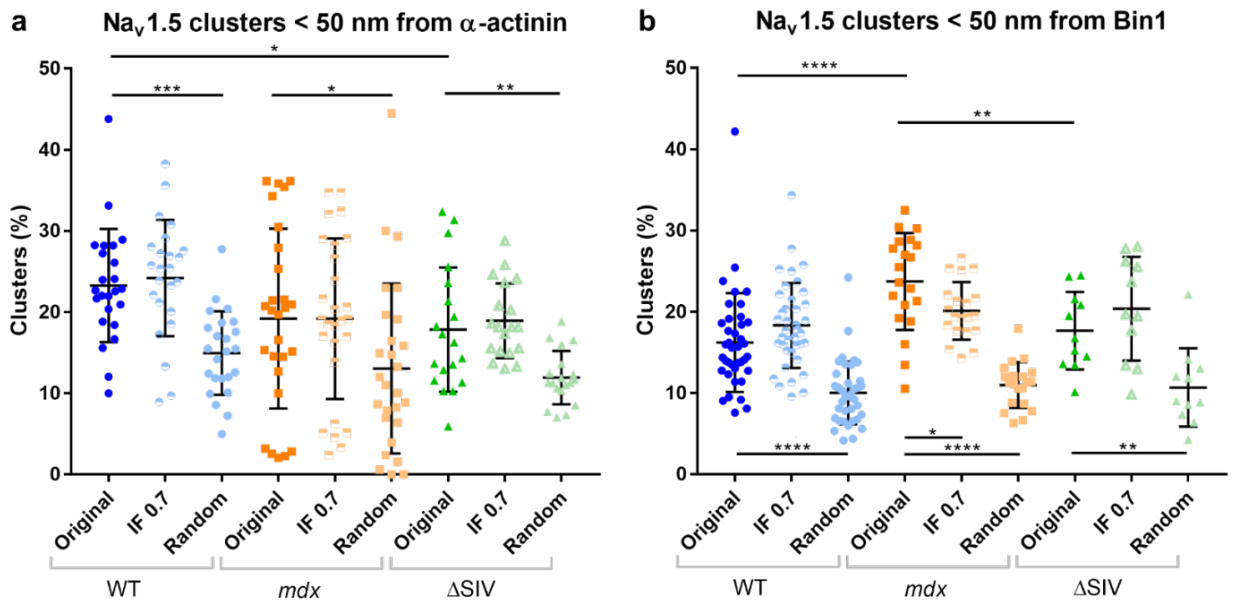


**Supplemental figure 3. Comparing cluster distances of experimental SMLM images to simulations**. Proportion of $Na_v1.5$ clusters within 50 nm from α-actinin at the lateral membrane (**a**) and Bin1 inside the cell (**b**). SMLM images from wild-type (blue), *mdx* (orange), and ΔSIV (green) cells are compared to their respective high affinity (IF 0.7) and random simulations. **a**, Wild type $N = 3$, $n = 24$; *mdx* $N = 3$, $n = 27$; ΔSIV $N = 3$, $n = 19$. **b**, Wild type $N = 3$, $n = 39$; *mdx* $N = 3$, $n = 20$; ΔSIV $N = 3$, $n = 11$. *, $p = 0.0194$ (**a**, ΔSIV-WT), $p = 0.017$ (**b**, *mdx*); **, $p = 0.0074$ (**a**, ΔSIV) $p = 0.0019$ (**b**, ΔSIV), $p = 0.0095$ (**b**, *mdx*-ΔSIV); ***, $p < 0.001$, ****, $p < 0.0001$, unpaired T-test (**b**, wild type) and Mann Whitney test (all others).

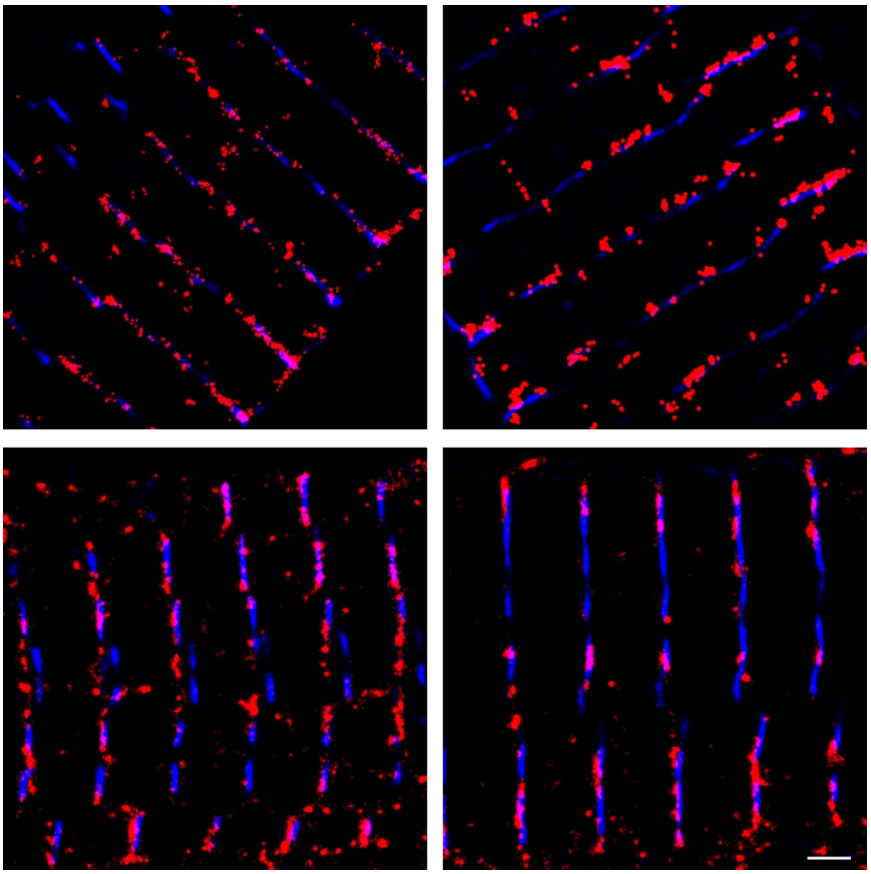

**Supplemental figure 4. Bin1 antibody validation.** Representative SMLM images of Bin1 (red) and α-actinin (blue) showing close proximity of Bin1 to α-actinin. This indicates that the anti-Bin1 antibody is most likely specific, as Bin1 binds the T-tubular membrane, and most T-tubules run along α-actinin lines, which constitute the sarcomeric Z-discs. Bin1 signal in between α-actinin lines may indicate axial T-tubular branches. *N* = 3, *n* = 57; scale bar 1 µm.

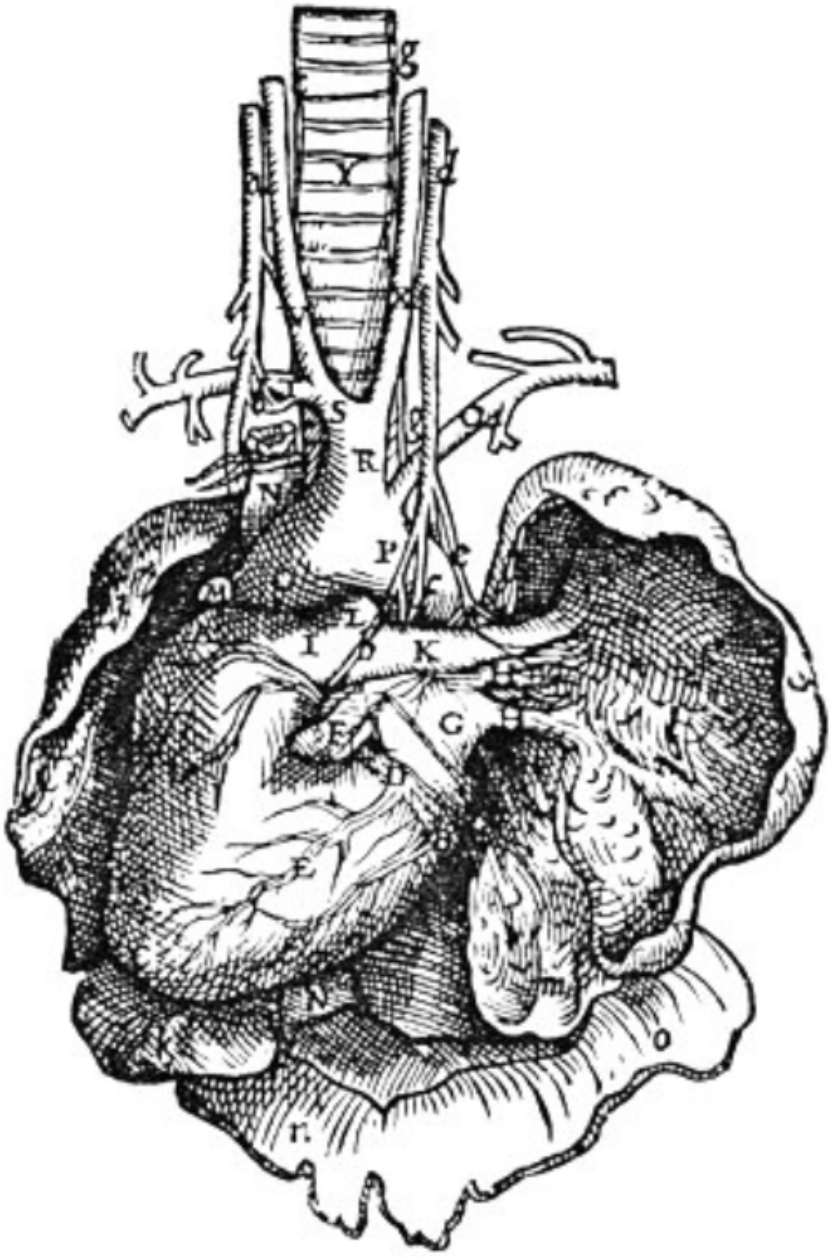

# RESULTS

# PUBLICATION #4

## 3.2 Publication 4: Transcriptomic analyses of murine ventricular cardiomyocytes

This publication was a collaborative effort of our lab and the Interfaculty Bioinformatics Unit and Swiss Institute of Bioinformatics at the University of Bern. I analyzed the data, made the tables and figures, and wrote the Data Descriptor.

This manuscript is published in *Nature Scientific Data*[76]. Online-only tables are available under *https://www.nature.com/articles/sdata2018170*.

The full dataset is available at the *Gene Expression Omnibus* (GSE102772) (see *https://www.ncbi.nlm.nih.gov/geo/*).

### 3.2.1 Additional discussion

Using the next-generation RNA-seq data as presented in this manuscript, we determined which voltage-gated ion channels are expressed in murine ventricular cardiomyocytes (**Figure 1** and **Table 1** in the manuscript). In the context of this thesis, it must be noted that of the α-subunits we identified only *Scn5a, Scn4a*, and *Scn7a* mRNA, encoding $Na_v1.5$, $Na_v1.4$, and $Na_v2.1$, respectively. Of the β-subunits, we found only *Scn1b* and *Scn4b*, encoding the $\beta_1$- and $\beta_4$-subunits, respectively.

Although mRNA levels do not necessarily correlate with protein levels, based on previous data from our group we expect a high protein expression of $Na_v1.5$ in cardiomyocytes from the respective mouse models[85,87], while $Na_v1.4$ protein expression has not been investigated yet in these cells. $Na_v2.1$ protein expression has not been investigated in these mice; however, we may extrapolate from the very low mRNA expression that protein expression is likely low as well. This would correspond to the absence of publications discussing $Na_v2.1$ or *Scn7a* expression in the heart (illustrated by its absence in the following reviews[3,8,168,174]). $Na_v2.1$ is a controversial channel: it is listed under voltage-gated sodium channels by the Hugo Gene Nomenclature Committee (see *https://www.genenames.org/data/gene-symbol-report/#!/hgnc_id/HGNC:10594*), yet is also classified as a voltage-insensitive sodium-concentration-sensitive channel that is poorly homologous to voltage-gated sodium channels[176]. Whether $Na_v2.1$ plays a role in cardiac function remains an open question.

#### 3.2.1.1 Functional notes on $Na_v1.5$, $Na_v1.4$, $\beta_1$, and $\beta_4$ expression

The biophysical properties of $Na_v1.5$ and $Na_v1.4$ are markedly different: in HEK cells, $Na_v1.4$ steady-state inactivation and activation curves are shifted in the hyperpolarized direction compared to $Na_v1.5$ (activation: $V_{1/2,\ Nav1.4}$ = -18 mV; $V_{1/2,\ Nav1.5}$ = -32 mV; inactivation: $V_{1/2,\ Nav1.4}$ = -59 mV; $V_{1/2,\ Nav1.5}$ = -75 mV)[177]. These findings correspond to very recent unpublished data by Urs Thomet (**Figure 13**).

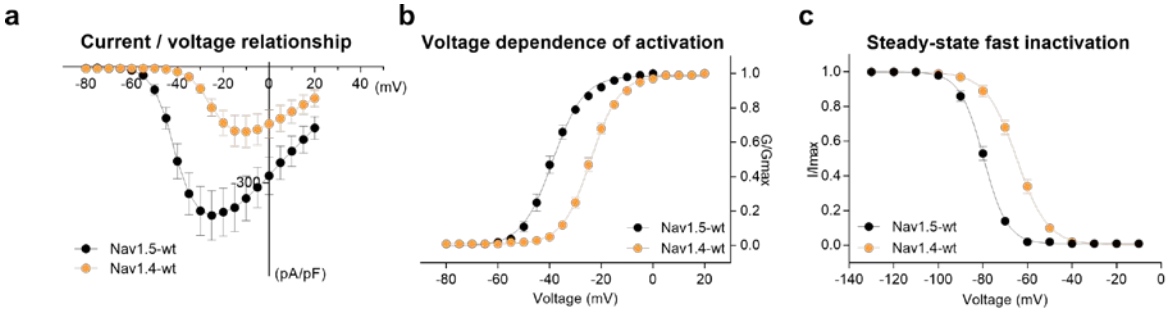


**Figure 13. Biophysical properties of $Na_v1.5$ and $Na_v1.4$.** Sodium currents were recorded in HEK cells transfected with wild-type *SCN5A* (encoding $Na_v1.5$; black) or *SCN4A* (encoding $Na_v1.4$; orange). Current-voltage relationship (**A**) and voltage dependence of activation (**B**) show a positive shift in activation of the $Na_v1.4$-mediated current compared to $Na_v1.5$. Steady-state fast inactivation (**C**) shows a comparable shift of $Na_v1.4$ current compared to $Na_v1.5$. Unpublished data collected by Urs Thomet.

These biophysical effects are modulated by the β-subunits, although findings greatly differ between experimental conditions and model systems; therefore, the functional implications of $\beta_1$- and $\beta_4$-expression on sodium channel function in cardiomyocytes are still unclear.

Moreover, the composition of complexes of $Na_v1.5$ and/or $Na_v1.4$ with $\beta_1$- and/or $\beta_4$-subunits in cardiomyocytes remains unknown. Given that the $\beta_1$-subunit is mainly expressed at the intercalated disc while $\beta_4$ seems to be specific to the T-tubules[178], the composition of these complexes likely differs between cardiomyocyte domains.

Functional implications of $Na_v1.5$, $Na_v1.4$, $\beta_1$-, and $\beta_4$-expression are further discussed in the general conclusion (**Chapter 4**).

SCIENTIFIC DATA

OPEN

# Data Descriptor: Transcriptomic analyses of murine ventricular cardiomyocytes

Morgan Chevalier[1,*], Sarah H. Vermij[1,*], Kurt Wyler[2], Ludovic Gillet[3,4], Irene Keller[5] & Hugues Abriel[1]

Received: 19 October 2017
Accepted: 14 June 2018
Published: 21 August 2018

Mice are used universally as model organisms for studying heart physiology, and a plethora of genetically modified mouse models exist to study cardiac disease. Transcriptomic data for whole-heart tissue are available, but not yet for isolated ventricular cardiomyocytes. Our lab therefore collected comprehensive RNA-seq data from wildtype murine ventricular cardiomyocytes as well as from knockout models of the ion channel regulators CASK, dystrophin, and SAP97. We also elucidate ion channel expression from wild-type cells to help forward the debate about which ion channels are expressed in cardiomyocytes. Researchers studying the heart, and especially cardiac arrhythmias, may benefit from these cardiomyocyte-specific transcriptomic data to assess expression of genes of interest.

| | |
|---|---|
| **Design Type(s)** | parallel group design • gene expression analysis objective • sequence analysis objective |
| **Measurement Type(s)** | transcription profiling assay |
| **Technology Type(s)** | RNA sequencing |
| **Factor Type(s)** | genotype • phenotype • biological replicate • candidate_gene |
| **Sample Characteristic(s)** | Mus musculus • cardiac muscle fiber |

[1]Ion Channels and Channelopathies Laboratory, Institute for Biochemistry and Molecular Medicine, University of Bern, 3012 Bern, Switzerland. [2]Interfaculty Bioinformatics Unit and Swiss Institute of Bioinformatics, University of Bern, 3012 Bern, Switzerland. [3]Pain Center, Department of Anesthesiology, University Hospital Center (CHUV) and Faculty of Biology and Medicine (FBM), University of Lausanne, 1011 Lausanne, Switzerland. [4]Department of Fundamental Neurosciences, Faculty of Biology and Medicine (FBM), University of Lausanne, 1005 Lausanne, Switzerland. [5]Department for BioMedical Research and Swiss Institute of Bioinformatics, University of Bern, 3007 Bern, Switzerland. *These authors contributed equally to this work. Correspondence and requests for materials should be addressed to H.A. (email: hugues.abriel@ibmm.unibe.ch).

## Background & Summary

In this study, we present next-generation RNA sequencing (RNA-seq) data of murine ventricular cardiomyocytes (CMC). To date, only whole-heart RNA-seq data have been published[1–3], in which a variety of cell types, such as fibroblasts, endothelial cells, and atrial and ventricular cardiomyocytes, are pooled. We endeavoured to provide RNA-seq data of isolated CMCs for several reasons. Firstly, since the pump function of the heart relies on proper CMC function, CMCs are the most thoroughly studied cardiac cell type. Researchers studying CMCs may benefit from CMC-specific RNA-seq data from which expression of genes of interest can be extracted. Secondly, because of the crucial role of ion channels in cardiac electrical excitability and arrhythmogenesis, researchers that study cardiac arrhythmias have debated the question of which ion channels are expressed in CMCs. However, existing ion channel expression data are low-throughput, often contradictory[4–6], fragmented[7], or expression is assessed in the whole heart. The present work reveals the expression of the more than 350 ion channel family members, including pore-forming and auxiliary subunits, in CMCs (see Fig. 1 and Tables 1–3 (available online only)). We therefore believe that these data will be valuable for ion channel researchers attempting to resolve the ongoing debate.

We have also included cardiac-specific knockout models of the ion channel regulators dystrophin, synapse-associated protein-97 (SAP97), and calmodulin-activated serine kinase (CASK). They interact with ion channels and modify their cell biological properties, such as membrane localization[3,8–11]. Notably, CASK provides a direct link between ion channel function and gene expression. It regulates transcription factors (TFs) in the nucleus, such as Tbr-1, and induces transcription of T-element-containing genes[12]. CASK also regulates TFs of the basic helix-loop-helix family, which bind E-box elements in promoter regions, by modulating the inhibitor of the DNA-binding-1 TF[13]. Additionally, CASK and SAP97 directly interact with each other[11]. For these reasons, we include CASK, SAP97, and dystrophin knockout mice to investigate whether these three proteins have a similar effect on gene expression, which may suggest their involvement in similar pathways. However, research beyond the scope of this paper would be needed to determine whether CASK-dependent TF regulation caused the differential expression that we observed.

To date, mutations in approximately 27 ion channel genes have been associated with cardiac arrhythmias, such as congenital short- and long-QT syndrome (SQTS and LQTS), Brugada syndrome (BrS), and conduction disorders (see http://omim.org)[14–16]. Notably, our ion channel expression data, as presented in Fig. 1 and Tables 1–3 (available online only), reveal that several arrhythmia-associated ion channel genes are not or are scarcely expressed in murine ventricular CMCs (including Kcne2, Kcne3, Scn2b, and Scn3b). Although murine and human ion channel expression may differ, we are presently unaware of any available transcriptome of human CMCs[17,18]. We are also unable to either exclude or assess the effect of enzymatic isolation on the transcriptome. Finally, other cardiac cell types such as (myo)fibroblasts may express these ion channels and therefore may be important for arrhythmogenesis. Indeed, many ion channel genes that are not expressed in cardiomyocytes have been reported in murine whole-heart tissue[2]. These include Scn1a, Scn3b, 10 voltage-gated $Ca^{2+}$ channels, 10 $K_v$ channels, and four two-pore $K^+$ channels. Conversely, all ion channel genes expressed in CMCs are also reported in whole-heart expression data.

In sum, this study presents RNA-seq data from wildtype murine ventricular CMCs, as well as from SAP97, CASK, and dystrophin knockouts and controls (see Fig. 2 for a schematic overview of study design). We performed differential gene expression analysis to compare the knockouts to their controls, and we extracted wildtype ion channel gene expression data (Tables 1–3 (available online only), Fig. 1). We believe that these data will be valuable for researchers studying cardiomyocytes and ion channels to assess expression of genes of interest.

## Methods

### Mouse models

All animal experiments conformed to the *Guide to the Care and Use of Laboratory Animals* (US National Institutes of Health, publication No. 85-23, revised 1996); have been approved by the Cantonal Veterinary Administration, Bern, Switzerland; and have complied with the Swiss Federal Animal Protection Law. Mice were kept on a 12-hour light/dark cycle. Lights were on from 6:30 AM to 6:30 PM. To avoid the influence of circadian rhythm, mice were sacrificed between 10:00 AM and 1:00 PM. Mice were all male and were between the ages of 8 and 15 weeks.

**MHC-Cre**. The cardiac-specific murine alpha-myosin heavy chain (μMHC) promoter drives the expression of Cre recombinase, which, in turn, can recombine LoxP sequences. The μMHC-Cre strain was generated as previously described[19] and acquired from the Jackson Laboratory (stock #011038).

**CASK and SAP97 knockout mice**. CASK KO and SAP97/Dlg1 KO mice were generated as previously described[9,20]. Both the CASK and SAP97 mouse lines were on mixed backgrounds. The appropriate control mice were selected in accordance with the publications that characterized both mouse lines[9,20]. CASK control mice express Cre while the first CASK exon is not floxed. SAP97 control mice are Cre-negative and the first SAP97 gene was floxed.

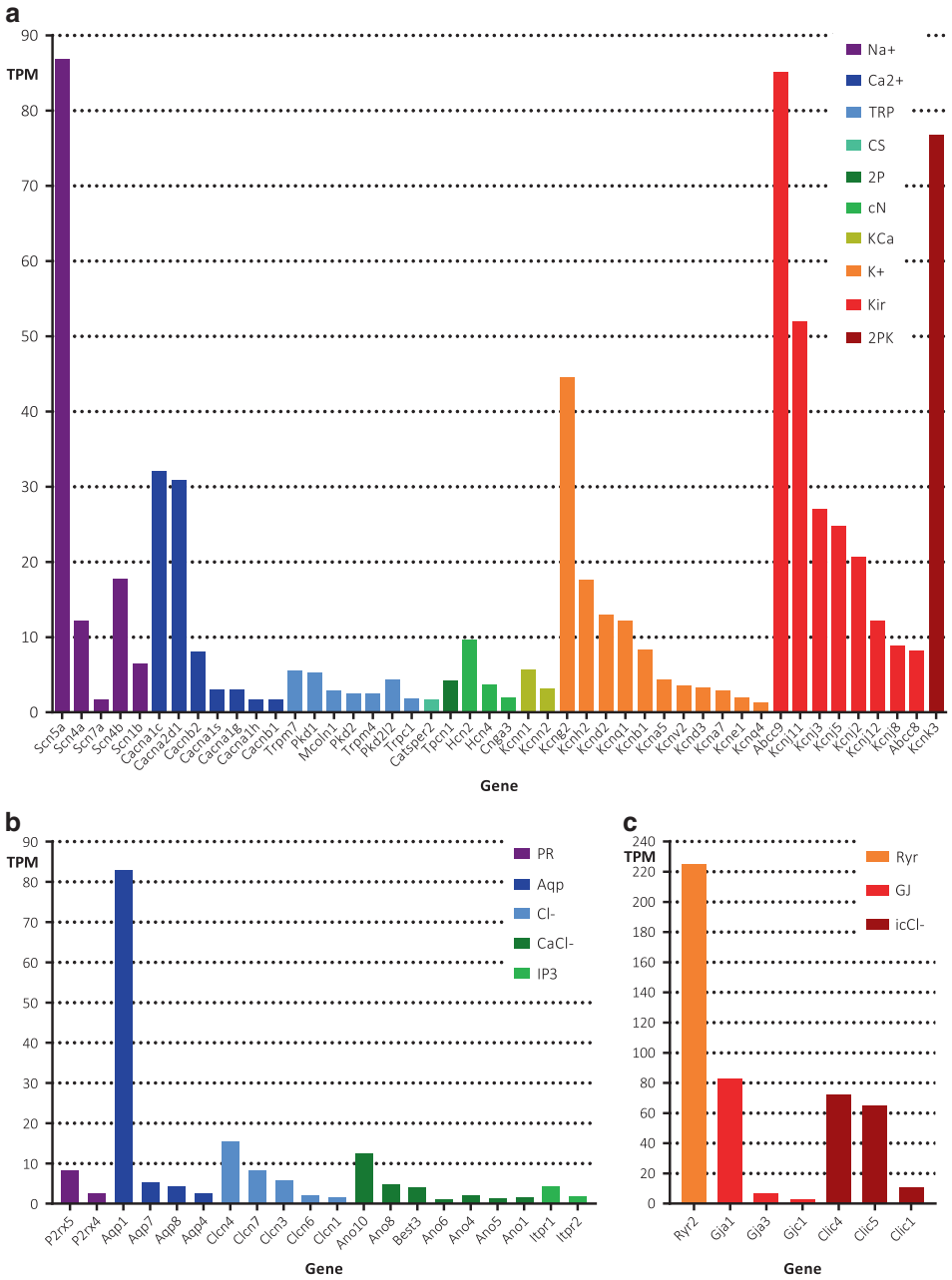


**Figure 1. Gene expression of ion channels in murine ventricular cardiomyocytes.** (**a**) Expression levels of voltage-gated ion channel genes: voltage-gated sodium channels (Na+; purple), voltage-gated calcium channels (Ca2+; blue), transient receptor potential cation channels (TRP; light blue), CS, CatSper channels (aqua), two-pore channels (2P; green), cyclic-nucleotide-regulated channels (cN; light green), calcium-activated potassium channels (KCa; ochre), voltage-gated potassium channels (K+; orange), inwardly rectifying potassium channels (Kir; red) and two-pore potassium channels (2PK; burgundy). (**b**) Expression levels of the ligand-gated purinergic receptor gene (PR; purple) and of ion channel genes from the "other" category: aquaporins (Aqp; blue), voltage-sensitive chloride channels (Cl-; light blue), calcium-activated chloride channels (CaCl-; green) and inositol triphosphate receptors (IP3; light green). (**c**) Expression levels of more ion channel genes from the "other" category: ryanodine receptors (Ryr; orange), gap junction proteins (GJ; red) and chloride intracellular channels (icCl-; burgundy). All expression levels are average TPM values of WT samples ($n = 5$). Shown are genes with more than 75 reads per gene (normalized for gene length, prior to conversion to TPM) from Tables 1–3 (available online only).

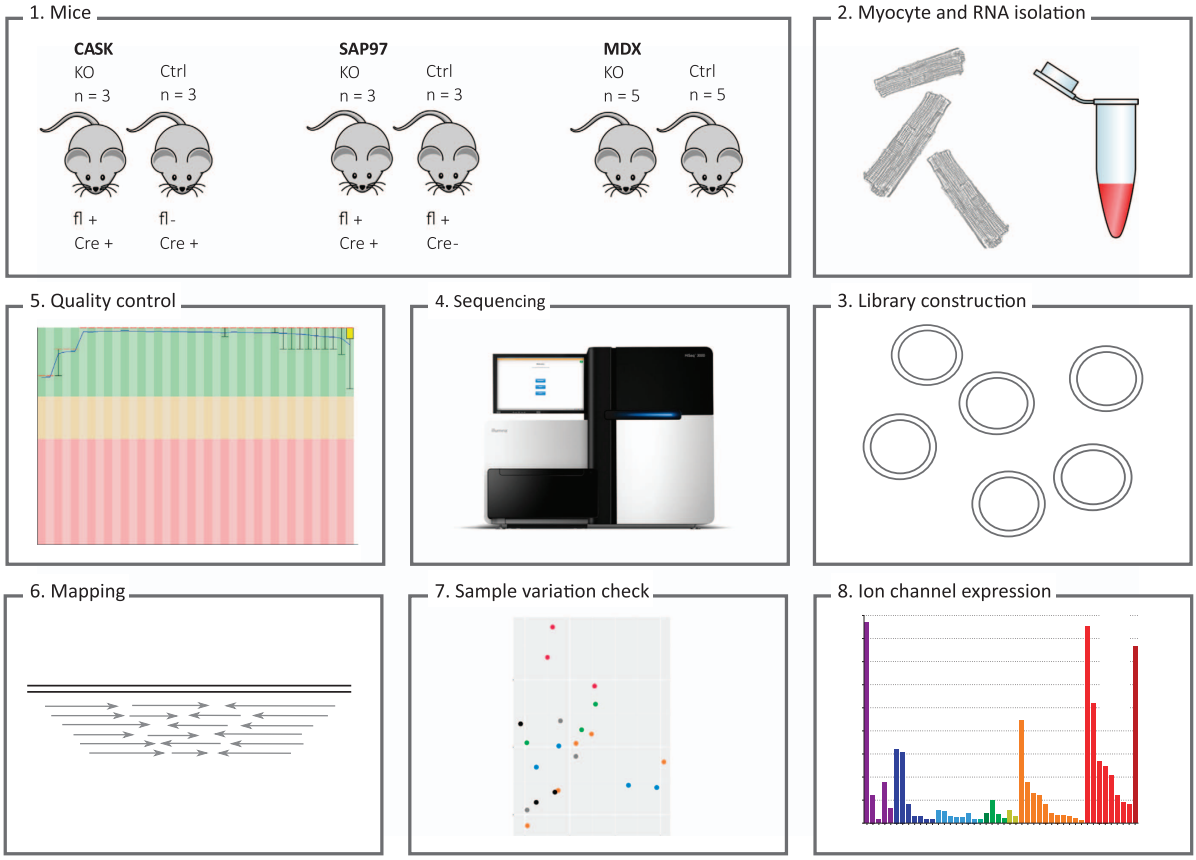


**Figure 2. Experimental design and workflow.** (1) 22 mice with six different genetic backgrounds (CASK KO and control, SAP97 KO and control, and MDX and control) were used. fl+, first exon of gene is floxed; Cre+, Cre recombinase is expressed. (2) Cardiomyocytes were isolated on a Langendorff system and RNA was isolated with a FFPE Clear RNAready kit. (3) Libraries were constructed with 1 µg RNA per sample using a TrueSeq Stranded Total RNA protocol and (4) sequenced on an Illumina HiSeq3000 machine. (5) Quality of the reads was assessed with FastQC, and (6) reads were mapped to the *Mus musculus* reference genome (GRCm38.83) with Tophat. (7) To assess sample variation within each group, we performed principle component analyses (PCA) (see Fig. 3). (8) Lastly, ion channel expression was determined.

**Dystrophin knockout (MDX-5CV) mice.** The MDX-5CV strain demonstrates total deletion of the dystrophin protein. It was created as previously described[21], and acquired from the Jackson laboratory (stock #002379). MDX mice were on pure Bl6/Ros backgrounds. Control mice were on pure Bl6/J background, except for MDX_Ct5 and MDX_5, which were Bl6/Ros mice backcrossed three times on Bl6/J.

### Cardiomyocyte isolation

Mice ($n = 3$–5 per genotype, male, age 10–15 weeks) were heparinized (intraperitoneal injection of 100 µL heparin (5000 U/mL; Biochrom AG)) and killed by cervical dislocation. Hearts were excised, and the aortas were cannulated in ice-cold phosphate-buffered saline (PBS). Subsequently, hearts were perfused on a Langendorff system in a retrograde manner at 37 °C with 5 mL perfusion buffer (1.5 mL/min; in mM: 135 NaCl, 4 KCl, 1.2 $NaH_2PO_4$, 1.2 $MgCl_2$, 10 HEPES, 11 glucose), followed by the application of type II collagenase (Worthington CLS2; 25 mL of 1 mg/mL in perfusion buffer with 50 µM $CaCl_2$). Left and right ventricles were triturated in PBS to dissociate individual ventricular cardiomyocytes and then filtered through a 100 µm filter.

### RNA extraction and sequencing

RNA-seq was performed by the Next Generation Sequencing Platform at the University of Bern. Total RNA was isolated from freshly dissociated cardiomyocytes with an FFPE Clear RNAready kit (AmpTec, Germany), which included a DNase treatment step. RNA quality was assessed with Qubit and Bioanalyzer, and RNA quantity was checked with Qubit.

| Sample ID | Genotype | # read pairs total | # non-rRNA read pairs | % of total | Insert size | # read pairs mapping to a gene | % of total | # no-feature read pairs | % of total | # ambiguous read pairs | % of total |
|---|---|---|---|---|---|---|---|---|---|---|---|
| CASK_Ct1 | WT+Cre | 47,543,799 | 47,343,548 | 99.58 | 492 | 34,076,980 | 71.67 | 2,721,942 | 5.73 | 8,287,647 | 17.43 |
| CASK_Ct2 | WT+Cre | 45,437,500 | 45,287,356 | 99.67 | 476 | 33,988,592 | 74.8 | 1,440,229 | 3.17 | 7,578,641 | 16.68 |
| CASK_Ct3 | WT+Cre | 55,117,414 | 54,944,721 | 99.69 | 479 | 40,469,641 | 73.42 | 1,790,829 | 3.25 | 11,381,005 | 20.65 |
| CASK_KO1 | CASK_fl+Cre | 45,685,573 | 45,565,815 | 99.74 | 472 | 32,765,612 | 71.72 | 5,738,568 | 12.56 | 5,504,670 | 12.05 |
| CASK_KO2 | CASK_fl+Cre | 55,895,769 | 55,607,105 | 99.48 | 511 | 39,344,558 | 70.39 | 2,372,238 | 4.24 | 12,476,403 | 22.32 |
| CASK_KO3 | CASK_fl+Cre | 56,437,329 | 56,008,449 | 99.24 | 499 | 42,159,185 | 74.7 | 2,804,256 | 4.97 | 9,655,232 | 17.11 |
| MDX_1 | MDX | 17,485,935 | 17,320,513 | 99.05 | 380 | *(sample exluded)* | | | | | |
| MDX_2 | MDX | 39,536,744 | 39,037,330 | 98.74 | 447 | 27,475,113 | 69.49 | 3,258,092 | 8.24 | 6,543,268 | 16.55 |
| MDX_3 | MDX | 39,626,959 | 39,432,254 | 99.51 | 455 | 27,841,146 | 70.26 | 2,169,924 | 5.48 | 7,327,584 | 18.49 |
| MDX_4 | MDX | 42,406,246 | 40,919,896 | 96.49 | 488 | 29,805,158 | 70.28 | 2,905,415 | 6.85 | 6,497,990 | 15.32 |
| MDX_5 | MDX | 50,934,677 | 47,518,076 | 93.29 | 484 | 34,233,480 | 67.21 | 1,864,210 | 3.66 | 10,028,518 | 19.69 |
| MDX_Ct1 | WT | 48,311,563 | 46,288,106 | 95.81 | 380 | 32,827,800 | 67.95 | 4,353,181 | 9.01 | 7,779,264 | 16.1 |
| MDX_Ct2 | WT | 47,283,192 | 46,988,962 | 99.38 | 446 | 32,237,279 | 68.18 | 2,304,142 | 4.87 | 10,939,883 | 23.14 |
| MDX_Ct3 | WT | 35,275,617 | 34,938,284 | 99.04 | 427 | 24,235,276 | 68.7 | 3,631,537 | 10.29 | 4,922,208 | 13.95 |
| MDX_Ct4 | WT | 33,977,175 | 32,900,815 | 96.83 | 515 | 25,298,933 | 74.46 | 1,713,065 | 5.04 | 4,619,558 | 13.6 |
| MDX_Ct5 | WT | 49,379,536 | 45,499,492 | 92.14 | 485 | 32,227,570 | 65.27 | 1,210,708 | 2.45 | 10,698,976 | 21.67 |
| SAP_Ct1 | WT+Cre | 47,930,112 | 47,715,719 | 99.55 | 461 | 34,192,649 | 71.34 | 1,965,652 | 4.1 | 9,896,590 | 20.65 |
| SAP_Ct2 | WT+Cre | 44,934,245 | 44,566,395 | 99.18 | 444 | 30,350,071 | 67.54 | 4,879,732 | 10.86 | 7,491,483 | 16.67 |
| SAP_Ct3 | WT+Cre | 43,586,968 | 43,382,766 | 99.53 | 451 | 29,836,839 | 68.45 | 1,332,267 | 3.06 | 8,751,881 | 20.08 |
| SAP_KO1 | SAP_fl+Cre | 44,319,566 | 44,146,526 | 99.61 | 452 | 34,155,235 | 77.07 | 2,606,959 | 5.88 | 5,090,692 | 11.49 |
| SAP_KO2 | SAP_fl+Cre | 41,547,517 | 41,397,099 | 99.64 | 469 | 28,697,320 | 69.07 | 3,765,768 | 9.06 | 7,431,842 | 17.89 |
| SAP_KO3 | SAP_fl+Cre | 46,143,349 | 45,812,985 | 99.28 | 443 | 30,710,635 | 66.55 | 5,476,238 | 11.87 | 8,174,538 | 17.72 |

**Table 4. RNA-seq raw data and mapping metrics.** Total and non-ribosomal RNA read pairs, average RNA fragment size (bp), and mapping metrics, including absolute number and percentages of read pairs mapping to all annotated exons of the mouse reference genome, and no-feature and ambiguous reads, per sample. Note the low number of read pairs in MDX_1, which is therefore excluded from further analysis. CASK KO and Ctrl, SAP97 KO and Ctrl $ns = 3$, MDX KO $n = 4$, MDX Ctrl $n = 5$.

To allow sequencing of long non-coding RNA (lncRNA), libraries were constructed with 1 μg RNA using the TruSeq Stranded Total RNA kit after Ribo-Zero Gold (Illumina) treatment for rRNA depletion. Library molecules with inserts $< 300$ base pairs (bp) were removed. Paired-end libraries (2x150 bp) were sequenced on an Illumina HiSeq3000 machine.

## RNA-seq data analysis

Between 17.5 and 56.4 million read pairs were obtained per sample and the quality of the reads was assessed using FastQC v.0.11.2 (http://www.bioinformatics.babraham.ac.uk/projects/fastqc/). Ribosomal RNA (rRNA) was removed by mapping the reads with Bowtie2 v.2.2.1 (ref. 22) to a collection of rRNA sequences (NR_003279.1, NR_003278.3 and NR_003280.2) downloaded from NCBI (www.ncbi.nlm.nih.gov). No quality trimming was required.The remaining reads were mapped to the *Mus musculus* reference genome (GRCm38.83) with Tophat v.2.0.13 (ref. 23). We used htseq-count v.0.6.1 (ref. 24) to count the number of reads overlapping with each gene, as specified in the Ensembl annotation (GRCm38.83). Detailed information about the genes including the Entrez Gene ID, the MGI symbol and the description of the gene was obtained using the Bioconductor package BioMart v.2.26.1 (ref. 25).

Raw reads were corrected for gene length and TPM (transcripts per million) values were calculated to compare the expression levels among samples. Gene lengths for the latter step were retrieved from the Ensembl annotation (GRCm38.83) as the total sum of all exons.

Principal component analysis (PCA) plots were done in DESeq2 v.1.10.1 (ref. 26) (https://bioconductor.org/packages/release/bioc/html/DESeq2.html) using the 500 genes with the most variable expression across samples. A regularized log transformation was applied to the counts before performing the PCA.

## Statistics

To assess differential gene expression between genotypes, a Wald test was performed with the Bioconductor package DESeq2 v.1.10.1 (ref. 26). We considered $p$ values of up to 0.01, accounting for a Benjamini-Hochberg false discovery rate adjustment, to indicate significant difference. Statistical tools used included DESeq2, R-3.2.5 (https://cran.r-project.org), and Biomart_2.26.1 (www.biomart.org).

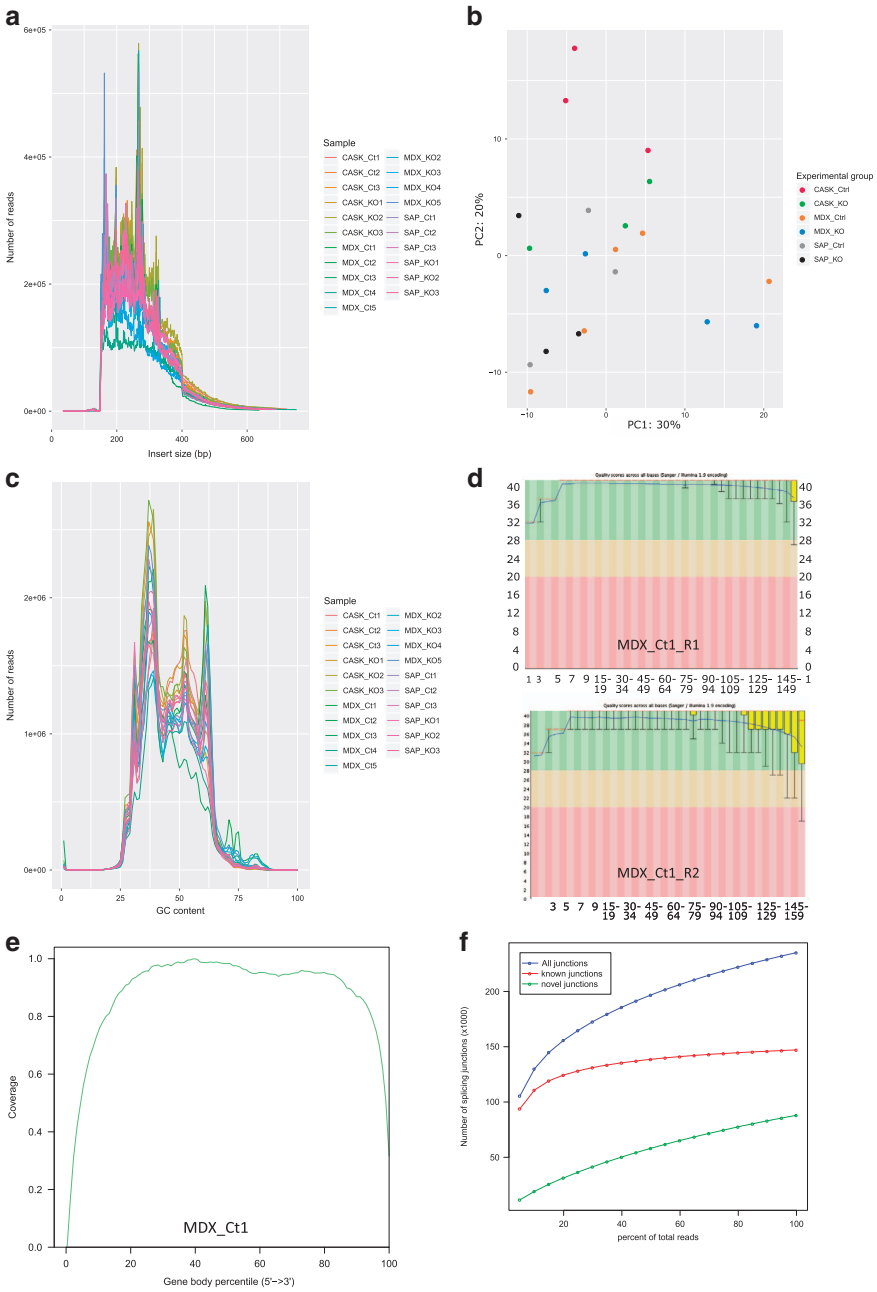


**Figure 3.** **Quality control.** (**a**) Histogram of inferred insert size for each sample, which represents distance between the two reads of one RNA fragment. (**b**) Principle component analyses (PCA) plots were performed to assess variability of samples within and between groups. Plot of the first two axes from a PCA based on the 500 genes with the most variable expression across all samples except MDX_1. CASK control (red, $n = 3$) and KO (green, $n = 3$); MDX control (orange, $n = 5$) and KO (blue, $n = 4$); SAP97 control (grey, $n = 3$) and KO (black, $n = 3$). (**c**) Distribution of GC content of the reads for each sample. (**d**) Base quality (Phred scores) along the length of the reads in each FastQC file of MDX_Ct1 as representative sample. The box plots are drawn as follows: red line, median; yellow box, range between upper and lower quartiles; whiskers, range between 10 and 90% quantiles. The blue line shows the mean quality. Y-axis represents quality scores across all bases. X-axis represents position in read (bp). (**e**) Gene body coverage. Distribution of reads along the length of the genes (5'-end on the left, 3'-end on the right). Shown image of sample MDX_Ct1 is representative for all samples. (**f**) Saturation report, depicting the number of splice junctions detected using different subsets of the data from 5 to 100% of all reads. Red, known junction based on the provided genome annotation; green, novel junctions; blue, all junctions. The red line reaches a plateau where adding more data does not increase the number of detected junctions, indicating that the sequencing depth suffices for performing alternative splicing analysis.

## Data Records

The data were submitted to NCBI Gene Expression Omnibus (GEO) (Data Citation 1). This GEO project contains raw data and TPM values from all samples, and differential gene expression analysis between knockout and control samples.

## Technical Validation

### RNA metrics

RNA-seq yielded 1.0 billion read pairs in total, with an average of 44.5 million read pairs per sample (standard deviation 8.4 million). The number of read pairs (in millions) was 306 for CASK KO and Ctrl, 268 for SAP97 KO and Ctrl, and 404 for MDX and Ctrl (see Table 4 for an overview of RNA-seq metrics, including mapping rates). One sample (MDX_1) yielded few reads and was therefore excluded from further analyses. The proportion of reads mapping to annotated exons ranged from 65 to 77%. Mapping, no-feature (2–13%), and ambiguous (11–23%) read pairs together accounted for 89–97% of the total number of RNA reads (Table 4). Read pairs covered 49,671 genes of the *Mus musculus* reference genome (GRCm83.38).

### Quality assessment

The quality of all samples was assessed with FastQC. Except for MDX_1, all samples were of high quality. Where applicable, a representative example (MDX_Ct1) is shown. Firstly, the insert size histogram (Fig. 3a) shows that the inferred insert size of each sample exceeded 150 base pairs, demonstating that the sequencing was not contaminated by adapter sequences. Secondly, the GC content plot (Fig. 3c) ideally shows a roughly normal distribution centred around the average GC content of the genome, which varies between species. The peaks observed in Fig. 3c are likely caused by sequences that are detected at high copy numbers, and should not pose problems for downstream analyses. Furthermore, Phred scores (Fig. 3d) are well within the green area of the graph indicating good base quality along the length of reads. As well, the gene coverage graph (Fig. 3e) of sample MDX_Ct1 shows that reads are distributed evenly along the length of the gene body. Because the gene coverage for all other samples is highly comparable to that of MDX_Ct1, only one example is shown. Lastly, the saturation report (Fig. 3f) represents the number of splice junctions detected using different subsets of the data from 5 to 100% of all reads. At sequencing depths sufficient to perform alternative splicing analysis, at least the red line, representing known junctions, should reach a plateau where adding more data does not much increase the number of detected junctions. Only MDX_1 does not reach this plateau.

### Gene expression variation of biological replicates

We performed Principle Component Analyses (PCA) to assess whether samples from the same experimental group have similar gene expression profiles (Fig. 3b). Of note, samples within each sample group still show considerable variation. The mixed genetic background of most sample groups may explain this variation; only the MDX control mice are on a pure Bl6/J background. The variation seen in MDX control mice is likely due to a batch effect, as two rounds of samples were sequenced. However, considering that PCA plots are based on the 500 genes with the highest variability in one sample, our genes of interest, including all ion channel genes, show similar expression levels throughout all samples.

### Ion channel expression

Based on the list of ion channel genes from HUGO Gene Nomenclature Committee (https://www.genenames.org/cgi-bin/genefamilies/set/177), we distilled ion channel expression from WT mice expressed as TPM (Tables 1–3 (available online only), Fig. 1).

## References


1. Cerrone, M. *et al.* Plakophilin-2 is required for transcription of genes that control calcium cycling and cardiac rhythm. *Nat Commun* **8,** 106 (2017).
2. Harrell, M. D., Harbi, S., Hoffman, J. F., Zavadil, J. & Coetzee, W. A. Large-scale analysis of ion channel gene expression in the mouse heart during perinatal development. *Physiol. Genomics* **28,** 273–283 (2007).
3. Petitprez, S. *et al.* SAP97 and dystrophin macromolecular complexes determine two pools of cardiac sodium channels Nav1.5 in cardiomyocytes. *Circ. Res.* **108,** 294–304 (2011).
4. Zimmer, T., Haufe, V. & Blechschmidt, S. Voltage-gated sodium channels in the mammalian heart. *Glob. Cardiol. Sci. Pract* **4,** 449–463 (2014).
5. Balse, E. *et al.* Dynamic of ion channel expression at the plasma membrane of cardiomyocytes. *Physiol. Rev.* **92,** 1317–1358 (2012).
6. Westenbroek, R. E. *et al.* Localization of sodium channel subtypes in mouse ventricular myocytes using quantitative immunocytochemistry. *J. Mol. Cell. Cardiol.* **64,** 69–78 (2013).
7. Stroud, D. M. *et al.* Contrasting Nav1.8 Activity in Scn10a-/- Ventricular Myocytes and the Intact Heart. *J. Am. Heart Assoc* **5,** 1–10 (2016).
8. Leonoudakis, D., Conti, L. R., Radeke, C. M., McGuire, L. M. & Vandenberg, C. A. A multiprotein trafficking complex composed of SAP97, CASK, Veli, and Mint1 is associated with inward rectifier Kir2 potassium channels. *J. Biol. Chem.* **279,** 19051–19063 (2004).
9. Eichel, C. A. *et al.* Lateral membrane-specific MAGUK CASK down-regulates NaV1.5 channel in cardiac myocytes. *Circ. Res.* **119,** 544–556 (2016).
10. Abriel, H., Rougier, J. S. & Jalife, J. Ion channel macromolecular complexes in cardiomyocytes: roles in sudden cardiac death. *Circ. Res.* **116,** 1971–1988 (2015).

11. Nafzger, S. & Rougier, J. S. Calcium/calmodulin-dependent serine protein kinase CASK modulates the L-type calcium current. *Cell Calcium* **61,** 10–21 (2017).
12. Hsueh, Y. P., Wang, T. F., Yang, F. C. & Sheng, M. Nuclear translocation and transcription regulation by the membrane-associated guanylate kinase CASK/LIN-2. *Nature* **404,** 298–302 (2000).
13. Sun, R. *et al.* Human calcium/calmodulin-dependent serine protein kinase regulates the expression of p21 via the E2A transcription factor. *Biochem. J.* **419,** 457–466 (2009).
14. Ashcroft, F. M. From molecule to malady. *Nature* **440,** 440–447 (2006).
15. Rickert-Sperling, S., Kelly, R. G. & Driscoll, D. J. *Congenital Heart Diseases: The Broken Heart* 721–736 (Springer-Verlag, 2016).
16. Lahrouchi, N., Behr, E. R. & Bezzina, C. R. Next-generation sequencing in post-mortem genetic testing of young sudden cardiac death cases. *Front. Cardiovasc. Med* **3,** 13 (2016).
17. Heinig, M. A. *et al.* Natural genetic variation of the cardiac transcriptome in non-diseased donors and patients with dilated cardiomyopathy. *Genome Biol.* **18,** 170 (2017).
18. van den Berg, C. W. *et al.* Transcriptome of human foetal heart compared with cardiomyocytes from pluripotent stem cells. *Development* **142,** 3231–3238 (2015).
19. Agah, R. *et al.* Gene recombination in postmitotic cells. Targeted expression of Cre recombinase provokes cardiac-restricted, site-specific rearrangement in adult ventricular muscle in vivo. *J. Clin. Invest.* **100,** 169–179 (1997).
20. Gillet, L. *et al.* Cardiac-specific ablation of synapse-associated protein SAP97 in mice decreases potassium currents but not sodium current. *Heart Rhythm* **12,** 181–192 (2015).
21. Chapman, V. M., Miller, D. R., Armstrong, D. & Caskey, C. T. Recovery of induced mutations for X chromosome-linked muscular dystrophy in mice. *Proc. Natl. Acad. Sci. USA* **86,** 1292–1296 (1989).
22. Langmead, B. & Salzberg, S. L. Fast gapped-read alignment with Bowtie 2. *Nat. Methods* **9,** 357–359 (2012).
23. Kim, D. *et al.* TopHat2: accurate alignment of transcriptomes in the presence of insertions, deletions and gene fusions. *Genome Biol.* **14,** R36 (2013).
24. Anders, S., Pyl, P. T. & Huber, W. HTSeq--a Python framework to work with high-throughput sequencing data. *Bioinformatics* **31,** 166–169 (2015).
25. Durinck, S. *et al.* BioMart and Bioconductor: a powerful link between biological databases and microarray data analysis. *Bioinformatics* **21,** 3439–3440 (2005).
26. Love, M. I., Huber, W. & Anders, S. Moderated estimation of fold change and dispersion for RNA-seq data with DESeq2. *Genome Biol.* **15,** 550 (2014).

## Data Citation

1. *Gene Expression Omnibus* GSE102772 (2017).

## Acknowledgements

The research was financially supported by Swiss National Science Foundation Grant 310030_165741 (HA). We thank the Next Generation Sequencing Platform of the University of Bern, in particular Muriel Fragnière, for performing the high-throughput sequencing experiments; prof. Rolf Jaggi for excellent technical advice on RNA isolation from cardiomyocytes; and Joseph Allan for language editing.

## Author Contributions

M.C. planned and performed experiments on KO and control samples, and submitted data to the repositories. S.H.V. wrote the Data Descriptor, analyzed the data, and made tables and figures. K.W. performed bioinformatic analyses, and made tables and figures. I.K. performed bioinformatic analyses, made tables and figures, and co-supervised the work. L.G. performed experiments on WT samples. H.A. planned the experiments, obtained funding, and supervised the project

## Additional Information

Tables 1, 2 and 3 are available only in the online version of this paper.

**Competing interests**: The authors declare no competing interests.

**How to cite this article**: Chevalier, M. *et al*, Transcriptomic analyses of murine ventricular cardiomyocytes. *Sci. Data* 5:180170 doi: 10.1038/sdata.2018.170 (2018).

**Publisher's note**: Springer Nature remains neutral with regard to jurisdictional claims in published maps and institutional affiliations.

SCIENTIFIC DATA

# Corrigendum: Transcriptomic analyses of murine ventricular cardiomyocytes

Published: 9 October 2018

**Morgan Chevalier, Sarah H. Vermij, Kurt Wyler, Ludovic Gillet, Irene Keller & Hugues Abriel**

Correction to: *Scientific Data* https://doi.org/10.1038/sdata.2018.170, published online 21 August 2018.

In the CASK and SAP97 knockout mice sub-section of the Methods in this Data Descriptor it is incorrectly stated that CASK KO mice were generated as previously published in references 9 and 20. This is incorrect. Instead, mice in which the first coding exon of the CASK gene is flanked by *loxP* sites ($CASK^{tm1Sud}$, purchased from the Jackson Laboratory, stock #006382) were crossed with αMHC-Cre mice.

In the same section of the Data Descriptor it is incorrectly stated that in SAP97 mice the first SAP97 gene was floxed. In actuality the first three coding exons were floxed.

In Table 4 of the Data Descriptor, the genotype of samples SAP_Ct1, SAP_Ct2 and SAP_Ct3 is incorrectly listed as WT+Cre. The correct genotype is WT_fl, consistent with Figure 2 and the Mouse models sub-section of the Methods.



Correspondence and requests for materials should be addressed to H.A. (email: hugues.abriel@ibmm.unibe.ch)

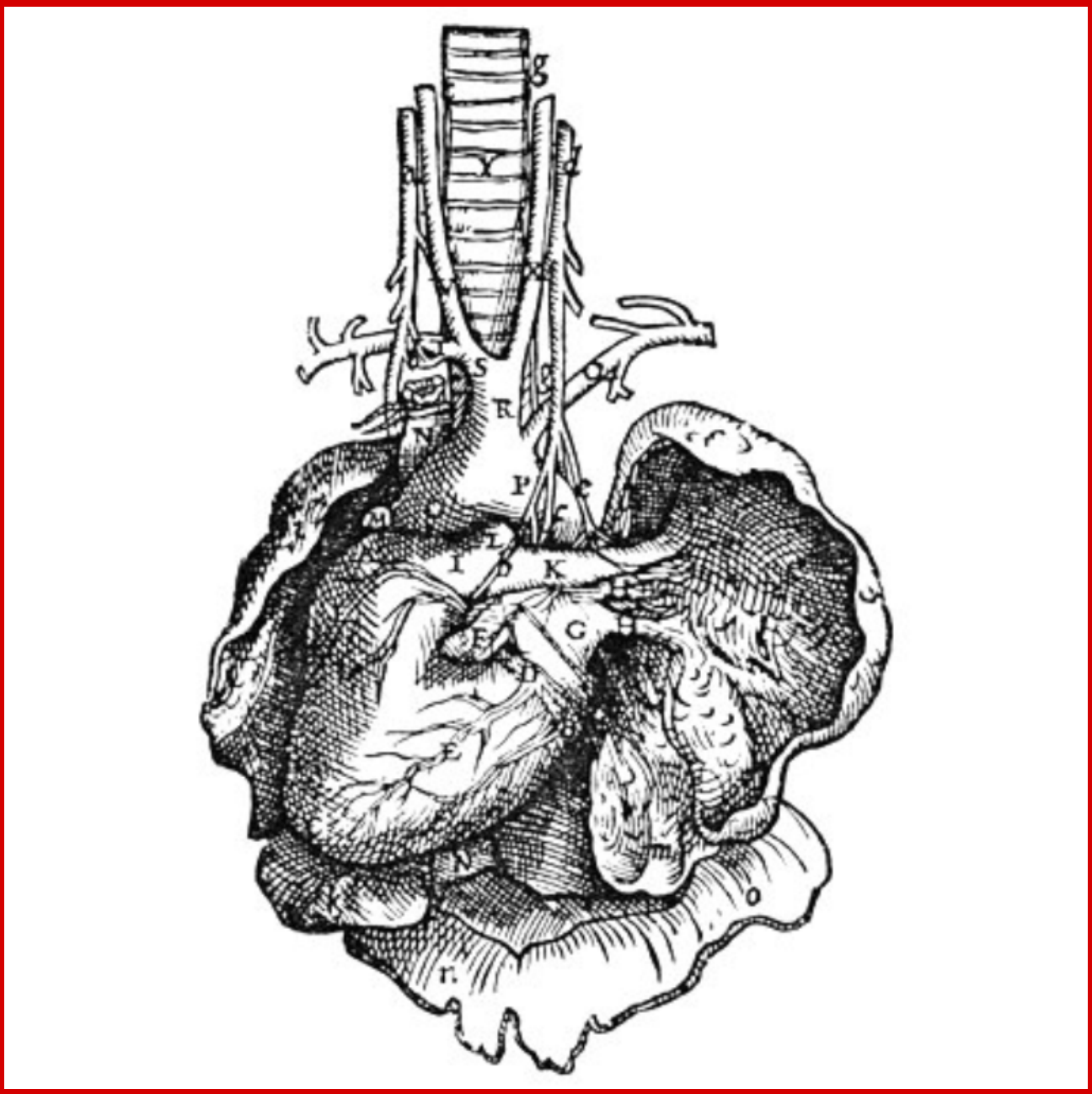

# RESULTS
# PUBLICATION #5

## 3.3 Publication 5: Modeling depolarization delay, sodium currents, and electrical potentials in cardiac transverse tubules

I conceptualized and wrote this publication, and I was involved in developing the methodology and analyzing the data. Prof Jan Kucera wrote the *in silico* model and performed the computer simulations.

This manuscript is uploaded on bioRxiv[179] and currently in revision.

# Modelling depolarization delay, sodium currents, and electrical potentials in cardiac transverse tubules

Sarah H. Vermij[a*], Hugues Abriel[a], Jan P. Kucera[b]


## ABSTRACT

T-tubules are invaginations of the lateral membrane of striated muscle cells that provide a large surface for ion channels and signaling proteins, thereby supporting excitation-contraction coupling. T-tubules are often remodeled in heart failure. To better understand the electrical behavior of T-tubules of cardiac cells in health and disease, this study addresses two largely unanswered questions regarding their electrical properties: (1) the delay of T-tubular membrane depolarization and (2) the effects of T-tubular sodium current on T-tubular potentials.

Here, we present an elementary computational model to determine the delay in depolarization of deep T-tubular membrane segments as the narrow T-tubular lumen provides resistance against the extracellular current. We compared healthy tubules to tubules with constrictions and diseased tubules from mouse and human, and conclude that constrictions greatly delay T-tubular depolarization, while diseased T-tubules depolarize faster than healthy ones due to tubule widening. We moreover modeled the effect of T-tubular sodium current on intraluminal T-tubular potentials. We observed that extracellular potentials become negative during the sodium current transient (up to -50 mV in constricted T-tubules), which feedbacks on sodium channel function (self-attenuation) in a manner resembling ephaptic effects that have been described for intercalated discs where opposing membranes are very close together.

These results show that (1) the excitation-contraction coupling defects seen in diseased cells cannot be explained by T-tubular remodeling alone; and (2) the sodium current may modulate intraluminal potentials. Such extracellular potentials might also affect excitation-contraction coupling.



**AFFILIATIONS**

**a,** Institute of Biochemistry and Molecular Medicine, University of Bern, Bühlstrasse 28, 3012 Bern, Switzerland;

**b,** Department of Physiology, University of Bern, Bühlplatz 5, 3012 Bern, Switzerland.

*** CORRESPONDENCE**
sarah.vermij@ibmm.unibe.ch


## INTRODUCTION

Transverse (T-)tubules are deep invaginations of the lateral membrane of skeletal and cardiac muscle cells. In mammalian ventricular cardiomyocytes, T-tubules form a complex network throughout the cell, especially in species with high heart rates such as mice (Pinali et al., 2013; Jayasinghe et al., 2015), and carry many ion channels and regulatory proteins (reviewed in (Bers, 2002; Hong and Shaw, 2017; Bhogal et al., 2018)). Consequently, T-tubules function as a platform for excitation-contraction coupling and signaling, which is essential for the initiation and regulation of muscle contraction (Hong and Shaw, 2017). Importantly, T-tubular remodeling has been reported for several cardiac diseases (Crocini et al., 2017; Crossman et al., 2017a). In particular, T-tubules widen (Wagner et al., 2012; Pinali et al., 2017; Seidel et al., 2017). Understanding the electrical properties of T-tubules in health and disease is therefore paramount to understanding cardiac physiology and pathophysiology. Several questions regarding the electrical properties of T-tubules however remain largely open (Vermij et al., 2019).

A first question concerns the delay after which deep segments of T-tubules depolarize has hardly been assessed. Based on measurements of dextran diffusion out of T-tubules and corresponding modeling of this diffusion process, Uchida and Lopatin recently calculated that T-tubular constrictions and dilations increase the time constant of membrane depolarization from ~10 to ~100 µs, but they did not assess in their experiments

the delay of membrane depolarization of deep T-tubular membrane (Uchida and Lopatin, 2018). Since linear cable theory is unsuitable to determine depolarization delay in a structurally complex T-tubule, we present an *in silico* model of a simple T-tubule, an overall constricted tubule, and a tubule with successive constrictions. We quantify the depolarization delay of deep T-tubular segments compared to cell surface, and show that the threshold of voltage-gated channels deep in the cell will be reached slightly later than near the surface.

A second question concerns the role played by a T-tubular sodium current. Although the existence of a T-tubular pool of sodium channels is still under debate (Rougier et al., 2019), several studies have suggested that sodium channels are present in T-tubules and that the T-tubular sodium current may be substantial (Maier et al., 2004; Mohler et al., 2004; Brette and Orchard, 2006; Westenbroek et al., 2013; Koleske et al., 2018; Ponce-Balbuena et al., 2018). To date, the effects of a tubular sodium current and the interactions between the sodium current and the extracellular potentials have scarcely been investigated. The effects of a large T-tubular sodium current have been already simulated by Hatano *et al.* using an elaborate 3D model of T-tubules without branches, constrictions, and dilations (Hatano et al., 2015). With a sodium current density of 30 mS/µF, the extracellular potential was slightly negative (-1 mV), and sodium current was 8% smaller than at the cell surface. However, the authors did not investigate this phenomenon or discuss its physiological importance in further detail. Therefore, in the present work, we extended our model with a T-tubular sodium current. We explore extracellular potentials in our T-tubular model with and without constrictions, investigate the biophysical properties and magnitude of the sodium current throughout the T-tubule, and discuss the physiological implications.

## METHODS

Our model approximated one T-tubule as a cylinder that was divided in 100 segments (for a mouse T-tubule) or 20 segments (for a human T-tubule), separating 101 or 21 nodes, respectively (**Figure 1A, Table 1**). Intracellular resistivity was assumed negligible. T-tubular radius, length, extracellular resistivity, membrane capacitance, and membrane conductance were set as in **Table 1**.

In this T-tubular model, sodium current in the different nodes was modeled according to Luo & Rudy (Luo and Rudy, 1991) with modifications by Livshitz & Rudy (Livshitz and Rudy, 2009). A voltage pulse from -85 to +20 mV was applied at the mouth of the tubule (-80 to +20 mV for simulations without sodium current). This situation mimics a cell that is perfectly voltage clamped at the level of its bulk membrane. The value of -20 mV was chosen to elicit a large sodium current. The sodium current maximal conductance was set to 23 mS/µF, the same value as used in whole-cell simulations (Luo and Rudy, 1991). Note that this value is probably on the high side, as the intercalated discs contain a relatively high density of voltage-gated sodium channels and carries a significant proportion of the whole-cell sodium current (Shy et al., 2014). Calcium channels were not included in the model as these channels open

**Table 1.** Parameters for T-tubular model of healthy and post-myocardial infarction (MI) T-tubules of human and mouse. Radius ($r$) and length ($l$) are based on previously published values. Constrictions of healthy mouse T-tubule are also specified. *, Parameters of each of the constrictions from the five-constrictions model; **, parameters of the overall constricted model. Numbers between brackets correspond to the following publications: (1) (Wagner et al., 2012), (2) (Hong et al., 2014), (3) (Crossman et al., 2017b), (4) (Cannell et al., 2006). The resistivity of the extracellular space ($\rho_e$) is set at 100 Ω·cm. Conductance of resting membrane ($g_m$) is set at 0.143 mS/cm$^2$ (Uchida and Lopatin, 2018), which is attributable to a small $I_{K1}$ and leak currents. Capacitance ($C_m$) was set at 2 µF/cm$^2$ in healthy cells to simulate microfolds, and at 1 µF/cm$^2$ to simulate the loss of microfolds in disease (Page, 1978; Hong et al., 2014).

| Species | $r$ (nm) | $l$ (µm) | $\rho_e$ (Ω·cm) | $C_m$ (µF/cm$^2$) | $g_m$ (mS/cm$^2$) | Nodes |
|---|---|---|---|---|---|---|
| Healthy mouse | 98.5 (1) | 9 (2) | 100 | 2 | 0.143 | 101 |
| Constrictions | 9.85 (1) | 0.45*/9** | 100 | 2 | 0.143 | 5*/101** |
| Post-MI mouse | 108 (1) | 9 (2) | 100 | 1 | 0.143 | 101 |
| Healthy human | 147 (3) | 2 (4) | 100 | 2 | 0.143 | 21 |
| Post-MI human | 218 (3) | 2 (4) | 100 | 1 | 0.143 | 21 |

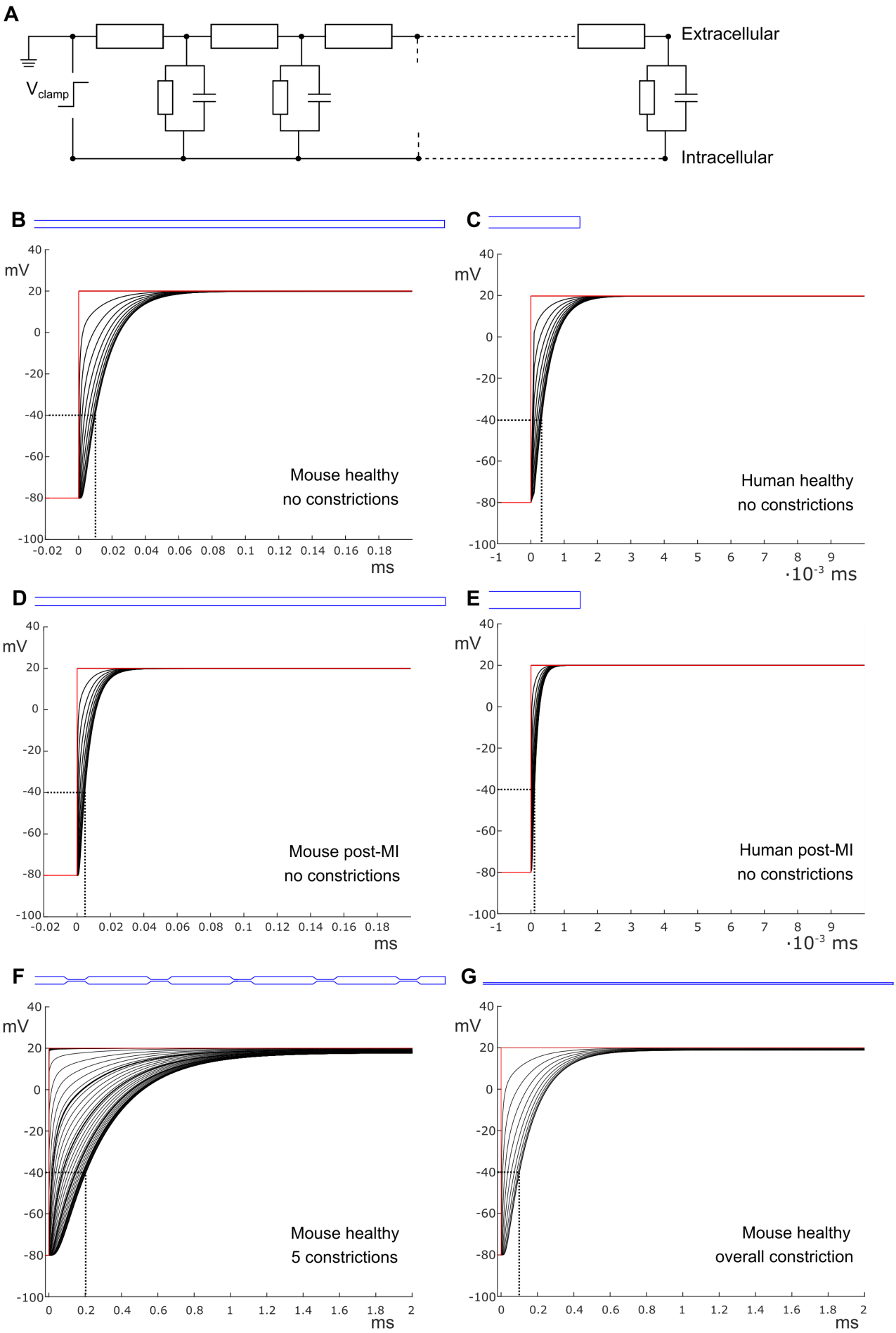
A
Extracellular
Intracellular
V clamp
B
C
mV
ms
Mouse healthy
no constrictions
Human healthy
no constrictions
·10-3 ms
D
E
Mouse post-MI
no constrictions
Human post-MI
no constrictions
F
G
Mouse healthy
5 constrictions
Mouse healthy
overall constriction

**Figure 1 (previous page). Delay of membrane depolarization in constricted T-tubules.** (**A**) Schematic representation of the model. T-tubule is subdivided in approximately 100-nm-long segments consisting of intraluminal resistance, membrane capacitance, and membrane resistance. Cytosolic resistance is assumed negligible and T-tubular mouth is assumed perfectly clamped. Panels (**B**-**G**) depict simulations of different T-tubules: healthy mouse (**B**), healthy human (**C**), mouse post-myocardial infarction (MI) (**D**), human post-MI (**E**), healthy mouse with five constrictions (**F**), and healthy mouse overall constricted (**G**). T-tubular geometries are schematically depicted in blue and detailed in **Table 1**. (**F**), Curves spaced further apart represent segments of a constriction, curves close together represent wide segments. Red lines indicate the perfectly clamped mouth of the T-tubule. Note the differences in time scales between mouse with and without constrictions and human. The membrane potentials of every tenth (**B,D,G**) and second (**C,F**) node are depicted. Dotted lines indicate the opening threshold for voltage-gated calcium channels (around -40 mV).

only when the majority of sodium channels have already inactivated.

The model was implemented numerically using a one-dimensional finite-difference scheme. Membrane potential ($V_m$) and the gating variables of the sodium current were integrated using the forward Euler method using a constant time step of 0.25 ns. Simulations were implemented and run in MATLAB (version 2015a, The MathWorks, Natick, MA, USA).

## RESULTS

### DELAY OF T-TUBULAR MEMBRANE DEPOLARIZATION

First, we set out to answer the question how long it takes to charge the membrane as a capacitor and depolarize the T-tubules in the absence of sodium current. In other words: what is the delay between depolarization at the plasma membrane and deep in the T-tubules?

When we consider an electrophysiological experiment in which a cardiomyocyte is voltage-clamped, a voltage step at the pipette site will first induce a capacitive current into the cell membrane, which will cause depolarization. While this current can travel unhindered through the cytoplasm into the T-tubular membrane, the narrow T-tubules will oppose an extracellular "exit resistance" against the capacitive current as it leaves the T-tubule again. The deeper and narrower the T-tubule, the higher the exit resistance, the longer it takes for the T-tubular membrane to depolarize. This delay in membrane depolarization in deep T-tubules can directly affect the ion channels in the T-tubule: the deeper in the T-tubule, the later they can open. According to our model, for a typical mouse T-tubule, the threshold of voltage-gated calcium channels (~ -40 mV) in the innermost node of the T-tubule will be reached after ~10 µs (**Figure 1B**). For a human T-tubule [6], the membrane depolarization would reach the threshold of the innermost calcium channels much faster than for a murine T-tubule, after ~0.3 µs (**Figure 1C**). On a side note, in cardiac disease, T-tubules generally widen [16]. Myocardial infarction (MI) induces an increase in T-tubular diameter of 9% in mice [3], and as much as 33% in humans [5]. Therefore, the "exit resistance" of T-tubules decreases and calcium channels deep in the T-tubule open quicker. For a murine T-tubule after myocardial infarction, the delay to reach the threshold of L-type calcium channels is ~7 µs (**Figure 1D**), and in a T-tubule from human post-myocardial infarction, ~0.1 µs (**Figure 1E**).

For a homogeneous tubule with a cylindrical geometry, classical cable theory (Jack et al., 1975) can be used to predict the voltage drop from the mouth to the end, at steady state, once the capacitive loading is complete. First, one calculates the length constant $\lambda$ as

$$\lambda = \sqrt{\frac{r}{2 g_m \rho_e}} \quad \text{(Eq. 1)}$$

where $r$ is the T-tubular radius, $g_m$ is the conductance of the membrane per unit area, and $\rho_e$ is the resistivity of extracellular space. It follows that the length constant for the healthy mouse T-tubule (characteristics specified in **Table 1**) is 186 µm. One may then be tempted to use an exponential function (valid for an infinite cable) to describe the decay of membrane potential as

$$\Delta V_{inf}(x) = \Delta V_0 \, e^{-\frac{x}{\lambda}}, \quad \text{(Eq. 2)}$$

where $\Delta V_0$ = 100 mV is the voltage applied at the tubule mouth and $x$ is the distance from the tubule mouth. This approach is however erroneous, because the T-tubule has a sealed end. For sealed-end cables, by applying the reflection and superposition principle, the correct approach is to use a hyperbolic cosine function instead of an exponential (Weidmann, 1952; Jack et al., 1975):

$$\Delta V_{\text{sealed}}(x) = \Delta V_0 \, \frac{\cosh\left(\frac{L-x}{\lambda}\right)}{\cosh\left(L/\lambda\right)}, \quad \text{(Eq. 3)}$$

For the healthy mouse T-tubule Eq. 1 yields a voltage drop of 4.72 mV, while Eq. 2 yields only 0.117 mV. This corresponds to the negligible voltage drop depicted in **Figure 1B**. Although the other conditions we modeled lead to different length constants ($\lambda_{\text{mouse post-MI}}$ = 194 µm; $\lambda_{\text{human healthy}}$ = 227 µm; $\lambda_{\text{human post-MI}}$ = 276 µm), the voltage drops are negligible in all cases (mouse post-MI: $\Delta V_{\text{inf}}$ = 0.108 mV, $\Delta V_{\text{sealed}}$ = 0.045 mV; human healthy: $\Delta V_{\text{inf}}$ = 0.877 mV, $\Delta V_{\text{sealed}}$ = 0.0039 mV; human post-MI $\Delta V_{\text{inf}}$ = 0.722 mV, $\Delta V_{\text{sealed}}$ = 0.0026 mV).

#### EFFECTS OF T-TUBULAR CONSTRICTIONS ON MEMBRANE DEPOLARIZATION

To quantitatively assess how constrictions change the delay of depolarization deep in a T-tubule, we incorporated constrictions into our model of an unbranched cylindrical T-tubule. We used the parameters for the healthy mouse T-tubule, as these parameters led to the longest depolarization delay (10 µs to depolarize the innermost T-tubule segment to -40 mV). We introduced five 450-nm-long constrictions with a tenfold diameter reduction to 19.7 nm, its centers spaced 1.8 µm apart (**Figure 1F, Table 1**). This is similar to the model of Uchida and Lopatin (Uchida and Lopatin, 2018), which included 20-nm-wide constrictions every 2 µm. For this purpose, the resistances and capacitors depicted in **Figure 1A** were scaled accordingly. With the constrictions in our model, the threshold for $Ca_v$ channels (-40 mV) in the deepest tubular segment was reached 200 µs later than at the surface (**Figure 1F**). This is 20 times later than in the simpler model without constrictions, where the threshold was reached after 10 µs (**Figure 1B**).

Constricting the tubule 10 times to a diameter of 19.7 nm over its full length (**Figure 1G**) increased the depolarization delay in the deep segment 10 times (compare **Figure 1B** and **G**), in agreement with cable theory (capacitive load 10 times smaller and resistance 100 times larger). Interestingly, this increase of the delay was nevertheless smaller than in the presence of five successive constrictions. The difference lies in fact that each widening following each constriction represents a large capacitive load, and the accumulation of these successive loads contributes to the slowing of the spread of electrotonic depolarization.

Additionally, we observed a voltage drop of 2.3 mV in the tubule with five constrictions (**Figure 1F**) and 1.2 mV in the overall constricted tubule (**Figure 1G**), which is ~10 to ~20 times higher than the voltage drop of 0.117 mV calculated for the healthy murine T -tubule.

#### IMPLICATIONS OF T-TUBULAR SODIUM CURRENT

As a next step, we investigated the effect of putative voltage-gated sodium ($Na_v$) channels on tubular depolarization (see **Table 1** for parameters). Results using the non-constricted T-tubule, the T-tubule with five constrictions and the T-tubule constricted over its entire length are presented in **Figures 2, 3, and 4**, respectively. **Figure 2B** shows that in a non-constricted T-tubule, the sodium current is smaller deep inside the T-tubule than at the mouth. This smaller current is due to the appearance of a negative extracellular potential in the T-tubule (**Figure 2C**), which results from the flow of current along the narrow tubule. This negative extracellular potential contributes to the depolarization of the membrane a few mV beyond -20 mV (**Figure 2B**). The extracellular potential becomes a few mV negative at deep T-tubular nodes of the cylindrical mouse tubule (**Figure 2C**), and up to -50 and -40 mV in the tubule with five constrictions and the overall constricted tubule, respectively (**Figures 3 and 4**). This negative extracellular potential brings the transmembrane potential closer to the Nernst potential of sodium ($E_{\text{Na}}$ = 55 mV). This leads to diminished sodium current (~15% reduction in an unconstructed T-tubule, ~40% in an overall constricted T-tubule, and ~45% in a T-tubule with five constrictions) (**Figures 2D, 3D, 4D**). Thus, the sodium current is smaller in deeper T-tubular membrane segments.

Constricting the T-tubule leads to a delay in sodium current activation from 0.03 ms (no constrictions) to 0.15 ms (overall constriction) and 2.7 ms (five constrictions) (**Figures 2D, 3D, 4D**). Interestingly, in the model with five constrictions, the peak sodium current increases over the course of the first constriction (**Figure 3D**). This is explained by the following factors. Firstly, the membrane is not depolarized to -20 mV yet (**Figure 3B**), so the driving force (defined as $V_{\text{m}}$ - $E_{\text{Na}}$) is larger. Secondly, the maximal open probability ($P_{\text{o}}$) in the deep segments is increased compared to the mouth segment (**Figure 3G**), which is a direct result of the voltage-dependence of the activation and inactivation gates (**Figure 3E-F**). For voltage-gated sodium channels, open probability is defined in the Livshitz-Rudy model as $P_{\text{o}} = m^3hj$, where $m$ is the activation gate (there are three activation gates), and $h$ and $j$ the fast and slow inactivation gates, respectively. Since the open probability is only

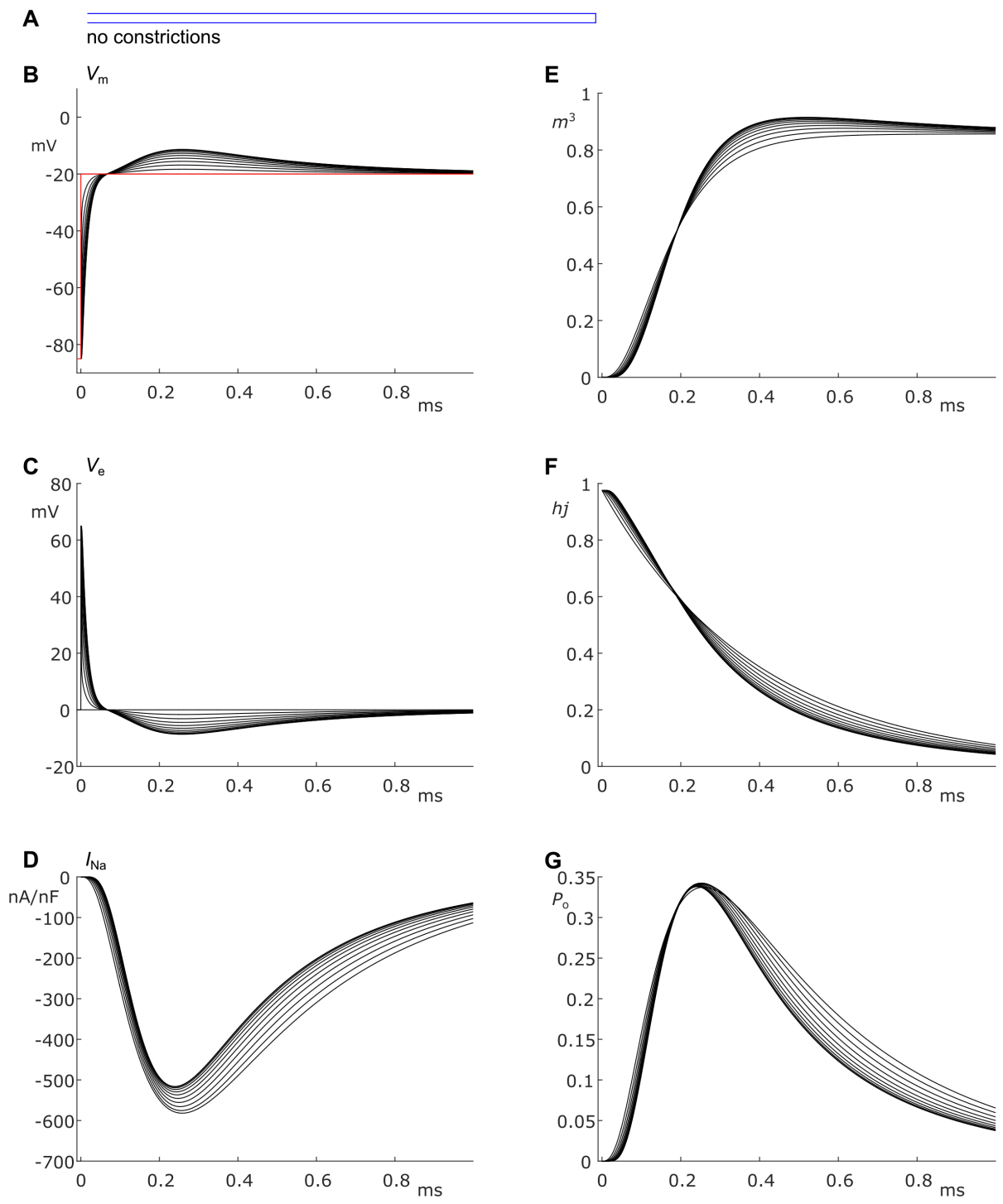


**Figure 2**. **Modeling sodium current in a healthy mouse T-tubule.** A voltage-gated sodium current (formulated according to (Luo and Rudy, 1991; Livshitz and Rudy, 2009)) with a conductance of 23 mS/µF (Luo and Rudy, 1991) was introduced to each segment of the healthy mouse T-tubule model in parallel to membrane resistance (see **Figure 1A**). (**A**), Schematic representation of the morphology of a healthy murine T-tubule (see **Table 1**). Membrane potentials (**B**), extracellular potentials (**C**), and simulated sodium current density upon a voltage-clamp step of the tubule mouth from -85 to -20 mV (**D**) are given. Note the decrease of sodium current amplitude and delayed activation in deeper segments of the tubules (**D**). This correlates with changes in the biophysical properties of the sodium current: product of activation gates ($m^3$, **E**) and inactivation gates ($hj$, **F**) show faster activation and inactivation in deeper T-tubular segments, respectively; and peak open probability slightly increases in deeper T-tubular segments ($P_o$ defined as $m^3hj$, **G**).

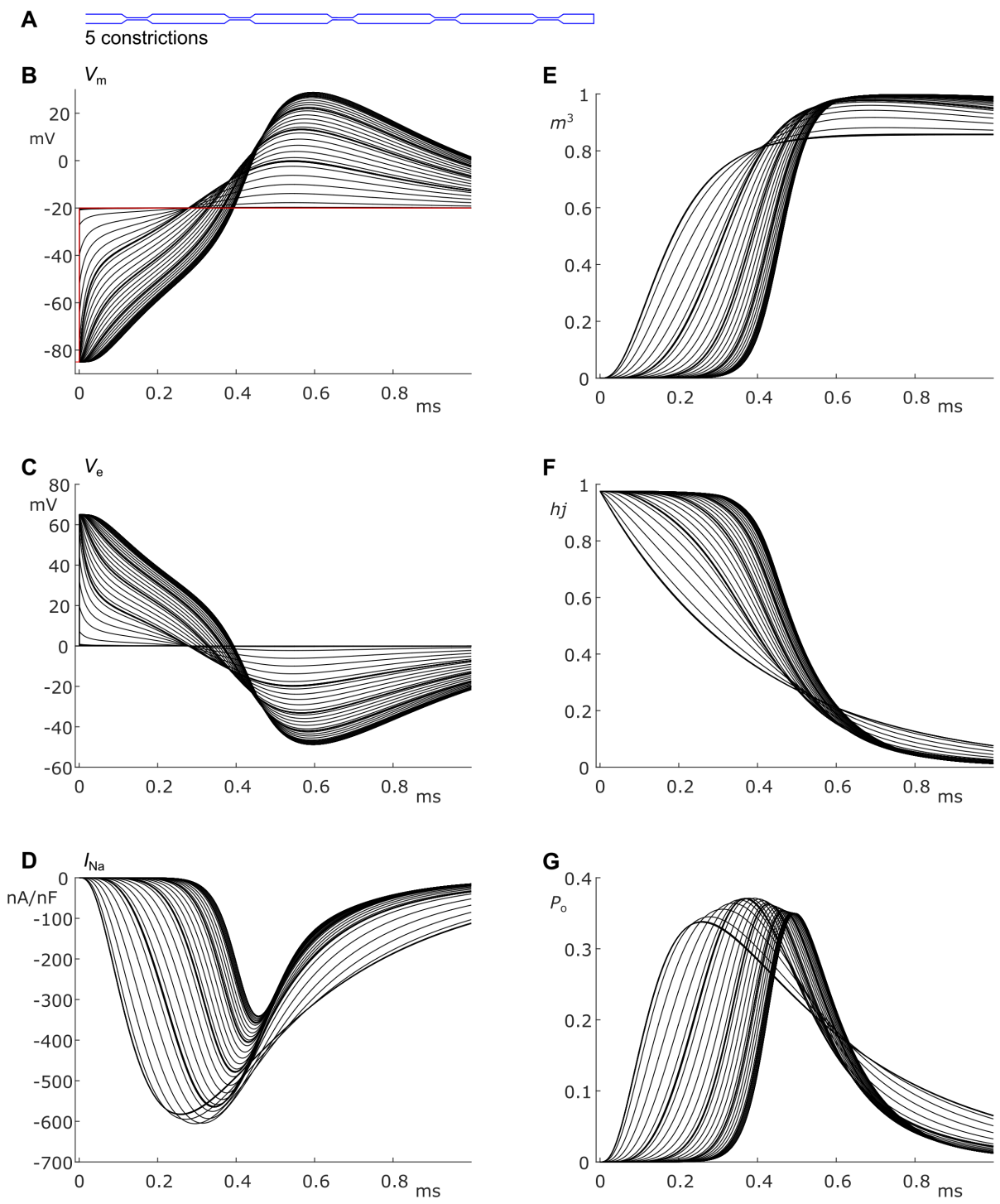


**Figure 3**. **Modeling sodium current in a murine T-tubule with five constrictions.** (**A**), Schematic representation of the morphology of the tubule (see **Table 1**). Membrane potentials (**B**), extracellular potential (**C**), and simulated sodium current density upon a voltage-clamp step of the tubule mouth from -85 to -20 mV (**D**) are given. The sodium current amplitude increases over the first constriction and decreases over the other constrictions, while activation is delayed and inactivation is faster in deeper segments of the tubules (**D**). This correlates with a higher driving force (**B**), and changes in the activation gates ($m^3$, **E**) and inactivation gates ($hj$, **F**). Peak open probability slightly increases in deeper T-tubular segments ($P_o$ defined as $m^3hj$, **G**).

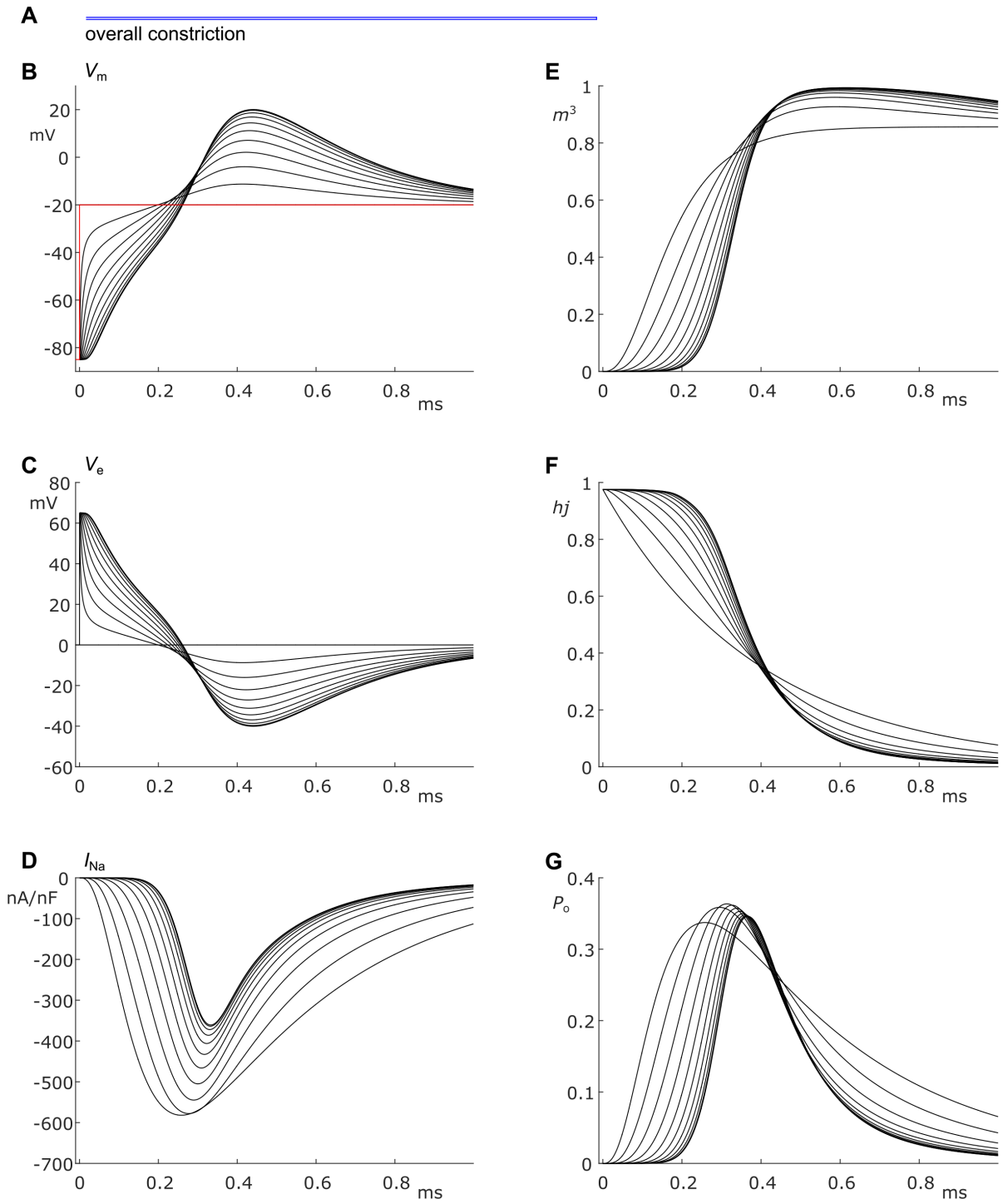


**Figure 4**. **Modeling sodium current in an overall constricted murine T-tubule.** (**A**), Schematic representation of the morphology of the tubule (see **Table 1**). Membrane potentials (**B**), extracellular potential (**C**), and simulated sodium current density upon a voltage-clamp step of the tubule mouth from -85 to -20 mV (**D**) are given. The sodium current decreases in deeper segments, while activation is delayed and inactivation is faster in deeper segments of the tubules (**D**). This correlates with a higher driving force (**B**), and changes in the activation gates ($m^3$, **E**) and inactivation gates ($hj$, **F**). Peak open probability slightly increases in deeper T-tubular segments ($P_o$ defined as $m^3hj$, **G**).

increased by a few percent, the increased driving force contributes more to the increase in peak sodium current.

## DISCUSSION

The results of our computational model show that the delay in T-tubular depolarization and T-tubular sodium current depend on the exact geometry of the T-tubule. The exact location of the constrictions and T-tubular branches are also expected to modulate these factors. We observed that L-type voltage gated calcium channels in deep T-tubular segments attain the activation threshold within a very short time after the cell surface is excited when the "exit resistance" of capacitive current is taken into account (~0.01 ms for a mouse T-tubule without constrictions and up to ~0.2 ms with five constrictions). Thus, the delay of depolarization of mouse and human T-tubules is sufficiently short to ensure excitation-contraction coupling. The T-tubular delay represents no major latency for the sodium current considering that the conduction time along a 100-µm-long cell with a macroscopic conduction velocity of 100 cm/s would be 100 µs (Rohr, 2004).

Human T-tubules depolarize quicker than murine T-tubules because they are relatively wide and short. On a cross-section of a cardiomyocyte, human T-tubules look like spokes on a wheel, and do not form intricate networks like in murine cells (Jayasinghe et al., 2015). The depolarization delay in human T-tubules is therefore negligible in this model. When adapting our model to simulate remodeled T-tubules after myocardial infarction, the activation threshold of calcium channels is reached even faster due to the loss of microfolds (Hong et al., 2014) and increase of luminal diameter (Wagner et al., 2012; Crossman et al., 2017b). The disturbed calcium cycling associated with disease should therefore have other causes, such as dyad uncoupling (Song et al., 2006). The T-tubular widening might however reduce the relative depletion of calcium and accumulation of potassium in the restricted T-tubular lumen, increasing the driving force of their respective ion channels (Hong and Shaw, 2017).

Without dilatations and constrictions, our model gives a negligible voltage drop of 0.117 mV (or 0.117%) at steady state from mouth to deep T-tubular node. This is comparable to previously reported results: for a rat T-tubule of 6.84 µm (Soeller and Cannell, 1999), Scardigli *et al.* calculated a length constant of 290 ± 90 µm and a voltage drop from the surface sarcolemma to the core of ~ -4 mV (Scardigli et al., 2017). Scardigli *et al.* however applied the equation for an infinite cable (Eq. 2); applying Eq. 3 for a sealed cable gives a voltage drop of 0.028 mV. A slightly larger but still minuscule value is found for the considerably smaller length constant of 68 µm derived by Uchida *et al.* in a finite element model of dextran diffusion in branched T-tubules with constrictions (Uchida and Lopatin, 2018). When assuming a murine T-tubule of 9 µm, the voltage drop would be 13 mV for an infinite cable and 0.870 mV for a sealed-end cable and is therefore still negligible. However, care must be taken when interpreting these values, since classic linear cable theory cannot be applied straightforwardly to morphologically heterogeneous T-tubules. Indeed, our simulation of a T-tubule with five constrictions show a voltage drop of -2.3 mV, about 20 times higher than the non-constricted tubule. This voltage drop does not affect the opening of voltage-gated channels, which open at much lower potentials.

When inserting the sodium current in our computational model, we found that the sodium current self-attenuates deep in the T-tubules, and the extracellular potential becomes negative (**Figure 2**). This is explained by the very small T-tubule diameter. At the cardiac intercalated disc, where two opposing membranes are also very close together, a similar effect has been predicted (Rhett et al., 2013; Veeraraghavan et al., 2015; Hichri et al., 2018). Importantly, sodium depletion in the T-tubule caused by sodium entering the cell may even augment the self-attenuation of the sodium current because this depletion will decrease the Nernst potential of sodium. Such a phenomenon has been modeled computationally at intercalated discs, but the influence of extracellular potentials nevertheless prevails over sodium depletion (Mori et al., 2008).

The self-attenuation of the sodium current will not affect the calcium current as this effect dies out before the calcium channels open. Interestingly, peak sodium current was increased in the first constriction of our five-constriction model due to a higher channel open probability and a greater driving force. Moreover, sodium current showed faster activation and inactivation kinetics in the deeper segments of the tubule due to the negative extracellular potentials, and the resulting more positive transmembrane potentials.

Given the self-attenuation of the sodium current, it may be interesting to investigate whether the late sodium current in deep T-tubular segments is also

quenched. This sodium current self-attenuation has also been predicted to occur at the intercalated disc (Greer-Short et al., 2017). However, this process might not play a substantial role in human cardiac arrhythmias, as human ventricular cardiomyocytes contain shorter and wider T-tubules than the murine tubules we modeled here.

Taken together, this study shows that biophysical properties of the sodium current as well as T-tubular depolarization greatly depend on T-tubular geometry. In our model, we did not incorporate elaborate tubular shapes (e.g., tapering of tubules next to constrictions, and tubule branching) or ion concentration changes. The first would require a finite element modeling approach and the second would require the implementation of ion fluxes using the Nernst-Planck equation. Both are numerically much more elaborate and demanding. Still, our simple model provides worthy insights into the electrical behavior of T-tubular nanodomains, and we believe that more advanced modeling would yield qualitatively similar results. Should the presence of functional sodium channels be confirmed in the future, it will therefore become of interest to develop such models to obtain a more comprehensive picture.

## CONFLICT OF INTEREST

The authors declare that the research was conducted in the absence of any commercial or financial relationships that could be construed as a potential conflict of interest.

## AUTHOR CONTRIBUTIONS

Conceptualization (SV), methodology (SV & JK), visualization (SV & JK), writing- original draft preparation (SV), reviewing and editing (SV, HA, JK), supervision (HA & JK), software (JK), formal analysis (JK).


## FUNDING

This work was supported by the Swiss National Science Foundation [grant no. 310030_165741 to HA; 310030_184707 to JK ].

## ACKNOWLEDGMENTS

The authors express their gratitude to Dr. Jean-Sébastien Rougier for thorough feedback on the manuscript.


## REFERENCES


Bers, D.M. (2002). Cardiac excitation-contraction coupling. *Nature* 415 (6868)**,** 198-205. doi: 10.1038/415198a.

Bhogal, N.K., Hasan, A., and Gorelik, J. (2018). The development of compartmentation of cAMP signaling in cardiomyocytes: the role of T-tubules and caveolae microdomains. *J Cardiovasc Dev Dis* 5(2). doi: 10.3390/jcdd5020025.

Brette, F., and Orchard, C.H. (2006). Density and sub-cellular distribution of cardiac and neuronal sodium channel isoforms in rat ventricular myocytes. *Biochem Biophys Res Commun* 348(3)**,** 1163-1166. doi: 10.1016/j.bbrc.2006.07.189.

Cannell, M.B., Crossman, D.J., and Soeller, C. (2006). Effect of changes in action potential spike configuration, junctional sarcoplasmic reticulum micro-architecture and altered t-tubule structure in human heart failure. *J Muscle Res Cell Motil* 27(5-7)**,** 297-306. doi: 10.1007/s10974-006-9089-y.

Crocini, C., Ferrantini, C., Coppini, R., and Sacconi, L. (2017). Electrical defects of the transverse-axial tubular system in cardiac diseases. *J Physiol* 595(12)**,** 3815-3822. doi: 10.1113/JP273042.

Crossman, D.J., Jayasinghe, I.D., and Soeller, C. (2017a). Transverse tubule remodelling: a cellular pathology driven by both sides of the plasmalemma? *Biophys Rev* 9(6)**,** 919-929. doi: 10.1007/s12551-017-0273-7.

Crossman, D.J., Shen, X., Jullig, M., Munro, M., Hou, Y., Middleditch, M., et al. (2017b). Increased collagen within the transverse tubules in human heart failure. *Cardiovasc Res* 113(8)**,** 879-891. doi: 10.1093/cvr/cvx055.

Greer-Short, A., George, S.A., Poelzing, S., and Weinberg, S.H. (2017). Revealing the Concealed Nature of Long-QT Type 3 Syndrome. *Circ Arrhythm Electrophysiol* 10(2)**,** e004400. doi: 10.1161/CIRCEP.116.004400.

Hatano, A., Okada, J., Washio, T., Hisada, T., and Sugiura, S. (2015). An integrated finite element simulation of cardiomyocyte function based on triphasic theory. *Front Physiol* 6**,** 287. doi: 10.3389/fphys.2015.00287.

Hichri, E., Abriel, H., and Kucera, J.P. (2018). Distribution of cardiac sodium channels in clusters potentiates ephaptic interactions in the intercalated disc. *J Physiol* 596(4)**,** 563-589. doi: 10.1113/JP275351.

Hong, T., and Shaw, R.M. (2017). Cardiac T-tubule microanatomy and function. *Physiol Rev* 97(1)**,** 227-252. doi: 10.1152/physrev.00037.2015.

Hong, T., Yang, H., Zhang, S.S., Cho, H.C., Kalashnikova, M., Sun, B., et al. (2014). Cardiac BIN1 folds T-tubule membrane, controlling ion flux and limiting arrhythmia. *Nat Med* 20 (6)**,** 624-632. doi: 10.1038/nm.3543.

Jack, J.J.B., Noble, D., and Tsien, R.W. (1975). "Nonlinear cable theory: conduction," in *Electric current flow in excitable cells*. (Oxford: Clarendon Press), 292-296.

Jayasinghe, I.D., Clowsley, A.H., Munro, M., Hou, Y., Crossman, D.J., and Soeller, C. (2015). Revealing T-tubules in striated muscle with new optical super-resolution microscopy techniquess. *European Journal of Translational Myology* 25(1)**,** 4747. doi: 10.4081/ejtm.2015.4747.

Koleske, M., Bonilla, I., Thomas, J., Zaman, N., Baine, S., Knollmann, B.C., et al. (2018). Tetrodotoxin-sensitive Navs contribute to early and delayed afterdepolarizations in long QT arrhythmia models. *J Gen Physiol* 150(7)**,** 991-1002. doi: 10.1085/jgp.201711909.

Livshitz, L., and Rudy, Y. (2009). Uniqueness and stability of action potential models during rest, pacing, and conduction using problem-solving environment. *Biophys J* 97

(5), 1265-1276. doi: 10.1016/j.bpj.2009.05.062.
Luo, C.H., and Rudy, Y. (1991). A model of the ventricular cardiac action potential. Depolarization, repolarization, and their interaction. *Circ Res* 68(6), 1501-1526.
Maier, S.K., Westenbroek, R.E., McCormick, K.A., Curtis, R., Scheuer, T., and Catterall, W.A. (2004). Distinct subcellular localization of different sodium channel alpha and beta subunits in single ventricular myocytes from mouse heart. *Circulation* 109(11), 1421-1427. doi: 10.1161/01.CIR.0000121421.61896.24.
Mohler, P.J., Rivolta, I., Napolitano, C., LeMaillet, G., Lambert, S., Priori, S.G., et al. (2004). Nav1.5 E1053K mutation causing Brugada syndrome blocks binding to ankyrin-G and expression of Nav1.5 on the surface of cardiomyocytes. *Proceedings of the National Academy of Sciences, USA* 101(50), 17533-17538. doi: 10.1073/pnas.0403711101.
Mori, Y., Fishman, G.I., and Peskin, C.S. (2008). Ephaptic conduction in a cardiac strand model with 3D electrodiffusion. *Proc Natl Acad Sci U S A* 105(17), 6463-6468. doi: 10.1073/pnas.0801089105.
Page, E. (1978). Quantitative ultrastructural analysis in cardiac membrane physiology. *American Journal of Physiology: Cell Physiology* 235(5), C147-158. doi: 10.1152/ajpcell.1978.235.5.C147.
Pinali, C., Bennett, H., Davenport, J.B., Trafford, A.W., and Kitmitto, A. (2013). Three-dimensional reconstruction of cardiac sarcoplasmic reticulum reveals a continuous network linking transverse -tubules: this organization is perturbed in heart failure. *Circulation Research* 113(11), 1219-1230. doi: 10.1161/CIRCRESAHA.113.301348.
Pinali, C., Malik, N., Davenport, J.B., Allan, L.J., Murfitt, L., Iqbal, M.M., et al. (2017). Post-Myocardial Infarction T-tubules Form Enlarged Branched Structures With Dysregulation of Junctophilin-2 and Bridging Integrator 1 (BIN-1). *J Am Heart Assoc* 6(5). doi: 10.1161/JAHA.116.004834.
Ponce-Balbuena, D., Guerrero-Serna, G., Valdivia, C.R., Caballero, R., Diez-Guerra, F.J., Jimenez-Vazquez, E.N., et al. (2018). Cardiac Kir2.1 and NaV1.5 channels traffic together to the sarcolemma to control excitability. *Circ Res* 122(11), 1501-1516. doi: 10.1161/circresaha.117.311872.
Rhett, J.M., Veeraraghavan, R., Poelzing, S., and Gourdie, R.G. (2013). The perinexus: sign-post on the path to a new model of cardiac conduction? *Trends Cardiovasc Med* 23(6), 222-228. doi: 10.1016/j.tcm.2012.12.005.
Rohr, S. (2004). Role of gap junctions in the propagation of the cardiac action potential. *Cardiovascular Research* 62 (2), 309-322. doi: 10.1016/j.cardiores.2003.11.035.
Rougier, J.-S., Essers, M.C., Gillet, L., Guichard, S., Sonntag, S., Shmerling, D., et al. (2019). A Distinct Pool of Nav1.5 Channels at the Lateral Membrane of Murine Ventricular Cardiomyocytes. *Frontiers in Physiology* 10(834). doi: 10.3389/fphys.2019.00834.
Scardigli, M., Crocini, C., Ferrantini, C., Gabbrielli, T., Silvestri, L., Coppini, R., et al. (2017). Quantitative assessment of passive electrical properties of the cardiac T-tubular system by FRAP microscopy. *Proceedings of the National Academy of Sciences, USA* 114(22), 5737-5742. doi: 10.1073/pnas.1702188114.
Seidel, T., Navankasattusas, S., Ahmad, A., Diakos, N.A., Xu, W.D., Tristani-Firouzi, M., et al. (2017). Sheet-like remodeling of the transverse tubular system in human heart failure impairs excitation-contraction coupling and functional recovery by mechanical unloading. *Circulation* 135(17), 1632-1645. doi: 10.1161/circulationaha.116.024470.
Shy, D., Gillet, L., Ogrodnik, J., Albesa, M., Verkerk, A.O., Wolswinkel, R., et al. (2014). PDZ domain-binding motif regulates cardiomyocyte compartment -specific NaV1.5 channel expression and function. *Circulation* 130(2), 147-160. doi: 10.1161/circulationaha.113.007852.
Soeller, C., and Cannell, M.B. (1999). Examination of the transverse tubular system in living cardiac rat myocytes by 2-photon microscopy and digital image-processing techniques. *Circ Res* 84(3), 266-275.
Song, L.S., Sobie, E.A., McCulle, S., Lederer, W.J., Balke, C.W., and Cheng, H. (2006). Orphaned ryanodine receptors in the failing heart. *Proceedings of the National Academy of Sciences, USA* 103(11), 4305-4310. doi: 10.1073/pnas.0509324103.
Uchida, K., and Lopatin, A.N. (2018). Diffusional and electrical properties of T-tubules are governed by their constrictions and dilations. *Biophys J* 114(2), 437-449. doi: 10.1016/j.bpj.2017.11.3742.
Veeraraghavan, R., Lin, J., Hoeker, G.S., Keener, J.P., Gourdie, R.G., and Poelzing, S. (2015). Sodium channels in the Cx43 gap junction perinexus may constitute a cardiac ephapse: an experimental and modeling study. *Pfluegers Archiv/European Journal of Physiology* 467(10), 2093-2105. doi: 10.1007/s00424-014-1675-z.
Vermij, S.H., Abriel, H., and Kucera, J.P. (2019). A fundamental evaluation of the electrical properties and function of cardiac transverse tubules. *Biochimica et Biophysica Acta (BBA) - Molecular Cell Research*. doi: https://doi.org/10.1016/j.bbamcr.2019.06.016.
Wagner, E., Lauterbach, M.A., Kohl, T., Westphal, V., Williams, G.S., Steinbrecher, J.H., et al. (2012). Stimulated emission depletion live-cell super-resolution imaging shows proliferative remodeling of T-tubule membrane structures after myocardial infarction. *Circ Res* 111(4), 402-414. doi: 10.1161/circresaha.112.274530.
Weidmann, S. (1952). The electrical constants of Purkinje fibres. *J Physiol* 118(3), 348-360.
Westenbroek, R.E., Bischoff, S., Fu, Y., Maier, S.K., Catterall, W.A., and Scheuer, T. (2013). Localization of sodium channel subtypes in mouse ventricular myocytes using

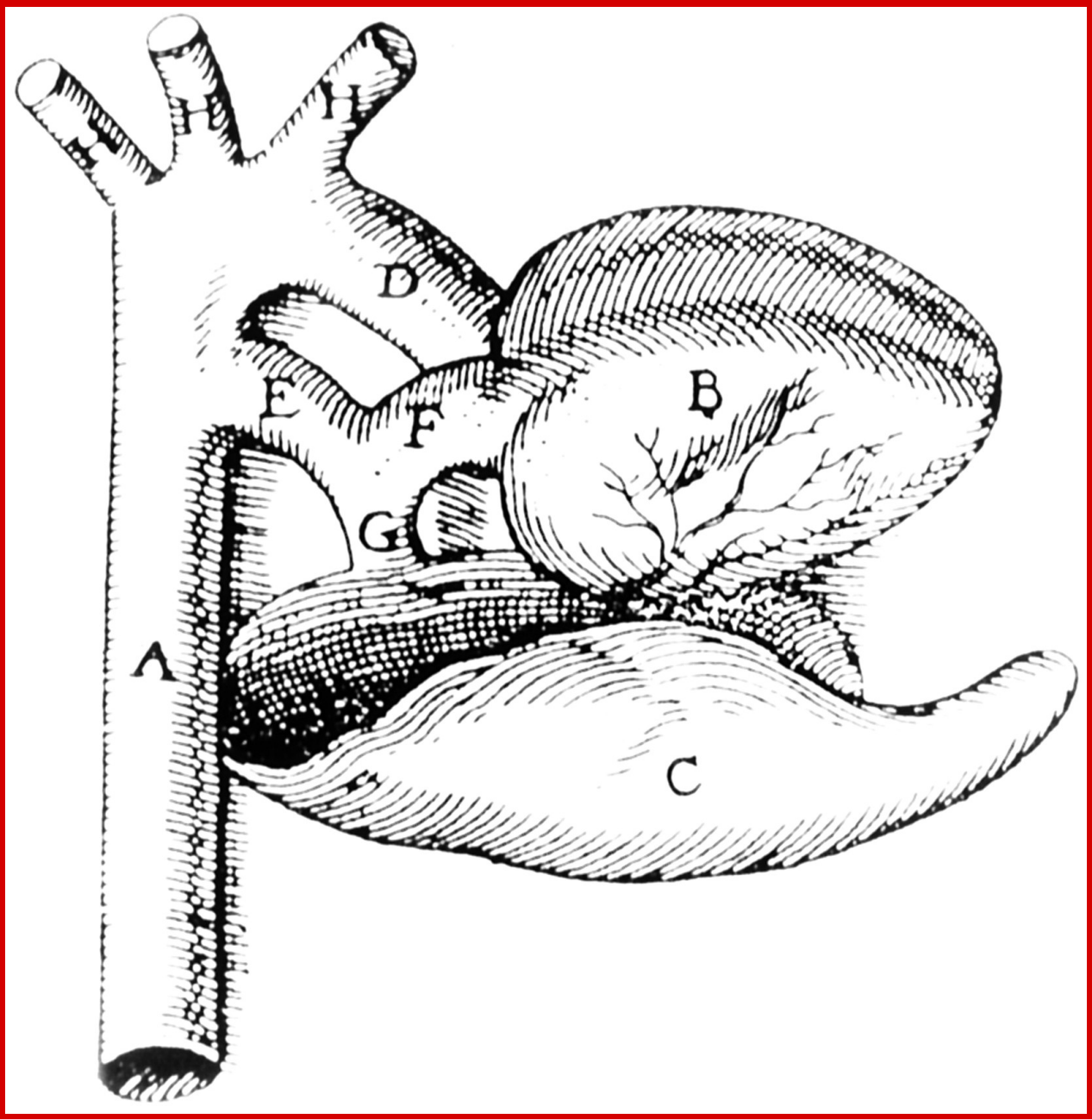


# GENERAL CONCLUSION

# 4. GENERAL CONCLUSION

Motivated by the unexplained variability of *SCN5A*-related arrhythmias, this thesis aimed to contribute to the fundamental understanding of cardiac excitability by differentiating $Na_v1.5$ expression, organization, and function within the cardiomyocyte landscape.

The main findings of this thesis are that (1) $Na_v1.5$ is expressed in murine T-tubules; (2) a large T-tubular sodium current would self-attenuate slightly; (2) $Na_v1.5$ cluster organization and density at the lateral membrane and T-tubules of murine cardiomyocytes partly depend on dystrophin and the $Na_v1.5$ C-terminal SIV motif; (3) of the voltage-gated sodium channels, murine Black/6J cardiomyocytes express mRNA encoding only $Na_v1.5$, $Na_v1.4$, and (much less) $Na_v2.1$, and β-subunits $\beta_1$ and $\beta_4$.

The specific functions of the T-tubular population of $Na_v1.5$ channels remain unknown. They are firstly expected to support macroscopic conduction (see **Figure 3** in **Section 1.7.3**). The loss of T-tubules in heart disease would affect conduction depending on the concomitant change in overall sodium channel density: if the sodium channel density is higher in the bulk sarcolemma than in the T-tubules, a loss of T-tubules may result in a net increase in conduction velocity. When heart disease however correlates with a loss-of-function mutation in *SCN5A* or *SCN5A* haploinsufficiency, loss of T-tubules may still result in a net reduction in conduction velocity, even considering the loss in membrane load.

We observed that T-tubular $Na_v1.5$ channels have different biophysical properties than those at the lateral membrane due to T-tubular constrictions and dilations, likely without significantly affecting the action potential (see **Figures 2-4** in **Section 3.3**). T-tubular microfolds may slow luminal ion diffusion and cause sodium depletion during the upstroke of the action potential, which may limit the T-tubular peak sodium current. We however did not model geometrical microfold shapes, but did consider an increase in the membrane capacitance due to the microfold-induced increase in membrane load (**Section 3.3**). In heart disease, T-tubular widening and loss of microfolds likely increase ion diffusion, which might have arrhythmogenic effects[180] as the amplitude of the T-tubular sodium current increases and the sodium current no longer self-attenuates. To understand heart disease on a T-tubular level, these changes in sodium channel function have to be considered together with structural changes such as dyad uncoupling and physical obstruction of T-tubules[181,182]. *Mdx* cardiomyocytes moreover show dyad uncoupling and T-tubular remodeling, in addition to costamere and crest remodeling, leading to calcium dysregulation and a fragile sarcolemma[183]. When considering our observation of increased T-tubular $Na_v1.5$ expression in these cells (see **Section 3.1**), one may hypothesize that this will lead to a relative increase of intracellular sodium concentration during the upstroke of the action potential, which may lead to a stronger NCX-mediated inward $Ca^{2+}$ current. This may contribute to the calcium handling defects observed in *mdx* cells[127], but the opposite, aiding excitation-contraction coupling, may also be possible[184]. Future research should investigate these possibilities.

We may hypothesize that a high proportion of sodium channels exposed to very narrow extracellular spaces – at the T-tubules, intercalated disc, and possibly even at tight-junction-like structures at the lateral membrane[7] – may protect against cardiac arrhythmias. This hypothesis is based on extension of the findings from Greer-Short *et al.*[163], who found that the narrow intercellular cleft at the intercalated disc could suppress the late sodium current, which might also occur in the T-tubules. In disease, T-tubular widening and microfold loss would then expose the late sodium current when a sodium channel mutation increased the open probability of the channel, which might have arrhythmogenic effects. Although computer models of sodium currents in T-tubules and at the intercalated disc exist[73,78,163,179,185], the variability in extracellular spaces have not yet been integrated into a whole-cell model. This would be a very interesting field of further study, although it would require considerable computational power.

$Na_v1.5$ at the T-tubules may also has non-canonical effects. Preliminary data from our group indicate that $Na_v1.5$ and $Ca_v1.2$ interact in heterologous expression systems (unpublished data). In cardiomyocytes, such an interaction is primarily expected in T-tubules and suggests the presence of a sodium-calcium-handling microdomain and possibly even joint transcription, translation, and/or trafficking of these channels. Bin1 may play a role in this interaction, as it is involved in trafficking and scaffolding of $Ca_v1.2$[186]. If the interaction $Ca_v1.2$-$Na_v1.5$ is confirmed in cardiomyocytes, it is likely that $Na_v1.5$ is very close to the dyad. An inward sodium current at the dyad would induce the reverse mode of NCX during phase 0 of the action potential, which might prime the dyadic cleft with calcium and support excitation-contraction coupling[187]. In heart disease, dyad uncoupling may therefore have deleterious effects due to the loss of $Na_v1.5$-mediated dyadic priming as well as due to the loss of the "classical" $Ca_v1.2$-mediated calcium-induced calcium release[68]. A loss-of-function mutation in *SCN5A* may also abolish this dyadic priming and delay excitation-contraction coupling without structurally affecting the dyad. Conversely, an increased $I_{Na,late}$ due to a gain-of-function *SCN5A* mutation can lead to calcium dysregulation. The $I_{Na,late}$-mediated sodium loading of the cytoplasm reduces the gradient for NCX-mediated calcium efflux, and causes intracellular calcium overload[149]. This may lead to arrhythmogenic DADs.

Unfortunately, we could not record a T-tubular sodium current (see **Section 3.1**). Alternative techniques are currently not available; cell-attached patch-clamp recordings do not allow access to the T-tubules[117] and scanning ion conductance microscopy cannot clamp an entire T-tubule or go deep enough inside[170]. Assessing the T-tubular sodium current requires a much more specific approach. Theoretically, this could be addressed in channelrhodopsin-expressing cardiomyocytes. T-tubules could be loaded with fluorescent dye, electrically isolated, and excited with light while tracking the depolarization with an electron-multiplying charge-coupled device (EMCCD) or sCMOS camera (as

described in **Section 3.1**). Based on the different TTX sensitivity of $Na_v$ isoforms[188], Adding different TTX concentrations would then confirm the presence or absence of cardiac or neuronal $Na_v$ isoforms.

Of the voltage-gated sodium channels, mRNAs encoding only $Na_v1.5$, $Na_v1.4$, and $Na_v2.1$ are found in cardiomyocytes from our Black6/J mice; however, their relative protein expression levels, contribution to whole-cell sodium current, localization patterns, and respective macromolecular complexes remain unknown. Of note, sodium channel expression seems to differ greatly between animal models (see **Section 1.7.3**). It is therefore pivotal to thoroughly characterize any animal model before using it for ion channel studies. Although mRNA levels are not necessarily proportional to protein levels, we hypothesize that the *Scn7a*-encoded channel $Na_v2.1$ would not conduct a significant sodium current in Black6/J cardiomyocytes – especially since this channel is sodium concentration rather than voltage sensitive[176]. We expect significant $Na_v1.4$ protein expression, but given the positive shift in voltage dependence of activation compared to $Na_v1.4$ (see **Section 3.2.1**), whether $Na_v1.4$ contributes significantly to cardiac conduction remains an open question.

Preliminary data from our group obtained in heterologous expression systems show that $Na_v1.5$ and $Na_v1.4$ may interact (unpublished data). This interaction may occur at the lateral membrane, as Lin *et al.* reported that TTX-sensitive channels – including $Na_v1.4$[189] – are more prevalent at the lateral membrane than at the intercalated disc[88]. At the lateral membrane, steady-state activation was shifted in the depolarized direction and steady-state inactivation in the hyperpolarized direction compared to the intercalated disc[88]. Therefore, Lin *et al.* concluded that TTX-sensitive channels contribute little to whole-cell sodium current under control conditions[88]. These findings correlate with the positive shift in $Na_v1.4$ steady-state inactivation and activation curves compared to $Na_v1.5$ that our group identified in HEK cells[177] (see also **Figure 13** and **Section 3.3.1**). Although no data on $Na_v1.4$ localization in cardiomyocytes are available, we may deduce from our[76] and Lin *et al.*'s[88] findings that $Na_v1.4$ is expressed at the lateral membrane. $Na_v1.4$ might play noncanonical roles[92], for instance in the trafficking of other ion channels, or conduct significant sodium currents in certain disease conditions, such as in the context of *SCN5A* loss-of-function mutations.

The differences in biophysical properties of the sodium channel between the lateral membrane and the intercalated disc may also be caused by differences in macromolecular complex, which have been addressed in **Section 1.6.4**. The $\beta_1$-subunit seems to be confined to the intercalated disc, whereas $\beta_4$ seems to be expressed at the T-tubules[178]; however, this requires more detailed investigation. Interestingly, $\beta_3$-subunits have been shown to assemble into trimers and $Na_v1.5$ seems to have four $\beta_3$-binding sites[105]. Whether $Na_v1.5$ and $\beta_1$, the latter being structurally similar to $\beta_3$[112], assemble in a similar way in cardiomyocytes remains an open question.

The groove-specific reduction of $Na_v1.5$ expression in ΔSIV mice may indicate that the syntrophin-dystrophin complex partially anchors $Na_v1.5$ to the groove. The high variability of $Na_v1.5$ expression in *mdx* mice masked any effect that might have occurred, which implies that dystrophin-deficient cells may apply many different compensatory mechanisms. To better understand $Na_v1.5$ cluster organization at the lateral membrane, we first need to direct our efforts to improve the preservation of the crest, as euthanasia by cervical dislocation tends to disrupt the crest structure, and mitochondria under the crest tend to remodel very fast *ex vivo*[7]. Claudin may serve as a good crest marker to characterize $Na_v1.5$ clusters specifically at the crest in different genetic backgrounds[7].

The simpler cluster shapes we observed at the lateral membrane of *mdx* cells and at the T-tubules of *mdx* and ΔSIV cells (see **Section 3.1**) may reflect a change in composition of their respective macromolecular complexes. Future research should be directed to addressing the organization of (candidate) site-specific interacting proteins, including CASK, $\alpha_1$-syntrophin, ankyrins, Dp71, and SAP97.

In summary, these findings indicate that the cardiomyocyte lateral membrane and T-tubules are crucial stages for differential $Na_v1.5$ function and regulation. Understanding these fundamental processes in their cellular microdomains is probably crucial to link a mutation to a detailed cellular phenotype and the respective clinical manifestation.

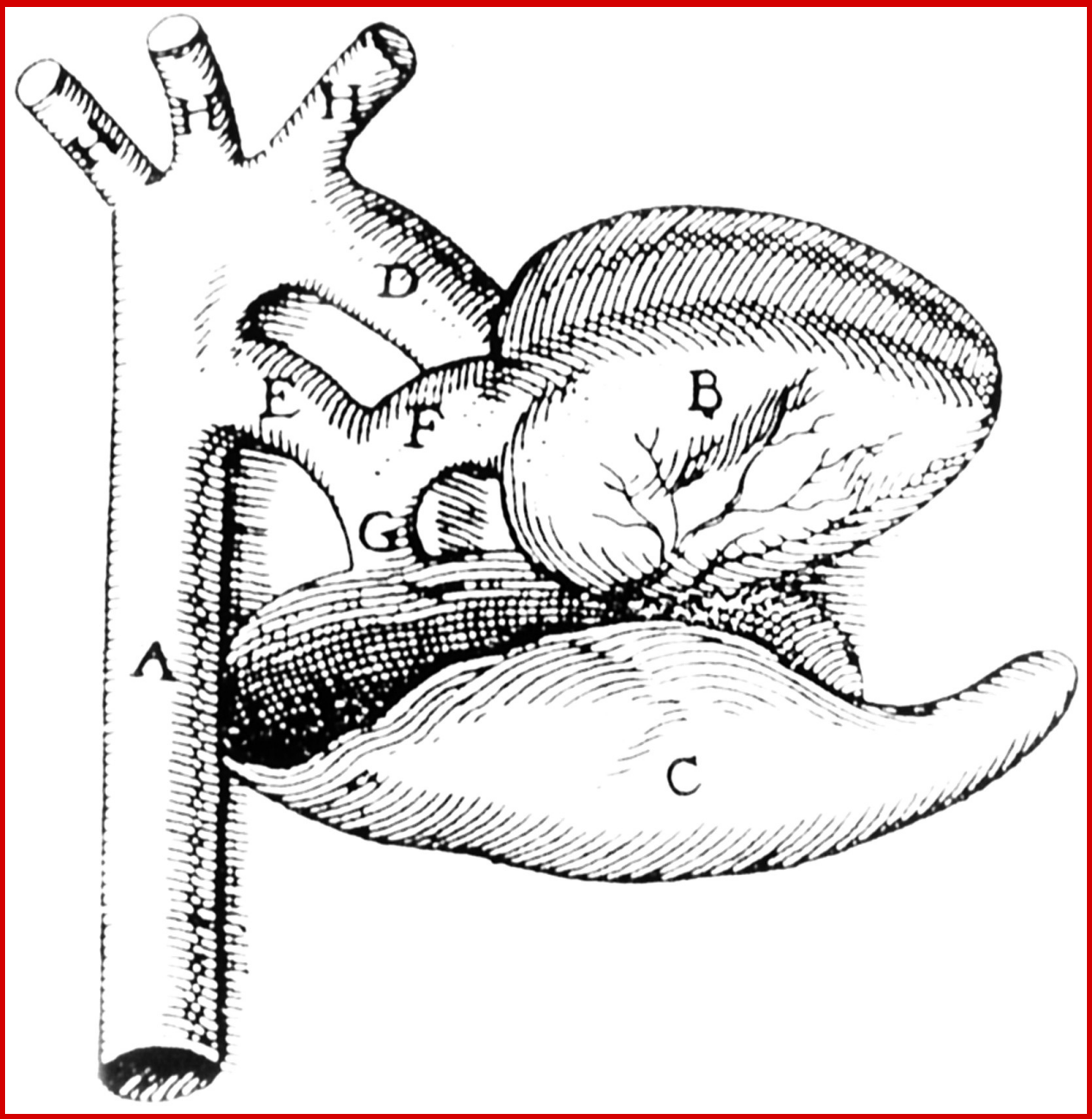


# REFERENCES

# 5. REFERENCES


1 Loukas, M., Youssef, P., Gielecki, J., Walocha, J., Natsis, K. & Tubbs, R. S. History of cardiac anatomy: a comprehensive review from the Egyptians to today. *Clin. Anat.* **29**, 270-284, doi:10.1002/ca.22705 (2016).

2 Hinard, V., Britan, A., Rougier, J. S., Bairoch, A., Abriel, H. & Gaudet, P. ICEPO: the ion channel electrophysiology ontology. *Database (Oxford)* **2016**, doi:10.1093/database/baw017 (2016).

3 Vermij, S. H., Abriel, H. & van Veen, T. A. Refining the molecular organization of the cardiac intercalated disc. *Cardiovasc. Res.* **113**, 259-275, doi:10.1093/cvr/cvw259 (2017).

4 Netter, F. H. *Atlas der Anatomie*. 6. Auflage ed. (Elsevier Urban & Fischer, 2014).

5 Luo, C. H. & Rudy, Y. A model of the ventricular cardiac action potential. Depolarization, repolarization, and their interaction. *Circ. Res.* **68**, 1501-1526 (1991).

6 Lab, M. J., Bhargava, A., Wright, P. T. & Gorelik, J. The scanning ion conductance microscope for cellular physiology. *Am. J. Physiol. Heart Circ. Physiol.* **304**, H1-11, doi:10.1152/ajpheart.00499.2012 (2013).

7 Guilbeau-Frugier, C., Cauquil, M., Karsenty, C. *et al.* Structural evidence for a new elaborate 3D-organization of the cardiomyocyte lateral membrane in adult mammalian cardiac tissues. *Cardiovasc. Res.* **115**, 1078-1091, doi:10.1093/cvr/cvy256 (2019).

8 Abriel, H., Rougier, J. S. & Jalife, J. Ion channel macromolecular complexes in cardiomyocytes: roles in sudden cardiac death. *Circ. Res.* **116**, 1971-1988, doi:10.1161/CIRCRESAHA.116.305017 (2015).

9 Catterall, W. A. & Zheng, N. Deciphering voltage-gated Na(+) and Ca(2+) channels by studying prokaryotic ancestors. *Trends Biochem. Sci.* **40**, 526-534, doi:10.1016/j.tibs.2015.07.002 (2015).

10 Pan, X., Li, Z., Zhou, Q. *et al.* Structure of the human voltage-gated sodium channel Nav1.4 in complex with beta1. *Science* **362**, doi:10.1126/science.aau2486 (2018).

11 Conti, C. R. *The Netter Collection of Medical Illustrations: Cardovascular System*. 2nd ed. (2014).

12 Fisch, C. Centennial of the string galvanometer and the electrocardiogram. *J. Am. Coll. Cardiol.* **36**, 1737-1745 (2000).

13 Nerbonne, J. M., Nichols, C. G., Schwarz, T. L. & Escande, D. Genetic manipulation of cardiac K(+) channel function in mice: what have we learned, and where do we go from here? *Circ. Res.* **89**, 944-956 (2001).

14 Luderitz, B. Wenn das Herz aus dem Takt gerät... Zur Geschichte der Herzrhzthmusstörungen und ihrer Therapie mit antiarrhythmischen Substanzen. *Z Kardiol* **85 Suppl 6**, 11-23 (1996).

15 Hong, T. & Shaw, R. M. Cardiac T-tubule microanatomy and function. *Physiol. Rev.* **97**, 227-252, doi:10.1152/physrev.00037.2015 (2017).

16 Asfaw, T. N. & Bondarenko, V. E. A Mathematical Model of the Human Cardiac Na(+) Channel. *J. Membr. Biol.* **252**, 77-103, doi:10.1007/s00232-018-00058-x (2019).

17 Ghosh, S., Tran, K., Delbridge, L. M. D., Hickey, A. J. R., Hanssen, E., Crampin, E. J. & Rajagopal, V. Insights on the impact of mitochondrial organisation on bioenergetics in high-resolution computational models of cardiac cell architecture. *PLoS Comput Biol* **14**, e1006640, doi:10.1371/journal.pcbi.1006640 (2018).

18 Maguy, A., Hebert, T. E. & Nattel, S. Involvement of lipid rafts and caveolae in cardiac ion channel function. *Cardiovasc. Res.* **69**, 798-807, doi:10.1016/j.cardiores.2005.11.013 (2006).

19 Levin, K. R. & Page, E. Quantitative studies on plasmalemmal folds and caveolae of rabbit ventricular myocardial cells. *Circ. Res.* **46**, 244-255 (1980).

20 Doroudgar, S. & Glembotski, C. C. New concepts of endoplasmic reticulum function in the heart: programmed to conserve. *J. Mol. Cell Cardiol.* **55**, 85-91, doi:10.1016/j.yjmcc.2012.10.006 (2013).

21 Michalak, M. & Opas, M. Endoplasmic and sarcoplasmic reticulum in the heart. *Trends Cell Biol.* **19**, 253-259, doi:10.1016/j.tcb.2009.03.006 (2009).

22 Boron, W. F. & Boulpaep, E. L. *Medical Physiology*. 2nd edition ed. (Saunders Elsevier, 2009).

23 Vermij, R. *Kleine geschiedenis van de wetenschap*. 3rd ed. (Niewezijds, 2007).

24 Castellano, N. *The Book of the Dead was Egyptians' inside guide to the underworld*, <https://www.nationalgeographic.com/archaeology-and-history/magazine/2016/01-02/egypt-book-of-the-dead/> (2019).

25 Fauklner, R. O. A., C.; Wasserman, J. *The Egyptian Book of the Dead: The book of going forth by day*. (Chronicle Books, 2008).

26 Hajar, R. Learning Ancient Greek Medicine from Homer. *Heart Views* **3** (2002).

27 Bonuccelli, G., Sotgia, F., Schubert, W. *et al.* Proteasome inhibitor (MG-132) treatment of mdx mice rescues the expression and membrane localization of dystrophin and dystrophin-associated proteins. *Am J Pathol* **163**, 1663-1675, doi:10.1016/S0002-9440(10)63523-7 (2003).

28 Katz, A. M. & Katz, P. B. Diseases of the heart in the works of Hippocrates. *Br Heart J* **24**, 257-264, doi:10.1136/hrt.24.3.257 (1962).
29 Crivellato, E. & Ribatti, D. Aristotle: the first student of angiogenesis. *Leukemia* **20**, 1209-1210, doi:10.1038/sj.leu.2404256 (2006).
30 Baruch, J. Z. *Leven en werk van Andreas Vesalius*. (Kruzeman's, 1964).
31 Margocsy, D., Somos, M. & Joffe, S. N. Sex, religion and a towering treatise on anatomy. *Nature* **560**, 304-305, doi:10.1038/d41586-018-05941-0 (2018).
32 Pagel, W. *William Harvey's Biological Ideas*. (S. Karger, 1967).
33 Tubbs, R. S., Gianaris, N., Shoja, M. M., Loukas, M. & Cohen Gadol, A. A. "The heart is simply a muscle" and first description of the tetralogy of "Fallot". Early contributions to cardiac anatomy and pathology by bishop and anatomist Niels Stensen (1638-1686). *Int J Cardiol* **154**, 312-315, doi:10.1016/j.ijcard.2010.09.055 (2012).
34 Bradham, R. R. & Parker, E. F. The cardiac lymphatics. *Ann Thorac Surg* **15**, 526-535 (1973).
35 Schölvinck, A.-F. M., Pittens, C. A. C. M. & Broerse, J. E. W. The Research Priorities of People with Visual Impairments in the Netherlands. *Journal of Visual Impairment & Blindness* **111**, 201-217, doi:10.1177/0145482x1711100302 (2017).
36 van der Zwaard, W. *Welfare chauvinism* MA History thesis, Utrecht University, (2014).
37 Giovanni Maria Lancisi (2019). In: *Encyclopædia Brittanica,* ed.
38 Clark-Kennedy, A. E. Stephen Hales, DD, FRS. *Br. Med. J.* **2**, 1656-1658, doi:10.1136/bmj.2.6103.1656 (1977).
39 Galvani, Luigi (1911). In: *Encyclopædia Britannica,* 11th ed.
40 Matteucci, M. C. Deuxième mémoire sur le courant électrique propre de la grenouille et sur celui des animaux a sang chaud. *Annales de Chimie et de Physique* **3** (1842).
41 Fye, W. B. Rudolf Albert von Koelliker. *Clin Cardiol* **22**, 376-377, doi:10.1002/clc.4960220517 (1999).
42 Carmeliet, E. From Bernstein's rheotome to Neher-Sakmann's patch electrode. The action potential. *Physiol Rep* **7**, e13861, doi:10.14814/phy2.13861 (2019).
43 Hodgkin, A. L. The relation between conduction velocity and the electrical resistance outside a nerve fibre. *J. Physiol.* **94**, 560-570, doi:10.1113/jphysiol.1939.sp003702 (1939).
44 Miller, D. J. Sydney Ringer; physiological saline, calcium and the contraction of the heart. *J. Physiol.* **555**, 585-587, doi:10.1113/jphysiol.2004.060731 (2004).
45 Silverman, M. E. Willem Einthoven--the father of electrocardiography. *Clin Cardiol* **15**, 785-787, doi:10.1002/clc.4960151020 (1992).
46 Glynn, I. *Elegance in Science: The Beauty of Simplicity*. (Oxford University Press Inc., 2010).
47 Hille, B. *Ion channels of exitable membranes*. 3rd ed. (Sinauer Associates, Inc., 2001).
48 Carmeliet, E. Conduction in cardiac tissue. Historical reflections. *Physiol Rep* **7**, e13860, doi:10.14814/phy2.13860 (2019).
49 Zhou, P. & Pu, W. T. Recounting Cardiac Cellular Composition. *Circ. Res.* **118**, 368-370, doi:10.1161/CIRCRESAHA.116.308139 (2016).
50 Pinto, A. R., Ilinykh, A., Ivey, M. J. *et al.* Revisiting Cardiac Cellular Composition. *Circ. Res.* **118**, 400-409, doi:10.1161/CIRCRESAHA.115.307778 (2016).
51 Hulsmans, M., Clauss, S., Xiao, L. *et al.* Macrophages Facilitate Electrical Conduction in the Heart. *Cell* **169**, 510-522 e520, doi:10.1016/j.cell.2017.03.050 (2017).
52 Gaborit, B., Venteclef, N., Ancel, P. *et al.* Human epicardial adipose tissue has a specific transcriptomic signature depending on its anatomical peri-atrial, peri-ventricular, or peri-coronary location. *Cardiovasc. Res.* **108**, 62-73, doi:10.1093/cvr/cvv208 (2015).
53 Tracy, R. E. & Sander, G. E. Histologically measured cardiomyocyte hypertrophy correlates with body height as strongly as with body mass index. *Cardiol Res Pract* **2011**, 658958, doi:10.4061/2011/658958 (2011).
54 Sorenson, A. L., Tepper, D., Sonnenblick, E. H., Robinson, T. F. & Capasso, J. M. Size and shape of enzymatically isolated ventricular myocytes from rats and cardiomyopathic hamsters. *Cardiovasc. Res.* **19**, 793-799, doi:10.1093/cvr/19.12.793 (1985).
55 Paradis, A. N., Gay, M. S. & Zhang, L. Binucleation of cardiomyocytes: the transition from a proliferative to a terminally differentiated state. *Drug Discov. Today* **19**, 602-609, doi:10.1016/j.drudis.2013.10.019 (2014).
56 Bensley, J. G., De Matteo, R., Harding, R. & Black, M. J. Three-dimensional direct measurement of cardiomyocyte volume, nuclearity, and ploidy in thick histological sections. *Scientific Reports* **6**, 23756, doi:10.1038/srep23756 (2016).
57 Stephen, M. J., Poindexter, B. J., Moolman, J. A., Sheikh-Hamad, D. & Bick, R. J. Do binucleate cardiomyocytes have a role in myocardial repair? Insights using isolated rodent myocytes and cell culture. *Open Cardiovasc Med J* **3**, 1-7, doi:10.2174/1874192400903010001 (2009).

58 Kleber, A. G. & Rudy, Y. Basic mechanisms of cardiac impulse propagation and associated arrhythmias. *Physiol. Rev.* **84**, 431-488, doi:10.1152/physrev.00025.2003 (2004).

59 Plonsey, R. & Barr, R. C. in *Bioelectricity, a quantitative approach* (3rd ed.) Ch. 9, 267-323 (Springer, New York, 2007).

60 Brandenburg, S., Pawlowitz, J., Fakuade, F. E. *et al.* Axial tubule junctions activate atrial Ca(2+) release across species. *Front. Physiol.* **9**, 1227, doi:10.3389/fphys.2018.01227 (2018).

61 Brandenburg, S., Arakel, E. C., Schwappach, B. & Lehnart, S. E. The molecular and functional identities of atrial cardiomyocytes in health and disease. *Biochim. Biophys. Acta* **1863**, 1882-1893, doi:10.1016/j.bbamcr.2015.11.025 (2016).

62 Bhogal, N. K., Hasan, A. & Gorelik, J. The development of compartmentation of cAMP signaling in cardiomyocytes: the role of T-tubules and caveolae microdomains. *J. Cardiovasc. Dev. Dis.* **5**, doi:10.3390/jcdd5020025 (2018).

63 Vatta, M., Ackerman, M. J., Ye, B. *et al.* Mutant caveolin-3 induces persistent late sodium current and is associated with long-QT syndrome. *Circulation* **114**, 2104-2112, doi:10.1161/CIRCULATIONAHA.106.635268 (2006).

64 Yarbrough, T. L., Lu, T., Lee, H. C. & Shibata, E. F. Localization of cardiac sodium channels in caveolin-rich membrane domains: regulation of sodium current amplitude. *Circ. Res.* **90**, 443-449 (2002).

65 Dague, E., Genet, G., Lachaize, V. *et al.* Atomic force and electron microscopic-based study of sarcolemmal surface of living cardiomyocytes unveils unexpected mitochondrial shift in heart failure. *J. Mol. Cell Cardiol.* **74**, 162-172, doi:10.1016/j.yjmcc.2014.05.006 (2014).

66 Glancy, B., Hartnell, L. M., Combs, C. A. *et al.* Power Grid Protection of the Muscle Mitochondrial Reticulum. *Cell Rep.* **19**, 487-496, doi:10.1016/j.celrep.2017.03.063 (2017).

67 Hayashi, T., Martone, M. E., Yu, Z. *et al.* Three-dimensional electron microscopy reveals new details of membrane systems for Ca2+ signaling in the heart. *J. Cell Sci.* **122**, 1005-1013, doi:10.1242/jcs.028175 (2009).

68 Bers, D. M. Cardiac excitation-contraction coupling. *Nature* **415**, 198-205, doi:10.1038/415198a (2002).

69 Avila-Medina, J., Mayoral-Gonzalez, I., Dominguez-Rodriguez, A. *et al.* The Complex Role of Store Operated Calcium Entry Pathways and Related Proteins in the Function of Cardiac, Skeletal and Vascular Smooth Muscle Cells. *Front. Physiol.* **9**, 257, doi:10.3389/fphys.2018.00257 (2018).

70 Schram, G., Pourrier, M., Melnyk, P. & Nattel, S. Differential distribution of cardiac ion channel expression as a basis for regional specialization in electrical function. *Circ. Res.* **90**, 939-950 (2002).

71 Shaw, R. M. & Rudy, Y. Ionic mechanisms of propagation in cardiac tissue. Roles of the sodium and L-type calcium currents during reduced excitability and decreased gap junction coupling. *Circ. Res.* **81**, 727-741 (1997).

72 Rohr, S., Kucera, J. P. & Kleber, A. G. Slow conduction in cardiac tissue, I: effects of a reduction of excitability versus a reduction of electrical coupling on microconduction. *Circ. Res.* **83**, 781-794 (1998).

73 Hichri, E., Abriel, H. & Kucera, J. P. Distribution of cardiac sodium channels in clusters potentiates ephaptic interactions in the intercalated disc. *J. Physiol.* **596**, 563-589, doi:10.1113/JP275351 (2018).

74 Zhang, X. C., Yang, H., Liu, Z. & Sun, F. Thermodynamics of voltage-gated ion channels. *Biophys Rep* **4**, 300-319, doi:10.1007/s41048-018-0074-y (2018).

75 Silverthorn, D. U. *Human Physiology: An Integrated Approach*. 4th ed. (Pearson Education, Inc., 2009).

76 Chevalier, M., Vermij, S. H., Wyler, K., Gillet, L., Keller, I. & Abriel, H. Transcriptomic analyses of murine ventricular cardiomyocytes. *Sci. Data* **5**, 180170, doi:10.1038/sdata.2018.170 (2018).

77 Gourdie, R. G. The Cardiac Gap Junction has Discrete Functions in Electrotonic and Ephaptic Coupling. *Anat Rec (Hoboken)* **302**, 93-100, doi:10.1002/ar.24036 (2019).

78 Mori, Y., Fishman, G. I. & Peskin, C. S. Ephaptic conduction in a cardiac strand model with 3D electrodiffusion. *Proc Natl Acad Sci U S A* **105**, 6463-6468, doi:10.1073/pnas.0801089105 (2008).

79 Rhett, J. M., Veeraraghavan, R., Poelzing, S. & Gourdie, R. G. The perinexus: sign-post on the path to a new model of cardiac conduction? *Trends Cardiovasc. Med.* **23**, 222-228, doi:10.1016/j.tcm.2012.12.005 (2013).

80 Veeraraghavan, R., Hoeker, G. S., Alvarez-Laviada, A. *et al.* The adhesion function of the sodium channel beta subunit (beta1) contributes to cardiac action potential propagation. *Elife* **7**, doi:10.7554/eLife.37610 (2018).

81 Lin, J. & Keener, J. P. Ephaptic coupling in cardiac myocytes. *IEEE Trans. Biomed. Eng.* **60**, 576-582, doi:10.1109/TBME.2012.2226720 (2013).

82 Kucera, J. P., Rohr, S. & Rudy, Y. Localization of sodium channels in intercalated disks modulates cardiac conduction. *Circ. Res.* **91**, 1176-1182 (2002).

83 Hogues, H., Leon, L. J. & Roberge, F. A. A model study of electric field interactions between cardiac myocytes. *IEEE Trans. Biomed. Eng.* **39**, 1232-1243, doi:10.1109/10.184699 (1992).

84 McKusick, V. A. & Hamosh, A. *Timothy syndrome; TS*, <https://www.omim.org/entry/601005> (2019).

85 Remme, C. A., Verkerk, A. O., Hoogaars, W. M. *et al.* The cardiac sodium channel displays differential distribution in the conduction system and transmural heterogeneity in the murine ventricular myocardium. *Basic Res Cardiol* **104**, 511-522, doi:10.1007/s00395-009-0012-8 (2009).
86 Leo-Macias, A., Agullo-Pascual, E., Sanchez-Alonso, J. L. *et al.* Nanoscale visualization of functional adhesion/excitability nodes at the intercalated disc. *Nat Commun* **7**, 10342, doi:10.1038/ncomms10342 (2016).
87 Shy, D., Gillet, L., Ogrodnik, J. *et al.* PDZ domain-binding motif regulates cardiomyocyte compartment-specific NaV1.5 channel expression and function. *Circulation* **130**, 147-160, doi:10.1161/circulationaha.113.007852 (2014).
88 Lin, X., Liu, N., Lu, J. *et al.* Subcellular heterogeneity of sodium current properties in adult cardiac ventricular myocytes. *Heart Rhythm* **8**, 1923-1930, doi:10.1016/j.hrthm.2011.07.016 (2011).
89 Rivaud, M. R., Agullo-Pascual, E., Lin, X. *et al.* Sodium Channel Remodeling in Subcellular Microdomains of Murine Failing Cardiomyocytes. *J Am Heart Assoc* **6**, doi:10.1161/JAHA.117.007622 (2017).
90 Wang, J., Ou, S.-W. & Wang, Y.-J. Distribution and function of voltage-gated sodium channels in the nervous system. *Channels* **11**, 534-554, doi:10.1080/19336950.2017.1380758 (2017).
91 Veerman, C. C., Wilde, A. A. & Lodder, E. M. The cardiac sodium channel gene SCN5A and its gene product NaV1.5: Role in physiology and pathophysiology. *Gene* **573**, 177-187, doi:10.1016/j.gene.2015.08.062 (2015).
92 Black, J. A. & Waxman, S. G. Noncanonical roles of voltage-gated sodium channels. *Neuron* **80**, 280-291, doi:10.1016/j.neuron.2013.09.012 (2013).
93 Rook, M. B., Evers, M. M., Vos, M. A. & Bierhuizen, M. F. Biology of cardiac sodium channel Nav1.5 expression. *Cardiovasc. Res.* **93**, 12-23, doi:10.1093/cvr/cvr252 (2012).
94 van Stuijvenberg, L., Yildirim, C., Kok, B. G. *et al.* Alternative promoter usage and splicing of the human SCN5A gene contribute to transcript heterogeneity. *DNA Cell Biol.* **29**, 577-587, doi:10.1089/dna.2009.0999 (2010).
95 Makielski, J. C., Ye, B., Valdivia, C. R., Pagel, M. D., Pu, J., Tester, D. J. & Ackerman, M. J. A ubiquitous splice variant and a common polymorphism affect heterologous expression of recombinant human SCN5A heart sodium channels. *Circ. Res.* **93**, 821-828, doi:10.1161/01.RES.0000096652.14509.96 (2003).
96 Yamagishi, T., Janecki, M., Marban, E. & Tomaselli, G. F. Topology of the P segments in the sodium channel pore revealed by cysteine mutagenesis. *Biophys. J.* **73**, 195-204, doi:10.1016/S0006-3495(97)78060-3 (1997).
97 Payandeh, J., Scheuer, T., Zheng, N. & Catterall, W. A. The crystal structure of a voltage-gated sodium channel. *Nature* **475**, 353, doi:10.1038/nature10238 (2011).
98 West, J. W., Patton, D. E., Scheuer, T., Wang, Y., Goldin, A. L. & Catterall, W. A. A cluster of hydrophobic amino acid residues required for fast Na(+)-channel inactivation. *Proc Natl Acad Sci U S A* **89**, 10910-10914, doi:10.1073/pnas.89.22.10910 (1992).
99 Kellenberger, S., Scheuer, T. & Catterall, W. A. Movement of the Na+ channel inactivation gate during inactivation. *J. Biol. Chem.* **271**, 30971-30979, doi:10.1074/jbc.271.48.30971 (1996).
100 Sula, A., Booker, J., Ng, L. C., Naylor, C. E., DeCaen, P. G. & Wallace, B. A. The complete structure of an activated open sodium channel. *Nat Commun* **8**, 14205, doi:10.1038/ncomms14205 (2017).
101 Shen, H., Zhou, Q., Pan, X., Li, Z., Wu, J. & Yan, N. Structure of a eukaryotic voltage-gated sodium channel at near-atomic resolution. *Science* **355**, doi:10.1126/science.aal4326 (2017).
102 Marionneau, C. & Abriel, H. Regulation of the cardiac Na+ channel NaV1.5 by post-translational modifications. *J. Mol. Cell Cardiol.* **82**, 36-47, doi:10.1016/j.yjmcc.2015.02.013 (2015).
103 Zhang, Y., Hartmann, H. A. & Satin, J. Glycosylation influences voltage-dependent gating of cardiac and skeletal muscle sodium channels. *J. Membr. Biol.* **171**, 195-207 (1999).
104 Stocker, P. J. & Bennett, E. S. Differential sialylation modulates voltage-gated Na+ channel gating throughout the developing myocardium. *J. Gen. Physiol.* **127**, 253-265, doi:10.1085/jgp.200509423 (2006).
105 Mercier, A., Clement, R., Harnois, T., Bourmeyster, N., Bois, P. & Chatelier, A. Nav1.5 channels can reach the plasma membrane through distinct N-glycosylation states. *Biochim. Biophys. Acta* **1850**, 1215-1223, doi:10.1016/j.bbagen.2015.02.009 (2015).
106 Rougier, J. S., van Bemmelen, M. X., Bruce, M. C. *et al.* Molecular determinants of voltage-gated sodium channel regulation by the Nedd4/Nedd4-like proteins. *Am. J. Physiol. Cell Physiol.* **288**, C692-701, doi:10.1152/ajpcell.00460.2004 (2005).
107 Luo, L., Ning, F., Du, Y. *et al.* Calcium-dependent Nedd4-2 upregulation mediates degradation of the cardiac sodium channel Nav1.5: implications for heart failure. *Acta Physiol (Oxf)* **221**, 44-58, doi:10.1111/apha.12872 (2017).
108 Minegishi, S., Ishigami, T., Kawamura, H. *et al.* An Isoform of Nedd4-2 Plays a Pivotal Role in Electrophysiological Cardiac Abnormalities. *Int J Mol Sci* **18**, doi:10.3390/ijms18061268 (2017).

109 Edokobi, N. & Isom, L. L. Voltage-Gated Sodium Channel beta1/beta1B Subunits Regulate Cardiac Physiology and Pathophysiology. *Front. Physiol.* **9**, 351, doi:10.3389/fphys.2018.00351 (2018).

110 Namadurai, S., Balasuriya, D., Rajappa, R. *et al.* Crystal structure and molecular imaging of the Nav channel beta3 subunit indicates a trimeric assembly. *J. Biol. Chem.* **289**, 10797-10811, doi:10.1074/jbc.M113.527994 (2014).

111 Abriel, H. Cardiac sodium channel Na(v)1.5 and interacting proteins: Physiology and pathophysiology. *J. Mol. Cell Cardiol.* **48**, 2-11, doi:10.1016/j.yjmcc.2009.08.025 (2010).

112 O'Malley, H. A. & Isom, L. L. Sodium channel beta subunits: emerging targets in channelopathies. *Annu. Rev. Physiol.* **77**, 481-504, doi:10.1146/annurev-physiol-021014-071846 (2015).

113 Kazarinova-Noyes, K., Malhotra, J. D., McEwen, D. P. *et al.* Contactin associates with Na+ channels and increases their functional expression. *J. Neurosci.* **21**, 7517-7525 (2001).

114 Matamoros, M., Perez-Hernandez, M., Guerrero-Serna, G. *et al.* Nav1.5 N-terminal domain binding to alpha1-syntrophin increases membrane density of human Kir2.1, Kir2.2 and Nav1.5 channels. *Cardiovasc. Res.* **110**, 279-290, doi:10.1093/cvr/cvw009 (2016).

115 Yang, B., Jung, D., Rafael, J. A., Chamberlain, J. S. & Campbell, K. P. Identification of alpha-syntrophin binding to syntrophin triplet, dystrophin, and utrophin. *J. Biol. Chem.* **270**, 4975-4978, doi:10.1074/jbc.270.10.4975 (1995).

116 Petitprez, S., Zmoos, A. F., Ogrodnik, J. *et al.* SAP97 and dystrophin macromolecular complexes determine two pools of cardiac sodium channels Nav1.5 in cardiomyocytes. *Circ. Res.* **108**, 294-304, doi:10.1161/CIRCRESAHA.110.228312 (2011).

117 Rougier, J.-S., Essers, M. C., Gillet, L., Guichard, S., Sonntag, S., Shmerling, D. & Abriel, H. A Distinct Pool of Nav1.5 Channels at the Lateral Membrane of Murine Ventricular Cardiomyocytes. *Front. Physiol.* **10**, doi:10.3389/fphys.2019.00834 (2019).

118 Gillet L, J. R., D Shy, S Sonntag, N Mougenot, M Essers, D Shmerling, E Balse, SN Hatem, H Abriel. Cardiac-specific ablation of synapse-associated protein SAP97 in mice decreases potassium currents but not sodium current. *Heart Rhythm* **12**, 181-192, doi:10.1016/j.hrthm.2014.09.057 (2015).

119 Abi-Char, J., El-Haou, S., Balse, E., Neyroud, N., Vranckx, R., Coulombe, A. & Hatem, S. N. The anchoring protein SAP97 retains Kv1.5 channels in the plasma membrane of cardiac myocytes. *Am. J. Physiol. Heart Circ. Physiol.* **294**, H1851-1861, doi:10.1152/ajpheart.01045.2007 (2008).

120 El-Haou, S., Balse, E., Neyroud, N. *et al.* Kv4 potassium channels form a tripartite complex with the anchoring protein SAP97 and CaMKII in cardiac myocytes. *Circ. Res.* **104**, 758-769, doi:10.1161/CIRCRESAHA.108.191007 (2009).

121 Godreau, D., Vranckx, R., Maguy, A., Goyenvalle, C. & Hatem, S. N. Different isoforms of synapse-associated protein, SAP97, are expressed in the heart and have distinct effects on the voltage-gated K+ channel Kv1.5. *J. Biol. Chem.* **278**, 47046-47052, doi:10.1074/jbc.M308463200 (2003).

122 Yaffe, M. B. MAGUK SH3 domains--swapped and stranded by their kinases? *Structure* **10**, 3-5 (2002).

123 Jaka, O., Casas-Fraile, L., Lopez de Munain, A. & Saenz, A. Costamere proteins and their involvement in myopathic processes. *Expert Rev Mol Med* **17**, e12, doi:10.1017/erm.2015.9 (2015).

124 Gao, Q. Q. & McNally, E. M. The Dystrophin Complex: Structure, Function, and Implications for Therapy. *Compr Physiol* **5**, 1223-1239, doi:10.1002/cphy.c140048 (2015).

125 D'Amario, D., Amodeo, A., Adorisio, R. *et al.* A current approach to heart failure in Duchenne muscular dystrophy. *Heart* **103**, 1770-1779, doi:10.1136/heartjnl-2017-311269 (2017).

126 Gavillet, B., Rougier, J. S., Domenighetti, A. A. *et al.* Cardiac sodium channel Nav1.5 is regulated by a multiprotein complex composed of syntrophins and dystrophin. *Circ. Res.* **99**, 407-414, doi:10.1161/01.RES.0000237466.13252.5e (2006).

127 Lorin, C., Gueffier, M., Bois, P., Faivre, J. F., Cognard, C. & Sebille, S. Ultrastructural and functional alterations of EC coupling elements in mdx cardiomyocytes: an analysis from membrane surface to depth. *Cell Biochem Biophys* **66**, 723-736, doi:10.1007/s12013-013-9517-8 (2013).

128 Fanchaouy, M., Polakova, E., Jung, C., Ogrodnik, J., Shirokova, N. & Niggli, E. Pathways of abnormal stress-induced Ca2+ influx into dystrophic mdx cardiomyocytes. *Cell Calcium* **46**, 114-121, doi:10.1016/j.ceca.2009.06.002 (2009).

129 Batchelor, C. L. & Winder, S. J. Sparks, signals and shock absorbers: how dystrophin loss causes muscular dystrophy. *Trends Cell Biol.* **16**, 198-205, doi:10.1016/j.tcb.2006.02.001 (2006).

130 Albesa, M., Ogrodnik, J., Rougier, J. S. & Abriel, H. Regulation of the cardiac sodium channel Nav1.5 by utrophin in dystrophin-deficient mice. *Cardiovasc. Res.* **89**, 320-328, doi:10.1093/cvr/cvq326 (2011).

131 Garcia-Pelagio, K. P., Bloch, R. J., Ortega, A. & Gonzalez-Serratos, H. Biomechanics of the sarcolemma and costameres in single skeletal muscle fibers from normal and dystrophin-null mice. *J. Muscle Res. Cell Motil.* **31**, 323-336, doi:10.1007/s10974-011-9238-9 (2011).

132 Eichel, C. A., Beuriot, A., Chevalier, M. Y. *et al.* Lateral membrane-specific MAGUK CASK down-regulates NaV1.5 channel in cardiac myocytes. *Circ. Res.* **119**, 544-556, doi:10.1161/circresaha.116.309254 (2016).
133 Nafzger, S. & Rougier, J. S. Calcium/calmodulin-dependent serine protein kinase CASK modulates the L-type calcium current. *Cell Calcium* **61**, 10-21, doi:10.1016/j.ceca.2016.10.001 (2017).
134 Chevalier, M. *Regulation of the cardiac sodium channel Nav1.5 by CASK and calcineurin* PhD in Biomedical Sciences thesis, University of Bern, (2017).
135 Sun, R., Su, Y., Zhao, X. *et al.* Human calcium/calmodulin-dependent serine protein kinase regulates the expression of p21 via the E2A transcription factor. *Biochem. J.* **419**, 457-466, doi:10.1042/BJ20080515 (2009).
136 Hsueh, Y. P., Wang, T. F., Yang, F. C. & Sheng, M. Nuclear translocation and transcription regulation by the membrane-associated guanylate kinase CASK/LIN-2. *Nature* **404**, 298-302, doi:10.1038/35005118 (2000).
137 Atack, T. C., Stroud, D. M., Watanabe, H. *et al.* Informatic and functional approaches to identifying a regulatory region for the cardiac sodium channel. *Circ. Res.* **109**, 38-46, doi:10.1161/CIRCRESAHA.110.235630 (2011).
138 Macke, J. P. & Kniffin, C. L. *Calcium/calmodulin-dependent serine protein kinase; CASK*, <https://www.omim.org/entry/300172> (2013).
139 Reinstein, E., Tzur, S., Bormans, C. & Behar, D. M. Exome sequencing identified mutations in CASK and MYBPC3 as the cause of a complex dilated cardiomyopathy phenotype. *Genet Res (Camb)* **98**, e8, doi:10.1017/S0016672316000045 (2016).
140 Savio-Galimberti, E., Argenziano, M. & Antzelevitch, C. Cardiac Arrhythmias Related to Sodium Channel Dysfunction. *Handb Exp Pharmacol* **246**, 331-354, doi:10.1007/164_2017_43 (2018).
141 Aoki, H., Nakamura, Y., Ohno, S., Makiyama, T. & Horie, M. Cardiac conduction defects and Brugada syndrome: A family with overlap syndrome carrying a nonsense SCN5A mutation. *J Arrhythm* **33**, 35-39, doi:10.1016/j.joa.2016.05.007 (2017).
142 Remme, C. A., Wilde, A. A. & Bezzina, C. R. Cardiac sodium channel overlap syndromes: different faces of SCN5A mutations. *Trends Cardiovasc. Med.* **18**, 78-87, doi:10.1016/j.tcm.2008.01.002 (2008).
143 Probst, V., Kyndt, F., Potet, F. *et al.* Haploinsufficiency in combination with aging causes SCN5A-linked hereditary Lenegre disease. *J. Am. Coll. Cardiol.* **41**, 643-652, doi:10.1016/S0735-1097(02)02864-4 (2003).
144 Brugada, P. Brugada syndrome: More than 20 years of scientific excitement. *J Cardiol* **67**, 215-220, doi:10.1016/j.jjcc.2015.08.009 (2016).
145 Dolz-Gaiton, P., Nunez, M., Nunez, L. *et al.* Functional characterization of a novel frameshift mutation in the C-terminus of the Nav1.5 channel underlying a Brugada syndrome with variable expression in a Spanish family. *PLoS One* **8**, e81493, doi:10.1371/journal.pone.0081493 (2013).
146 Brugada, P. & Brugada, J. Right bundle branch block, persistent ST segment elevation and sudden cardiac death: a distinct clinical and electrocardiographic syndrome. A multicenter report. *J. Am. Coll. Cardiol.* **20**, 1391-1396 (1992).
147 Remme, C. A. Cardiac sodium channelopathy associated with SCN5A mutations: electrophysiological, molecular and genetic aspects. *J. Physiol.* **591**, 4099-4116, doi:10.1113/jphysiol.2013.256461 (2013).
148 Chadda, K. R., Jeevaratnam, K., Lei, M. & Huang, C. L. Sodium channel biophysics, late sodium current and genetic arrhythmic syndromes. *Pflugers Arch* **469**, 629-641, doi:10.1007/s00424-017-1959-1 (2017).
149 Noble, D. & Noble, P. J. Late sodium current in the pathophysiology of cardiovascular disease: consequences of sodium-calcium overload. *Heart* **92 Suppl 4**, iv1-iv5, doi:10.1136/hrt.2005.078782 (2006).
150 Koleske, M., Bonilla, I., Thomas, J. *et al.* Tetrodotoxin-sensitive Navs contribute to early and delayed afterdepolarizations in long QT arrhythmia models. *J. Gen. Physiol.* **150**, 991-1002, doi:10.1085/jgp.201711909 (2018).
151 Radwanski, P. B., Johnson, C. N., Gyorke, S. & Veeraraghavan, R. Cardiac Arrhythmias as Manifestations of Nanopathies: An Emerging View. *Front. Physiol.* **9**, 1228, doi:10.3389/fphys.2018.01228 (2018).
152 Yang, T., Atack, T. C., Stroud, D. M., Zhang, W., Hall, L. & Roden, D. M. Blocking Scn10a channels in heart reduces late sodium current and is antiarrhythmic. *Circ. Res.* **111**, 322-332, doi:10.1161/CIRCRESAHA.112.265173 (2012).
153 Mishra, S., Reznikov, V., Maltsev, V. A., Undrovinas, N. A., Sabbah, H. N. & Undrovinas, A. Contribution of sodium channel neuronal isoform Nav1.1 to late sodium current in ventricular myocytes from failing hearts. *J. Physiol.* **593**, 1409-1427, doi:10.1113/jphysiol.2014.278259 (2015).
154 Chambers, J. C., Zhao, J., Terracciano, C. M. *et al.* Genetic variation in SCN10A influences cardiac conduction. *Nat. Genet.* **42**, 149-152, doi:10.1038/ng.516 (2010).

155 Radwanski, P. B., Ho, H. T., Veeraraghavan, R. *et al.* Neuronal Na(+) Channels Are Integral Components of Pro-arrhythmic Na(+)/Ca(2+) Signaling Nanodomain That Promotes Cardiac Arrhythmias During beta-adrenergic Stimulation. *JACC Basic Transl. Sci.* **1**, 251-266, doi:10.1016/j.jacbts.2016.04.004 (2016).
156 Marionneau, C., Lichti, C. F., Lindenbaum, P., Charpentier, F., Nerbonne, J. M., Townsend, R. R. & Merot, J. Mass spectrometry-based identification of native cardiac Nav1.5 channel alpha subunit phosphorylation sites. *J. Proteome Res.* **11**, 5994-6007, doi:10.1021/pr300702c (2012).
157 Wu, G., Ai, T., Kim, J. J. *et al.* alpha-1-syntrophin mutation and the long-QT syndrome: a disease of sodium channel disruption. *Circ Arrhythm Electrophysiol* **1**, 193-201, doi:10.1161/CIRCEP.108.769224 (2008).
158 McKusick, V. A. & O'Neill, M. J. F. *Syntrophin, Alpha-1; SNTA1*, <https://www.omim.org/entry/601017> (2019).
159 Crotti, L., Johnson, C. N., Graf, E. *et al.* Calmodulin mutations associated with recurrent cardiac arrest in infants. *Circulation* **127**, 1009-1017, doi:10.1161/CIRCULATIONAHA.112.001216 (2013).
160 London, B., Michalec, M., Mehdi, H. *et al.* Mutation in glycerol-3-phosphate dehydrogenase 1 like gene (GPD1-L) decreases cardiac Na+ current and causes inherited arrhythmias. *Circulation* **116**, 2260-2268, doi:10.1161/CIRCULATIONAHA.107.703330 (2007).
161 Scicluna, B. P., Wilde, A. A. & Bezzina, C. R. The primary arrhythmia syndromes: same mutation, different manifestations. Are we starting to understand why? *J Cardiovasc Electrophysiol* **19**, 445-452, doi:10.1111/j.1540-8167.2007.01073.x (2008).
162 Casini, S., Verkerk, A. O., van Borren, M. M., van Ginneken, A. C., Veldkamp, M. W., de Bakker, J. M. & Tan, H. L. Intracellular calcium modulation of voltage-gated sodium channels in ventricular myocytes. *Cardiovasc. Res.* **81**, 72-81, doi:10.1093/cvr/cvn274 (2009).
163 Greer-Short, A., George, S. A., Poelzing, S. & Weinberg, S. H. Revealing the Concealed Nature of Long-QT Type 3 Syndrome. *Circ Arrhythm Electrophysiol* **10**, e004400, doi:10.1161/CIRCEP.116.004400 (2017).
164 Kane, C. & Terracciano, C. M. N. Concise Review: Criteria for Chamber-Specific Categorization of Human Cardiac Myocytes Derived from Pluripotent Stem Cells. *Stem Cells* **35**, 1881-1897, doi:10.1002/stem.2649 (2017).
165 Sanford, J. L., Edwards, J. D., Mays, T. A., Gong, B., Merriam, A. P. & Rafael-Fortney, J. A. Claudin-5 localizes to the lateral membranes of cardiomyocytes and is altered in utrophin/dystrophin-deficient cardiomyopathic mice. *J. Mol. Cell Cardiol.* **38**, 323-332, doi:10.1016/j.yjmcc.2004.11.025 (2005).
166 Mays, T. A., Binkley, P. F., Lesinski, A. *et al.* Claudin-5 levels are reduced in human end-stage cardiomyopathy. *J. Mol. Cell Cardiol.* **45**, 81-87, doi:10.1016/j.yjmcc.2008.04.005 (2008).
167 Viola, H. M., Adams, A. M., Davies, S. M., Fletcher, S., Filipovska, A. & Hool, L. C. Impaired functional communication between the L-type calcium channel and mitochondria contributes to metabolic inhibition in the mdx heart. *Proc Natl Acad Sci U S A* **111**, E2905-2914, doi:10.1073/pnas.1402544111 (2014).
168 Balse, E., Steele, D. F., Abriel, H., Coulombe, A., Fedida, D. & Hatem, S. N. Dynamic of ion channel expression at the plasma membrane of cardiomyocytes. *Physiol. Rev.* **92**, 1317-1358, doi:10.1152/physrev.00041.2011 (2012).
169 Gu, Y., Gorelik, J., Spohr, H. A. *et al.* High-resolution scanning patch-clamp: new insights into cell function. *FASEB J.* **16**, 748-750, doi:10.1096/fj.01-1024fje (2002).
170 Bhargava, A., Lin, X., Novak, P., Mehta, K., Korchev, Y., Delmar, M. & Gorelik, J. Super-resolution scanning patch clamp reveals clustering of functional ion channels in adult ventricular myocyte. *Circ. Res.* **112**, 1112-1120, doi:10.1161/CIRCRESAHA.111.300445 (2013).
171 Duan, D. D. Phenomics of cardiac chloride channels. *Compr Physiol* **3**, 667-692, doi:10.1002/cphy.c110014 (2013).
172 Wright, P. T., Sanchez-Alonso, J. L., Lucarelli, C. *et al.* Partial Mechanical Unloading of the Heart Disrupts L-Type Calcium Channel and Beta-Adrenoceptor Signaling Microdomains. *Front. Physiol.* **9**, 1302, doi:10.3389/fphys.2018.01302 (2018).
173 Severs, N. J., Bruce, A. F., Dupont, E. & Rothery, S. Remodelling of gap junctions and connexin expression in diseased myocardium. *Cardiovasc. Res.* **80**, 9-19, doi:10.1093/cvr/cvn133 (2008).
174 Vermij, S. H., Abriel, H. & Kucera, J. P. A fundamental evaluation of the electrical properties and function of cardiac transverse tubules. *Biochim. Biophys. Acta*, doi:https://doi.org/10.1016/j.bbamcr.2019.06.016 (2019).
175 Vermij, S. H., Rougier, J.-S., Agulló-Pascual, E., Rothenberg, E., Delmar, M. & Abriel, H. Single-molecule localization of Na<sub>v</sub>1.5 reveals different modes of reorganization at the lateral membrane and T-tubules of cardiomyocytes. *bioRxiv*, 674275, doi:10.1101/674275 (2019).
176 Matsumoto, M., Hiyama, T. Y., Kuboyama, K., Suzuki, R., Fujikawa, A. & Noda, M. Channel properties of Nax expressed in neurons. *PLoS One* **10**, e0126109, doi:10.1371/journal.pone.0126109 (2015).

177 Amarouch, M.-Y., Kasimova, M. A., Tarek, M. & Abriel, H. Functional interaction between S1 and S4 segments in voltage-gated sodium channels revealed by human channelopathies. *Channels* **8**, 414-420, doi:10.4161/19336950.2014.958922 (2014).
178 Kaufmann, S. G., Westenbroek, R. E., Maass, A. H. *et al.* Distribution and function of sodium channel subtypes in human atrial myocardium. *J. Mol. Cell Cardiol.* **61**, 133-141, doi:10.1016/j.yjmcc.2013.05.006 (2013).
179 Vermij, S. H., Abriel, H. & Kucera, J. P. Modelling depolarization delay, sodium currents, and electrical potentials in cardiac transverse tubules. *bioRxiv*, 611558, doi:10.1101/611558 (2019).
180 Hong, T., Yang, H., Zhang, S. S. *et al.* Cardiac BIN1 folds T-tubule membrane, controlling ion flux and limiting arrhythmia. *Nat. Med.* **20**, 624-632, doi:10.1038/nm.3543 (2014).
181 Scardigli, M., Crocini, C., Ferrantini, C. *et al.* Quantitative assessment of passive electrical properties of the cardiac T-tubular system by FRAP microscopy. *Proc. Natl. Acad. Sci. USA* **114**, 5737-5742, doi:10.1073/pnas.1702188114 (2017).
182 Song, L. S., Sobie, E. A., McCulle, S., Lederer, W. J., Balke, C. W. & Cheng, H. Orphaned ryanodine receptors in the failing heart. *Proc. Natl. Acad. Sci. USA* **103**, 4305-4310, doi:10.1073/pnas.0509324103 (2006).
183 Prins, K. W., Asp, M. L., Zhang, H., Wang, W. & Metzger, J. M. Microtubule-Mediated Misregulation of Junctophilin-2 Underlies T-Tubule Disruptions and Calcium Mishandling in mdx Mice. *JACC Basic Transl. Sci.* **1**, 122-130, doi:10.1016/j.jacbts.2016.02.002 (2016).
184 Kekenes-Huskey, P. M., Cheng, Y., Hake, J. E. *et al.* Modeling effects of L-type ca(2+) current and na(+)-ca(2+) exchanger on ca(2+) trigger flux in rabbit myocytes with realistic T-tubule geometries. *Front. Physiol.* **3**, 351, doi:10.3389/fphys.2012.00351 (2012).
185 Hatano, A., Okada, J., Washio, T., Hisada, T. & Sugiura, S. An integrated finite element simulation of cardiomyocyte function based on triphasic theory. *Front. Physiol.* **6**, 287, doi:10.3389/fphys.2015.00287 (2015).
186 Hong, T. T., Smyth, J. W., Gao, D. *et al.* BIN1 localizes the L-type calcium channel to cardiac T-tubules. *PLoS Biol.* **8**, e1000312, doi:10.1371/journal.pbio.1000312 (2010).
187 Neco, P., Rose, B., Huynh, N., Zhang, R., Bridge, J. H., Philipson, K. D. & Goldhaber, J. I. Sodium-calcium exchange is essential for effective triggering of calcium release in mouse heart. *Biophys. J.* **99**, 755-764, doi:10.1016/j.bpj.2010.04.071 (2010).
188 Lee, C. H. & Ruben, P. C. Interaction between voltage-gated sodium channels and the neurotoxin, tetrodotoxin. *Channels* **2**, 407-412, doi:10.4161/chan.2.6.7429 (2008).
189 Tsukamoto, T., Chiba, Y., Wakamori, M. *et al.* Differential binding of tetrodotoxin and its derivatives to voltage-sensitive sodium channel subtypes (Nav 1.1 to Nav 1.7). *Br. J. Pharmacol.* **174**, 3881-3892, doi:10.1111/bph.13985 (2017).

## 5.1 Illustrations title pages

- Introduction:
  - Open-source anatomical drawing of the heart (*https://www.kisscc0.com/clipart/drawing-anatomy-heart-diagram-organ-anatomical-hea-45dw6d/*)
- Aims & Hypotheses:
  - Tools of Vesalius' trade featured in *De humani corporis fabrica* (1543). (*https://publicdomainreview.org/2013/04/18/vesalius-and-the-body-metaphor/*)
- Results:
  - Woodcut illustration of the heart and surrounding anatomical structures by Vesalius from *De humani corporis fabrica*, 1543. (*https://tinyurl.com/VesaliusHeart*)
- General conclusion & References:
  - Fetal great vessels, heart, ductus arteriosus, and lung by Fabricius from *De formato foetu*, 1600. (*https://fn.bmj.com/content/88/2/F157*)
- CV, acknowledgments, declaration of originality:
  - An experiment by William Harvey from *Exercitato anatomica de motu cordis et sanguinis in animalibus*, 1628. *(https://tinyurl.com/HarveyDeMotu*)

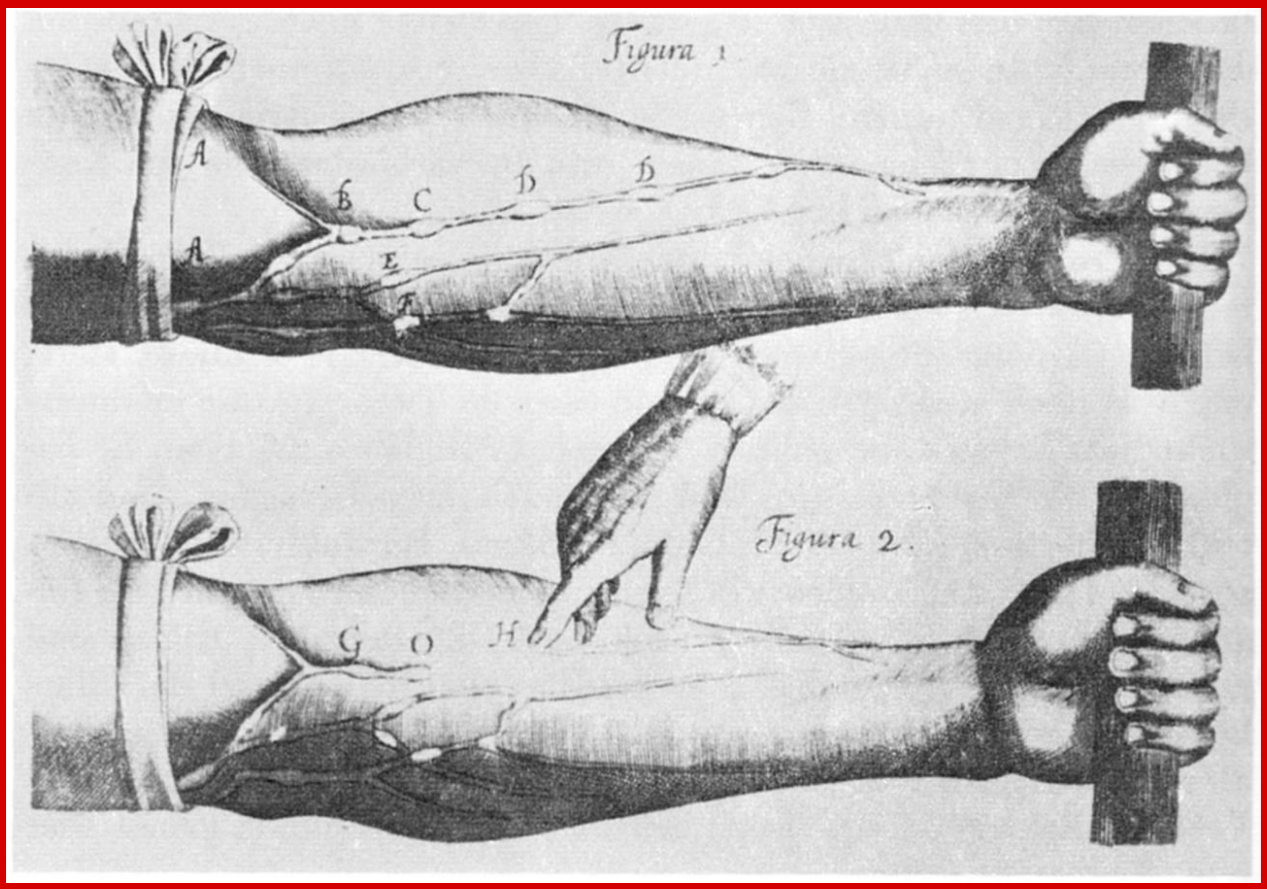


# CV, ACKNOWLEDGMENTS, DECLARATION OF ORIGINALITY

# 6. ACKNOWLEDGMENTS

This thesis is by no means a one-woman operation, and I wish to thank everyone who has been a part of my journey during these last four years.

I'm especially grateful to Hugues: you welcomed me to your group, taught me a lot, created many opportunities to travel to other labs and conferences, and gave me lots of freedom to do research my way, which wasn't always easy, but which I really started to appreciate during the second half of my PhD. I've enjoyed our discussions, whether they were on science, feminism, or hyphens, especially when we did not agree.

I'm very grateful to the members of my thesis committee: to Stephan Rohr for our good discussions on science and scientific careers; to Daniel Fuster for keeping track of my progress; and to Carol Ann Remme for taking the time to carefully read my thesis.

I had the privilege of performing 10 months of research in New York, which wouldn't have been possible without Mario Delmar. Mario, I'm very grateful that you invited me into your lab again, you're inspiring to work with, and I learned so much from you. Eli Rothenberg: thank you very much for letting me play with your microscopes, and for your thorough feedback on my writing! It's been a privilege to work with you.

Furthermore, I'd like to express my gratitude towards Jan Kucera and Toon van Veen. Jan, I learned so much from you about physiology. I'm amazed by how spontaneously you got on board on the T-tubules project, and how much time and effort you invested to make our two publications a success. I'm also very grateful that you invited me to the Ephaptic conference in Roanoke, and I very much enjoyed our discussions on science, music, and whiskey. Toon, I am very happy that you rekindled my enthusiasm for science during my master's degree. Thanks for sending me to Mario's lab, where I met Hugues, so this thesis wouldn't have existed without your guidance. Thanks also for your efforts turning my master's thesis into a great publication!

I am much indebted to all the members of the lab. You have made the everyday lab life a real pleasure. Firstly, to JS for always (always!) being available for questions and discussions, for constantly being in a good mood (incredible!), and for caring so much about my - and everyone's - projects. Also to Maria: thanks for your dedication to the lab, your help with everything, and the many chats we had! Sabi, it's been a lot of fun (practically) sharing a desk with you. You're very smart and full of temperament. Thanks for your great work managing the mice.

Many thanks to the postdocs and fellow PhD students, past and present: Zizun, Prakash, Mey, Ludo, Lijo, Urs, Diana, Dani, Valentin, Beatrice, Morgan, Yao-Peng and Yassine. Zizun, you're remarkably driven, meticulous and fun, and you brighten up the lab as soon as you set foot in it. Please never let

go of your label writer. Dani, you're a great scientist and I'll never forget your huge zucchini and your home-made Apfelschnaps! Diana, thanks for teaching me invaluable lessons in your last and my first months in the lab. And a very special thanks to Morgan. We've been through a lot together: bringing mice to Paris, driving through a snow storm in the middle of the night, swimming with horse shoe crabs in Woods Hole, Massachusetts...

Thanks to Christian for invaluable confocal microscopy advice, and to Patricia, Kathrin, and Ronja - it's been great to work with you! Also many thanks to Laurent: you were amazing in accommodating all my terabytes of data and finding me a great new PC to work with my huge files.

Also many thanks to Verena and Kevin for their fantastic work as secretaries, and for being so nice throughout all the bureaucracy I needed you for.

I'm also incredibly grateful to my awesome colleagues in New York: Esperanza, Sandra, Marta, Kim, Ming, Lin, Joanne, and Kabir in the Delmar lab, and to Yandong, Chelsea, Donna and Maria in the Rothenberg lab. Esperanza, thanks for your friendship and your technical advice. Sandra and Marta, thanks for all the good times inside and outside of the lab, and for being such a great help whenever I needed you (which was often :)). Joanne, het was ontzettend leuk om je te leren kennen! Yandong and Chelsea, you taught me so much about the setup, data processing, and image analysis, and most of all, thanks to your good taste I always looked forward to the food at the lab meetings.

David Fenjö and Sarah Keegan: you were of great help in image analysis, and I'm very happy I could use your codes.

Now there's also such a thing as a work-life balance, and thanks to many wonderful friends, I never had to worry about that. As for my "Swiss" friends, I especially want to thank the Tschakkas from the bottom of my oliebollen-shaped heart: Ann-Ka, Diana, Frauke, Julia, Kika, and Liselot, we're PhD partners in crime and such a great mix of disciplines and cultures. I cherish a plethora of good memories with you and I'm sure each of you will be friends for life. And to all the other wonderful people I met in Bern from all corners of the world: thanks for making me feel at home. You're so many I don't dare to mention each one of you!

I am also very grateful to all my Dutch friends for staying so close despite the distance: de Stinkclub; de allerliefste exen Willemijn en Anne-Floor; Marjon, Elise en Cecile (al 20 jaar!); Suzanne en Annalena; Het Schoone Woord; Nicoline en Dave; Fransien, Inez, en Elisah; Elena, and all the other lovely Dutchies I know.

Also thanks to my New York friends: all the members of the Greenwich Village Orchestra, Joe, and Saurabh: thanks for being so awesome and welcoming.

Also, a big thank you to my family: firstly for a good set of genes, and secondly for teaching me the importance of discipline as well as of fun, for creating an academically and musically stimulating environment (in other words, for turning me into a snob), and for your trust in me to just go out into the world and do my own thing.

Last but not least, a very big merci viumau to my favorite German Andreas. I tend to be a tad on the busy side, and you've been very good at helping me ground and bringing liveliness at the same time.

## Declaration of Originality

**Last name, first name:** Vermij, Sarah

**Matriculation number:** 15-126-337

I hereby declare that this thesis represents my original work and that I have used no other sources except as noted by citations.

All data, tables, figures and text citations which have been reproduced from any other source, including the internet, have been explicitly acknowledged as such.

I am aware that in case of non-compliance, the Senate is entitled to withdraw the doctorate degree awarded to me on the basis of the present thesis, in accordance with the "Statut der Universität Bern (Universitätsstatut; UniSt)", Art. 69, of 7 June 2011.

Place, date

Bern, 29 August 2019

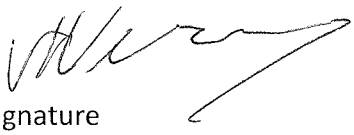

Signature